SEMI-ACTIVE MAGNETO-RHEOLOGICAL DAMPER AND APPLICATIONS IN TENSION LEG PLATFORM / SEMI-SUBMERSIBLE

A Dissertation

by

HOOI SIANG KANG

Submitted to the Office of Graduate and Professional Studies of
Texas A&M University
in partial fulfillment of the requirements for the degree of

DOCTOR OF PHILOSOPHY

Chair of Committee,	Moo Hyun Kim
Committee Members,	Shankar S. Bhat Aramanadka
	Stefan Hurlebaus
	Richard S. Mercier
	Alejandro H. Orsi
Head of Department,	Robin Autenrieth

December 2015

Major Subject: Ocean Engineering

ABSTRACT

A reliable and cost-effective way to protect the hydrocarbon production modules in harsher environments has been crucial to the success of offshore oil and gas projects. Nevertheless, the excessive tension variations in the top-tensioned risers (TTRs) can lead to catastrophic structural integrity issues. Magneto-rheological (MR) damper is a controllable device which can reduce the tension variations. However, the integration and behaviors of MR damper are remained as significant challenge for floating platforms. The main purpose of this research is to develop numerical analysis tool to analyze the specific characteristics of MR damper in offshore structural dynamics and interactively changing the structural behaviors correspond to various external loadings.

The research methodologies were initiated by modeling the hydro-pneumatic tensioner (HPT) of TTR in component-level, which included hydro-pneumatic components and viscous fluid frictional effect. The HPT model was numerically incorporated with MR damper. This numerical tool combined with CHARM3D, a fully-coupled time-domain dynamic analysis program for floating bodies, mooring lines, and risers. The responses of combined numerical model were simulated by coupling with tension leg platform (TLP) and dry-tree semi-submersibles (DTS), respectively, under 100-year extreme condition and 1000-year survival condition of central Gulf of Mexico (GOM). The MR damper was controlled by using semi-active controllers that were developed in fuzzy-logic and skyhook schemes. Mathieu's stability analysis was utilized to predict TTR's parametric stability.

The results manifested that total required stroke length in DTS can be reduced by as much as 0.963 meter in the studied case after MR damper was incorporated with semi-active fuzzy logic controller. By providing damped and deformed contact surface, MR damper was able to redistribute the excessive tension in the tensioner cylinders during extreme bottom-out motion. Moreover, the dynamic tension variations of TTR can be suppressed by 94 percent in the case of TLP. In conclusion, these results are beneficial to assure service life span of TTR's tensioner and moderate the relevant operational expenditure (OPEX). In addition, the reductions of the total required stroke length and tension variations in DTS have enabled the platform designer to be more flexible in the sizing of the DTS and TTR tensioners.

DEDICATION

This dissertation is dedicated, with love and respect, to my parents, my wife, and my children.

ACKNOWLEDGEMENTS

I would like to express the deepest appreciation to my advisor, Dr. Moo-Hyun Kim, for his enlightened guidance, benevolent support, and continuous encouragement throughout the study. For me, he is an exemplary academician inspiring my future career in academia.

Great gratitude to Dr. S. Bhat Aramanadka for his wholehearted involvement and continuous supports in making this research become a reality. His expertise and knowledge from the industry always enlighten my research.

Sincere appreciation to my committee members, Dr. Hurlebaus, Dr. Mercier, Dr. Orsi, and Dr. Zhang for their insightful guidance and generous support.

Thanks also go to my colleagues, Dr. YH Bae, Dr. KS Kim, Dr. HY Kang in Texas A&M University, Mr. Zaid, Mr. L Yong in Shell Oil Company, and my friends, Dr. GC Han, Dr. XC Yu, Dr. ZY Su, Dr. C Peng, Dr. YB Bai, Mr. DX Jia, Mr. YJ Liu, Mr. YZ Zhi, Mr. C Cifuentes, Mr. CK Jin, Mr. JH Jung, Mr. F. Bakti for sharing their valuable knowledge and experience in the ocean engineering. Thanks to my friends and the department faculty and staff for making my time at Texas A&M University a great experience.

Finally, most of all thanks to my parents, parents-in-law, my sister Joanne Kang, my god-sister Evelyn Zhang for their solicitude and encouragement, and to my wife Sandia Sun, for her contribution and love.

NOMENCLATURE

DTS	Dry Tree Semi-submersible
FE	Finite Element
FLC	Fuzzy Logic Controller
HP	Hydro-Pneumatic
HF	High Frequency
LF	Low Frequency
LSRS	Long-Stroke Ram-Style
MR	Magneto-Rheological
NHAF	Nonlinear Hysteretic Arctangent Function
SA	Semi-Active
TLP	Tension Leg Platform
TTF	Top Tension Factor
TTR	Top Tension Riser
WF	Wave Frequency

TABLE OF CONTENTS

Page

Page

Page

LIST OF FIGURES

Page

Page

Page

Page

Page

Page

Page

Page

Page

Page

LIST OF TABLES

Page

1. INTRODUCTION

1.1 Background and Literature Reviews

The exploration and extraction of offshore hydrocarbon as one of the significant energy sources has contributed large amounts of national revenue. Offshore floating structures are designed and treated separately from other existing land-based buildings due to the surrounded environments are the open sea and therefore these structures are prompted to harsher environment impacts and loadings, such as from wind, wave, and ocean current. Typically, the servicing life span of an offshore floating structure is more than twenty years without any significant structural failure. Moreover, the floating structures must be able to survive during the natural extreme conditions, the Hurricane, for instance, to prevent from catastrophic disaster and irreversible environmental and ecological impacts. Hence, the integrity of an offshore floating structure must comply strictly with the standards and regulations enforced by the Minerals Management Services (MMS), the Bureau of Ocean Energy Management, Regulation and Enforcement (BOEMRE), American Petroleum Institute (API), and classification societies. Nevertheless, there are currently stricter revised environmental criteria in the requirements of structural integrity of offshore platform. The dynamic motion control and integrity management of the offshore floating platforms in the United States are critical at this point, especially after this phase of high reoccurrences of 1000-year Hurricane, such as Katrina, Rita, and Ike, and the structural aging of conventional

floating structures and facilities. These risk factors increase the possibilities of the accident and the occurrence of catastrophic disaster.

On the other hand, the newly developing offshore oil and gas fields to deeper water, as shown in Fig. 1.1, lead to different challenges from the previous experiences in the floating platform applicability, dynamic responses, structural integrity, and safety management. The production floaters have been increasing operational water depth from nearly 1,800 m (*5,906 ft*) to nearly 2,500 m (*8,202 ft*) over the last ten years. If there was a reliable and cost-effective way to protect the hydrocarbon production modules (such as marine risers) in unfamiliar harsher environments, the safety of these structures could be more assured while simultaneously providing the expansion of offshore water depth limits to more unconventional areas, with more effective expenditures.

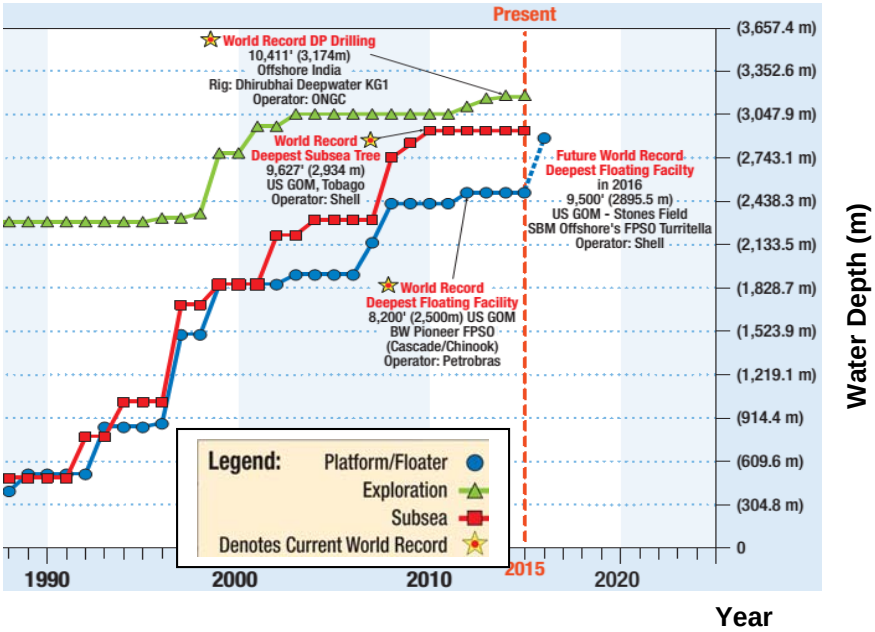

Figure 1.1 Worldwide progression of water depth capabilities for offshore drilling and production (Courtesy of Wood Group Mustang, and PennWell Corporation).

An increasing number of floating offshore production platforms are planned, designed, and built, as illustrated in Fig. 1.2. The main players are floating production storage offloading unit (FPSO), semi-submersible, tension leg platform (TLP), and Spar. With offshore oil field becoming deeper, being moved out further at sea and subjected to ever greater wind and wave forces, it is necessary to analyze the dynamics and minimize the responses of these structures (Colwell and Basu, 2009). According to Patil and Jangid (2005), the wave-induced dynamic force is one of the most important excitations to be dealt with in the design of offshore structures. Furthermore, the coupled motion between the TLP platform and the additional wind-wave-current loadings that induce the vibration in time domain and frequency domain become significant in order to provide an appropriate dynamical model for response mitigation.

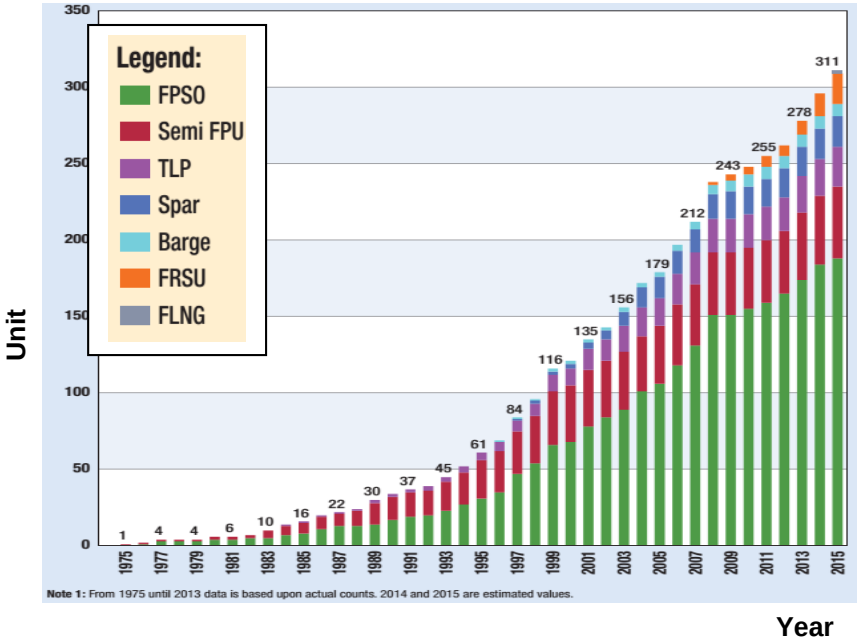

Figure 1.2 Growth in floating production system (1975-2015) (Courtesy of World Energy Report LLC, and PennWell Corporation).

One of the most attractive production selection is the *dry-tree* solution where the production system, such as blow-out preventor (BOP)-stack and production tree can be located on the platform, as illustrated in Fig. 1.3. The intervention and maintenance of the production tree can be directly accessed during the operation (instead of using subsea remote-operating vehicle (ROV) and maintenance vessel to access the production tree located on the seabed) which has significantly reduced the operational expenditures (OPEX). However, the *dry-tree* production system, which is accomplished with top-tension risers (TTRs), is strictly restrained by the vertical motions of the host platform. Therefore, the *dry-tree* technology is currently well-proven only in TLP and Spar type platforms.

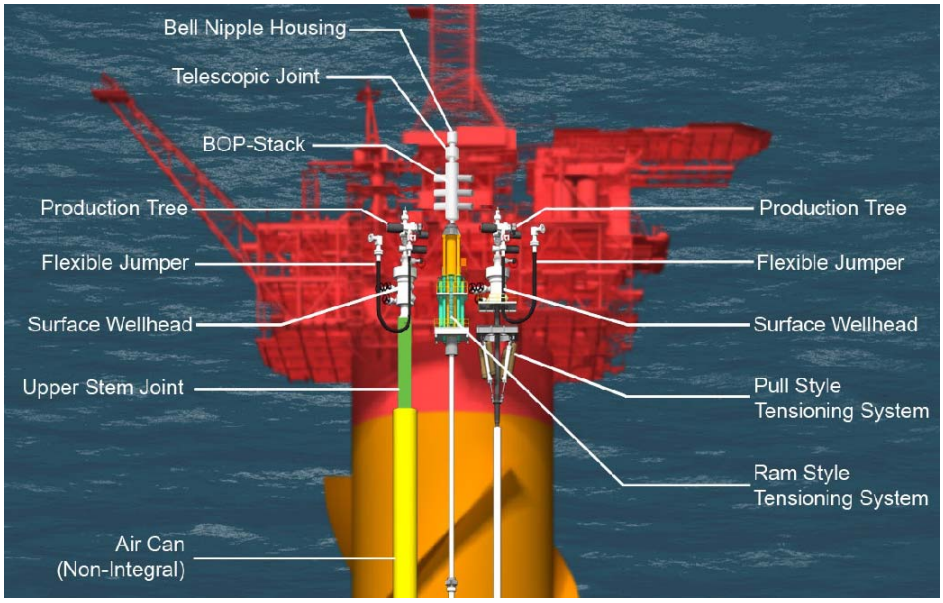

Figure 1.3 Types of top tension risers (TTRs) dry-tree interface (Courtesy of Technip, and PennWell Corporation).

The direct-acting hydro-pneumatic (HP) tensioning systems have become dominant in the more recent offshore field developments. The direct-acting tensioners (DATs) are designed for relatively short strokes and therefore this system is predominately utilized in tension-leg platform (TLP) due to the low heave characteristics of the hull, combined with the relatively small riser length changes associated with small heave motion and set down due to the parallelogram arrangement formed by the platform, tendons, risers, and the seafloor well pattern (Crotwell and Yu, 2011). On the other hand, the ram-style (push style) tensioners with long stroke are to be considered in the newly developed *dry-tree* Semi-submersible concepts (Xiang et al., 2014). The dynamic interaction between the TLP hull and its tendon/riser system plays a significant role in the functionality and safety of the system (Kanda et al., 1998; Kim et al., 2001). As the water depth gets deeper and deeper and the inertia effect increases, the interaction effect greatly influences body and risers motions (Kim, 2004). One of the essential factors to consider is the riser tensioner stroke lengths increasing rapidly with larger vessel offsets and heave displacements in the survival conditions of ultra-deep water (Koos, 2013). A typical top tension riser (TTR) system with the TLP host floater is shown in Fig. 1.4.

For a safer and more reliable design of a TLP in such large depths, the TLP heave-pitch responses and stroke of top tension riser (TTR) at its top joint are very critical issues and need to be seriously considered. In ultra-deep seas, the mass and length of tendons and risers become greater; thus, an accurate estimate of the damping and inertia effects of tendons and risers on the hull motions can only be achieved by

fully coupled analysis programs (Ran, 2000). Kim *et al*. (2001) have conducted nonlinear hull/tendon/riser coupled dynamic analyses of offshore platforms for the first-order and second-order sum- and difference-frequency wave loads and other hydrodynamic coefficients.

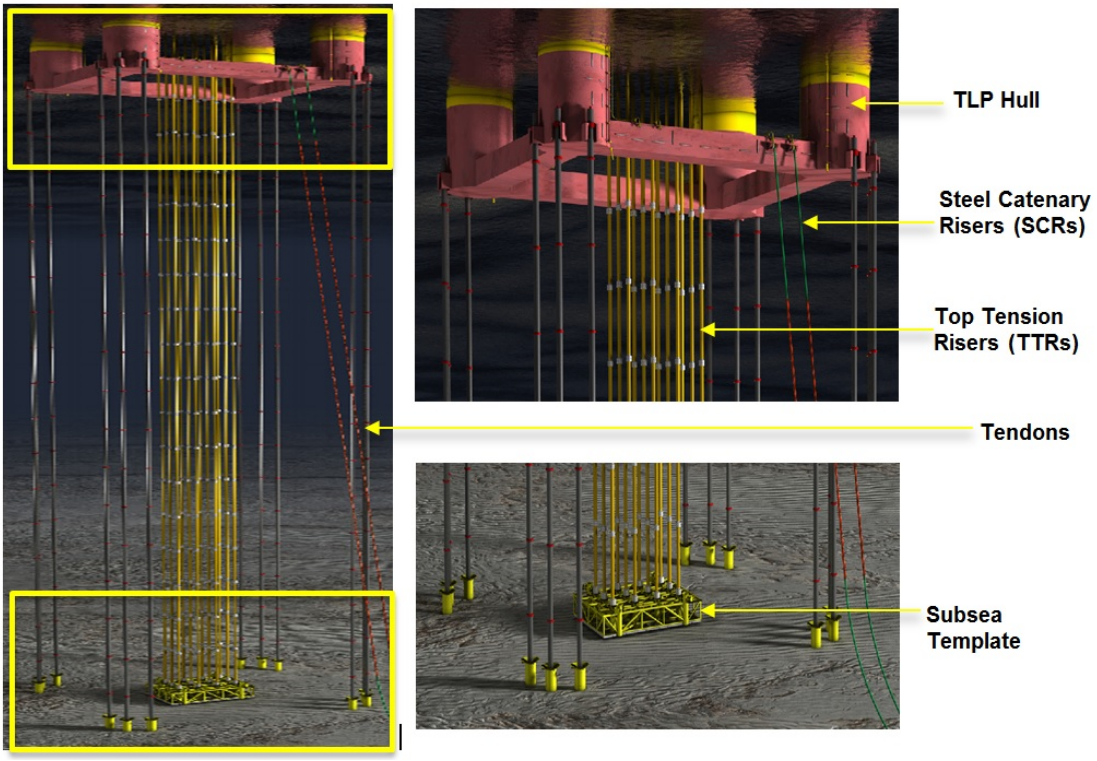

Figure 1.4 Top tension risers (TTRs) and steel catenary risers (SCRs) with TLP (Courtesy of Wood Group Kenney, and PennWell Corporation).

Motion control is a critical part of mitigating the excessive dynamical responses of the modules in floating structures, such as the riser system. The interactive control of the motion of production modules can greatly improve the efficiency and reliability of

offshore hydrocarbon extraction and reduce the risk of system failures. Moreover, offshore floating structures are prompted to long term periodically excitation forces, there are many hidden defects, such as metallically fatigue, could be prevented. Mitigating the dynamic responses of production units in TLP and semisubmersible will require enormous efforts and significant breakthrough in real-time monitoring and structural integrity management; but it would do much to direct the offshore structures toward a safer and more reliable operational limits. If there is a reliable and cost-effective way to monitor the real-time condition and control the vibration of platform and its operating modules, such as the *stroke* of drilling riser, the risk of system failures can be reduced.

Compared to the TLP and Spar, there is an increasing interest from the industry for drilling with high-pressure risers and surface BOPs from the semi-submersible platform units (Zeng et al., 2013), this concept is named as Dry-Tree Semisubmersible (DTS), as illustrated in Fig. 1.5. The DTS has the advantages of (1) easy access to production tree for operations, maintenance, and inspections; (2) direct vertical access for drilling, completion, and workover operation; (3) improve recovery of hydrocarbons (Poll et al., 2013). Xiang et al. (2014) presented the overall design of a TTR system for a DTS interface including ram style tensioner, riser conductor, and riser top assembly design with keel joint. Zeng et al. (2013) discussed the development of DTS by addressing the total value and efficiency of the integrated system during entire life cycle of the product, including design, construction, integration, and installation, operation, and decommission, as well as component reliably and safety.

Nevertheless, the motions of typical semi-submersible platforms are not compatible with existing *dry tree* systems. All dry tree interface system, as illustrated in Fig. 1.3, must allow the TTR to move vertically relative to the hull within the allowable stroke limits. The amount of required stroke depends on the platform heave motion, offset, set-down, thermal growth of the risers, pressure growth across the riser wall, draft changes of the hull, deflection of the riser in the water column, and so on (Poll et al., 2013).

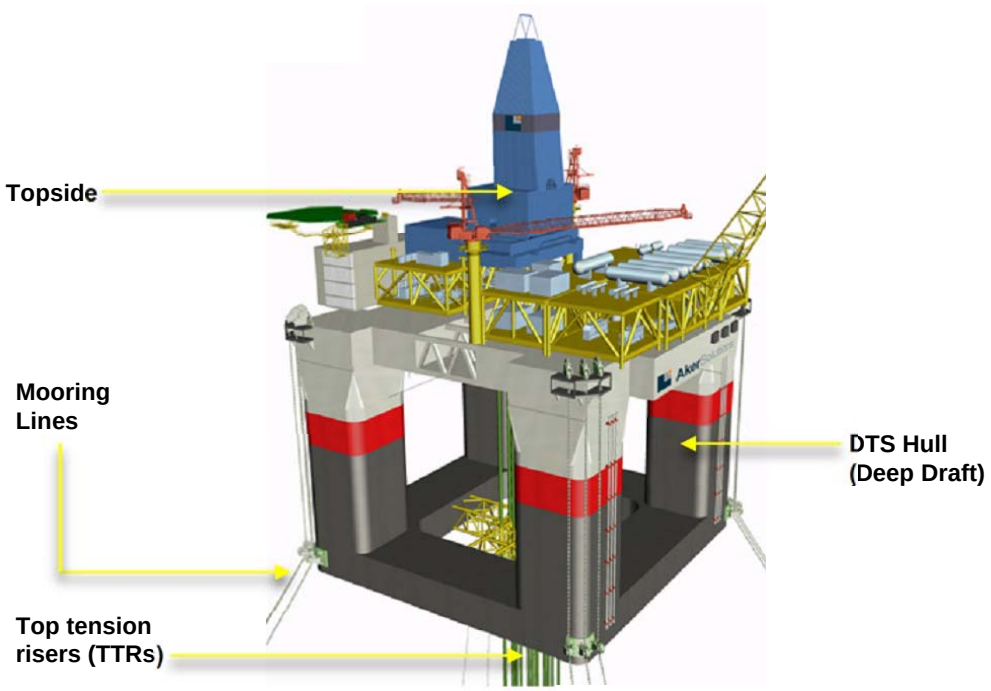

Figure 1.5 Semi-submersible with dry-tree interface (Courtesy of Aker Solution, and PennWell Corporation).

Recently, the latest development trend of DTS concepts includes both directions and trade-off in between the DTS heave motion and TTR stroke limits. However, the solution will be more complex when it involved the integration of these two systems (a deeper draft Semi and a longer stroke tensioner) into a fully coupled system. As riser tensioners increase in stroke length and capacity to accommodate high riser loads, well bay configurations and tensioner interfaces have a significant impact on the design of the Semi platform (Koos, 2013). The DTS hulls were configured considering the balance between the tensioner stroke-load characteristic, larger vessel offsets, platform heave displacements, hull draft, well-bay arrangement, quayside integration, transportation, installation, and updated Regulatory requirements for survival conditions (Koos, 2013; Xiang et al., 2014). The DTS heave motion is predominantly governed by its hull draft. An increase in the hull draft causes a commensurate reduction in heave motion and required tensioner stroke range (Zeng et al., 2013). As results, Zeng et al. (2013) proposed a deep draft DTS comprises a two-axis symmetrical hull with draft in the range of 100 ft to 155 ft (*30.48 m to 47.24 m*) to accommodate the tensioner stroke in the range of 35 ft to 45 ft (*10.67 m to 13.72 m*). Poll et al. (2013) designed a Paired-Column Semisubmersible Hull (PC-Semi) with draft of 175 ft (*53.34 m*) to accommodate the tensioner stroke of 28 ft (*8.53 m*). In addition, Bian and Xiang (2013) also suggested a DTS hull with the draft of 150 ft (*45.72 m*) to support the tensioner stroke within 35 ft (*10.67 m*), all under the Central GOM 1000-year survival condition with allowable occasional tensioner bottom out.

1.2 Objectives and Scopes

The main objective of this research is to develop a coupled dynamic analysis tool for the TLP and DTS, incorporated with magneto-rheological (MR) dampers under various conditions. The specific characteristic of MR dampers in alternating the damping force exerted into the structural dynamics has demonstrated a great potential to interactively changing the structural behaviors correspond to various external loadings, and reduce the motion of the controlled modules, which is the top-tensioned risers (TTRs) in this research. As mentioned earlier, if there was a reliable and cost-effective way to protect the hydrocarbon production modules in unfamiliar harsher environments, the safety of these structures could be more assured while simultaneously providing the expansion of offshore water depth limits to more unconventional areas, with more effective expenditures.

The innovation in this research is inspired from the successful engineering applications of MR dampers in land-based buildings as isolators against the earthquake and large-amplitude vibration. The system integration of MR dampers with the floating platforms is expected beneficial in the structural integrity management and to improve survivability in harsher environments, as per forecasted from the experiences of its applications in the land-based buildings. However, the implementation of MR dampers in offshore platform is currently very limited, and most of them concentrated on the fixed platforms (Ou et al., 2007; Yu et al., 2011; Wang et al., 2012) to the best of the author's knowledge. Hence, an effective analysis tool for studying the applications of MR dampers in the floating platforms, equipment, and oil and gas production modules is

significant. For this reason, the first part of this research is focusing on the robust dynamic simulation of a top tension riser incorporating a MR damper system under extreme conditions.

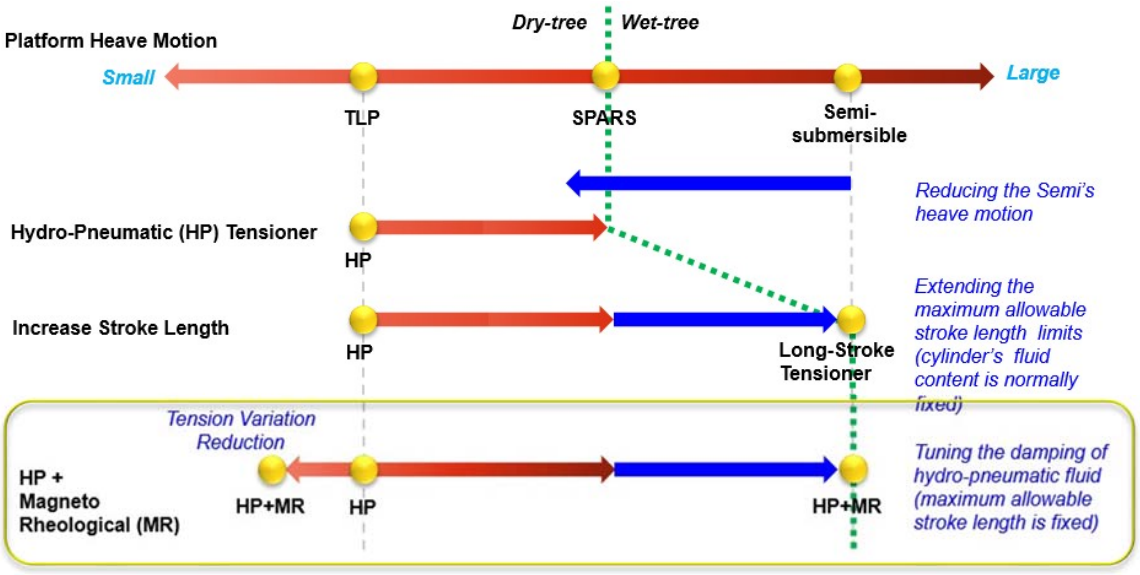

Figure 1.6 Research road map.

The main issues of installing TTR into TLP and DTS are different, as illustrated in Fig. 1.6. Therefore, the functions of MR dampers to be incorporated into both platforms are different. In the TLP platform, since the heave motion is restrained by the high-stiffed tendons, the axial tension variations of TTR caused by the platform set-down will be studied in more details. Since the TTR is originally designed for the host platform of TLP, the developed analysis tools to calculate the TTR tension are available. However, most of these tools were primarily used *pneumatic*-based equation to

approximate the tension variations of a hydro-pneumatic (HP) tensioner system, where the viscous fluid frictional effects in the HP tensioner system is not considered in the calculation of tension variations. In this research, a more comprehensive formulation, that considered the hydraulic viscous fluid effects as well, is developed to improve the reliability of TTR tension under certain circumstances. The exertion of excessive tension variations in the tensioner system leads to the necessity of reduction of tension variations which can be achieved by using magneto-rheological (MR) damper. The specific characteristics of MR damper in alternating the damping forces have great potential to interactively suppress the tension variations corresponding to various sea conditions.

The DTS is potential to enlarge the issues of TTR which can be negligible in the application in the TLP. The DTS is vulnerable to larger heave motion; therefore deeper draft hull and long stroke tensioner are required for the reality of this concept. Safety prevention on the production modules during survival conditions is in critical concern. The MR damper will be incorporated with the Ram-style tensioner to provide more flexibility to the DTS developers in handling the trade-off for the dilemma of tensioner stroke / platform draft, and additional stiffness / platform motion. The research objectives in this dissertation include:

(i) Dynamic coupling between numerical MR damper and CHARM3D;

(ii) Development of coupled analysis tools for MR damper with the TLP and DTS platform;

(iii) Implement the MR damper to reduce the riser tension variations;

(iv) Integrate the MR damper to improve DTS survivability;

(v) Mathieu's stability analysis for the riser.

The *merit* of this research will be shown with the advancement in the structural integrity management and motion mitigation in the offshore structures. The cutting-edge knowledge regarding the dynamic response and structural integrity of TTR *dry-tree* interface will allow the extraction of offshore hydrocarbon to be operated more effectively within the requirements set forth by the authorities. The *business impacts* of this work can be seen in the wide variety of locations that this technology can be utilized. This research allows many offshore structures to benefit from a cost-effective and reliable solution with more effective management of existing structures and equipment. Since offshore hydrocarbon extraction is inherently a multi-disciplinary field, this research will also have a direct impact on the work being performed in the fields of ocean engineering and mechanical engineering and indirect effect on the work of environmentalists and oceanographers. Moreover, potential technology implication to other offshore structures and relevant engineering disciplines enable a huge enhancement in effectively motion control of offshore structures.

2. DYNAMICS OF THE OFFSHORE FLOATING PLATFORM, RISERS, AND MOORING LINES

2.1 Introduction

In this Section, the wave loads, dynamic responses, finite modeling, and time domain solution scheme of the offshore floating platform, risers and mooring lines in the CHARM3D are reviewed. The CHARM3D is a fully-coupled time-domain dynamic-analysis program for floating bodies, mooring lines/tendons, and risers developed by Texas A&M University (Ran, 2000; Kang et al., 2014).

There must be acknowledged that the CHARM3D were progressively developed by the researchers leaded by Professor Moo Hyun Kim in Texas A&M University (Ran, 2000; Kim et al., 2001; Tahar and Kim, 2003; Yang and Kim, 2010; Bae, 2013). Hence, part of this Section which discusses the theoretical fundamentals in CHARM3D is highly relied on the previous works from Ran (2000) and Bae (2013).

2.2 Wave Theory

The wave theory in CHARM3D is derived from a Laplace's equation with the assumptions of incompressible, inviscid and irrotational properties, as stated (Ran, 2000):

$$\nabla^2 \Phi = 0 \tag{2.1}$$

To solve this Laplace equation, water waves must satisfy the proper kinematic and dynamic boundary conditions on the free surface. For the kinematic boundary

condition, water particles on the free surface must remain on the free surface, the formulation can be stated as:

$$\frac{\partial \eta}{\partial t} + u\frac{\partial \eta}{\partial x} + v\frac{\partial \eta}{\partial y} - \frac{\partial \Phi}{\partial t} = 0 \qquad \text{at } z = \eta(x, y, t) \tag{2.2}$$

where $\eta(x, y, t)$ is the wave elevation on the free surface. For the dynamic boundary condition, the pressure along the free surface must be equal to the constant atmospheric pressure, and can be formulated as:

$$\rho\frac{\partial \Phi}{\partial t} + \frac{1}{2}\left(\Phi_x^2 + \Phi_y^2 + \Phi_z^2\right) + \rho g z = 0 \qquad \text{at } z = \eta(x, y, t) \tag{2.3}$$

For bottom boundary condition, the velocity of water particle in vertical direction is zero:

$$\frac{\partial \Phi}{\partial z} = 0 \qquad \text{at } z = -d \tag{2.4}$$

where d is water depth. This boundary condition indicates that the water particles cannot penetrate the sea bottom.

There is noteworthy that the exact solution of above Laplace equation is difficult to solve due to the nonlinear terms of the free surface boundary conditions. Therefore, the perturbation method with small wave amplitude assumption is used to obtain an approximated solution of a certain order of accuracy (Ran, 2000). The first order velocity potentials and free surface elevations are stated as:

$$\Phi^{(1)} = \mathrm{Re}\left[-\frac{igA}{\omega}\frac{\cosh k(z+d)}{\cosh kd}e^{i(kx\cos\theta + ky\sin\theta - \omega t)}\right] \tag{2.5}$$

$$\eta^{(1)} = A\cos\left(kx\cos\theta + ky\sin\theta - \omega t\right) \tag{2.6}$$

and the second order velocity potential and free surface elevation are defined as:

$$\Phi^{(2)} = \mathrm{Re}\left[-\frac{3}{8}\omega A^2 \frac{\cosh 2k\left(z+d\right)}{\sinh^4 kd} e^{i\left(2kx\cos\theta + 2ky\sin\theta - 2\omega t\right)}\right] \tag{2.7}$$

$$\eta^{(2)} = A^2 \frac{\cosh kd}{\sinh^3 kd}\cos\left(2kx\cos\theta + 2ky\sin\theta - 2\omega t\right) \tag{2.8}$$

where A is the wave amplitude, ω is the wave frequency, k is the wave number, and θ is the incident wave heading angle.

A fully developed wave condition in the random sea environment is modeled by using wave spectra. The simulated random wave time series from the given wave spectrum $S(\omega)$ can be expressed by superposition of a large number of linear wave components with random phases (Bae, 2013),

$$\eta\left(x,t\right) = \sum_{i=1}^{N} A_i \cos\left(k_i x + \omega_i t + \varepsilon_i\right) = \mathrm{Re}\left[\sum_{i=1}^{N} A_i e^{i\left(k_i x - \omega_i t + \varepsilon_i\right)}\right] \tag{2.9}$$

$$A_i = \sqrt{2S\left(\omega_i\right)\Delta\omega} \tag{2.10}$$

where N and $\Delta\omega$ are the number of wave components and intervals of frequency division, and ε_i is a random phase angle generated by random function. To avoid the repetition of random wave realization with a limited number of wave components, some modifications were made and rewritten as below (Ran, 2000):

$$\eta\left(x,t\right) = \mathrm{Re}\left[\sum_{i=1}^{N} A_i e^{i\left(k_i x - \omega_i' t + \varepsilon_i\right)}\right] \tag{2.11}$$

where $\omega_i' = \omega_i + \delta\omega_i$ and $\delta\omega_i$ is the random perturbation number uniformly distributed between $-\Delta\omega/2$ and $\Delta\omega/2$.

2.3 Wave Loads on Structures

The prediction of wave loads acting on the floating structure is crucial in the analysis of the structural static and dynamic behaviors. The diffraction of waves around the platform in the deep water causes important loading pattern on the floating platform. On the other hand, Morison's formula is widely used for slender body. Therefore, the diffraction theory and Morison's equation are studied in this Subsection.

2.3.1 Diffraction and Radiation Theory

The total velocity potential Φ satisfies the Laplace equations, free surface boundary conditions, and the bottom boundary condition can be rewritten as combination of the incident potential Φ_I, diffraction potential Φ_D, and radiation potential Φ_R. By expressing the velocity potential Φ in a perturbation series with respect to the wave slope parameter ε (Ran, 2000):

$$\Phi = \sum_{n=1}^{\infty} \varepsilon^n \Phi^{(n)} = \sum_{n=1}^{\infty} \varepsilon^n \left(\Phi_I^{(n)} + \Phi_D^{(n)} + \Phi_R^{(n)} \right) \tag{2.12}$$

where $\Phi^{(n)}$ denotes the n th order solution of Φ. In the CHARM3D, the solutions up to second order is considered.

The boundary condition on the floating structure body is needed in order to solve the wave-structure interaction problem. The body boundary condition can be defined as:

$$\frac{\partial \Phi}{\partial \mathbf{n}} = V_n \qquad \text{on body surface} \tag{2.13}$$

where $\mathbf{n}$ is the surface normal vector, and V_n is the normal velocity vector of the body at its surface.

Moreover, the diffraction potential Φ_D and radiation potential Φ_R must satisfy the Sommerfeld radiation condition at the far field boundary (Ran, 2000):

$$\lim_{r\to\infty} \sqrt{r}\left(\frac{\partial \Phi_{D,R}}{\partial r} \pm ik\Phi_{D,R} \right) = 0 \tag{2.14}$$

where r denotes the radial distance from the center of the floating body.

2.3.2 First Order Boundary Value Problem

The first order potential can be rewritten by separating the time dependency explicitly as (Bae, 2013):

$$\Phi^{(1)} = \varepsilon\left(\Phi_I^{(1)} + \Phi_D^{(1)} + \Phi_R^{(1)} \right) = \mathrm{Re}\left\{ \left[\phi_I^{(1)}(x,y,z) + \phi_D^{(1)}(x,y,z) + \phi_R^{(1)}(x,y,z) \right] e^{-i\omega t} \right\} \tag{2.15}$$

and the first order incident potential $\phi_I^{(1)}$ is rewritten as:

$$\phi_I^{(1)}(x,y,z) = \mathrm{Re}\left[-\frac{igA}{\omega} \frac{\cosh k(z+d)}{\cosh kd} e^{i\mathbf{K}\cdot\mathbf{x}} \right] \tag{2.16}$$

where $\mathbf{K}$ denotes a vector wave number with Cartesian components $(k\cos\theta, k\sin\theta, 0)$, $\mathbf{x}$ is the position vector in the fluid domain, and θ is the angle of the incident wave relative to the positive x axis.

Hence, the boundary value problem governing the first order diffraction potential and radiation potential can be summarized as (Bae, 2013):

$$\nabla^2 \phi_{D,R}^{(1)} = 0 \qquad \text{in the fluid } (z < 0) \tag{2.17}$$

$$\left(-\omega^2 + g\frac{\partial}{\partial z}\right)\phi_{D,R}^{(1)} = 0 \qquad \text{on the free surface } (z = 0) \tag{2.18}$$

$$\frac{\partial \phi_{D,R}^{(1)}}{\partial z} = 0 \qquad \text{on the bottom } (z = -d) \tag{2.19}$$

$$\frac{\partial \phi_{R}^{(1)}}{\partial n} = -i\omega \mathbf{n} \cdot \left(\boldsymbol{\xi}^{(1)} + \boldsymbol{\alpha}^{(1)} \times \mathbf{r}\right) \qquad \text{on the body surface} \tag{2.20}$$

$$\lim_{r\to\infty} \sqrt{r}\left(\frac{\partial}{\partial r} \pm ik\right)\phi_{D,R}^{(1)} = 0 \qquad \text{at far field} \tag{2.21}$$

where $\mathbf{r}$ is the position vector on the body surface, r is the radial distance from the origin, and $\mathbf{n}$ represents the unit normal vector pointing into the fluid domain at the body surface. The first-order motions of the body in the translational $\Xi^{(1)}$ and rotational $\Theta^{(1)}$ directions have the forms (Bae, 2013):

$$\Xi^{(1)} = \mathrm{Re}\left\{\boldsymbol{\xi}^{(1)} e^{-i\omega t}\right\} \qquad \boldsymbol{\xi}^{(1)} = \left\{\xi_1^{(1)}, \xi_2^{(1)}, \xi_3^{(1)}\right\} \tag{2.22}$$

$$\Theta^{(1)} = \mathrm{Re}\left\{\boldsymbol{\alpha}^{(1)} e^{-i\omega t}\right\} \qquad \boldsymbol{\alpha}^{(1)} = \left\{\alpha_1^{(1)}, \alpha_2^{(1)}, \alpha_3^{(1)}\right\} \tag{2.23}$$

where the subscripts 1, 2, and 3 represent the translational (surge, sway, and heave) and rotational (roll, pitch, and yaw) modes with respect to the x, y, and z axes respectively. The six degrees of freedom of first order motion can be rewritten as (Bae, 2013):

$$\zeta_i = \xi_i^{(1)} \qquad \text{for } i = 1,2,3 \tag{2.24}$$

$$\zeta_i = \alpha_{i-3}^{(1)} \qquad \text{for } i = 4,5,6 \tag{2.25}$$

The radiation potential represents the fluid disturbance due to the floating body motion is decomposed as:

$$\phi_R^{(1)} = \sum_{i=1}^{6} \zeta_i \phi_i^{(1)} \tag{2.26}$$

where ϕ_i is the first order velocity potential of the rigid body motion, under the conditions of unit amplitude in the i th mode and without incident waves. The body boundary condition of each mode can be further expressed by replacing $\phi_i^{(1)}$ as (Bae, 2013):

$$\frac{\partial \phi_i^{(1)}}{\partial n} = n_i \qquad i = 1,2,3 \tag{2.27}$$

$$\frac{\partial \phi_i^{(1)}}{\partial n} = \left(\mathbf{r} \times \mathbf{n}\right)_{i-3} \qquad i = 4,5,6 \tag{2.28}$$

on the body surface.

The first order diffraction potential $\phi_D^{(1)}$ denotes the disturbance to the incident wave caused by the existence of the structure body in its fixed position. The velocity potential of the wave diffraction must satisfy the body surface boundary condition as follow (Ran, 2000):

$$\frac{\partial \phi_D^{(1)}}{\partial n} = -\frac{\partial \phi_I^{(1)}}{\partial n} \qquad \text{on the body surface} \tag{2.29}$$

2.3.3 First Order Potential Forces

By solving the first order diffraction potential $\phi_D^{(1)}$ and radiation potential $\phi_R^{(1)}$, the first order hydrodynamic potential force exerted on the floating structure can be approximated. The hydrodynamic pressure $P(t)$ can be expressed by using the perturbation method as (Ran, 2000):

$$P^{(1)} = -\rho \frac{\partial \Phi^{(1)}}{\partial t} \tag{2.30}$$

The total force and moment exerted on the floating structure body can be approximated by using integration over the instantaneous wetted body surface $S(t)$ (Bae, 2013):

$$\mathbf{F}(t)_i = \begin{cases} \iint_{S_b} P n_i dS & i = 1,2,3 \\ \iint_{S_b} P(\mathbf{r} \times \mathbf{n})_i \, dS & i = 4,5,6 \end{cases} \tag{2.31}$$

where S_b is the body surface at rest.

Therefore, the total first order force and moment can be represented as:

$$\mathbf{F}^{(1)} = \mathbf{F}_{HS}^{(1)} + \mathbf{F}_R^{(1)} + \mathbf{F}_{EX}^{(1)} \tag{2.32}$$

where the subscript HS represents the hydrostatic restoring force and moment, R denotes the force and moment from the radiation potential, and EX represents the wave exciting force and moment from the incident and diffraction potentials.

The first order hydrostatic restoring force and moment $\mathbf{F}_{HS}^{(1)}$ are induced by the changes of hydrostatic pressure on the body caused by the motion of the floating structure, which can be defined as:

$$\mathbf{F}_{HS}^{(1)} = -\mathbf{K}\left\{\zeta^{(1)}\right\} \tag{2.33}$$

where $\zeta^{(1)}$ is the first order motion of the floating structure, and $\mathbf{K}$ is the hydrostatic restoring stiffness.

The first order force and moment on the floating body exerted from the radiation potential $\mathbf{F}_{R}^{(1)}$ can be represented as:

$$\mathbf{F}_{R}^{(1)} = \mathrm{Re}\left(\left[\mathbf{f}\right]\left\{\zeta^{(1)}\right\}\right) \tag{2.34}$$

where

$$\mathbf{f} = f_{ij} = -\rho\iint_{S_b}\frac{\partial\phi_i}{\partial n}\phi_j dS \qquad i,j = 1,2,...,6 \tag{2.35}$$

and f_{ij} is complex variable depends on the frequency ω. Its real and imaginary coefficients can be rewritten as:

$$f_{ij} = -\omega^2 M_{ij}^{a} - i\omega C_{ij} \tag{2.36}$$

Therefore, the force and moment from the radiation potential can be expressed as (Bae, 2013):

$$\mathbf{F}_{R}^{(1)} = \mathrm{Re}\left(\left[\mathbf{M}^{a}\right]\left\{\ddot{\zeta}^{(1)}\right\} + \left[\mathbf{C}\right]\left\{\dot{\zeta}^{(1)}\right\}\right) \tag{2.37}$$

where $\mathbf{M}^{a}$ is the added mass coefficients and $\mathbf{C}$ is the radiation damping coefficients.

The term $\mathbf{F}_{EX}^{(1)}$ denotes the first order wave excitation forces and moments exerted from the incident and diffraction wave potentials can be defined as (Ran, 2000):

$$\mathbf{F}_{EX}^{(1)} = \mathrm{Re}\left(-\rho A e^{i\omega t} \iint_{S_0} \left(\phi_I + \phi_D\right) \frac{\partial \phi_j}{\partial n} dS \right) \qquad j = 1, 2, ..., 6 \tag{2.38}$$

where A is wave amplitude. The first order wave excitation forces and moments are proportional to wave amplitude, which is frequency dependent, is called Linear Transfer Function (LTF) that represents the relationship between incident wave elevation and the first order diffraction forces on the floating body (Bae, 2013).

2.3.4 Wave Loads in Time Domain

In the CHARM3D, the linear wave forces are computed at a specified wave frequency, and the second order sum and difference frequency forces are obtained from the interactions of bi-chromatic waves (Bae, 2013). The linear and second-order hydrodynamic forces on a body due to stationary Gaussian random seas can be expressed as a two-term Volterra series in time domain (Ran, 2000):

$$\mathbf{F}^{(1)}(t) + \mathbf{F}^{(2)}(t) = \int_{-\infty}^{\infty} h_1(\tau)\eta(t-\tau)d\tau + \int_{-\infty}^{\infty}\int_{-\infty}^{\infty} h_2(\tau_1, \tau_2)\eta(t-\tau_1)\eta(t-\tau_2)d\tau_1 d\tau_2 \tag{2.39}$$

where $h_1(\tau)$ and $h_2(\tau_1, \tau_2)$ are the linear and quadratic impulse response function, respectively, and $\eta(t)$ represents the ambient wave free surface position at the reference point.

For unidirectional seas with N wave components, the wave exciting forces from incident wave potential and diffraction potential in unidirectional waves can be expressed as (Bae, 2013):

$$\mathbf{F}_I^{(1)}(t) = \mathrm{Re}\left[\sum_{i=1}^{N} A_i \mathbf{L}(\omega_i) e^{i\omega_i t}\right] \tag{2.40}$$

$$\mathbf{F}_I^{(2)}(t) = \mathrm{Re}\left[\sum_{j=1}^{N}\sum_{k=1}^{N} A_j A_k^* \mathbf{D}(\omega_j, -\omega_k) e^{i(\omega_j-\omega_k)t} + \sum_{j=1}^{N}\sum_{k=1}^{N} A_j A_k \mathbf{S}(\omega_j, \omega_k) e^{i(\omega_j+\omega_k)t}\right] \tag{2.41}$$

where $(*)$ denotes the complex conjugate of the quantity, $\mathbf{L}(\omega_j)$ is the linear force transfer functions (LTF), $\mathbf{D}(\omega_j, -\omega_k)$ and $\mathbf{S}(\omega_j, \omega_k)$ are the difference and sum frequency quadratic force transfer functions (QTF), respectively.

For multi-directional waves, the wave exciting forces can be represented as (Bae, 2013):

$$\mathbf{F}_I^{(1)}(t) = \mathrm{Re}\left[\sum_{j=1}^{N}\sum_{l=1}^{M} A_{jl} \mathbf{L}(\omega_j, \theta_l) e^{-i\omega_i t}\right] \tag{2.42}$$

$$\mathbf{F}_I^{(2)}(t) = \mathrm{Re}\left[\begin{array}{l} \displaystyle\sum_{j=1}^{N}\sum_{k=1}^{N}\sum_{l=1}^{M}\sum_{m=1}^{M} A_{jl} A_{km}^* \mathbf{D}(\omega_j, -\omega_k, \theta_l, \theta_m) e^{-i(\omega_j-\omega_k)t} \\ \displaystyle+\sum_{j=1}^{N}\sum_{k=1}^{N}\sum_{l=1}^{M}\sum_{m=1}^{M} A_{jl} A_{km}^* \mathbf{S}(\omega_j, \omega_k, \theta_l, \theta_m) e^{-i(\omega_j+\omega_k)t} \end{array}\right] \tag{2.43}$$

where A_{jl} is wave amplitude, $\mathbf{L}(\omega_j, \theta_l)$ is the linear transfer function (LTF) at frequency ω_i in θ_l direction, $\mathbf{D}(\omega_j, -\omega_k, \theta_l, \theta_m)$ is the difference frequency quadratic transfer function (QTF), and $\mathbf{S}(\omega_j, \omega_k, \theta_l, \theta_m)$ is sum frequency QTF generated by unit

amplitude wave pair at frequency ω_j in θ_l direction and at frequency ω_k in θ_m direction.

On the other hand, the force exerted from radiation potential, which is same for both first and second order motions, can be represented in time domain as (Ran, 2000):

$$\mathbf{F}_R(t) = -\mathbf{M}^a(\infty)\ddot{\zeta} - \int_{-\infty}^{t} \mathbf{R}(t-\tau)\dot{\zeta}(\tau)\,d\tau \tag{2.44}$$

where $\mathbf{M}^a(\infty)$ is the added mass at infinite frequency, the convolution integral represents the memory effects of the wave forces on the platform from the wave generated by platform motion prior to time t. $\mathbf{R}(t)$ is called the retardation function and is related to the frequency domain solution of the radiation problem as follow (Bae, 2013):

$$\mathbf{R}(t) = \frac{2}{\pi}\int_0^{\infty} C(\omega)\frac{\sin \omega t}{\omega}\,d\omega \tag{2.45}$$

where $C(\omega)$ is the wave damping coefficient at frequency ω. The $\mathbf{M}^a(\infty)$ is a constant equivalent to the added mass of the body at infinite frequency (Ran, 2000):

$$\mathbf{M}^a(\infty) = \mathbf{M}^a(\omega) - \int_0^{\infty} \mathbf{R}(t)\cos \omega t\,dt \tag{2.46}$$

where $\mathbf{M}^a(\omega)$ is the added mass at frequency ω.

The total wave loads in the time domain can be obtained by summing each force component as follows (Bae, 2013):

$$\mathbf{F}_{total}(t) = \mathbf{F}_I(t) + \mathbf{F}_R(t) \tag{2.47}$$

where $\mathbf{F}_{total}(t) = \mathbf{F}^{(1)}(t) + \mathbf{F}^{(2)}(t)$ is the total wave exciting force, $\mathbf{F}_I(t) = \mathbf{F}_I^{(1)}(t) + \mathbf{F}_I^{(2)}(t)$ is the sum of the Eqns. (2.40) - (2.41), and $\mathbf{F}_R(t)$ is the radiation term from the Eqn. (2.44).

2.3.5 Morison's Formula

The viscous effect is dominant on the slender cylindrical structures where the diffraction effect is usually negligible. The inertia effect of the slender body that includes the added mass and damping effect can be estimated by using Morison's formula (Morison et al., 1950). The Morison's formula states that the wave load per unit length of the structure normal to the elemental section with diameter D which is small compared to the wave length is obtained by the sum of an inertial, added mass, and drag force (Bae, 2013):

$$F_m = C_m \rho \frac{\pi D^2}{4} \dot{u}_n - C_a \rho \frac{\pi D^2}{4} \ddot{\zeta}_n + \frac{1}{2} \rho C_D D_S \left(u_n - \dot{\zeta}_n\right) \left|u_n - \dot{\zeta}_n\right| \tag{2.48}$$

where F_m denotes Morison's force, $C_m = 1 + C_a$ is the inertia coefficient, C_a is the added mass coefficient, C_D is the drag coefficient, D_S is the breadth or diameter of the structure, $\dot{u}_n$ and u_n are the acceleration and the velocity of the fluid normal to the body, respectively, $\ddot{\zeta}_n$ and $\dot{\zeta}_n$ are the normal acceleration and the velocity of the fluid body, respectively. In the right-hand-side (RHS) of Eqn. (2.48), the first term is the inertia force exerted from the Froude-Krylov force, the second term is the inertia force generated from the added mass effect, and the last term is the drag force exerted on the

sleder body in the relative velocity form. The relative-velocity form indicates that the drag force contributes to both the exciting force and damping force on the motion of the structure (Bae, 2013). In this study, the viscous effects of slender members such as the cylindrical hull, TLP columns or truss members are computed by Morison's formula and are combined with the potential forces to compute the wave forces on the platform (Ran, 2000; Bae, 2013).

2.3.6 Time Domain Solution of the Platform Motions

The motion equation of platform in time domain can be represented by breaking down the total external force exerted on the platform as (Ran, 2000):

$$\left[\mathbf{M}+\mathbf{M}^{a}\left(\infty\right)\right]\ddot{\zeta}+\mathbf{K}\zeta=\mathbf{F}_{I}\left(t\right)+\mathbf{F}_{C}\left(t,\dot{\zeta}\right)+\mathbf{F}_{m}\left(t,\zeta\right) \tag{2.49}$$

where

$$\mathbf{F}_{C}\left(t,\dot{\zeta}\right)=-\int_{-\infty}^{t}\mathbf{R}\left(t-\tau\right)\dot{\zeta}d\tau \tag{2.50}$$

where $\mathbf{F}_{I}\left(t\right)$ denotes the first and second order wave exciting forces defined in Eqns. (2.40) – (2.41), and $\mathbf{F}_{m}\left(t,\zeta\right)$ represents the nonlinear drag forces from the Morison's formula in Eqn. (2.48).

The second-order Adams-Moulton method (or mid-point method) is used in the numerical modeling in this study. The reason for using this method is that the finite element analysis of the mooring lines in time domain is developed using the same method and eventually the coupled equations of mooring line-platform are formed and

solved together at each time step (Ran, 2000). The Eqn. (2.49) is firstly reduced to two first-order differential equations (Ran, 2000):

$$\bar{\mathbf{M}}\dot{\xi} = \mathbf{F}_I(t) + \mathbf{F}_C\left(t, \dot{\zeta}\right) + \mathbf{F}_m\left(t, \zeta\right) - \mathbf{K}\zeta \tag{2.51}$$

$$\dot{\zeta} = \xi \tag{2.52}$$

where

$$\bar{\mathbf{M}} = \mathbf{M} + \mathbf{M}^a(\infty) \tag{2.53}$$

After integrating the above equations from time step $t^{(n)}$ to $t^{(n+1)}$;

$$\bar{\mathbf{M}}\xi^{(n+1)} - \bar{\mathbf{M}}\xi^{(n)} = \int_{t^{(n)}}^{t^{(n+1)}} \left(\mathbf{F}_I(t) + \mathbf{F}_C\left(t, \dot{\zeta}\right) + \mathbf{F}_m\left(t, \zeta\right)\right) dt - \int_{t^{(n)}}^{t^{(n+1)}} \mathbf{K}\zeta\, dt \tag{2.54}$$

$$\zeta^{(n+1)} - \zeta^{(n)} = \int_{t^{(n)}}^{t^{(n+1)}} \xi dt \tag{2.55}$$

and applying the Adams-Moulton scheme: $\int_{t^{(n)}}^{t^{(n+1)}} x dt = \frac{\Delta t}{2}\left[x^{(n)} + x^{(n+1)}\right]$ (2.56)

$$\begin{aligned}\bar{\mathbf{M}}\xi^{(n+1)} = \bar{\mathbf{M}}\xi^{(n)} &+ \frac{\Delta t}{2}\left(\mathbf{F}_I^{(n+1)} + \mathbf{F}_I^{(n)} + \mathbf{F}_C^{(n+1)} + \mathbf{F}_C^{(n)} + \mathbf{F}_m^{(n+1)} + \mathbf{F}_m^{(n)}\right) \\ &- \frac{\Delta t}{2}\mathbf{K}\left(\zeta^{(n+1)} - \zeta^{(n)}\right)\end{aligned} \tag{2.57}$$

$$\zeta^{(n+1)} - \zeta^{(n)} = \frac{\Delta t}{2}\left(\xi^{(n+1)} + \xi^{(n)}\right) \;\rightarrow\; \boldsymbol{\xi}^{(n+1)} = \frac{2}{\Delta t}\left(\zeta^{(n+1)} - \zeta^{(n)}\right) - \boldsymbol{\xi}^{(n)} \tag{2.58}$$

There is noteworthy that the Eqns. (2.57) and (2.58) are linear algebraic equations with unknown quantities $\boldsymbol{\xi}^{(n+1)}$ and $\zeta^{(n+1)}$. Also, the convolution integral and drag force are functions of the platform velocity, which is unknown, at time step $(n+1)$. Thus, in order to solve the equations, an iterative process is needed with an initial guess

of the $\boldsymbol{\xi}^{(n+1)}$ in computing the $\mathbf{F}_C^{(n+1)}$ and $\mathbf{F}_m^{(n+1)}$ (Ran, 2000). In this study, the iterative procedure is avoided by using the *Adams-Bashforth* scheme for the following nonlinear force terms (Ran, 2000):

$$\int_{t^{(n)}}^{t(n+1)} \mathbf{F}_C dt = \frac{\Delta t}{2}\left(3\mathbf{F}_C^{(n)} - \mathbf{F}_C^{(n-1)}\right) \text{ and } = \Delta t \mathbf{F}_C^{(0)} \text{ for } n = 0 \tag{2.59}$$

$$\int_{t^{(n)}}^{t(n+1)} \mathbf{F}_m dt = \frac{\Delta t}{2}\left(3\mathbf{F}_m^{(n)} - \mathbf{F}_m^{(n-1)}\right) \text{ and } = \Delta t \mathbf{F}_m^{(0)} \text{ for } n = 0 \tag{2.60}$$

The final form of platform motion equation in time domain can be obtained by combining the Eqns. (2.57)-(2.60):

$$\left(\frac{4}{\Delta t^2}\bar{\mathbf{M}} + \mathbf{K}\right)\Delta\zeta = \frac{4}{\Delta t}\bar{\mathbf{M}}\boldsymbol{\xi}^{(n)} + \left(\mathbf{F}_I^{(n+1)} + \mathbf{F}_I^{(n)}\right) + \left(3\mathbf{F}_C^{(n)} - \mathbf{F}_C^{(n-1)}\right) + \left(3\mathbf{F}_m^{(n)} - \mathbf{F}_m^{(n-1)}\right) - 2\mathbf{K}\zeta^{(n)} + 2\mathbf{F}_0 \tag{2.61}$$

where $\Delta\zeta = \zeta^{(n+1)} - \zeta^{(n)}$ (2.62)

There is noteworthy that the term $\mathbf{F}_0$ is introduced into the Eqn. (2.61) to represent a constant force, such as a net buoyancy force on the platform which is used to balance the mooring load (Ran, 2000).

2.4 Dynamics of Risers and Mooring Lines

In this Subsection, the modeling of risers and mooring lines in the CHARM3D is discussed based on a three-dimensional elastic rod theory (Garrett, 1982). The coupling forces and moments from the mooring lines and top tensioned risers are important in this research. The tension-leg platform (TLP) is connected with taut vertical mooring lines or

tendons (which made of steel pipes) to the seabed under high pretension. If the tendons of the TLP lost the pretension, the TLP hull and topside structure are vulnerable to instability phenomenon. On the other hand, even though the dry tree semi-submersible (DTS) are installed with catenary mooring lines that have allowances to the larger vertical motion compared with the TLP tendons, however, the dry-tree interface equipped with top-tensioned risers can increase the total payload and vertical stiffness of the DTS and induce the vertical resonance if the vertical stiffness over the limits. Hence, a reliable modeling of risers and mooring lines is the essential part in this research.

2.4.1 Theory of Rod

The behavior of a slender rod can be described by the position and deformation of the rod's centerline as a *space curve* $\boldsymbol{r}(s,t)$, as shown in Fig. 2.1 (Ran, 2000; Bae, 2013). The position vector $\boldsymbol{r}$ of space curve is a function of the arc-length s and time t. The rod is assumed to be inextensible where the arclength s is identical in both deformed and undeformed states. Thus the unit tangent vector to the space curve is r', and the principal normal vector is directed along r'' and the bi-normal is directed along $r' \times r''$, where the prime denotes the differentiation with respect to arclength (Garrett, 1982; Ran, 2000).

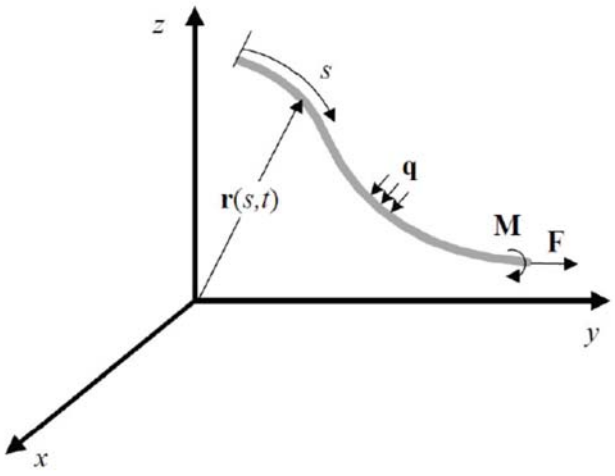

Figure 2.1 Coordinate system of slender rod (Bae, 2013).

The resultant force $\mathbf{F}$ and moment $\mathbf{M}$ acting along the rod's centerline can change the internal state of point stress on the rod. The equilibrium of the linear force and moment for a rod's *segment* with unit arclength can be represented by using the equations of motion (Garrett, 1982):

$$\mathbf{F}' + \mathbf{q} = \rho \ddot{\mathbf{r}} \tag{2.63}$$

$$\mathbf{M}' + \mathbf{r}' \times \mathbf{F} + \mathbf{m} = 0 \tag{2.64}$$

where $\mathbf{q}$ is applied force per unit length, ρ is rod's mass per unit length, and $\mathbf{m}$ is applied moment per unit length.

For elastic rod with equal principal stiffness, the bending moment is proportional to curvature and is directed along the bi-normal (Garrett, 1982; Ran, 2000). The resultant moment $\mathbf{M}$ is denoted as:

$$\mathbf{M} = \mathbf{r}' \times EI\mathbf{r}'' + H\mathbf{r}' \tag{2.65}$$

where the EI is the bending stiffness and H is the torque. Substituting the Eqn. (2.65) into Eqn. (2.64) (Garrett, 1982):

$$\mathbf{r}' \times \left[\left(EI\mathbf{r}'' \right)' + \mathbf{F} \right] + H'\mathbf{r}' + H\mathbf{r}'' + \mathbf{m} = \mathbf{0} \tag{2.66}$$

and the scalar product of the Eqn. (2.66) with $\mathbf{r}'$ yields:

$$H' + \mathbf{m} \cdot \mathbf{r}' = \mathbf{0} \tag{2.67}$$

There is noteworthy that if no distributed torsional moment $(\mathbf{m} \cdot \mathbf{r}')$, the torque H is independent with respect to the arclength s. The mooring lines, tethers, and riser mostly have circular cross sections thus there is no distributed torsional motion from the hydrodynamic forces (Ran, 2000). In addition, the torque in the lines are usually small and negligible (Garrett, 1982). Therefore, both H and $\boldsymbol{m}$ are assumed to be zero, so that the Eqn. (2.66) becomes (Ran, 2000):

$$\mathbf{r}' \times \left[\left(EI\mathbf{r}'' \right)' + \mathbf{F} \right] = \mathbf{0} \tag{2.68}$$

A scalar function $\lambda(s,t)$ is introduced into the above equation, where $\mathbf{F}$ can be rewritten as:

$$\mathbf{F} = -\left(EI\mathbf{r}'' \right)' + \lambda \mathbf{r}' \tag{2.69}$$

$$\lambda = \mathbf{F} \cdot \mathbf{r}' + \left(EI\mathbf{r}'' \right)' \cdot \mathbf{r}' \;\rightarrow\; \lambda = T - EI\kappa^2 \tag{2.70}$$

where T is the line's tension and κ is line's curvature.

Subsituting Eqn. (2.69) into Eqn. (2.63), the equation of motion for the rod can be defined as:

$$-\left(EI\mathbf{r}''\right)'' + \left(\lambda\mathbf{r}'\right)' + \mathbf{q} = \rho\ddot{\mathbf{r}} \tag{2.71}$$

In addition, $\mathbf{r}$ must satisfy the inextensibility condition (Ran, 2000):

$$\mathbf{r}' \cdot \mathbf{r}' = 1 \tag{2.72}$$

If the rod is considered stretchable and the stretch is linear and small, the above inextensibility condition can be approximated by (Ran, 2000):

$$\frac{1}{2}\left(\mathbf{r}' \cdot \mathbf{r}' - 1\right) = \frac{T}{AE} \approx \frac{\lambda}{AE} \tag{2.73}$$

The scalar function λ is a Lagrangian multiplier due to the assumption of inextensibility. The Eqns. (2.71) and (2.72) combined with initial conditions, boundary conditions and applied force q, are sufficient to determine the dependent variables $\mathbf{r}(s,t)$ and $\lambda(s,t)$ (Ran, 2000). The applied force on the rods (such as mooring line, riser, and tether) exerted from the hydrostatic force, hydrodynamic force, and the gravity force of the rod itself, therefore the applied force can be represented as:

$$\mathbf{q} = \mathbf{w} + \mathbf{F^s} + \mathbf{F^d} \tag{2.74}$$

where $\mathbf{w}$ is rod's weight per unit length, $\mathbf{F^s}$ is hydrostatic force/unit length, and $\mathbf{F^d}$ is hydrodynamic force/unit length. The hydrostatic force can be calculated by:

$$\mathbf{F^s} = \mathbf{B} - \left(P\mathbf{r}'\right)' \tag{2.75}$$

where $\mathbf{B}$ is buoyancy force on the rod / unit length, and P is scalar hydrostatic pressure at the point $\mathbf{r}$ on the rod.

On the other hand, the hydrodynamic force on the rod can be determined by Morison's formula:

$$\begin{aligned}\mathbf{F^d} &= -C_A\ddot{\mathbf{r}}^n + C_M\dot{\mathbf{V}}^n + C_D\left|\mathbf{V}^n - \dot{\mathbf{r}}^n\right|\left(\mathbf{V}^n - \dot{\mathbf{r}}^n\right) \\ &= -C_A\ddot{\mathbf{r}}^n + \overline{\mathbf{F}}^{\boldsymbol{d}}\end{aligned} \tag{2.76}$$

where C_A denotes the added mass coefficient (added mass / unit length), C_M is the inertial coefficient (inertial force / (unit length × unit normal acceleration)), C_D is the drag coefficient (drag force / (unit length × unit normal velocity)), $\mathbf{V}^n$ and $\dot{\mathbf{V}}^n$ are the fluid velocity and acceleration normal to the rod centerline, respectively. The fluid velocity and acceleration can be determined from the total fluid velocity and the tangent vector of the line (Ran, 2000):

$$\mathbf{V}^n = \left(\mathbf{V} - \dot{\mathbf{r}}\right) - \left[\left(\mathbf{V} - \dot{\mathbf{r}}\right)\cdot\mathbf{r}'\right]\cdot\mathbf{r}' \tag{2.77}$$

$$\dot{\mathbf{V}}^n = \dot{\mathbf{V}} - \left[\dot{\mathbf{V}}\cdot\mathbf{r}'\right]\cdot\mathbf{r}' \tag{2.78}$$

where $\dot{\mathbf{V}}$ and $\mathbf{V}$ are acceleration and velocity, respectively, water particles at the rod's centerline. The fluid field is assumed to be undisturbed by the presence of the rod.

The terms $\ddot{\mathbf{r}}^n$ and $\dot{\mathbf{r}}^n$ in Eqn. (2.76) are components of the rod's acceleration and velocity normal to its centerline:

$$\dot{\mathbf{r}}^n = \dot{\mathbf{r}} - \left[\dot{\mathbf{r}}\cdot\mathbf{r}'\right]\cdot\mathbf{r}' \tag{2.79}$$

$$\ddot{\mathbf{r}}^n = \ddot{\mathbf{r}} - \left[\ddot{\mathbf{r}}\cdot\mathbf{r}'\right]\cdot\mathbf{r}' \tag{2.80}$$

Subsituting Eqns. (2.74)-(2.76) into Eqn. (2.71), the equation of motion for the rod can be represented as:

$$
\begin{aligned}
-\left(EI\mathbf{r}''\right)'' + \left(\lambda\mathbf{r}'\right)' + \mathbf{w} + \mathbf{B} - \left(P\mathbf{r}'\right)' - C_A\ddot{\mathbf{r}}^n + \bar{\mathbf{F}}^d &= \rho\ddot{\mathbf{r}} \\
\rho\ddot{\mathbf{r}} + C_A\ddot{\mathbf{r}}^n + \left(EI\mathbf{r}''\right)'' - \left(\lambda\mathbf{r}'\right)' + \left(P\mathbf{r}'\right)' &= \mathbf{w} + \mathbf{B} + \bar{\mathbf{F}}^d \\
\rho\ddot{\mathbf{r}} + C_a\rho_w\ddot{\mathbf{r}}^n + \left(EI\mathbf{r}''\right)'' + \left(\bar{\lambda}\mathbf{r}'\right)' &= \bar{\mathbf{w}} + \bar{\mathbf{F}}^d
\end{aligned}
\tag{2.81}
$$

where

$$
C_A = C_a\rho_w \tag{2.82}
$$

$$
\bar{\mathbf{w}} = \mathbf{w} + \mathbf{B} \tag{2.83}
$$

$$
\begin{aligned}
\bar{\lambda} &= -\lambda + P = -\left(T - EI\kappa^2\right) + P = -T + EI\kappa^2 + P = -T + P + EI\kappa^2 \\
&= -(T - P - EI\kappa^2) \\
-\bar{\lambda} &= T - P - EI\kappa^2 = \bar{T} - EI\kappa^2
\end{aligned}
\tag{2.84}
$$

where $\bar{T}$ is the effective tension in the rod, and $\bar{\mathbf{w}}$ is the effective weight (or wet weight) of the rod.

2.4.2 Finite Element Modeling of Rod in CHARM3D

The governing equation and inextensibility condition of rod, Eqn. (2.81) and Eqn. (2.73), can be rewritten in subscript notation as:

$$
-\rho\ddot{r}_i - C_A\ddot{r}_i^n - \left(EIr_i''\right)'' + \left(\bar{\lambda}r_i'\right)' + \bar{w}_i + F_i^d = 0 \tag{2.85}
$$

$$
\frac{1}{2}\left(r_n'r_n' - 1\right) - \frac{\lambda}{AE} = 0 \tag{2.86}
$$

The governing equation of rod is discretized into elements with finite length, by using finite element method, and the algebraic are developed in the element level. For an

element, the variables $\lambda(s,t)$ and $r_i(s,t)$ along the rod with length L are approximated as (Ran, 2000):

$$r_i(s,t) = A_l(s)U_{il}(t) \tag{2.87}$$

$$\lambda(s,t) = P_m(s)\lambda_m(t) \tag{2.88}$$

where $0 \le s \le L$, and A_k and P_m are interpolation functions. The *Galerkin's* method is applied to the Eqn. (2.85) over the elemental length (Ran, 2000):

$$\int_0^L \delta r_i \left[-\rho \ddot{r}_i - C_A \ddot{r}_i^n - \left(EIr_i'' \right)'' + \left(\bar{\lambda} r_i' \right)' + \bar{w}_i + F_i^d \right] ds = 0 \tag{2.89}$$

The Eqn. (2.89) is solved by using integration by parts and the δU_{ij} in $\delta r_i = A_l \delta U_{il}(t)$ is assumed to be independent:

$$\int_0^L \left\{ \begin{array}{l} A_l \left(\rho \ddot{r}_i + C_A \ddot{r}_i^n \right) + EIA_l'' r_i'' \\ + \bar{\lambda} A_l' r_i' - A_l \left(\bar{w}_i + F_i^d \right) \end{array} \right\} ds = EIr_i''\ A_l' \Big|_0^L + \left[\bar{\lambda} r_i' - \left(EIr_i'' \right)' \right] A_l \Big|_0^L \tag{2.90}$$

Also, the stretching condition in Eqn. (2.73) is imposed by (Ran, 2000):

$$\int_0^L P_m \left\{ \frac{1}{2} \left(r_n' r_n' - 1 \right) - \frac{\lambda}{AE} \right\} ds = 0 \tag{2.91}$$

and *cubic* interpolating functions are applied for A_l while *quadratic* functions for P_m:

$$A_1 = 1 - 3\xi^2 + 2\xi^3\ ,\ A_2 = L\left(\xi - 2\xi^2 + \xi^3 \right)\ ,\ A_3 = 3\xi^2 - 2\xi^3\ ,\ A_4 = L\left(-\xi^2 + \xi^3 \right),$$

$$P_1 = 1 - 3\xi + 2\xi^2\ ,\ P_2 = 4\xi(1-\xi)\ ,\ P_3 = \xi(2\xi - 1) \tag{2.92}$$

where $\xi = \dfrac{S}{L}$ (2.93)

The position r_i, tangent $r_i^{'}$, and the *Lagrangian* multiplier λ are selected to be continuous at the node in between the adjacent elements, thus the parameter U_{il} and λ_m are written as (Ran, 2000):

$$U_{i1}=r_i(0,t),\ U_{i2}=r_i^{'}(0,t),\ U_{i3}=r_i(L,t),\ U_{i4}=r_i^{'}(L,t) \tag{2.94}$$

$$\lambda_1=\lambda(0,t)\ ,\ \lambda_2=\lambda\left(\frac{L}{2},t\right)\ ,\ \lambda_3=\lambda(L,t) \tag{2.95}$$

In this case, the unknown quantities need to be solved are the position vector r_i and tangent vectors $r_i^{'}$ at the two end nodes of the elements, and the scalar λ (Ran, 2000). By combining Eqns. (2.80), (2.87) and (2.88) with Eqn. (2.90), the equation of motion for the element can be represented as:

$$\left(M_{ijlk}+M_{ijlk}^{a}\right)\ddot{U}_{jk}+\left(K_{ijlk}^{1}+\lambda_n K_{nijlk}^{2}\right)U_{jk}-F_{il}=0 \tag{2.96}$$

where the derivation process from Eqn. (2.90) was conducted as:

$$\int_0^L\left\{\begin{array}{l}A_l\left(\rho\ddot{r}_i+C_A\ddot{r}_i^{n}\right)+EIA_l^{''}r_i^{''}\\ +\bar{\lambda}\,A_l^{'}r_i^{'}-A_l\left(\bar{w}_i+F_i^{d}\right)\end{array}\right\}ds=EIr_i^{''}\ A_l^{'}\Big|_0^{L}+\left[\bar{\lambda}r_i^{'}-\left(EIr_i^{''}\right)^{'}\right]A_l\Big|_0^{L} \tag{2.90}$$

$$\ddot{\boldsymbol{r}}^{n}=\ddot{r}_i-\left[\ddot{r}_i\cdot r_i^{'}\right]\cdot r_i^{'} \tag{2.80}$$

$$r_i(s,t)=A_l(s)U_{il}(t) \tag{2.87}$$

$$\lambda(s,t)=P_m(s)\lambda_m(t) \tag{2.88}$$

$$\int_0^L A_l\rho\ddot{r}_i ds=\int_0^L A_l\rho A_k\delta_{ij}ds\ddot{U}_{jk}=M_{ijlk}\ddot{U}_{jk} \tag{2.96a}$$

$$\int_0^L A_l C_A \ddot{r}_i^n ds = \int_0^L A_l C_A \left[\ddot{r}_i - \left(\ddot{r}_i \cdot r_i' \right) \cdot r_i' \right] ds = C_A \left[\int_0^L A_l \left[\ddot{r}_i \right] ds - \int_0^L A_l \left[\left(\ddot{r}_i \cdot r_i' \right) \cdot r_i' \right] ds \right]$$

$$= C_A \left[\int_0^L A_l A_k \delta_{ij} ds - \left(\int_0^L A_l A_k A_s' A_t' ds \right) U_{it} U_{js} \right] \ddot{U}_{jk} = M_{ijlk}^a \ddot{U}_{jk} \tag{2.96)b}$$

$$\int_0^L EIA_l'' r_i'' ds = \int_0^L EIA_l'' A_k'' \delta_{ij} ds U_{jk} = K_{ijlk}^1 U_{jk} \tag{2.96)c}$$

$$\int_0^L \bar{\lambda} A_l' r_i' ds = \lambda_n \int_0^L P_n A_l' A_k' \delta_{ij} ds U_{jk} = \lambda_n K_{nijlk}^2 U_{jk} \tag{2.96)d}$$

$$\int_0^L A_l \left(\bar{w}_i + F_i^d \right) ds = F_{il} \tag{2.96)e}$$

and δ_{ij} is the *Kronecker Delta function*. There is noteworthy that the resultant forces (moments) at the ends of the element (RHS of Eqn. (2.90)) are not included in the Eqn. (2.96) for the reason that these forces (moments) will cancel out with the neighboring element in the final assembly equation. The coefficients of Eqn. (2.96) are defined as:

$$M_{ijlk} = \int_0^L A_l \rho A_k \delta_{ij} ds \text{ = general mass term} \tag{2.97}$$

$$M_{ijlk}^a = C_A \left[\int_0^L A_l A_k \delta_{ij} ds - \left(\int_0^L A_l A_k A_s' A_t' ds \right) U_{it} U_{js} \right] \text{ = added mass} \tag{2.98}$$

$$K_{ijlk}^1 = \int_0^L EIA_l'' A_k'' \delta_{ij} ds \text{ = the general stiffness from the bending stiffness } EI \tag{2.99}$$

$$K_{nijlk}^2 = \int_0^L P_n A_l' A_k' \delta_{ij} ds \text{ = the general stiffness from rod tension rod and curvature} \tag{2.100}$$

$$F_{il} = \int_0^L A_l \left(\bar{w}_i + F_i^d \right) ds \tag{2.101}$$

On the other hand, the Eqn. (2.91) which imposed the stretching condition can be written as:

$$G_m = A_{mil} U_{ik} U_{lk} - B_m - C_{mt} \lambda_t \tag{2.102}$$

where the derivation process from Eqn. (2.91) was performed as:

$$\int_0^L P_m \left\{ \frac{1}{2} \left(r_n' r_n' - 1 \right) - \frac{\lambda}{AE} \right\} ds = 0 \tag{2.91}$$

$$\int_0^L P_m \left\{ \frac{1}{2} \left(r_n' r_n' \right) \right\} ds = \frac{1}{2} \int_0^L P_m A_i' A_l' ds U_{ik} U_{lk} = A_{mil} U_{ik} U_{lk} \tag{2.102a}$$

$$-\frac{1}{2} \int_0^L P_m ds = -B_m \tag{2.102b}$$

$$-\frac{1}{AE} \int_0^L P_m \lambda ds = -\frac{1}{AE} \int_0^L P_m P_t ds \lambda_t = -C_{mt} \lambda_t \tag{2.102c}$$

2.4.3 Formulation of Static Problem

To solve the static problem of the rod, the Eqn. (2.96) and Eqn. (2.102) can be formulated as:

$$\left(K_{ijlk}^1 + \lambda_n K_{nijlk}^2 \right) U_{jk} - F_{il} = R_{ij} = 0 \tag{2.103}$$

$$G_m = 0 \tag{2.104}$$

where F_{il} is combination forcing term exerted from the gravity force, drag force from the steady current, and other applied static force on the rod (line).

Due to the nonlinearity in Eqn. (2.103) and Eqn. (2.104), the iterative method (Newton's method) is used to solve these equations. Using Taylor series to expand the above two equations about the guessed solution, or solution from previous iteration, $U^{(n)}$ and $\lambda^{(n)}$ (n is the iteration number) and neglect the higher order terms (Ran, 2000):

$$R_{il}^{(n+1)} = R_{il}^{(n)} + \frac{\partial R_{il}}{\partial U_{jk}}\left(\Delta U_{jk}\right) + \frac{\partial R_{il}}{\partial \lambda_n}\left(\Delta \lambda_n\right) = 0 \tag{2.105}$$

$$G_m^{(n+1)} = G_m^{(n)} + \frac{\partial G_m}{\partial U_{jk}}\left(\Delta U_{jk}\right) + \frac{\partial G_m}{\partial \lambda_n}\left(\Delta \lambda_n\right) = 0 \tag{2.106}$$

Rearranging these terms into matrix form:

$$\begin{bmatrix} K_{ijlk}^{t0(n)} & K_{iln}^{t1(n)} \\ D_{mjk}^{t0(n)} & D_{mn}^{t1(n)} \end{bmatrix} \begin{Bmatrix} \Delta U_{jk} \\ \Delta \lambda_n \end{Bmatrix} = \begin{Bmatrix} -R_{il}^{(n)} \\ -G_m^{(n)} \end{Bmatrix} \tag{2.107}$$

where the derivation from Eqns. (2.105) and (2.106) are:

$$\begin{bmatrix} \dfrac{\partial R_{il}}{\partial U_{jk}} & \dfrac{\partial R_{il}}{\partial \lambda_n} \\ \dfrac{\partial G_m}{\partial U_{jk}} & \dfrac{\partial G_m}{\partial \lambda_n} \end{bmatrix} \begin{Bmatrix} \Delta U_{jk} \\ \Delta \lambda_n \end{Bmatrix} = \begin{Bmatrix} -R_{il}^{(n)} \\ -G_m^{(n)} \end{Bmatrix} \tag{2.107}a$$

$$R_{ij} = \left(K_{ijlk}^{1} + \lambda_n K_{nijlk}^{2}\right) U_{jk} - F_{il} \tag{2.107}b$$

$$\frac{\partial R_{il}}{\partial U_{jk}} = K_{ijlk}^{1} + \lambda_n^{(n)} K_{nijlk}^{2} = K_{ijlk}^{t0(n)} \tag{2.107}c$$

$$\frac{\partial R_{il}}{\partial \lambda_n} = K_{nijlk}^{2} U_{jk}^{(n)} = \left(\int_0^L P_n A_l' A_k' \delta_{ij} ds\right) U_{jk}^{(n)} = \left(\int_0^L P_n A_l' A_k' ds\right) U_{ik}^{(n)} = K_{iln}^{t1(n)} \tag{2.107}d$$

$$G_m = A_{mil}U_{ik}U_{lk} - B_m - C_{mt}\lambda_t = \frac{1}{2}\int_0^L P_m A_i' A_l' ds U_{ik}U_{lk} - \frac{1}{2}\int_0^L P_m ds - \frac{1}{AE}\int_0^L P_m P_t ds \lambda_t$$
$$= \int_0^L P_m \left\{ \frac{1}{2}\left[A_i' A_l' U_{ik}U_{lk} - 1 \right] - \frac{1}{AE} P_t \lambda_t \right\} ds \qquad (2.107)e$$

$$\frac{\partial G_m}{\partial U_{jk}} = \frac{\partial}{\partial U_{jk}}(G_m) = \frac{\partial}{\partial U_{jk}}\left(\int_0^L P_m \left\{ \frac{1}{2}\left[A_i' A_l' U_{ik}U_{lk} - 1 \right] - \frac{1}{AE} P_t \lambda_t \right\} ds \right)$$
$$= \left(\int_0^L P_m A_i' A_l' ds \right) U_{ik} = \left(\int_0^L P_m A_p' A_k' ds \right) U_{pj} = D_{mjk}^{t0(n)} \qquad (2.107)f$$

$$\frac{\partial G_m}{\partial \lambda_n} = \frac{\partial}{\partial \lambda_n}(G_m) = \frac{\partial}{\partial \lambda_n}\left(\int_0^L P_m \left\{ \frac{1}{2}\left[A_i' A_l' U_{ik}U_{lk} - 1 \right] - \frac{1}{AE} P_t \lambda_t \right\} ds \right)$$
$$= \int_0^L -\frac{1}{AE} P_m P_t ds = \int_0^L -\frac{1}{AE} P_m P_n ds = D_{mn}^{t1(n)} \qquad (2.107)g$$

In the CHARM3D, the global degree of freedom associated with the parameter U_{jk} and λ_n are re-numbered as (Ran, 2000):

For two-dimensions:

$$\text{DOF of } U_{jk} = \text{DOF of } U_{il} = \begin{bmatrix} 1 & 2 & 7 & 8 \\ 3 & 4 & 9 & 10 \end{bmatrix} \text{ for } i = 1, 2 \text{ and } l = 1, 2, 3, 4 \qquad (2.108)$$

$$\text{DOF of } \lambda_n = \text{DOF of } \lambda_m = \begin{bmatrix} 5 & 6 & 11 \end{bmatrix} \text{ for } m = 1, 2, 3 \qquad (2.109)$$

and for three-dimensions:

$$\text{DOF of } U_{jk} = \text{DOF of } U_{il} = \begin{bmatrix} 1 & 2 & 9 & 10 \\ 3 & 4 & 11 & 12 \\ 5 & 6 & 13 & 14 \end{bmatrix} \text{ for } i = 1, 2, 3 \text{ and } l = 1, 2, 3, 4 \qquad (2.110)$$

$$\text{DOF of } \lambda_n = \text{DOF of } \lambda_m = \begin{bmatrix} 7 & 8 & 15 \end{bmatrix} \text{ for } m = 1, 2, 3 \qquad (2.111)$$

After the renumbering, the Eqn. (2.107) can be represented as (Ran, 2000):

$$\boldsymbol{K}^{(n)}\left(\Delta \boldsymbol{y}\right)=\boldsymbol{F}^{(n)} \tag{2.112}$$

where the variables U_{jk} and λ_n form the vector $\boldsymbol{y}$:

$$\boldsymbol{y}^T=\left\{U_{11},\, U_{12},\, U_{21},\, U_{22},\, U_{31},\, U_{32},\, \lambda_1,\, \lambda_2,\, U_{13},\, U_{14},\, U_{23},\, U_{24},\, U_{33},\, U_{34},\, \lambda_3\right\} \tag{2.113}$$

and $\boldsymbol{K}$ is the stiffness matrix, $\boldsymbol{F}$ is the force vector:

$$\boldsymbol{F}^T=\left\{R_{11},\, R_{12},\, R_{21},\, R_{22},\, R_{31},\, R_{32},\, -G_1,\, -G_2,\, R_{13},\, R_{14},\, R_{23},\, R_{24},\, R_{33},\, R_{34},\, -G_3\right\} \tag{2.114}$$

From the RHS of Eqn. (2.90), the force vector can be defined as:

$$\boldsymbol{F}^r=\begin{bmatrix}
-\bar{\lambda}r_i^{'}+\left(EIr_i^{''}\right)^{'}\Big|_{s=0,i=1}\\
-EIr_i^{''}\Big|_{s=0,i=1}\\
-\bar{\lambda}r_i^{'}+\left(EIr_i^{''}\right)^{'}\Big|_{s=0,i=2}\\
-EIr_i^{''}\Big|_{s=0,i=2}\\
-\bar{\lambda}r_i^{'}+\left(EIr_i^{''}\right)^{'}\Big|_{s=0,i=3}\\
-EIr_i^{''}\Big|_{s=0,i=3}\\
0\\
0\\
\bar{\lambda}r_i^{'}-\left(EIr_i^{''}\right)^{'}\Big|_{s=L,i=1}\\
EIr_i^{''}\Big|_{s=L,i=1}\\
\bar{\lambda}r_i^{'}-\left(EIr_i^{''}\right)^{'}\Big|_{s=L,i=2}\\
EIr_i^{''}\Big|_{s=L,i=2}\\
\bar{\lambda}r_i^{'}-\left(EIr_i^{''}\right)^{'}\Big|_{s=L,i=3}\\
EIr_i^{''}\Big|_{s=L,i=3}\\
0
\end{bmatrix}=\begin{bmatrix}
-N_1^{[1]}\\
-L_1^{[1]}\\
-N_2^{[1]}\\
-L_2^{[1]}\\
-N_3^{[1]}\\
-L_3^{[1]}\\
0\\
0\\
N_1^{[2]}\\
L_1^{[2]}\\
N_2^{[2]}\\
L_2^{[2]}\\
N_3^{[2]}\\
L_3^{[2]}\\
0
\end{bmatrix} \tag{2.115}$$

where the superscript 1 denotes the first end of the element $(s=0)$ and the superscript 2 denotes the second end $(s=L)$ (Ran, 2000). From the definition of the resultant force and moment in Eqns. (2.64) and (2.69), there can be found that the $\boldsymbol{N}=\{N_1,\quad N_2,\quad N_3\}^T$ is the nodal resultant force and $\boldsymbol{L}=\{L_1,\quad L_2,\quad L_3\}^T$ is related to the nodal resultant moment $\boldsymbol{M}(\boldsymbol{M}=\boldsymbol{L}\times\boldsymbol{r}')$. After solving the model variables U and λ (at iteration $n+1$), the resultant force at the end nodes of an element can be obtained from force vector $\boldsymbol{F}^r$ as (Ran, 2000):

$$\boldsymbol{F}^r=-\boldsymbol{F}^{(n+1)} \tag{2.116}$$

2.4.4 Formulation of Dynamic Problem – Time Domain Integration

To solve the dynamic problem of the rod motion, recalling the equation of motion (Eqn. (2.96)) and the stretch condition (Eqn. (2.102)):

$$\left(M_{ijlk}+M^a_{ijlk}\right)\ddot{U}_{jk}+\left(K^1_{ijlk}+\lambda_n K^2_{nijlk}\right)U_{jk}-F_{il}=0 \tag{2.96}$$

$$G_m=A_{mil}U_{ik}U_{lk}-B_m-C_{mt}\lambda_t \tag{2.102}$$

The Eqn. (2.96) and Eqn. (2.102) can be rewritten as:

$$\begin{aligned}&\left(M_{ijlk}+M^a_{ijlk}\right)\ddot{U}_{jk}+\left(K^1_{ijlk}+\lambda_n K^2_{nijlk}\right)U_{jk}-F_{il}\\&=\left(\hat{M}_{ijlk}\right)\ddot{U}_{jk}+\left(K^1_{ijlk}+\lambda_n K^2_{nijlk}\right)U_{jk}-F_{il}=0\end{aligned} \tag{2.117}$$

$$\left(\hat{M}_{ijlk}\right)\ddot{U}_{jk}=-\left(K^1_{ijlk}+\lambda_n K^2_{nijlk}\right)U_{jk}+F_{il}=-F^1_{il}-F^2_{il}+F_{il}=\hat{F}_{il} \tag{2.118}$$

$$G_m=A_{mil}U_{ik}U_{lk}-B_m-C_{mt}\lambda_t=0 \tag{2.119}$$

where:

$$\hat{M}_{ijlk} = M_{ijlk} + M^{a}_{ijlk}, \quad F^{1}_{il} = K^{1}_{ijlk} U_{jk}, \quad F^{2}_{il} = \lambda_n K^{2}_{nijlk} U_{jk} \tag{2.120}$$

In order to derive the integration scheme, Eqn. (2.118) is rewritten into two first-order differential equations (Ran, 2000):

$$\hat{M}_{ijlk} \dot{V}_{jk} = \hat{F}_{il} \tag{2.121}$$

$$\dot{U}_{jk} = V_{jk} \tag{2.122}$$

These two first-order differential equations are integrated form time $t^{(n)}$ (at time step n) to $t^{(n+1)}$ (at time step $n+1$):

$$\int_{t^{(n)}}^{t^{(n+1)}} \hat{M}_{ijlk} \dot{V}_{jk} dt = \int_{t^{(n)}}^{t^{(n+1)}} \hat{F}_{il} dt \tag{2.123}$$

$$\int_{t^{(n)}}^{t^{(n+1)}} \dot{U}_{jk} dt = \int_{t^{(n)}}^{t^{(n+1)}} V_{jk} dt \tag{2.124}$$

There is noteworthy that the term $\hat{M}_{ijlk}$ in Eqn. (2.123) is varying with respect to time because it consisted of the added mass term M^{a}_{ijlk}, which is a function of the rod's position. By approximating the time varying $\hat{M}_{ijlk}$ in the time interval Δt $(= t^{(n+1)} - t^{(n)})$ to be a constant, $\hat{M}^{\left(n+\frac{1}{2}\right)}_{ijlk}$ which is the mass at time $t^{(n)} + \frac{\Delta t}{2}$, the integration of the LHS in Eqn. (2.123) can be simplified as follows while achieving second-order accuracy (numerical error is at $O\left(\Delta t^2\right)$) (Ran, 2000):

$$\int_{t^{(n)}}^{t^{(n+1)}} \hat{M}_{ijlk}\dot{V}_{jk}dt = \int_{t^{(n)}}^{t^{(n+1)}} \hat{F}_{il}dt$$

$$\hat{M}_{ijlk}^{\left(n+\frac{1}{2}\right)}V_{jk}^{(n+1)} - \hat{M}_{ijlk}^{\left(n+\frac{1}{2}\right)}V_{jk}^{(n)} = \int_{t^{(n)}}^{t^{(n+1)}} \hat{F}_{il}dt \tag{2.125}$$

The Eqn. (2.124) can be rearranged by using the trapezoidal method with second-order accuracy, as:

$$U_{jk}^{(n+1)} - U_{jk}^{(n)} = \frac{\Delta t}{2}\left[V_{jk}^{(n+1)} + V_{jk}^{(n)}\right]$$

$$U_{jk}^{(n+1)} = U_{jk}^{(n)} + \frac{\Delta t}{2}\left[V_{jk}^{(n+1)} + V_{jk}^{(n)}\right] \tag{2.126}$$

Rearranging the Eqns. (2.125) and (2.126) to obtain:

$$V_{jk}^{(n+1)} = \frac{2}{\Delta t}\left(U_{jk}^{(n+1)} - U_{jk}^{(n)}\right) - V_{jk}^{(n)} = \frac{2}{\Delta t}\left(\Delta U_{jk}\right) - V_{jk}^{(n)} \tag{2.127}$$

$$\hat{M}_{ijlk}^{\left(n+\frac{1}{2}\right)}V_{jk}^{(n+1)} = \hat{M}_{ijlk}^{\left(n+\frac{1}{2}\right)}V_{jk}^{(n)} + \int_{t^{(n)}}^{t^{(n+1)}} \hat{F}_{il}dt$$

$$\hat{M}_{ijlk}^{\left(n+\frac{1}{2}\right)}\left(\frac{2}{\Delta t}\left(\Delta U_{jk}\right) - V_{jk}^{(n)}\right) = \hat{M}_{ijlk}^{\left(n+\frac{1}{2}\right)}V_{jk}^{(n)} + \int_{t^{(n)}}^{t^{(n+1)}} \hat{F}_{il}dt$$

$$\frac{2}{\Delta t}\hat{M}_{ijlk}^{\left(n+\frac{1}{2}\right)}\left(\Delta U_{jk}\right) - \hat{M}_{ijlk}^{\left(n+\frac{1}{2}\right)}V_{jk}^{(n)} = \hat{M}_{ijlk}^{\left(n+\frac{1}{2}\right)}V_{jk}^{(n)} + \int_{t^{(n)}}^{t^{(n+1)}} \hat{F}_{il}dt$$

$$\frac{4}{\Delta t^2}\hat{M}_{ijlk}^{\left(n+\frac{1}{2}\right)}\left(\Delta U_{jk}\right) = \frac{4}{\Delta t}\hat{M}_{ijlk}^{\left(n+\frac{1}{2}\right)}V_{jk}^{(n)} + \frac{2}{\Delta t}\int_{t^{(n)}}^{t^{(n+1)}} \hat{F}_{il}dt \tag{2.128}$$

where $\Delta U_{jk} = U_{jk}^{(n+1)} - U_{jk}^{(n)}$, and the integral term in Eqn. (2.128) is:

$$\int_{t^{(n)}}^{t^{(n+1)}} \hat{F}_{il}dt = \int_{t^{(n)}}^{t^{(n+1)}} \left(-F_{il}^{1} - F_{il}^{2} + F_{il}\right)dt = -\int_{t^{(n)}}^{t^{(n+1)}} F_{il}^{1}dt - \int_{t^{(n)}}^{t^{(n+1)}} F_{il}^{2}dt + \int_{t^{(n)}}^{t^{(n+1)}} F_{il}dt \tag{2.129}$$

The *trapezoidal rules* is applied to the first and second terms at the RHS of Eqn. (2.129):

$$\begin{aligned}
\int_{t^{(n)}}^{t^{(n+1)}} F_{il}^{1} dt &= \frac{\Delta t}{2}\left(F_{il}^{1(n+1)} + F_{il}^{1(n)} \right) = \frac{\Delta t}{2}\left(K_{ijlk}^{1} U_{jk}^{(n+1)} + K_{ijlk}^{1} U_{jk}^{(n)} \right) \\
&= \frac{\Delta t}{2}\left(K_{ijlk}^{1} \left(U_{jk}^{(n+1)} + U_{jk}^{(n)} \right) \right) = \frac{\Delta t}{2}\left(K_{ijlk}^{1} \left(U_{jk}^{(n+1)} - U_{jk}^{(n)} + 2U_{jk}^{(n)} \right) \right) \\
&= \frac{\Delta t}{2}\left[K_{ijlk}^{1} \left(\Delta U_{jk} - 2U_{jk}^{(n)} \right) \right]
\end{aligned} \tag{2.130}$$

$$\begin{aligned}
\int_{t^{(n)}}^{t^{(n+1)}} F_{il}^{2} dt &= \frac{\Delta t}{2}\left(F_{il}^{2(n+1)} + F_{il}^{2(n)} \right) = \frac{\Delta t}{2}\left(\lambda_{n}^{(n+1)} K_{nijlk}^{2} U_{jk}^{(n+1)} + \lambda_{n}^{(n)} K_{nijlk}^{2} U_{jk}^{(n)} \right) \\
&\approx \frac{\Delta t}{2}\left(\lambda_{n}^{\left(n+\frac{1}{2}\right)} K_{nijlk}^{2} U_{jk}^{(n+1)} + \lambda_{n}^{\left(n+\frac{1}{2}\right)} K_{nijlk}^{2} U_{jk}^{(n)} \right) \\
&= \frac{\Delta t}{2}\left(\begin{array}{l} \left(2\lambda_{n}^{\left(n-\frac{1}{2}\right)} + 2\lambda_{n}^{\left(n+\frac{1}{2}\right)} - 2\lambda_{n}^{\left(n-\frac{1}{2}\right)} - \lambda_{n}^{\left(n+\frac{1}{2}\right)} \right) K_{nijlk}^{2} U_{jk}^{(n)} \\ + \lambda_{n}^{\left(n+\frac{1}{2}\right)} K_{nijlk}^{2} U_{jk}^{(n+1)} \end{array} \right) \\
&= \frac{\Delta t}{2}\left(\begin{array}{l} 2\lambda_{n}^{\left(n-\frac{1}{2}\right)} K_{nijlk}^{2} U_{jk}^{(n)} + 2\lambda_{n}^{\left(n+\frac{1}{2}\right)} K_{nijlk}^{2} U_{jk}^{(n)} - 2\lambda_{n}^{\left(n-\frac{1}{2}\right)} K_{nijlk}^{2} U_{jk}^{(n)} \\ + \lambda_{n}^{\left(n+\frac{1}{2}\right)} K_{nijlk}^{2} U_{jk}^{(n+1)} - \lambda_{n}^{\left(n+\frac{1}{2}\right)} K_{nijlk}^{2} U_{jk}^{(n)} \end{array} \right) \\
&= \frac{\Delta t}{2}\left(\begin{array}{l} 2\lambda_{n}^{\left(n-\frac{1}{2}\right)} K_{nijlk}^{2} U_{jk}^{(n)} + 2\left(\lambda_{n}^{\left(n+\frac{1}{2}\right)} - \lambda_{n}^{\left(n-\frac{1}{2}\right)} \right) K_{nijlk}^{2} U_{jk}^{(n)} \\ + \lambda_{n}^{\left(n+\frac{1}{2}\right)} K_{nijlk}^{2} \left(U_{jk}^{(n+1)} - U_{jk}^{(n)} \right) \end{array} \right) \\
&= \frac{\Delta t}{2}\left(2\lambda_{n}^{\left(n-\frac{1}{2}\right)} K_{nijlk}^{2} U_{jk}^{(n)} + 2\left(\Delta\lambda_{n} \right) K_{nijlk}^{2} U_{jk}^{(n)} + \lambda_{n}^{\left(n+\frac{1}{2}\right)} K_{nijlk}^{2} \left(\Delta U_{jk} \right) \right)
\end{aligned} \tag{2.131}$$

where

$$\Delta\lambda_{n} = \lambda_{n}^{\left(n+\frac{1}{2}\right)} - \lambda_{n}^{\left(n-\frac{1}{2}\right)} \tag{2.132}$$

The third term in the RHS of Eqn. (2.129), $\int_{t^{(n)}}^{t^{(n+1)}} F_{il}dt$, contains the applied force F_{il} which is from gravity force and hydrodynamic forces, $\left[F_{il} = \int_0^L A_l \left(\bar{w}_i + F_i^d \right) ds \right]$ (Ran, 2000). The hydrodynamic force is unknown at time step (n) due to it is a dependent of the rod's position and velocity at time step $(n+1)$. Hence, the *Adams-Bashforth* explicit scheme for the integral is employed here to predict the value of:

$$\int_{t^{(n)}}^{t^{(n+1)}} F_{il}dt = \frac{\Delta t}{2}\left(3F_{il}^{(n)} - F_{il}^{(n-1)}\right) = \Delta t F_{il}^{(0)} \text{ for step 1} \tag{2.133}$$

By combining Eqns. (2.125), (2.126), (2.130), (2.131) and (2.133), the dynamic integration scheme for the motion equation, Eqn. (2.118) can be rewritten as:

$$\left[\frac{4}{\Delta t^2}\hat{M}_{ijlk}^{\left(n+\frac{1}{2}\right)} + K_{ijlk}^1 + \lambda_n^{\left(n+\frac{1}{2}\right)} K_{nijlk}^2\right]\Delta U_{jk} + 2\left(\Delta\lambda_n\right)K_{nijlk}^2 U_{jk}^{(n)}$$
$$= \frac{4}{\Delta t}\hat{M}_{ijlk}^{\left(n+\frac{1}{2}\right)} V_{jk}^{(n)} - 2K_{ijlk}^1 U_{jk}^{(n)} - 2\lambda_n^{\left(n-\frac{1}{2}\right)} K_{nijlk}^2 U_{jk}^{(n)} + \left(3F_{il}^{(n)} - F_{il}^{(n-1)}\right) \tag{2.134}$$

where the derivation process is conducted as:

$$\left(\hat{M}_{ijlk}\right)\ddot{U}_{jk} = -\left(K_{ijlk}^1 + \lambda_n K_{nijlk}^2\right)U_{jk} + F_{il} = -F_{il}^1 - F_{il}^2 + F_{il} = \hat{F}_{il} \tag{2.118}$$

$$\hat{M}_{ijlk}^{\left(n+\frac{1}{2}\right)} V_{jk}^{(n+1)} - \hat{M}_{ijlk}^{\left(n+\frac{1}{2}\right)} V_{jk}^{(n)} = \int_{t^{(n)}}^{t^{(n+1)}} \hat{F}_{il}dt \tag{2.125}$$

$$U_{jk}^{(n+1)} = U_{jk}^{(n)} + \frac{\Delta t}{2}\left[V_{jk}^{(n+1)} + V_{jk}^{(n)}\right] \tag{2.126}$$

$$\int_{t^{(n)}}^{t^{(n+1)}} F_{il}^{1} dt = \frac{\Delta t}{2}\left[K_{ijlk}^{1}\left(\Delta U_{jk} - 2U_{jk}^{(n)}\right)\right] \tag{2.130}$$

$$\int_{t^{(n)}}^{t^{(n+1)}} F_{il}^{2} dt = \frac{\Delta t}{2}\left(2\lambda_n^{\left(n-\frac{1}{2}\right)} K_{nijlk}^{2} U_{jk}^{(n)} + 2\left(\Delta\lambda_n\right) K_{nijlk}^{2} U_{jk}^{(n)} + \lambda_n^{\left(n+\frac{1}{2}\right)} K_{nijlk}^{2}\left(\Delta U_{jk}\right)\right) \tag{2.131}$$

$$\int_{t^{(n)}}^{t^{(n+1)}} F_{il} dt = \frac{\Delta t}{2}\left(3F_{il}^{(n)} - F_{il}^{(n-1)}\right) \tag{2.133}$$

$$\begin{aligned}\frac{4}{\Delta t^2}\hat{M}_{ijlk}^{\left(n+\frac{1}{2}\right)}\left(\Delta U_{jk}\right) = {} & \frac{4}{\Delta t}\hat{M}_{ijlk}^{\left(n+\frac{1}{2}\right)} V_{jk}^{(n)} \\ & + \frac{2}{\Delta t}\left(\begin{array}{l} -\frac{\Delta t}{2}\left[K_{ijlk}^{1}\left(\Delta U_{jk} - 2U_{jk}^{(n)}\right)\right] \\ -\frac{\Delta t}{2}\left(\begin{array}{l} 2\lambda_n^{\left(n-\frac{1}{2}\right)} K_{nijlk}^{2} U_{jk}^{(n)} + 2\left(\Delta\lambda_n\right) K_{nijlk}^{2} U_{jk}^{(n)} \\ +\lambda_n^{\left(n+\frac{1}{2}\right)} K_{nijlk}^{2}\left(\Delta U_{jk}\right)\end{array}\right) \\ +\frac{\Delta t}{2}\left(3F_{il}^{(n)} - F_{il}^{(n-1)}\right)\end{array}\right)\end{aligned} \tag{2.134)a}$$

$$\begin{aligned}\frac{4}{\Delta t^2}\hat{M}_{ijlk}^{\left(n+\frac{1}{2}\right)}\left(\Delta U_{jk}\right) = {} & \frac{4}{\Delta t}\hat{M}_{ijlk}^{\left(n+\frac{1}{2}\right)} V_{jk}^{(n)} - \left[K_{ijlk}^{1}\left(\Delta U_{jk} - 2U_{jk}^{(n)}\right)\right] \\ & - \left[2\lambda_n^{\left(n-\frac{1}{2}\right)} K_{nijlk}^{2} U_{jk}^{(n)} + 2\left(\Delta\lambda_n\right) K_{nijlk}^{2} U_{jk}^{(n)} + \lambda_n^{\left(n+\frac{1}{2}\right)} K_{nijlk}^{2}\left(\Delta U_{jk}\right)\right] \\ & + \left(3F_{il}^{(n)} - F_{il}^{(n-1)}\right)\end{aligned} \tag{2.134)b}$$

$$\begin{aligned}\frac{4}{\Delta t^2}\hat{M}_{ijlk}^{\left(n+\frac{1}{2}\right)}\left(\Delta U_{jk}\right) = {} & \frac{4}{\Delta t}\hat{M}_{ijlk}^{\left(n+\frac{1}{2}\right)} V_{jk}^{(n)} - K_{ijlk}^{1}\Delta U_{jk} + 2K_{ijlk}^{1} U_{jk}^{(n)} - 2\lambda_n^{\left(n-\frac{1}{2}\right)} K_{nijlk}^{2} U_{jk}^{(n)} \\ & -2\left(\Delta\lambda_n\right) K_{nijlk}^{2} U_{jk}^{(n)} - \lambda_n^{\left(n+\frac{1}{2}\right)} K_{nijlk}^{2}\left(\Delta U_{jk}\right) + \left(3F_{il}^{(n)} - F_{il}^{(n-1)}\right)\end{aligned} \tag{2.134)c}$$

$$\frac{4}{\Delta t^2}\hat{M}_{ijlk}^{\left(n+\frac{1}{2}\right)}\left(\Delta U_{jk}\right)+K_{ijlk}^{1}\Delta U_{jk}+\lambda_n^{\left(n+\frac{1}{2}\right)}K_{nijlk}^{2}\left(\Delta U_{jk}\right)+2\left(\Delta\lambda_n\right)K_{nijlk}^{2}U_{jk}^{(n)}$$
$$=\frac{4}{\Delta t}\hat{M}_{ijlk}^{\left(n+\frac{1}{2}\right)}V_{jk}^{(n)}-2K_{ijlk}^{1}U_{jk}^{(n)}-2\lambda_n^{\left(n-\frac{1}{2}\right)}K_{nijlk}^{2}U_{jk}^{(n)}+\left(3F_{il}^{(n)}-F_{il}^{(n-1)}\right) \quad (2.134)\text{d}$$

and the mass term $\hat{M}_{ijlk}^{\left(n+\frac{1}{2}\right)}$ is approximated by using *Adams-Bashforth* method:

$$\hat{M}_{ijlk}^{\left(n+\frac{1}{2}\right)}=\frac{1}{2}\left(3\hat{M}_{ijlk}^{(n)}-\hat{M}_{ijlk}^{(n-1)}\right) \quad (2.135)$$

On the other hand, for the stretch condition Eqn. (2.119), the $G_m^{(n+1)}$ at time step $\left(n+1\right)$ can be approximated from $G_m^{(n)}$ at time step n by using Taylor expansion:

$$G_m=A_{mil}U_{ik}U_{lk}-B_m-C_{mt}\lambda_t=0 \quad (2.119)$$

$$0=G_m^{(n+1)}\approx G_m^{(n)}+\frac{\partial G_m^{(n)}}{\partial U_{jk}}\Delta U_{jk}+\frac{\partial G_m^{(n)}}{\partial\lambda_n}\Delta\lambda_n\rightarrow$$
$$0=2G_m^{(n+1)}\approx 2G_m^{(n)}+2\frac{\partial G_m^{(n)}}{\partial U_{jk}}\Delta U_{jk}+2\frac{\partial G_m^{(n)}}{\partial\lambda_n}\Delta\lambda_n$$
$$=2G_m^{(n)}+2D_{mjk}^{t0(n)}\Delta U_{jk}+2D_{mn}^{t1(n)}\Delta\lambda_n$$
$$=2G_m^{(n)}+2\left(\int_0^L P_n A_l' A_k' \delta_{ij} ds\right)U_{jk}^{(n)}\Delta U_{jk}+2D_{mn}^{t1(n)}\Delta\lambda_n$$
$$=2G_m^{(n)}+2K_{nijlk}^{2}U_{jk}^{(n)}\Delta U_{jk}+2D_{mn}^{t1(n)}\Delta\lambda_n \quad (2.136)$$

Thus, the Eqns. (2.134) and (2.136) are rewritten in a form for time domain problem as (Ran, 2000):

$$\left[\frac{4}{\Delta t^2}\hat{M}_{ijlk}^{\left(n+\frac{1}{2}\right)}+K_{ijlk}^{1}+\lambda_n^{\left(n+\frac{1}{2}\right)}K_{nijlk}^{2}\right]\Delta U_{jk}+2\left(\Delta\lambda_n\right)K_{nijlk}^{2}U_{jk}^{(n)}$$
$$=\frac{4}{\Delta t}\hat{M}_{ijlk}^{\left(n+\frac{1}{2}\right)}V_{jk}^{(n)}-2K_{ijlk}^{1}U_{jk}^{(n)}-2\lambda_n^{\left(n-\frac{1}{2}\right)}K_{nijlk}^{2}U_{jk}^{(n)}+\left(3F_{il}^{(n)}-F_{il}^{(n-1)}\right) \quad (2.134)$$

$$0 \approx 2G_m^{(n)} + 2K_{mijlk}^2 U_{il}^{(n)} \Delta U_{jk} + 2D_{mn}^{t1(n)} \Delta\lambda_n \tag{2.136}$$

$$\begin{bmatrix} \hat{K}_{ijlk}^{t0(n)} & \hat{K}_{iln}^{t1(n)} \\ \hat{D}_{mjk}^{t0(n)} & \hat{D}_{mn}^{t1(n)} \end{bmatrix} \begin{Bmatrix} \Delta U_{jk} \\ \Delta\lambda_n \end{Bmatrix} = \begin{Bmatrix} \hat{R}_{il}^{(n)} \\ -\hat{G}_m^{(n)} \end{Bmatrix} \tag{2.137}$$

where

$$\begin{aligned} \hat{K}_{ijlk}^{t0(n)} &= \frac{4}{\Delta t^2} \hat{M}_{ijlk}^{\left(n+\frac{1}{2}\right)} + K_{ijlk}^1 + \lambda_n^{\left(n+\frac{1}{2}\right)} K_{nijlk}^2 \\ &= \frac{4}{\Delta t^2} \frac{1}{2} \left(3\hat{M}_{ijlk}^{(n)} - \hat{M}_{ijlk}^{(n-1)} \right) + K_{ijlk}^1 + \lambda_n^{\left(n+\frac{1}{2}\right)} K_{nijlk}^2 \\ &= \frac{2}{\Delta t^2} \left(3\hat{M}_{ijlk}^{(n)} - \hat{M}_{ijlk}^{(n-1)} \right) + K_{ijlk}^1 + \lambda_n^{\left(n+\frac{1}{2}\right)} K_{nijlk}^2 \end{aligned} \tag{2.138}$$

$$\hat{K}_{iln}^{t1(n)} = 2K_{nijlk}^2 U_{jk}^{(n)} \tag{2.139}$$

$$\hat{D}_{mjk}^{t0(n)} = 2K_{mijlk}^2 U_{il}^{(n)} \tag{2.140}$$

$$\hat{D}_{mn}^{t1(n)} = 2D_{mn}^{t1(n)} \tag{2.141}$$

$$\begin{aligned} \hat{R}_{il}^{(n)} &= \frac{4}{\Delta t} \hat{M}_{ijlk}^{\left(n+\frac{1}{2}\right)} V_{jk}^{(n)} - 2K_{ijlk}^1 U_{jk}^{(n)} - 2\lambda_n^{\left(n-\frac{1}{2}\right)} K_{nijlk}^2 U_{jk}^{(n)} + \left(3F_{il}^{(n)} - F_{il}^{(n-1)} \right) \\ &= \frac{4}{\Delta t} \frac{1}{2} \left(3\hat{M}_{ijlk}^{(n)} - \hat{M}_{ijlk}^{(n-1)} \right) V_{jk}^{(n)} - 2K_{ijlk}^1 U_{jk}^{(n)} - 2\lambda_n^{\left(n-\frac{1}{2}\right)} K_{nijlk}^2 U_{jk}^{(n)} + \left(3F_{il}^{(n)} - F_{il}^{(n-1)} \right) \\ &= \frac{2}{\Delta t} \left(3\hat{M}_{ijlk}^{(n)} - \hat{M}_{ijlk}^{(n-1)} \right) V_{jk}^{(n)} - 2K_{ijlk}^1 U_{jk}^{(n)} - 2\lambda_n^{\left(n-\frac{1}{2}\right)} K_{nijlk}^2 U_{jk}^{(n)} + \left(3F_{il}^{(n)} - F_{il}^{(n-1)} \right) \end{aligned} \tag{2.142}$$

$$\hat{G}_m^{(n)} = 2G_m^{(n)} \tag{2.143}$$

The formulation of these coefficients (such as K_{ijlk}^1, K_{nijlk}^2 and $G_m^{(n)}$) are the same as that in the static analysis, with the superscript n indicating the nth time step instead of nth iteration, the final equation for a rod element can be written as (Ran, 2000):

$$\hat{\mathbf{K}}^{(n)}\left(\Delta\mathbf{y}\right)=\hat{\mathbf{F}}^{(n)} \text{ at time step } n \tag{2.144}$$

where $\boldsymbol{y}$ is defined in Eqn. (2.113) and the arrangement of the $\hat{\mathbf{K}}$ and $\hat{\mathbf{F}}$ is similar to that in the static problem. After solving the assembled element equations for time step $\left(n+1\right)$, the nodal resultant force can be obtained as:

$$\mathbf{F}^{r}=-\mathbf{F}^{(n+1)} \tag{2.145}$$

2.4.5 Spring Coupling Between the Platform and Mooring Line

The numerical modeling of the connection between the rods/lines (mooring lines and risers) and the floating platform is modeled as a combination of linear spring and rotational spring. The linear spring defines the translational motion between the platform's connecting point and the top of the line, while the rotational spring represents the rotation of the platform and the tangential direction of the line.

In the formulation of the line element equation, the terms at the RHS of the motion integral Eqn. (2.90) are the nodal resultant forces and moments, as recalled in the following expression:

$$\int_0^L \begin{Bmatrix} A_l\left(\rho\ddot{r}_i+C_A\ddot{r}_i^n\right)+EIA_l''r_i'' \\ +\bar{\lambda}A_l'r_i'-A_l\left(\bar{w}_i+F_i^d\right) \end{Bmatrix} ds = EIr_i''\ A_l'\Big|_0^{\boldsymbol{L}}+\left[\bar{\lambda}r_i'-\left(EIr_i''\right)'\right]A_l\Big|_0^L \tag{2.90}$$

and they are presented in the vector form in Eqn. (2.115), where $\boldsymbol{N}=\left\{N_1,\quad N_2,\quad N_3\right\}^T$ is the nodal resultant force and $\mathbf{L}=\left\{L_1,\quad L_2,\quad L_3\right\}^T$ is related to the nodal resultant moment $\mathbf{M}\left(\mathbf{M}=\mathbf{L}\times\mathbf{r}'\right)$ (Ran, 2000). The resultant force and moment of the

intermediate nodes are mutually canceled out when the adjacent elements are arranged into the assembly equation. On the other hand, for the node at the end of the line which is connected to the floating platform, the resultant force and moment are equal to the force and moment applied to the node from the springs. Under the assumption of *small angular motions* of the platform, the force exerted on the *node* at the end of line caused by the linear spring connector can be defined as (Ran, 2000):

$$\boldsymbol{N} = \left[\boldsymbol{K}^{L}\right]\left(\boldsymbol{X} + \boldsymbol{p} + \theta \times \boldsymbol{p} - \boldsymbol{r}\right) \tag{2.146}$$

where $\left[\boldsymbol{K}^{L}\right]$ denotes a 3×3 diagonal stiffness matrix of the linear spring with the nontrivial diagonal terms, K_1^L, K_2^L, K_3^L are the spring stiffness in x, y, z direction, respectively; $\boldsymbol{X}$ is the translational motion of the rigid body at its origin of the body coordinate system; θ is the angular motion of the rigid body; $\boldsymbol{p}$ represents the position vector (in body coordinate system) of the point on the platform where the springs are attached to; and $\boldsymbol{r}$ is the position of the end node of the line which is attached to the rigid body by springs.

The node attached to the platform is numbered as node ($s = L$) in the CHARM3D. Hence, Eqns. (2.94) and (2.95) can be labeled as:

$$U_{i1} = r_i(0,t),\ U_{i2} = r_i'(0,t),\ U_{i3} = r_i(L,t),\ U_{i4} = r_i'(L,t) \tag{2.94}$$

$$\lambda_1 = \lambda(0,t)\ ,\ \lambda_2 = \lambda\left(\frac{L}{2}, t\right)\ ,\ \lambda_3 = \lambda(L,t) \tag{2.95}$$

$$U_{13} = r_1(L,t),\quad U_{23} = r_2(L,t),\quad U_{33} = r_3(L,t) \tag{2.147}$$

Contributed from the linear spring connector, the force and moment exerted on the *platform* are:

$$\boldsymbol{F}^{L} = -\boldsymbol{N} \tag{2.148}$$

$$\boldsymbol{M}^{L} = \boldsymbol{p} \times -\boldsymbol{N} \tag{2.149}$$

On the other hand, the moment applied on the end *node* caused by the rotational spring connector is proportional to the angle between the direction vector of the spring and the tangent of the line at the connection. Under the assumption of *small angular motions* of the platform (Ran, 2000):

$$\boldsymbol{L} = K^{\theta}\left(\boldsymbol{E} - \frac{\boldsymbol{r}'}{|\boldsymbol{r}'|}\right) = K^{\theta}\left(\boldsymbol{e} + \theta \times \boldsymbol{e} - \frac{\boldsymbol{r}'}{|\boldsymbol{r}'|}\right) \tag{2.150}$$

where $\boldsymbol{r}'$ is tangent to the riser centerline. The $\frac{\boldsymbol{r}'}{|\boldsymbol{r}'|}$ is used to ensure the unity of the tangent; $\boldsymbol{E}$ denotes a unit vector in the direction of the spring reference; $\boldsymbol{e}$ is $\boldsymbol{E}$ in the rigid body coordinates; and K^{θ} is the rotational spring constant.

Contributed from the rotational spring connector, the force and moment exerted on the *platform* are:

$$\boldsymbol{F}^{\theta} = 0 \tag{2.151}$$

$$\boldsymbol{M}^{\theta} = \boldsymbol{L} \times \boldsymbol{r}' \approx \boldsymbol{L} \times \boldsymbol{e} \tag{2.152}$$

The connector force on the end node of the line can be rewritten in subscript notation as:

$$N_i = K_i^{L}\left(X_i + p_i + \theta_j C_{ji} - r_i\right) \tag{2.153}$$

$$L_i = K^{\theta}\left(e_i + \theta_j D_{ji} - \frac{r_i^{'}}{\left(r_k^{'} r_k^{'}\right)^{1/2}}\right) \tag{2.154}$$

and the connector force and moment on the *platform* (which is regarded as *rigid body*) are:

$$F_i = -N_i = -K_i^L\left(X_i + p_i + \theta_j C_{ji} - r_i\right) \tag{2.155}$$

$$M_i = M^L + M^{\theta} = N_k C_{ki} + L_k D_{ki} \tag{2.156}$$

where

$$\left[C\right] = \begin{bmatrix} 0 & -p_3 & p_2 \\ p_3 & 0 & -p_1 \\ -p_2 & p_1 & 0 \end{bmatrix} \tag{2.157}$$

$$\left[D\right] = \begin{bmatrix} 0 & -e_3 & e_2 \\ e_3 & 0 & -e_1 \\ -e_2 & e_1 & 0 \end{bmatrix} \tag{2.158}$$

for the three dimensional case.

In the *static* analysis of the mooring line where the Newton's method is used, the connector force at the end node (line element) connected to the springs in iteration $n+1$ form iteration n can be approxiamated as (Ran, 2000):

Equations for r_i:

$$\begin{aligned} N_i^{(n+1)} &= N_i^{(n)} + \frac{\partial N_i}{\partial r_j}\Delta r_j + \frac{\partial N_i}{\partial X_j}\Delta X_j + \frac{\partial N_i}{\partial \theta_j}\Delta\theta_j + \ldots \\ &= N_i^{(n)} - K_{ij}^{rr}\Delta r_j - K_{ij}^{rX}\Delta X_j - K_{ij}^{r\theta}\Delta\theta_j + \ldots \end{aligned} \tag{2.159}$$

Equations for r_i' :

$$L_i^{(n+1)} = L_i^{(n)} + \frac{\partial L_i}{\partial r_j'}\Delta r_j' + \frac{\partial L_i}{\partial \theta_j}\Delta\theta_j + \ldots$$
$$= L_i^{(n)} - K_{ij}^{r'r'}\Delta r_j' - K_{ij}^{r'\theta}\Delta\theta_j + \ldots \quad (2.160)$$

The equation of the line at the connected node (r and r') is coupled with the unknown motion of the platform by using symbol K_{ij}^{AB} to indicate the tangential stiffness coefficient for degree of freedom B_j in equation A_i (Ran, 2000):

$$K_{ij}^{rr} = -\frac{\partial N_i}{\partial r_j} = -\frac{\partial}{\partial r_j}\left[K_i^L\left(X_i + p_i + \theta_j C_{ji} - r_i\right)\right] = K_i^L\delta_{ij} \quad (2.161)$$

$$K_{ij}^{rX} = -\frac{\partial N_i}{\partial X_j} = -\frac{\partial}{\partial X_j}\left[K_i^L\left(X_i + p_i + \theta_j C_{ji} - r_i\right)\right] = -K_i^L\delta_{ij} \quad (2.162)$$

$$K_{ij}^{r\theta} = -\frac{\partial N_i}{\partial \theta_j} = -\frac{\partial}{\partial \theta_j}\left[K_i^L\left(X_i + p_i + \theta_j C_{ji} - r_i\right)\right] = -K_i^L C_{ij} \quad (2.163)$$

$$K_{ij}^{r'r'} = -\frac{\partial L_i}{\partial r_j'} = -\frac{\partial}{\partial r_j'}\left[K^\theta\left(e_i + \theta_j D_{ji} - \frac{r_i'}{\left(r_k' r_k'\right)^{1/2}}\right)\right] = K^\theta\left[\frac{\delta_{ij}}{\left(r_m' r_m'\right)^{1/2}} - \frac{r_i' r_j'}{\left(r_n' r_n'\right)^{3/2}}\right] \quad (2.164)$$

$$K_{ij}^{r'\theta} = -\frac{\partial L_i}{\partial \theta_j} = -\frac{\partial}{\partial \theta_j}\left[K^\theta\left(e_i + \theta_j D_{ji} - \frac{r_i'}{\left(r_k' r_k'\right)^{1/2}}\right)\right] = -K^\theta D_{ij} \quad (2.165)$$

The Newton's method is also applied to solve the equations of the platform (*rigid* body), which is coupled with the lines. The connector force exerted on the *rigid* body at iteration $n+1$ can be approximated by (Ran, 2000):

Equations for X_i:

$$F_i^{(n+1)} = F_i^{(n)} + \frac{\partial F_i}{\partial r_j}\Delta r_j + \frac{\partial F_i}{\partial X_j}\Delta X_j + \frac{\partial F_i}{\partial \theta_j}\Delta \theta_j + \ldots$$
$$= F_i^{(n)} - K_{ij}^{Xr}\Delta r_j - K_{ij}^{XX}\Delta X_j - K_{ij}^{X\theta}\Delta \theta_j + \ldots \tag{2.166}$$

Equations for θ_i :

$$M_i^{(n+1)} = M_i^{(n)} + \frac{\partial M_i}{\partial r_j}\Delta r_j + \frac{\partial M_i}{\partial r_j'}\Delta r_j' + \frac{\partial M_i}{\partial \theta_j}\Delta \theta_j + \frac{\partial M_i}{\partial X_j}\Delta X_j + \ldots$$
$$= M_i^{(n)} - K_{ij}^{\theta r}\Delta r_j - K_{ij}^{\theta r'}\Delta r_j' - K_{ij}^{\theta\theta}\Delta \theta_j - K_{ij}^{\theta X}\Delta X_j + \ldots \tag{2.167}$$

where the coefficients are:

$$K_{ij}^{Xr} = -\frac{\partial F_i}{\partial r_j} = -\frac{\partial}{\partial r_j}\left[-K_i^L\left(X_i + p_i + \theta_j C_{ji} - r_i\right)\right] = -K_i^L\delta_{ij} \tag{2.168}$$

$$K_{ij}^{XX} = -\frac{\partial F_i}{\partial X_j} = -\frac{\partial}{\partial X_j}\left[-K_i^L\left(X_i + p_i + \theta_j C_{ji} - r_i\right)\right] = K_i^L\delta_{ij} \tag{2.169}$$

$$K_{ij}^{X\theta} = -\frac{\partial F_i}{\partial \theta_j} = -\frac{\partial}{\partial \theta_j}\left[-K_i^L\left(X_i + p_i + \theta_j C_{ji} - r_i\right)\right] = K_i^L C_{ij} \tag{2.170}$$

$$K_{ij}^{\theta r} = -\frac{\partial M_i}{\partial r_j} = -\frac{\partial}{\partial r_j}\left[N_k C_{ki} + L_k D_{ki}\right]$$
$$= -\frac{\partial}{\partial r_j}\left[\left(K_i^L\left(X_i + p_i + \theta_j C_{ji} - r_i\right)\right)C_{ki} + \left(K^\theta\left(e_i + \theta_j D_{ji} - \frac{r_i'}{\left(r_k' r_k'\right)^{1/2}}\right)\right)D_{ki}\right]$$
$$= K_i^L C_{ij} \tag{2.171}$$

$$K_{ij}^{\theta r'} = -\frac{\partial M_i}{\partial r_j'} = -\frac{\partial}{\partial r_j'}\left[N_k C_{ki} + L_k D_{ki}\right]$$
$$= -\frac{\partial}{\partial r_j'}\left[\left(K_i^L\left(X_i + p_i + \theta_j C_{ji} - r_i\right)\right)C_{ki} + \left(K^\theta\left(e_i + \theta_j D_{ji} - \frac{r_i'}{\left(r_k' r_k'\right)^{1/2}}\right)\right)D_{ki}\right]$$
$$= K_i^\theta D_{ij} \tag{2.172}$$

$$
\begin{aligned}
K_{ij}^{\theta\theta} &= -\frac{\partial M_i}{\partial \theta_j} = -\frac{\partial}{\partial \theta_j}\left[N_k C_{ki} + L_k D_{ki}\right] \\
&= -\frac{\partial}{\partial \theta_j}\left[\left(K_i^L\left(X_i + p_i + \theta_j C_{ji} - r_i\right)\right)C_{ki} + \left(K^\theta\left(e_i + \theta_j D_{ji} - \frac{r_i^{'}}{\left(r_k^{'} r_k^{'}\right)^{1/2}}\right)\right)D_{ki}\right] \\
&= K_i^L C_{ij} C_{ki} + K_i^\theta D_{ij} D_{ki}
\end{aligned} \tag{2.173}
$$

In the iterative process, the line (rod) stiffness coefficients: K_{ij}^{rr} and $K_{ij}^{r'r'}$ will be included in the *elemental* equation (Eqn. (2.112)), the rigid body stiffness coefficients K_{ij}^{XX}, $K_{ij}^{X\theta}$, $K_{ij}^{\theta\theta}$ will be included in the motion equation of the *platform*, and the K_{ij}^{rX}, K_{ij}^{Xr}, $K_{ij}^{r\theta}$, $K_{ij}^{r'\theta}$, $K_{ij}^{\theta r}$, $K_{ij}^{\theta r'}$ are the *coupling* stiffness coefficients that will be included to a coupling matrix. In addition, the force vectors $N_i^{(n)}$, $L_i^{(n)}$, $F_i^{(n)}$, and $M_i^{(n)}$ are added to the force vector at the RHS of the equations of the *line* element and the *platform* (Ran, 2000).

In the time-domain integration, the connector force on the end node of the *line* is added to motion equation Eqn. (2.129) and is integrated from time $t^{(n)}$ to $t^{(n+1)}$ (Ran, 2000):

$$
\int_{t^{(n)}}^{t^{(n+1)}} \hat{F}_{il} dt = \int_{t^{(n)}}^{t^{(n+1)}} \left(-F_{il}^1 - F_{il}^2 + F_{il}\right) dt = -\int_{t^{(n)}}^{t^{(n+1)}} F_{il}^1 dt - \int_{t^{(n)}}^{t^{(n+1)}} F_{il}^2 dt + \int_{t^{(n)}}^{t^{(n+1)}} F_{il} dt \tag{2.129}
$$

Equations for r_i:

$$\int_{t^{(n)}}^{t^{(n+1)}} N_i dt = \frac{\Delta t}{2}\left(N_i^{(n+1)} + N_i^{(n)}\right) \approx \frac{\Delta t}{2}\left(\frac{\partial N_i}{\partial r_j}\Delta r_j + \frac{\partial N_i}{\partial X_j}\Delta X_j + \frac{\partial N_i}{\partial \theta_j}\Delta\theta_j + 2N_i^{(n)}\right)$$
$$= \frac{\Delta t}{2}\left(-K_{ij}^{rr}\Delta r_j - K_{ij}^{rX}\Delta X_j - K_{ij}^{r\theta}\Delta\theta_j + 2N_i^{(n)}\right) \tag{2.174}$$

Equations for r_i' :

$$\int_{t^{(n)}}^{t^{(n+1)}} L_i dt = \frac{\Delta t}{2}\left(L_i^{(n+1)} + L_i^{(n)}\right) \approx \frac{\Delta t}{2}\left(\frac{\partial L_i}{\partial r_j'}\Delta r_j' + \frac{\partial L_i}{\partial \theta_j}\Delta\theta_j + 2L_i^{(n)}\right)$$
$$= \frac{\Delta t}{2}\left(-K_{ij}^{r'r'}\Delta r_j' - K_{ij}^{r'\theta}\Delta\theta_j + 2L_i^{(n)}\right) \tag{2.175}$$

and for the connector force on the rigid *body*,

Equations for X_i :

$$\int_{t^{(n)}}^{t^{(n+1)}} F_i dt = \frac{\Delta t}{2}\left(F_i^{(n+1)} + F_i^{(n)}\right) \approx \frac{\Delta t}{2}\left(\frac{\partial F_i}{\partial r_j}\Delta r_j + \frac{\partial F_i}{\partial X_j}\Delta X_j + \frac{\partial F_i}{\partial \theta_j}\Delta\theta_j + 2F_i^{(n)}\right)$$
$$= \frac{\Delta t}{2}\left(-K_{ij}^{Xr}\Delta r_j - K_{ij}^{XX}\Delta X_j - K_{ij}^{X\theta}\Delta\theta_j + 2F_i^{(n)}\right) \tag{2.176}$$

Equations for θ_i :

$$\int_{t^{(n)}}^{t^{(n+1)}} M_i dt = \frac{\Delta t}{2}\left(M_i^{(n+1)} + M_i^{(n)}\right) \approx \frac{\Delta t}{2}\left(\frac{\partial M_i}{\partial r_j}\Delta r_j + \frac{\partial M_i}{\partial r_j'}\Delta r_j' + \frac{\partial M_i}{\partial \theta_j}\Delta\theta_j + 2M_i^{(n)}\right)$$
$$= \frac{\Delta t}{2}\left(-K_{ij}^{\theta r}\Delta r_j - K_{ij}^{\theta r'}\Delta r_j' - K_{ij}^{\theta\theta}\Delta\theta_j + 2M_i^{(n)}\right) \tag{2.177}$$

2.4.6 Modeling of the Damper Connection

In the original version of CHARM3D, a linear damper is modeled as a damping force linearly related to the relative translational velocity between the platform's

connecting point and the top node of the line. The damping force (N^D) on the connected node of the line element is defined as:

$$N_i^D = D\left(\dot{X}_i + \dot{\theta}_j C_{ji} - \dot{r}_i\right) \tag{2.178}$$

where D is linear damping coefficient, $\dot{X}$ and $\dot{\theta}$ are translational and rotational velocities of the rigid body, respectively, $\dot{r}$ is velocity of the attached node, and

$$C_{ij} \rightarrow [C] = \begin{bmatrix} 0 & -p_3 & p_2 \\ p_3 & 0 & -p_1 \\ -p_2 & p_1 & 0 \end{bmatrix} \tag{2.179}$$

On the other hand, the damping force exerted on the rigid *body* is $F_i^D = -N_i^D$. In the time-domain simulation, the integration of the connector force yields (Ran, 2000):

Equations for r_i:

$$\begin{aligned} \int_{t^{(n)}}^{t^{(n+1)}} N_i^D dt &= \int_{t^{(n)}}^{t^{(n+1)}} D\left(\dot{X}_i + \dot{\theta}_j C_{ji} - \dot{r}_i\right) dt = \int_{t^{(n)}}^{t^{(n+1)}} D\dot{X}_i dt + \int_{t^{(n)}}^{t^{(n+1)}} D\dot{\theta}_j C_{ji} dt - \int_{t^{(n)}}^{t^{(n+1)}} D\dot{r}_i dt \\ &= \int_{t^{(n)}}^{t^{(n+1)}} D dX_i + \int_{t^{(n)}}^{t^{(n+1)}} DC_{ji} d\theta_j - \int_{t^{(n)}}^{t^{(n+1)}} D dr_i \\ &= \left(D\right)\Delta X_i + \left(DC_{ji}\right)\Delta\theta_j - \left(D\right)\Delta r_i \end{aligned} \tag{2.180}$$

Equations for X_i:

$$\int_{t^{(n)}}^{t^{(n+1)}} F_i^D dt = -\int_{t^{(n)}}^{t^{(n+1)}} N_i^D dt = \left(-D\right)\Delta X_i + \left(DC_{ji}\right)\Delta\theta_j + \left(D\right)\Delta r_i \tag{2.181}$$

The damping coefficients are added to the equations of the *line* and the *platform* in the same way as the stiffness coefficients. There is noteworthy that there is no forcing term from the linear damping to be added to the RHS of the equation (Ran, 2000). The

finite element modeling of the linear damper connection by using another method which provides the same results can be found in the Appendix A.

2.4.7 Coefficient Matrix of Hull, Riser and Mooring Line Coupled Dynamics

For a 3-dimensions simulation, the assembled matrix has 8×(*N*+1)-1 rows (where *N* is the total number of element in a single *line*). In the CHARM3D, a *line* (mooring line or riser) is divided into *N* elements and *n* nodes (where *n*=*N*+1). In each step, the six degree-of-freedom motions of both end-nodes ($S = 0, L$) in an element are represented by ΔU_{jk}, and the tensions at ($S = 0, L/2, L$) are represented by $\Delta\lambda_n$, as stated in Eqn. (2.137).

$$\begin{bmatrix} \hat{K}_{ijlk}^{t0(n)} & \hat{K}_{iln}^{t1(n)} \\ \hat{D}_{mjk}^{t0(n)} & \hat{D}_{mn}^{t1(n)} \end{bmatrix} \begin{Bmatrix} \Delta U_{jk} \\ \Delta\lambda_n \end{Bmatrix} = \begin{Bmatrix} \hat{R}_{il}^{(n)} \\ -\hat{G}_m^{(n)} \end{Bmatrix} \tag{2.137}$$

where $\{\Delta U_{jk}, \quad \Delta\lambda_n\}^T$ is defined in Eqn. (2.113). The nodes in a *line* are labeled in sequence from *1st* for the first node which is connected to the seabed anchoring point, to *n-th* for the last node that attached to the platform, as illustrated in Fig. 2.2.

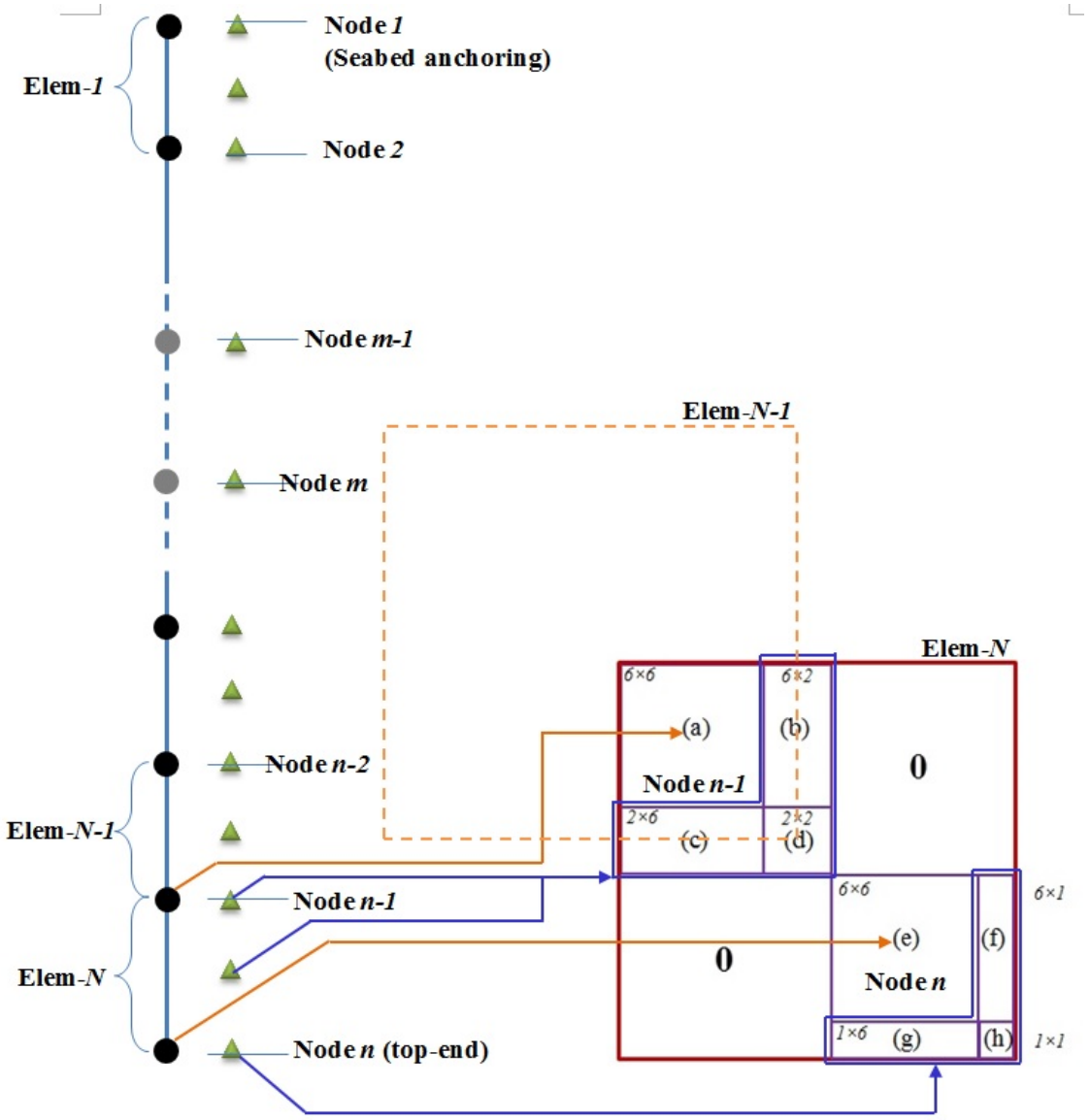

Figure 2.2 Arrangement of 15×15 stiffness matrix $\hat{\mathbf{K}}^{(n)}$ in the Eqn. (2.144) of *N*th-elements.

The stiffness matrix for each *element* is arranged into a 15×15 matrix according to the Eqn. (2.144) and Eqn. (2.137). For example, the stiffness matrix for *N*th element is shown in Fig. 2.2 and the parts from (a) to (h) are represented by the following coefficients in Eqn. (2.137), as

$$\begin{aligned}
&(a) = \hat{K}_{ijlk}^{t0(n)}\Big|_{n-1}^{6\times6}; \quad (b) = \hat{K}_{iln}^{t1(n)}\Big|_{n-1}^{6\times2}; \quad (c) = \hat{D}_{mjk}^{t0(n)}\Big|_{n-1}^{2\times6}; \quad (d) = \hat{D}_{mn}^{t1(n)}\Big|_{n-1}^{2\times2}; \\
&(e) = \hat{K}_{ijlk}^{t0(n)}\Big|_{n}^{6\times6}; \quad (f) = \hat{K}_{iln}^{t1(n)}\Big|_{n}^{6\times1}; \quad (g) = \hat{D}_{mjk}^{t0(n)}\Big|_{n}^{1\times6}; \quad (h) = \hat{D}_{mn}^{t1(n)}\Big|_{n}^{1\times1}
\end{aligned} \tag{2.182}$$

where the values of these coefficients can be calculated from Eqns. (2.138) to (2.141).

In a single *line*, the 15×15 stiffness matrix for each elements are assembled into a 8×(*N*+1)-1 square matrix as shown in Fig. 2.3.

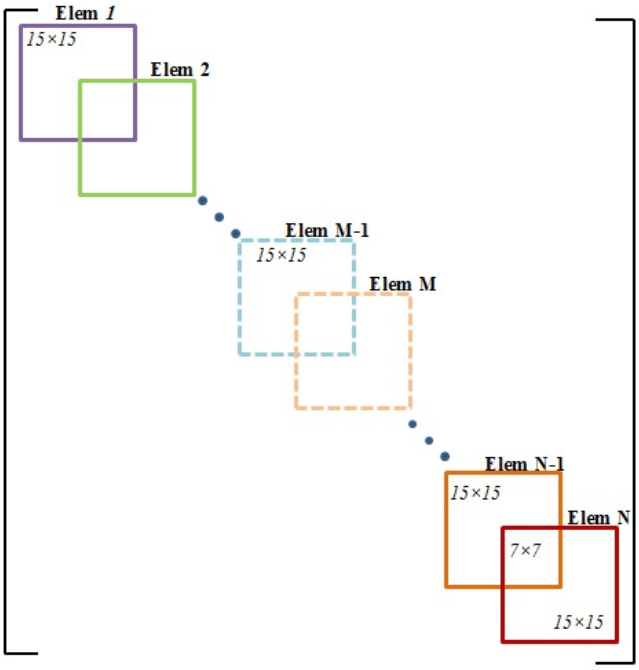

Figure 2.3 Stiffness matrix of single leg with assembly of Nth-elements, where each 15×15 stiffness matrix is based on $\hat{\mathbf{K}}^{(n)}$ in the Eqn. (2.144).

From the Eqns. (2.159) and (2.160), the element tangential stiffness matrix that needs to be added into the end node of the *line* is:

$$\begin{bmatrix} K_{ij}^{rr} & 0 \\ 0 & K_{ij}^{r'r'} \end{bmatrix}_{LS} \begin{Bmatrix} \Delta r_j \\ \Delta r_j' \end{Bmatrix} = \begin{Bmatrix} N_i \\ L_i \end{Bmatrix} \tag{2.183}$$

where the subscript *LS* is referred to 'Linear Spring' connection. Similarly, from the Eqns. (2.166) and (2.167), the element tangential stiffness matrix that needs to be added into the *rigid body* equation is:

$$\begin{bmatrix} K_{ij}^{XX} & K_{ij}^{X\theta} \\ K_{ij}^{\theta X} & K_{ij}^{\theta\theta} \end{bmatrix}_{LS} \begin{Bmatrix} \Delta X_j \\ \Delta \theta_j \end{Bmatrix} = \begin{Bmatrix} F_i \\ M_i \end{Bmatrix} \tag{2.184}$$

Finally, from Eqns. (2.159), (2.160), (2.166) and (2.167), the *coupling* terms of element tangential stiffness matrix that to be added into the global stiffness matrix is:

$$\begin{bmatrix} 0 & 0 & K_{ij}^{rX} & K_{ij}^{r\theta} \\ 0 & 0 & 0 & K_{ij}^{r'\theta} \\ K_{ij}^{Xr} & 0 & 0 & 0 \\ K_{ij}^{\theta r} & K_{ij}^{\theta r'} & 0 & 0 \end{bmatrix}_{LS} \begin{Bmatrix} \Delta r_j \\ \Delta r_j' \\ \Delta X_j \\ \Delta \theta_j \end{Bmatrix} = \begin{Bmatrix} N_i \\ L_i \\ F_i \\ M_i \end{Bmatrix} \tag{2.185}$$

The global stiffness after coupled the single line with the platform is illustrated in Fig. 2.4.

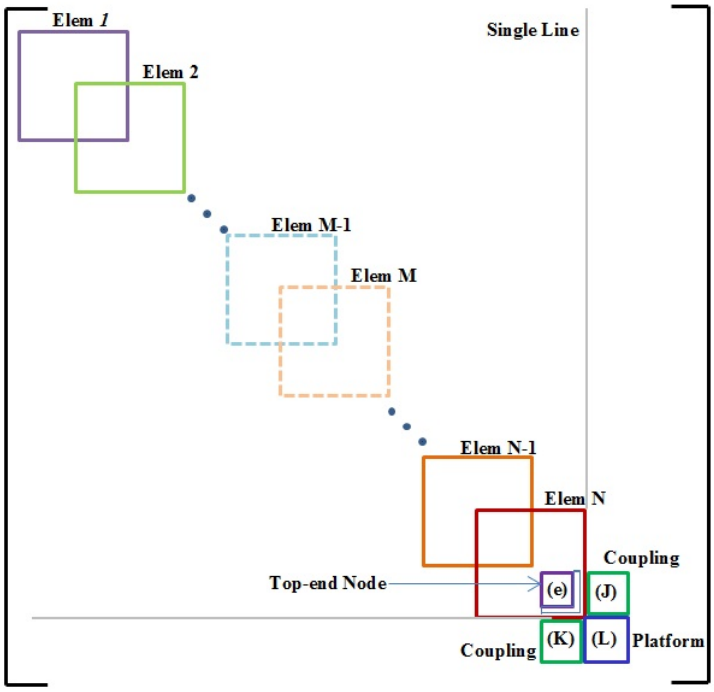

Figure 2.4 Global stiffness matrix of single leg with assembly of Nth-elements after coupled with host platform.

The matrix (e) is the 6×6 rod stiffness of the node which is attached to the platform and can be obtained by using Eqns. (2.161) and (2.164).

$$(\mathrm{e}) = \begin{bmatrix} K_{11}^{rr} & & & & & \\ & K_{11}^{r'r'} & & \mathbf{0} & & \\ & & K_{22}^{rr} & & & \\ & & & K_{22}^{r'r'} & & \\ & \mathbf{0} & & & K_{33}^{rr} & \\ & & & & & K_{33}^{r'r'} \end{bmatrix}_{6\times 6} \tag{2.186}$$

The matrix (L) is the 6×6 platform body stiffness which is a combination of the stiffness terms on the LHS of Eqn. (2.61) and from the connector forces acting on the body in Eqns. (2.169), (2.170), and (2.173);

$$(\mathrm{L}) = \begin{bmatrix} K_{11}^{XX} & & & & K_{15}^{X\theta} & K_{16}^{X\theta} \\ & K_{22}^{XX} & & K_{24}^{X\theta} & & K_{26}^{X\theta} \\ & & K_{33}^{XX} & K_{34}^{X\theta} & K_{35}^{X\theta} & \\ & K_{42}^{\theta X} & K_{43}^{\theta X} & K_{44}^{\theta\theta} & K_{45}^{\theta\theta} & K_{46}^{\theta\theta} \\ K_{51}^{\theta X} & & K_{53}^{\theta X} & K_{54}^{\theta\theta} & K_{55}^{\theta\theta} & K_{56}^{\theta\theta} \\ K_{61}^{\theta X} & K_{62}^{\theta X} & & K_{64}^{\theta\theta} & K_{65}^{\theta\theta} & K_{66}^{\theta\theta} \end{bmatrix}_{6\times 6} \tag{2.187}$$

The matrix (J) is the 7×6 coupling stiffness in between the platform and lines (mooring lines / risers) that can be obtained from Eqns. (2.162), (2.163), and (2.165). On the other hand, the 6×7 matrix (K) is the inverse matrix of (J).

$$(\mathrm{J}) = \begin{bmatrix} K_{11}^{rX} & & & & K_{12}^{r\theta} & K_{13}^{r\theta} \\ & & & & K_{12}^{r'\theta} & K_{13}^{r'\theta} \\ & K_{22}^{rX} & & K_{21}^{r\theta} & & K_{23}^{r\theta} \\ & & & K_{21}^{r'\theta} & & K_{23}^{r'\theta} \\ & & K_{33}^{rX} & K_{31}^{r\theta} & K_{32}^{r\theta} & \\ & & & K_{31}^{r'\theta} & K_{32}^{r'\theta} & \\ & & & & & \\ & & & & & \end{bmatrix}_{7\times 6} \tag{2.188}$$

2.4.8 Force Vector of Hull, Riser and Mooring Line Coupled Dynamics

For a 3-dimensions simulation, the RHS of Eqn. (2.137) is the forcing vector of single *line*-element.

$$\begin{bmatrix} \hat{K}_{ijlk}^{t0(n)} & \hat{K}_{iln}^{t1(n)} \\ \hat{D}_{mjk}^{t0(n)} & \hat{D}_{mn}^{t1(n)} \end{bmatrix} \begin{Bmatrix} \Delta U_{jk} \\ \Delta\lambda_n \end{Bmatrix} = \begin{Bmatrix} \hat{R}_{il}^{(n)} \\ -\hat{G}_m^{(n)} \end{Bmatrix} \tag{2.137}$$

where the $\left\{ \hat{R}_{il}^{(n)}, \quad -\hat{G}_m^{(n)} \right\}^T$ can be obtained from Eqns. (2.115) and (2.145).

After coupled with the platform, the force vector on the RHS for the *n*th node must be modified with the forces/moments *residue* terms on the RHS of the Eqns. (2.174), (2.175), (2.176), and (2.177).

The global stiffness matrix and forcing vector after coupled the lines with platform is shown in Fig. 2.5.

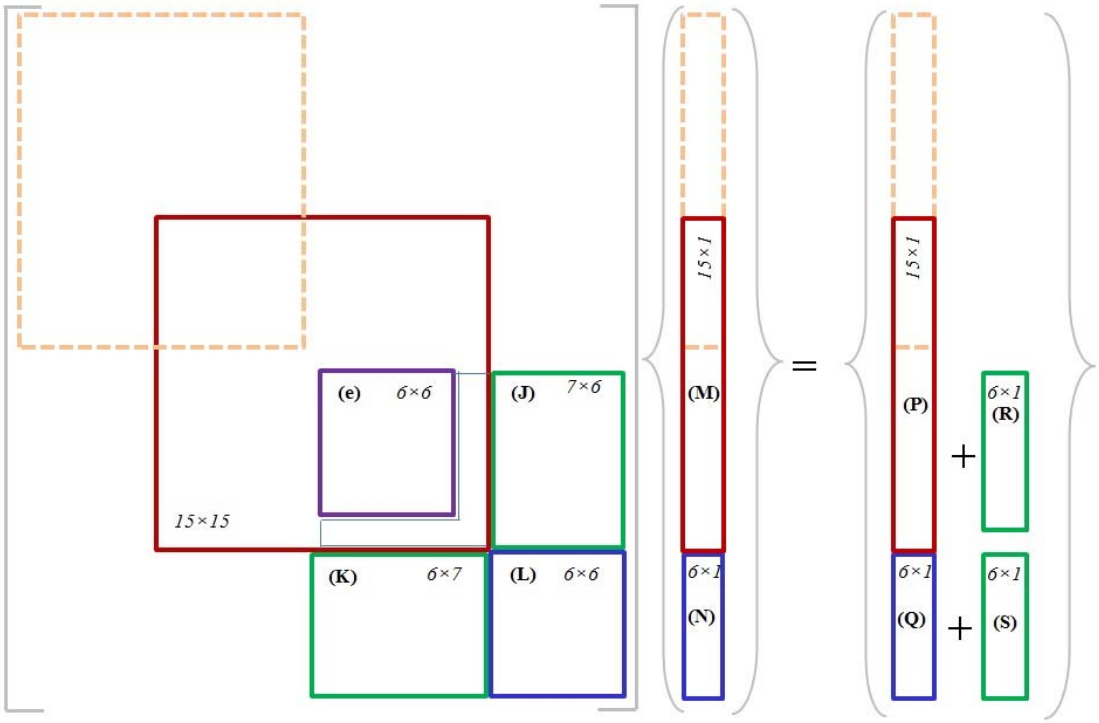

Figure 2.5 Global stiffness matrix and forcing vector.

The sub-matrices (e), (J), (K), and (L) are same as the descriptions in Subsection 2.4.7. The other matrices are:

(M) = 15×1 matrix that represents the $\left\{\Delta U_{jk},\ \ \Delta\lambda_n\right\}^T$ of the last *line* element as defined in Eqn. (2.113);

(N) = 6×1 matrix that represents the displacement of platform body $\Delta\zeta$ of the Eqn. (2.61);

(P) = 15×1 force vector of line that represents the $\left\{\hat{R}_{il}^{(n)},\ \ -\hat{G}_m^{(n)}\right\}^T$ as per derived from Eqn. (2.115);

(Q) = 6×1 force vector that represents the total RHS forces in the Eqn. (2.61);

(R) = 6×1 force vector that represents the connector forces on the end node of the line to be added to motion equation of *line* element, $\left\{N_i,\ \ L_i\right\}^T$ as per stated in the RHS of Eqn. (2.183);

(S) = 6×1 force vector that represents the connector forces on the end node of the line to be added to motion equation of *line* element, $\left\{F_i,\ \ M_i\right\}$ as per stated in the RHS of Eqn. (2.184).

3. MODELING OF MAGNETO-RHEOLOGICAL DAMPER

3.1 Introduction and Literature Reviews

In this Section, the structural integration of magneto-rheological (MR) damper with a top-tension riser was modeled in a coupled hull/risers/mooring lines analysis tool, CHARM3D. The behaviors of a MR damper were studied and to be represented into a mathematical formulation. Parameter identification of a MR damper was conducted in order to identify the process for obtaining the mathematical variables in the numerical model. The mathematical model of MR damper was integrated with the top tension riser, by deriving it into a finite element coupling model.

The advanced new materials have been applied to improve the performance of structures. Dominguez *et al*. (2008) reported that magneto-rheological (MR) dampers are devices that employ rheological fluids to modify their mechanical properties by changing the stiffness and damping coefficients when the rheological fluid is exposed to a magnetic field. The schematic and configuration of a MR damper is illustrated in Fig. 3.1. One special advantage of the MR damper is that its damping characteristics can be adaptively and quickly altered by a varying magnetic field (Tse and Chang, 2002). The rheological fluid is in a fluid state, and acting as a normal damper, when it is under the un-magnetized condition. On the other hand, if the rheological fluid is magnetized by a magnetic field induced by the electromagnetic coils built in the piston, the fluid particles across the piston passage surrounded by the electromagnetic coils will be rearranged into formation and temporary transformed into semi-solid state, which has higher resistance

force. Their mechanical simplicity, high dynamic range, lower power requirements, large force capacity, robustness and safe manner operation in case of fail have made them attractive devices to semi-active control in civil, aerospace and automotive applications (Dominguez et al., 2008).

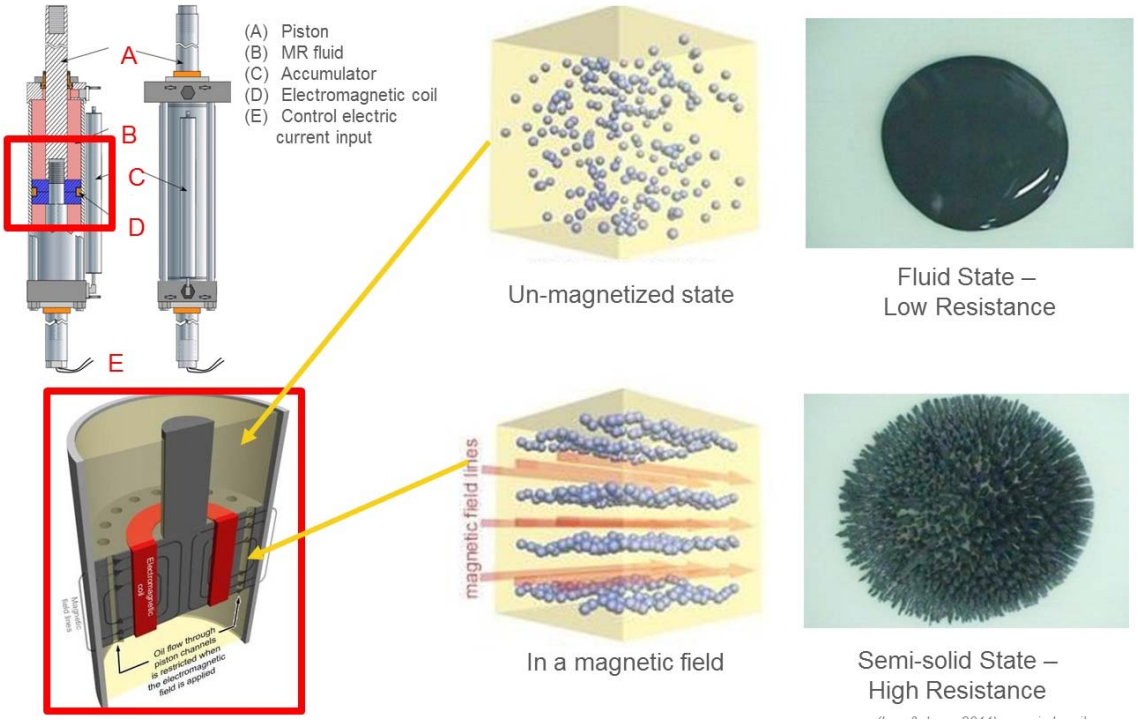

Figure 3.1 Schematic and configuration of a MR damper (Jiang et al., 2010; Lee and Jang, 2011)(Courtesy of Audi AG).

The technology of installing MR dampers in land-based building to minimize the structural vibration, especially during the earthquake (Hurlebaus and Gaul, 2006; Kim, 2007; Osman et. al, 2011), and the response reduction on the bridges (Duan et al., 2002; Yang et al., 2011) have gained successful results. The force response analysis is

performed and a phenomenological model based on the *Bouc–Wen* model was employed to estimate the MR damper behavior under dynamic loading (Spencer Jr et al., 1997; Yang *et al*., 2004). This model accommodates the MR fluid stiction phenomenon, as well as fluid inertial and shear thinning effects. Jansen and Dyke (2000) presented the results of various control algorithms used in semi-active control studies including the *Lyapunov* controller, decentralized *bang-bang* controller, modulated homogeneous friction algorithm, and a clipped optimal controller. Bahar *et al.* (2010) investigated a new inverse model, which considered a hybrid seismic control system, of semi-active devices for mitigation of structural vibrations by using magneto-rheological (MR) dampers. Bitaraf *et al.* (2010) developed a control strategy that combined Simple Adaptive Control (SAC) method and a genetic-based fuzzy control method to effectively control both displacement and acceleration response of a structure.

3.2 Model of Magneto-Rheological Damper

In this research, the *Nonlinear Hysteretic Arctangent Function* (NHAF) Model (Yang et al., 2011) is employed to model the nonlinear hysteretic model of MR damper. The schematic diagram of this model is shown in Fig. 3.2. The MR damper is represented by the combination of *stiffness* and *damping* components along with the *hysteresis* loop effects. The MR damper is arranged with the riser tensioner to form a *Kelvin-Voigt* element. This hysteresis model possesses an appealing mathematical simplicity and is able to represent a large class of hysteretic behavior, inelastic stress-

strain relationships of MR behavior. The force exerted by the MR damper f_{MR} can be represented by the following equation:

$$f_{MR} = c\dot{x}_{MR} + kx_{MR} + \alpha z_{MR} \tag{3.1}$$

$$z_{MR} = \tan^{-1}\left(\beta \dot{x}_{MR} + \delta \mathrm{sgn}\left(x_{MR}\right)\right) \tag{3.2}$$

where c is the viscous damping coefficient of the MR damper, k is the stiffness coefficient of the MR damper, x_{MR} and $\dot{x}_{MR}$ are the displacement and velocity of the piston of the MR damper, respectively.

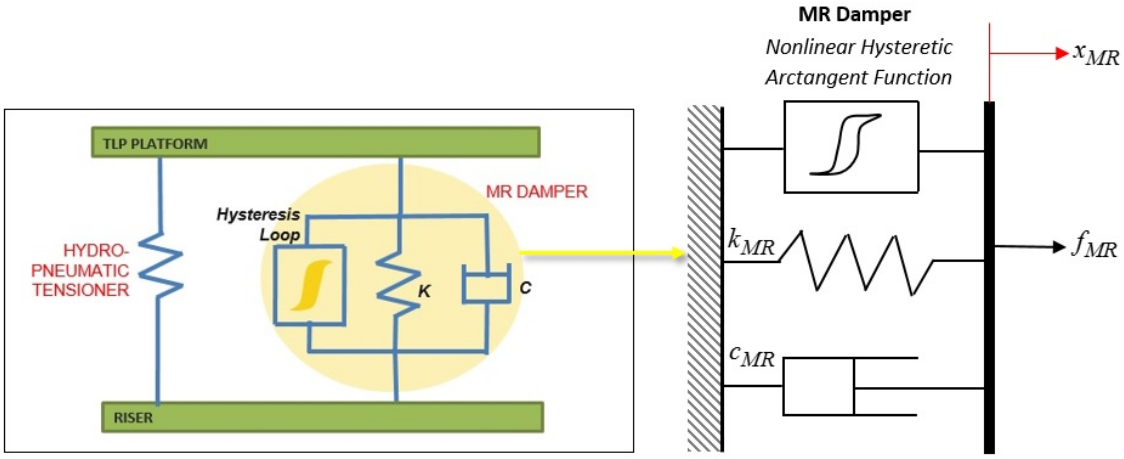

Figure 3.2 Schematic diagram of the incorporation of MR damper (NHAF model) into the conventional hydro-pneumatic tensioner system (HP+MR).

The hysteretic behavior of MR damper is expressed by the adjustable shape parameters of the hysteresis loops for the yielding element in the MR damper: α, β, and δ. The coulomb force describing the hysteretic behavior is represented by z_{MR}. The

α is the scale factor, β is the slope factor, and δ is the width factor (Kwok et al., 2006) of the hysteresis respectively, as illustrated in the Fig. 3.3 where increment of these parameters will cause increment of force-velocity *hysteresis* in the direction as indicated by the arrowhead. These parameters can control the linearity in the unloading and the smoothness of the transition from the pre-yield to the post-yield region.

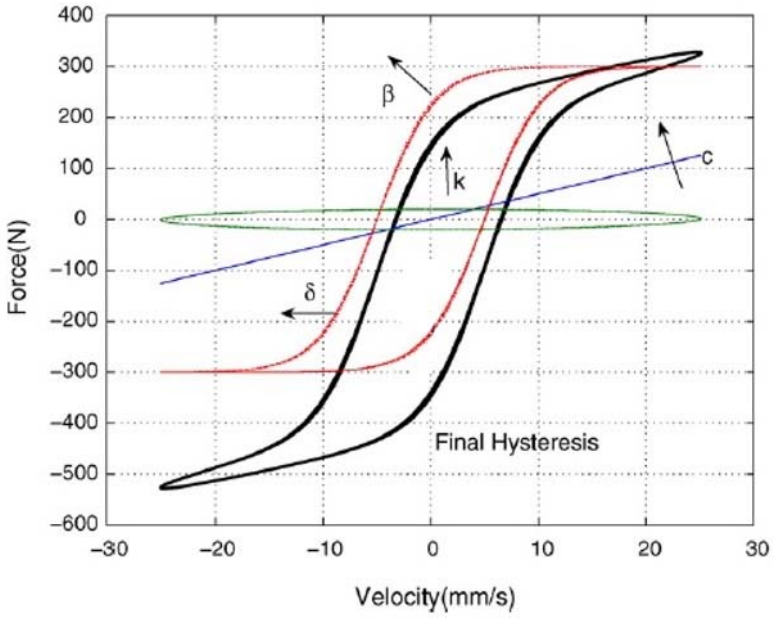

Figure 3.3 Hyteresis variables (Kwok et al., 2006).

The model parameters of the MR damper governing equation c, k, α, β, and δ are functions of the applied electric current i (Wang and Liao, 2011), and the parameter identification can be conducted by the post-processing of the experimental data of MR damper. The *nonlinear least square method* in MATLAB is utilized to determine the corresponding parametric coefficients as proposed by Yang *et al.* (2013b).

In this study, the proposed output force of MR damper is augmented in the following coefficients:

$$c = 8.5\times10^{5} i^{2} + 14.4\times10^{7} i + 6.0\times10^{6} \tag{3.3}$$

$$k = 1.2\times10^{5} i + 9.8\times10^{3} \tag{3.4}$$

$$\alpha = 2.571\times10^{6} i^{2} + 4.11\times10^{6} i + 8.0\times10^{4} \tag{3.5}$$

$$\beta = 2.205\times10^{1} i + 1.782\times10^{1} \tag{3.6}$$

$$\delta = 2.6i + 2.3 \tag{3.7}$$

There is noteworthy that these coefficients are proposed here to verify the effectiveness of the NHAF model in *large scale* force modeling. The idealistic capacity of this numerical MR damper based on the proposed coefficients from Eqns. (3.3) – (3.7) is up to ~4500 kN (*~1012 kips*) when sinusoidal excitation amplitude is 1.5 m (*4.92 ft*) and input current is 1.0 A. Nevertheless, the physically well-built large scale single unit MR damper is able to exert force up to 500 kN (*112 kips*) (Tu et al., 2011), while the very large output force requirement in the applications of offshore engineering can be achieved by multiplying the unit of MR damper in a group. Therefore, the exact output force scale and coefficients to be utilized in the later Sections (Section 5 and Section 7) will be further fine-tuned with respect to the required force sizing of the particular cases.

The force-displacements and force-velocities loops for different electric currents, frequencies, and amplitudes generated by the NHAF model with these coefficients from Eqns. (3.3) – (3.7) are depicted in Figs. 3.4 – 3.6. The characteristics of these figures are:

(i) the damping force increases with respect to the increasing electric current in the electromagnetic coils, and approaches a limiting value when the electric current reaches a certain value;

(ii) the ratio of the maximum damping force a 0.4 A to 0 A is about 2.5 times, which indicates that the adjustability of the damping force is preferable;

(iii) the force-displacement loops are close to an elliptical shape, and the force-velocity loops are nonlinear hysteretic, which demonstrate that the energy dissipation ability of the damper is adequate (Yang et al., 2013b);

(iv) the *frictional lagging effects* is not represented in these force-velocities plots based on the selection of fine-tuned coefficients employed in this NHAF model in order to simplify this model.

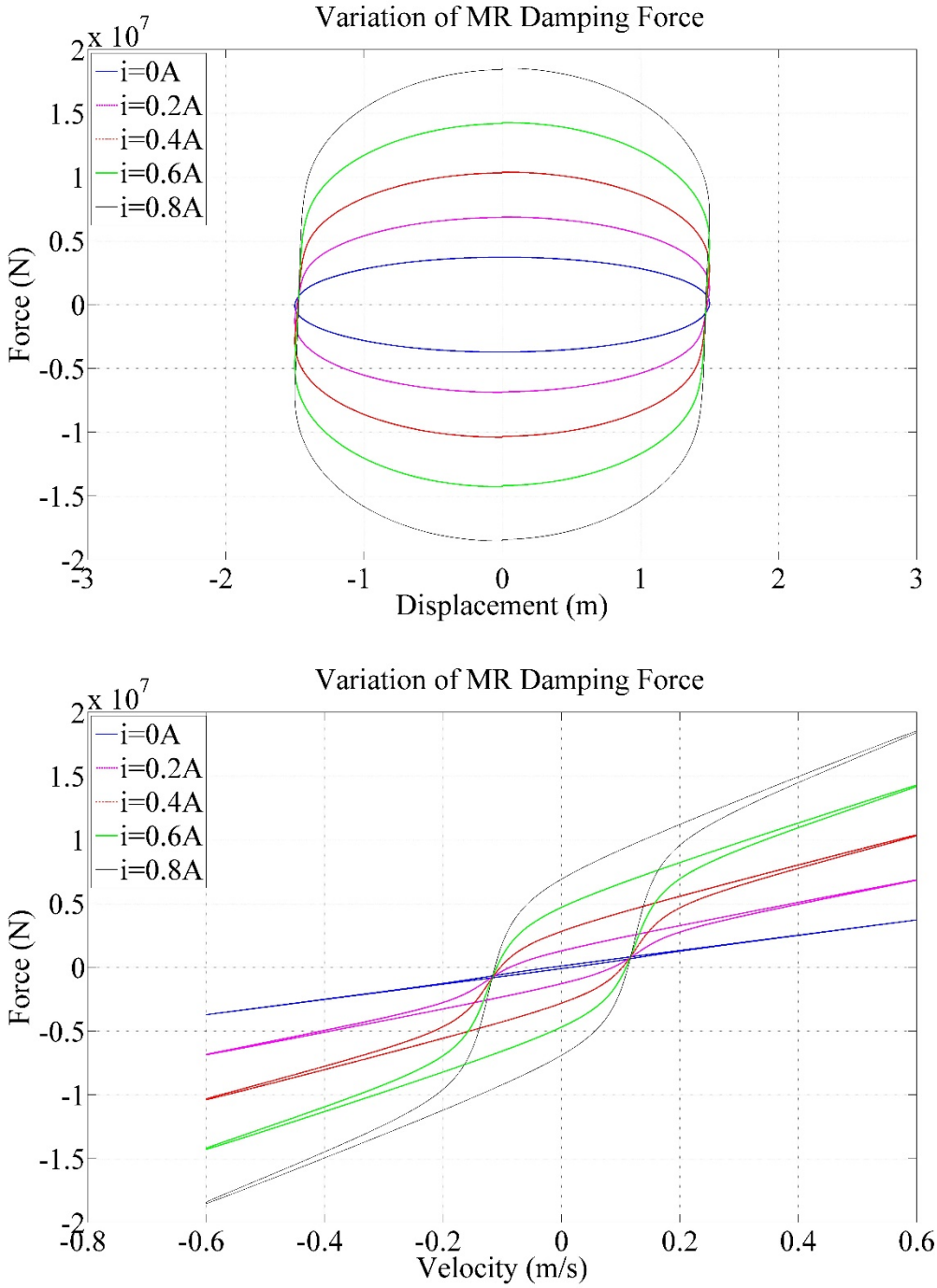

Figure 3.4 Variations of damping force with input currents, for (a) force vs. displacement, and (b) force vs. velocity; with sinusoidal excitation amplitude = 1.5 m (*4.92 ft*) and sinusoidal excitation frequency = 0.4 rad/s.

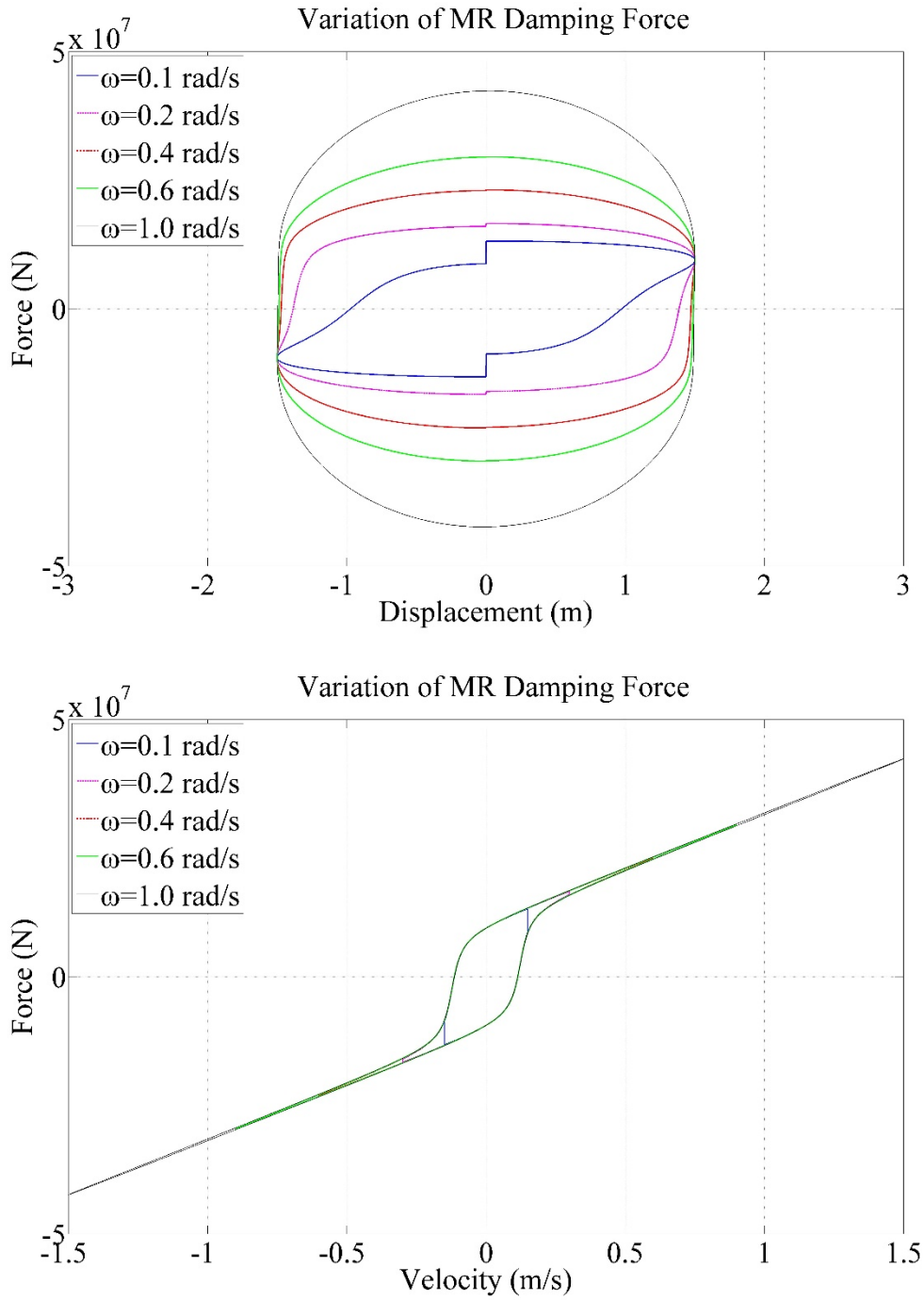

Figure 3.5 Variations of damping force with excitation frequencies, for (a) force vs. displacement, and (b) force vs. velocity; with sinusoidal excitation amplitude = 1.5 m (*4.92 ft*) and input current = 1.0 A.

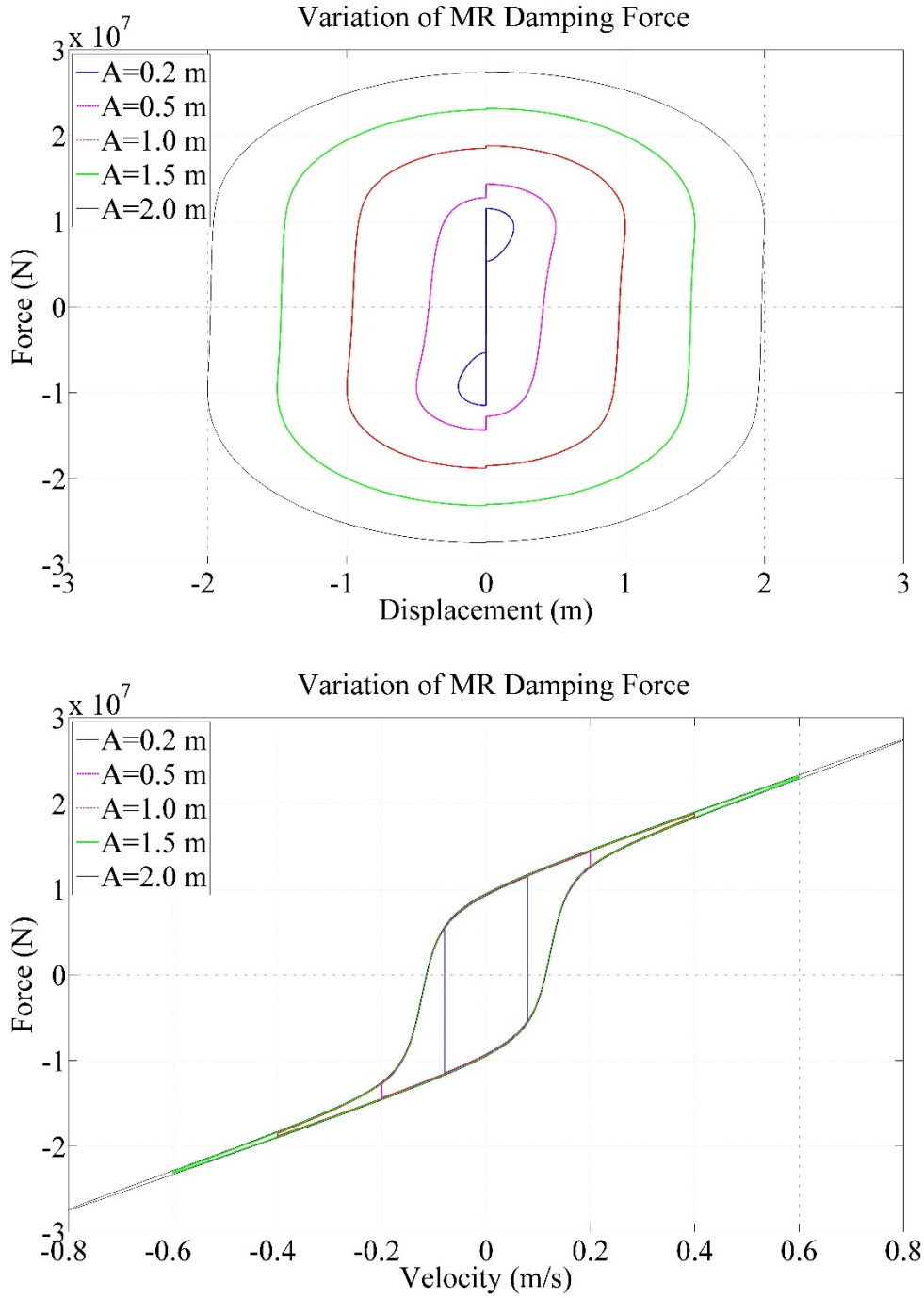

Figure 3.6 Variations of damping force with excitation amplitudes, for (a) force vs. displacement, and (b) force vs. velocity; with sinusoidal excitation frequency = 0.4 rad/s and input current = 1.0 A.

3.3 Parameter Identification of MR Damper

The dynamic responses of a physical MR damper must be modeled adequately in the numerical simulation in order to simulate the correct damping force to be exerted by the physical MR damper. In the general practice, the dynamic responses of a physical MR damper is collected by using data acquisition technique where the experimental data, including the damper displacement x_{MR}, velocity $\dot{x}_{MR}$ and the generated damping force f_{MR} are collected under a wide range of operating conditions. These experimental data are post-processed to construct a numerical MR damper model (Kwok et al., 2006).

In this study, an adequate *parameter identification* method was developed for constructing a numerical MR damper model based on the experimental data of the physical MR damper. The experimental data was *deliberately designed* for a large scale MR damper which has the capability of output damping force as shown in Figs. 3.4 – 3.6. There is noteworthy that the actual experimental data for such a large scale MR damper is not available and, therefore, a set of *pseudo*-experimental data was designed as the input of parameter identification based on the parameters as listed in Eqns. (3.3)-(3.7). The test conditions are listed in Table 3.1. There are six combinations of different frequency and displacement, and for each combination there are six current settings. These *pseudo*-experimental data sets were stored in corresponding data files and the damper model parameters were then numerically identified based on these data files by using the *Parameter Estimation method* in the *Design Optimization* toolbox in MATLAB/SIMULINK.

Table 3.1 Test conditions of parameter identification of MR damper.

Frequency (rad/s)	Displacement	Current (A)
0.4	0.2 m (*0.656 ft*)	[0.0, 0.2, 0.4, 0.6, 1.0, 1.2]
0.4	0.5 m (*1.640 ft*)	[0.0, 0.2, 0.4, 0.6, 1.0, 1.2]
0.4	0.8 m (*2.625 ft*)	[0.0, 0.2, 0.4, 0.6, 1.0, 1.2]
0.8	1.0 m (*3.281 ft*)	[0.0, 0.2, 0.4, 0.6, 1.0, 1.2]
0.8	1.5 m (*4.921 ft*)	[0.0, 0.2, 0.4, 0.6, 1.0, 1.2]
0.8	2.0 m (*6.562 ft*)	[0.0, 0.2, 0.4, 0.6, 1.0, 1.2]

The identified parameters (α , β , c, δ, and k) were grouped according to their *parameter estimation* results and were plotted against the electric command current i as shown in Fig. 3.7. These plots were identified by the *non-linear least square method* using the *Curve Fitting* toolbox in the MATLAB/SIMULINK (Yang et al., 2013b) to find a polynomial that represents the averaged values of each parameter under various tested conditions, as listed in the following equation:

$$
\begin{aligned}
c &= c_1 i^2 + c_2 i + c_3 \\
k &= k_1 i^2 + k_2 i + k_3 \\
\alpha &= \alpha_1 i^2 + \alpha_2 i + \alpha_3 \\
\beta &= \beta_1 i^2 + \beta_2 i + \beta_3 \\
\delta &= \delta_1 i^2 + \delta_2 i + \delta_3
\end{aligned}
\tag{3.8}
$$

The results of the parameter identification (the dotted lines in the Fig. 3.7) reproduce the following set of MR damper model parameters as tabulated in Table 3.2:

Table 3.2 Parameter identification of variables in MR damper model.

Variables	*Pseudo*-Experiment Data	Parameter Identification	Deviation (%)
c_1	8.5000×10^5	8.4456×10^5	-0.64
c_2	1.4400×10^7	1.4475×10^7	0.52
c_3	6.0000×10^6	6.0005×10^6	0.01
k_1	0	0	0
k_2	1.2000×10^5	1.4069×10^5	**17.24**
k_3	9.8000×10^3	1.4117×10^4	**44.05**
α_1	2.571×10^6	2.572×10^6	0.04
α_2	4.1100×10^6	4.0986×10^6	-0.28
α_3	8.0000×10^4	7.9691×10^4	-0.39
β_1	0	0	0
β_2	2.2050×10^1	2.2388×10^1	1.53
β_3	1.7820×10^1	1.8015×10^1	1.09
δ_1	0	0	0
δ_2	2.6000	2.6307	1.18
δ_3	2.3000	2.3222	0.97

As shown in Fig. 3.7, the parameters β , δ , and k can be approximated by using a first-order polynomial (the relationships between the parameters and the electric current is linear) while the parameters α and c are approximated by the second-order polynomial. There is noteworthy that the deviation of parameters k is apperantly larger than the other parameters, as listed in Table 3.2. It can be found that this deviation was caused by a larger offset of the plot in large displacement amplitude input (at 2.0 m (*6.562 ft*)). Technically, the effects of this deviation can be minimized in the models of MR damper where the total output is dominant by the damping coefficient, c which has at least two-order larger in magnitude than the k , in this case.

The set of polynomial fitted parameters in Table 3.2 were substituted back into Eqn. (3.8) and Eqns. (3.1) - (3.2) to reconstruct the hysteretic responses and compared to the one obtained from the *pseudo*-experimental data as shown in Fig. 3.8. The hysteretic responses obtained by the *pseudo*-experimental data and the reconstructed hysteresis using identified parameters in Table 3.2 are matching well. Therefore, the *parameter identification* method proposed here is adequate for numerically modeling MR damper based on the experimental data of a physical MR damper.

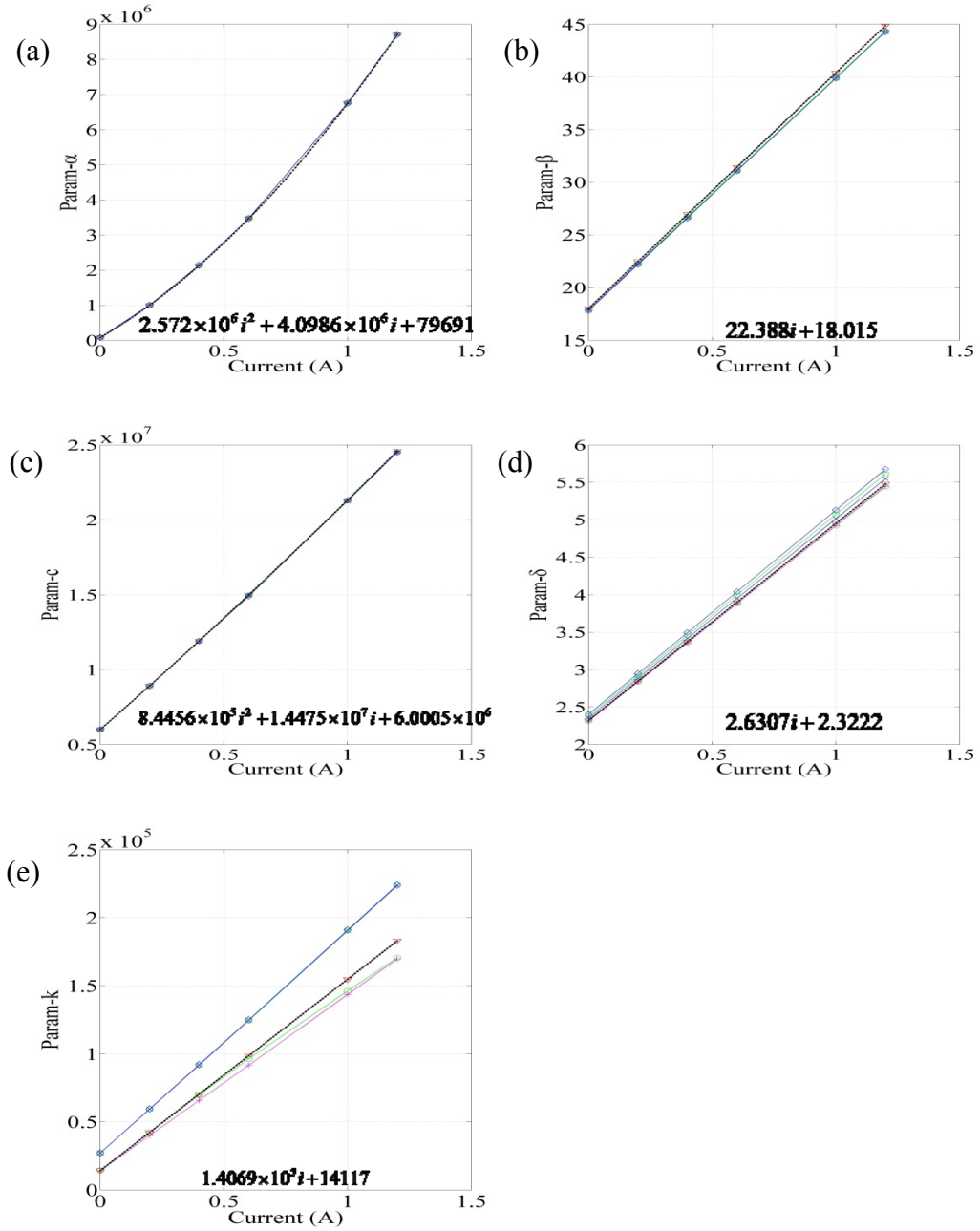

Figure 3.7 Parameter identification results (-) and polynomial fitted coefficients (…): (a) parameter-α , (b) parameter-β , (c) parameter-c, (d) parameter-δ , and (e) parameter-k.

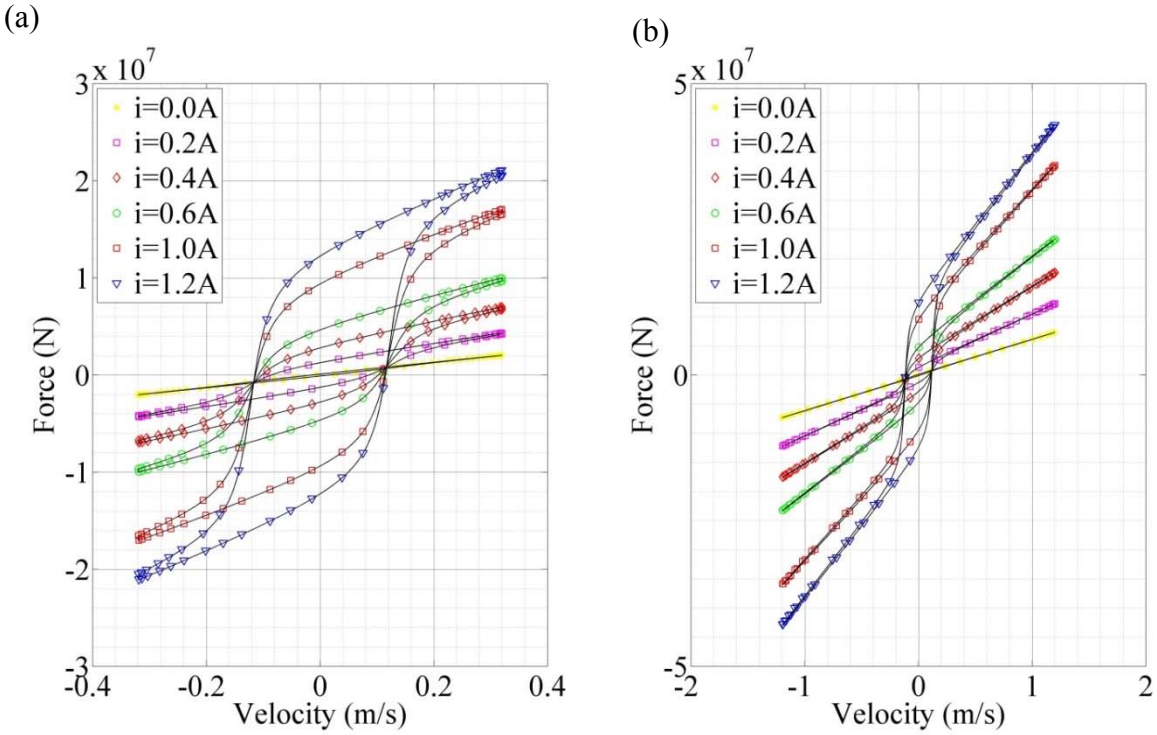

Figure 3.8 Pseudo-experimental data (markers) and the reconstruction of hysteresis from polynomial fitted parameters (solid line) for: (a) frequency = 0.4 rad/s, displacement = 0.8 m; and (b) frequency = 0.8 rad/s, displacement = 1.5 m (*4.92 ft*).

3.4 Riser Tensioner Equipped with MR Damper

In this Subsection, the free body diagrams (FBD) and equation of motion (EOM) in vertical direction of a riser tensioner and riser tensioner equipped with MR damper were derived. A direct-acting style tensioner, as illustrated in Fig. 3.9, is modeled as a lumped mass-spring-damper (MSD) system, the mass of host platform m_1 and tensioner m_2 are lumped, and the stiffness k_t and damping c_t of the tensioner are modeled as a spring and a dashpot, respectively. For conceptual simplicity, this model was assumed here to be in the vertical translation only while the rotations are assumed to be negligible. However, there is noteworthy that the rotational effects will be considered again in the CHARM3D numerical modeling in Subsection 3.5.

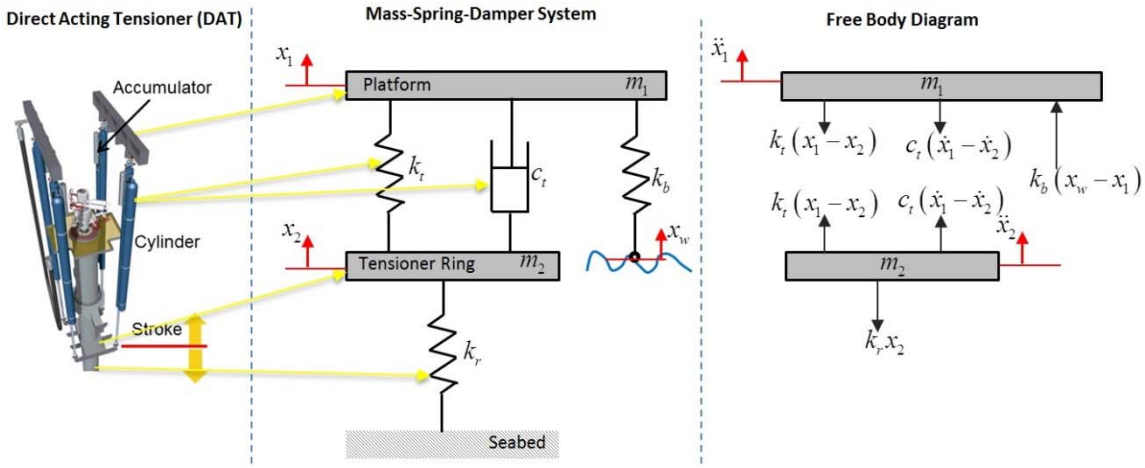

Figure 3.9 Schematic mass-spring-damper system of direct-acting style tensioner and free body diagram.

In Fig. 3.9, x_w denotes the displacement (elevation) of the wave, which is the external force acting on the platform, k_b is the stiffness of the platform body, and k_r is the stiffness of the riser which is connected to the tensioner ring on one end and the seabed on the other end. The x_1 and x_2 denote to the displacements of platform and tensioner ring, respectively. The equations of motion, as derived from the free-body diagram and Newton's second law are:

$$\sum F_z^{body} = m_1\ddot{x}_1 = k_b\left(x_w - x_1\right) - k_t\left(x_1 - x_2\right) - c_t\left(\dot{x}_1 - \dot{x}_2\right) \tag{3.9}$$

$$\sum F_z^{t-ring} = m_2\ddot{x}_2 = k_t\left(x_1 - x_2\right) + c_t\left(\dot{x}_1 - \dot{x}_2\right) - k_r x_2 \tag{3.10}$$

Rearranging the Eqns. (3.9) and (3.10), the equation of motion for *direct-acting style* tensioner in vertical direction can be represented as:

$$\begin{cases} m_1\ddot{x}_1 - k_t\left(x_2 - x_1\right) - c_t\left(\dot{x}_2 - \dot{x}_1\right) + k_b\left(x_1 - x_w\right) = 0 \\ m_2\ddot{x}_2 + k_t\left(x_2 - x_1\right) + c_t\left(\dot{x}_2 - \dot{x}_1\right) + k_r x_2 = 0 \end{cases} \tag{3.11}$$

For the *ram-style* tensioner, the schematic MSD system and the free-body diagram is illustracted in Fig. 3.10. The equations of motion can be derived, from Fig. 3.10, as:

$$\sum F_z^{body} = m_1\ddot{x}_1 = k_b\left(x_w - x_1\right) - k_t\left(x_1 - x_2\right) - c_t\left(\dot{x}_1 - \dot{x}_2\right) \tag{3.12}$$

$$\sum F_z^{t-ring} = m_2\ddot{x}_2 = k_t\left(x_1 - x_2\right) + c_t\left(\dot{x}_1 - \dot{x}_2\right) - k_r x_2 \tag{3.13}$$

and,

$$\begin{cases} m_1\ddot{x}_1 - k_t\left(x_2 - x_1\right) - c_t\left(\dot{x}_2 - \dot{x}_1\right) + k_b\left(x_1 - x_w\right) = 0 \\ m_2\ddot{x}_2 + k_t\left(x_2 - x_1\right) + c_t\left(\dot{x}_2 - \dot{x}_1\right) + k_r x_2 = 0 \end{cases} \tag{3.14}$$

It can be found that the equations of motion for the *ram-style* tensioner are same as the *direct-acting style* tensioner.

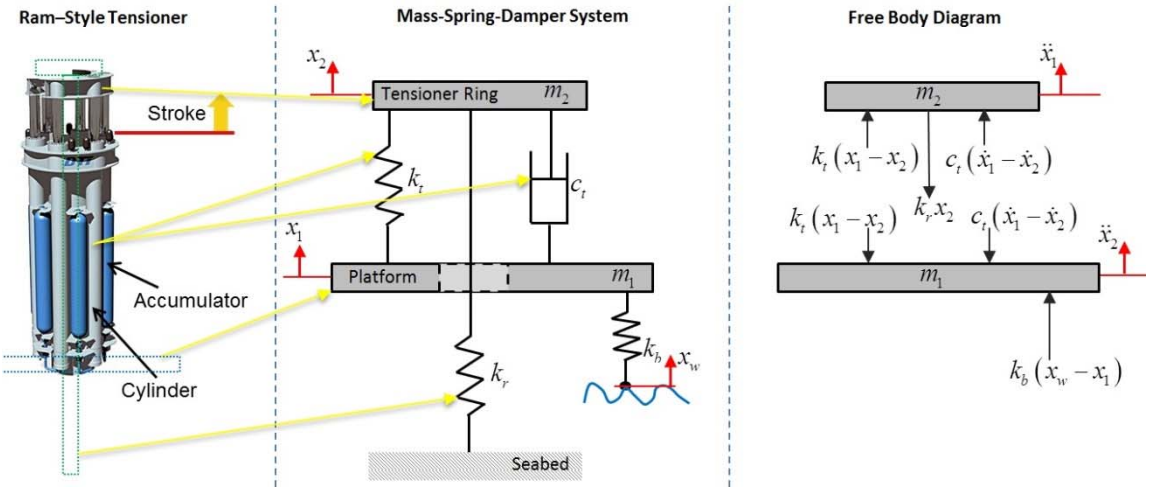

Figure 3.10 Schematic mass-spring-damper system of ram-style tensioner and free body diagram.

In this study, the MR damper is integrated into the tensioner system. The MR damper is working incoporately with the tensioner in order to reduce the required stroke on the tensioner with the trade-off of local tension increment, as to be discussed in more detailed in Section 4 and Section 7. The MSD system of direct-acting style tensioner equipped with MR damper and the corresponding free-body diagram are illustrated in Fig. 3.11. The equations of motion for this case can be derived as:

$$\sum F_z^{body} = m_1\ddot{x}_1 = k_b\left(x_w - x_1\right) - k_t\left(x_1 - x_2\right) - c_t\left(\dot{x}_1 - \dot{x}_2\right) - f_{MR}\big|_{x_1 - x_2} \tag{3.15}$$

$$\sum F_z^{t-ring} = m_2\ddot{x}_2 = k_t\left(x_1 - x_2\right) + c_t\left(\dot{x}_1 - \dot{x}_2\right) - k_r x_2 + f_{MR}\big|_{x_1 - x_2} \tag{3.16}$$

Recalling the force exerted by the MR damper f_{MR} can be represented by the following equations:

$$f_{MR} = c\dot{x}_{MR} + kx_{MR} + \alpha z_{MR} \tag{3.1}$$

$$z_{MR} = \tan^{-1}\left(\beta \dot{x}_{MR} + \delta \mathrm{sgn}\left(x_{MR}\right)\right) \tag{3.2}$$

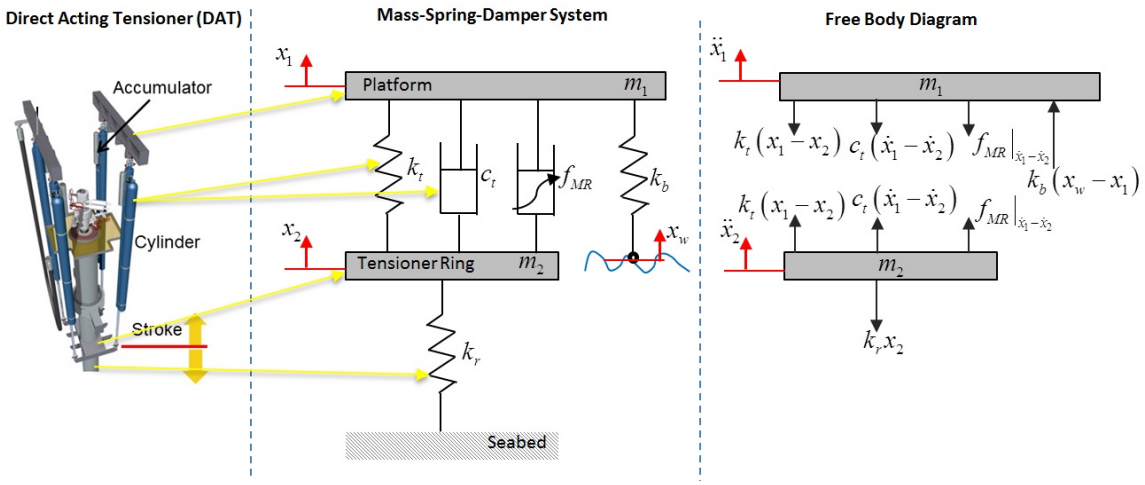

Figure 3.11 Schematic mass-spring-damper system of direct-acting style tensioner equipped with MR damper and free body diagram.

Therefore, the term $f_{MR}\big|_{x_1 - x_2}$ in Eqns. (3.15) and (3.16) can be represented as:

$$f_{MR}\big|_{x_1 - x_2} = c_{MR}\left(\dot{x}_1 - \dot{x}_2\right) + k_{MR}\left(x_1 - x_2\right) + \alpha z_{(\dot{x}_1 - \dot{x}_2)} \tag{3.17}$$

$$z_{(\dot{x}_1 - \dot{x}_2)} = \tan^{-1}\left(\beta\left(\dot{x}_1 - \dot{x}_2\right) + \delta \mathrm{sgn}\left(x_1 - x_2\right)\right) \tag{3.18}$$

and the equations of motion for *direct-acting style* tensioner equipped with MR damper, which is matching with the two-DOFs model with MR damper (Yao et al., 2002):

$$\begin{cases} m_1\ddot{x}_1-\left(k_t+k_{MR}\right)\left(x_2-x_1\right)-\left(c_t+c_{MR}\right)\left(\dot{x}_2-\dot{x}_1\right)+k_b\left(x_1-x_w\right)=\alpha z_{(\dot{x}_2-\dot{x}_1)} \\ m_2\ddot{x}_2+\left(k_t+k_{MR}\right)\left(x_2-x_1\right)+\left(c_t+c_{MR}\right)\left(\dot{x}_2-\dot{x}_1\right)+k_r x_2=-\alpha z_{(\dot{x}_2-\dot{x}_1)} \end{cases} \tag{3.19}$$

The schematic MSD system of *ram-style* tensioner equipped with MR damper and the corresponding free body diagram are depicted in Fig. 3.12. The equations of motion can be defined as:

$$\sum F_z^{body}=m_1\ddot{x}_1=k_b\left(x_w-x_1\right)-k_t\left(x_1-x_2\right)-c_t\left(\dot{x}_1-\dot{x}_2\right)-f_{MR}\big|_{x_1-x_2} \tag{3.20}$$

$$\sum F_z^{t-ring}=m_2\ddot{x}_2=k_t\left(x_1-x_2\right)+c_t\left(\dot{x}_1-\dot{x}_2\right)-k_r x_2+f_{MR}\big|_{x_1-x_2} \tag{3.21}$$

and the rearranged form is:

$$\begin{cases} m_1\ddot{x}_1-\left(k_t+k_{MR}\right)\left(x_2-x_1\right)-\left(c_t+c_{MR}\right)\left(\dot{x}_2-\dot{x}_1\right)+k_b\left(x_1-x_w\right)=\alpha z_{(\dot{x}_2-\dot{x}_1)} \\ m_2\ddot{x}_2+\left(k_t+k_{MR}\right)\left(x_2-x_1\right)+\left(c_t+c_{MR}\right)\left(\dot{x}_2-\dot{x}_1\right)+k_r x_2=-\alpha z_{(\dot{x}_2-\dot{x}_1)} \end{cases} \tag{3.22}$$

which is same as the one obtained in Eqn. (3.19) for the case of direct acting tensioner.

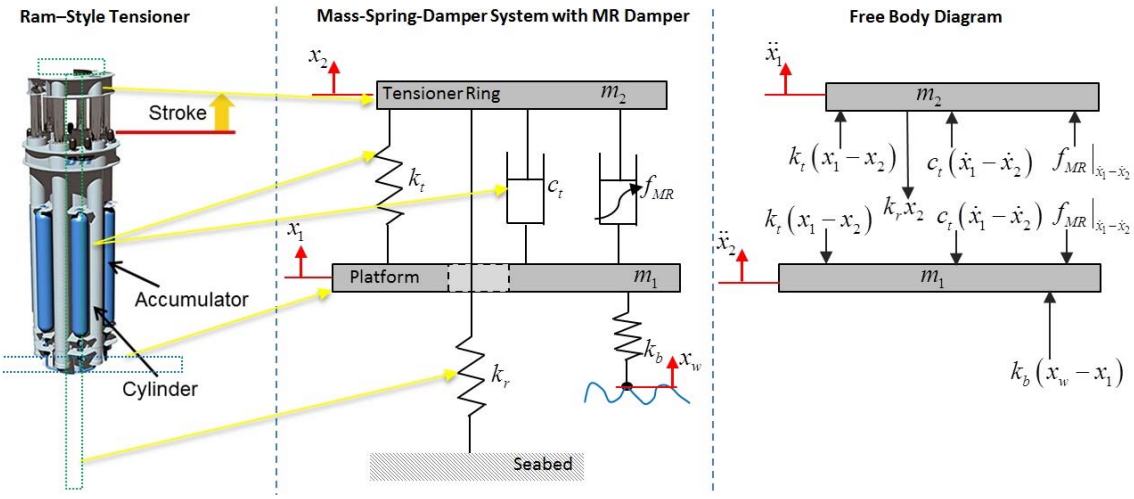

Figure 3.12 Schematic mass-spring-damper system of ram-style tensioner equipped with MR damper and free body diagram.

There can be found that the x_1 and x_2 are the displacements of platform and tensioner ring, respectively. By compared the x_1 and x_2 to the relative displacement terms in the Eqns. (2.146), (2.153) and (2.155), there can be found that the term $\left(X_i + p_i + \theta_j C_{ji} - r_i\right)$ is equivalent to the term $\left(x_1 - x_2\right)$ under the assumption that the rotational effects is negligible. Therefore, the Eqn. (3.22) can be further rearranged by separating the terms with relative displacement $\left(x_1 - x_2\right)$ on the RHS, for the *platform body*:

$$m_1\ddot{x}_1 + k_b\left(x_1 - x_w\right) = -\left(k_t + k_{MR}\right)\left(x_1 - x_2\right) - \left(c_t + c_{MR}\right)\left(\dot{x}_1 - \dot{x}_2\right) - \alpha z_{(\dot{x}_1 - \dot{x}_2)} \tag{3.23}$$

$$\begin{aligned} m_1\ddot{x}_1 + k_b\left(x_1 - x_w\right) = &-k_t\left(x_1 - x_2\right) - c_t\left(\dot{x}_1 - \dot{x}_2\right) \\ &-k_{MR}\left(x_1 - x_2\right) - c_{MR}\left(\dot{x}_1 - \dot{x}_2\right) - \alpha z_{(\dot{x}_1 - \dot{x}_2)} \end{aligned} \tag{3.24}$$

where if the damping c_1 is zero as assumed in the Subsection 2.4.5, the equation of motion for the *platform body* can be rewritten as:

$$m_1\ddot{x}_1 + k_b\left(x_1 - x_w\right) = F_i - f_{MR} \tag{3.25}$$

On the other hand, for the *riser rod* (on the tensioner ring);

$$m_2\ddot{x}_2 + k_r x_2 = \left(k_t + k_{MR}\right)\left(x_1 - x_2\right) + \left(c_t + c_{MR}\right)\left(\dot{x}_1 - \dot{x}_2\right) + \alpha z_{(\dot{x}_1 - \dot{x}_2)} \tag{3.26}$$

$$\begin{aligned} m_2\ddot{x}_2 + k_r x_2 = &k_t\left(x_1 - x_2\right) + c_t\left(\dot{x}_1 - \dot{x}_2\right) \\ &+k_{MR}\left(x_1 - x_2\right) + c_{MR}\left(\dot{x}_1 - \dot{x}_2\right) + \alpha z_{(\dot{x}_1 - \dot{x}_2)} \end{aligned} \tag{3.27}$$

where if the damping c_1 is zero as assumed in the Subsection 2.4.5, the equation of motion for the *riser rod* (on the tensioner ring) can be rewritten as:

$$m_2\ddot{x}_2 + k_r x_2 = N_i + f_{MR} \tag{3.28}$$

3.5 Modeling of MR-Damper Coupling with Platform/Lines (Risers) Connection

In this Subsection, the finite element modeling of a MR damper is integrated into the connection between the mooring lines (risers) and the platform as discussed in Subsection 2.4.5 and Subsection 3.4. Recalling the force exerted by the MR damper f_{MR} can be represented by the following equations:

$$f_{MR} = c\dot{x}_{MR} + kx_{MR} + \alpha z_{MR} \tag{3.1}$$

$$z_{MR} = \tan^{-1}\left(\beta\dot{x}_{MR} + \delta\,\mathrm{sgn}\left(x_{MR}\right)\right) \tag{3.2}$$

The **static** modeling of the MR damper can be conducted by rewriting the equation of MR damper force Eqn. (3.1) with Eqn. (2.146):

$$\begin{aligned} f_{MR} &= c\left(\dot{X}_i + \dot{\theta}_j C_{ji} - \dot{r}_i\right) + k\left(X_i + p_i + \theta_j C_{ji} - r_i\right) \\ &\quad + \alpha\left\{\tan^{-1}\left[\beta\left(\dot{X}_i + \dot{\theta}_j C_{ji} - \dot{r}_i\right) + \delta\,\mathrm{sgn}\left(X_i + p_i + \theta_j C_{ji} - r_i\right)\right]\right\} \end{aligned} \tag{3.29}$$

The MR damper can be represented by the combination of spring and damping force. Under the *static analysis*, the relative velocities in between the connected node and rigid body are equal to zero and only the *static part* remain, therefore the MR damper force f_{MR} is represented by the *static part* f_{MR}^{S} is:

$$\begin{aligned} f_{MR} &= f_{MR}^{S} \\ &= k\left(X_i + p_i + \theta_j C_{ji} - r_i\right) + \alpha\left\{\tan^{-1}\left[\delta\,\mathrm{sgn}\left(X_i + p_i + \theta_j C_{ji} - r_i\right)\right]\right\} \end{aligned} \tag{3.30}$$

The Newton's method is used to approximate the additional connector force exerted by the MR damper at the end node of line element connected to the springs in iteration $(n+1)$ from iteration (n) by expanding the *static part* of MR damper force in Taylor series expansion,

Equations for r_i:

$$f_{MR_i}^{S^{(n+1)}} = f_{MR_i}^{S^{(n)}} + \frac{\partial f_{MR_i}^{S^{(n)}}}{\partial r_j}\Delta r_j + \frac{\partial f_{MR_i}^{S^{(n)}}}{\partial X_j}\Delta X_j + \frac{\partial f_{MR_i}^{S^{(n)}}}{\partial \theta_j}\Delta \theta_j + \ldots \tag{3.31}$$

where

$$f_{MR}^{S} = k\left(X_i + p_i + \theta_j C_{ji} - r_i\right) + \alpha\left\{\tan^{-1}\left[\delta \operatorname{sgn}\left(X_i + p_i + \theta_j C_{ji} - r_i\right)\right]\right\} \tag{3.32}$$

Since the *signum* function $\operatorname{sgn}\left(X_i + p_i + \theta_j C_{ji} - r_i\right) = \pm 1$, the above equation can be further written as:

$$f_{MR}^{S} = k\left(X_i + p_i + \theta_j C_{ji} - r_i\right) + \alpha\left\{\tan^{-1}\left(\pm\delta\right)\right\} \tag{3.33}$$

The derivatives of $f_{MR_i}^{S^{(n)}}$ with respect to the position vector are:

$$\frac{\partial f_{MR_i}^{S^{(n)}}}{\partial r_j} = -k\,;\ \frac{\partial f_{MR_i}^{S^{(n)}}}{\partial X_j} = k\,;\ \frac{\partial f_{MR_i}^{S^{(n)}}}{\partial \theta_j} = kC_{ji} \tag{3.34}$$

where $i = 3$ because the MR damper is arranged to act in the vertical direction to the rod (riser). In the iterative process, using symbol K_{ij}^{AB} to indicate the tangential stiffness coefficients for freedom B_j in equation A_i, therefore the tangential stiffness coefficients of the rod, rigid-body and coupling after including the *static* MR-damper effects are shown as follows:

$$K_{ij}^{rr} = -\frac{\partial f_{MR_i}^S}{\partial r_j} = k\,; \qquad K_{ij}^{rX} = -\frac{\partial f_{MR_i}^S}{\partial X_j} = -k\,;$$

$$K_{ij}^{XX} = \frac{\partial f_{MR_i}^S}{\partial X_j} = k\,; \qquad K_{ij}^{r\theta} = -\frac{\partial f_{MR_i}^S}{\partial \theta_j} = -kC_{ji}\,;$$

$$K_{ij}^{X\theta} = \frac{\partial f_{MR_i}^S}{\partial \theta_j} = kC_{ji}\,; \qquad K_{ij}^{\theta\theta} = \left(K_i C_{ij}\right)_D C_{ki} + K_i^{\theta} D_{ij} D_{ki} \tag{3.35}$$

where $\left(K_i C_{ij}\right)_D = \frac{\partial f_{MR_i}^S}{\partial \theta_j} = kC_{ji}$ (3.36)

In the *time-domain* simulation, the *Average Acceleration Method* (AAM) (San Andrés, 2008) is used to approximate the numerical time integration of an equation of motion from time interval $t^{(n)}$ to $t^{(n+1)}$, which can be represented as:

$$M\Delta\ddot{X}_n + D\Delta\dot{X}_n + K\Delta X_n = \Delta F_n\left(t\right) \tag{3.37}$$

where, M is the mass matrix, D is the damping matrix, and K is the stiffness matrix of equation of motion. Also,

$$\Delta X_n = X_{n+1} - X_n\,; \qquad \Delta\dot{X}_n = \dot{X}_{n+1} - \dot{X}_n\,;$$

$$\Delta\ddot{X}_n = \ddot{X}_{n+1} - \ddot{X}_n\,; \qquad \Delta F_n = F_{n+1} - F_n \tag{3.38}$$

The detailed derivation of AAM is refered to Appendix B. The Eqn. (3.37) is rearranged to a form of Eqn. (2.144):

$$\hat{K}_n \Delta X_n = \Delta\hat{F}_n \tag{3.39}$$

where

$$\hat{K}_n = \left[K + \frac{2}{\Delta t_n} D + \frac{4}{\Delta t_n^2} M \right] \tag{3.40}$$

$$\Delta \hat{F}_n = \Delta F_n + 2M\ddot{X}_n + \left\{ 2D + \frac{4}{\Delta t_n} M \right\} \dot{X}_n \tag{3.41}$$

The $\hat{K}_i$ and $\Delta \hat{F}_i$ are known as *pseudo dynamic stiffness* and *dynamic force* respectively.

In order to couple the MR damper force into the spring-platform connection, the Eqn. (3.29) is derived to a form of *pseudo dynamic stiffness* and *dynamic force* as in Eqns. (3.40) and (3.41):

$$\begin{aligned} f_{MR} &= c\left(\dot{X}_i + \dot{\theta}_j C_{ji} - \dot{r}_i \right) + k\left(X_i + p_i + \theta_j C_{ji} - r_i \right) \\ &\quad + \alpha \left\{ \tan^{-1}\left[\beta \left(\dot{X}_i + \dot{\theta}_j C_{ji} - \dot{r}_i \right) + \delta \operatorname{sgn}\left(X_i + p_i + \theta_j C_{ji} - r_i \right) \right] \right\} \end{aligned} \tag{3.29}$$

where the p_i is a constant value and therefore $\dot{p}_i$ is zero. The *signum* function $\operatorname{sgn}\left(X_i + p_i + \theta_j C_{ji} - r_i \right) = \pm 1$, the above equation can be further written as:

$$\begin{aligned} f_{MR} &= c\left(\dot{X}_i + \dot{\theta}_j C_{ji} - \dot{r}_i \right) + k\left(X_i + p_i + \theta_j C_{ji} - r_i \right) \\ &\quad + \alpha \left\{ \tan^{-1}\left[\beta \left(\dot{X}_i + \dot{\theta}_j C_{ji} - \dot{r}_i \right) \pm \delta \right] \right\} \end{aligned} \tag{3.42}$$

By using the linear approximation of multivariable Tylor series expansion, the equation with respect to r_i and $\dot{r}_i$ (on the rod side) is:

$$\begin{aligned} f_{MR_i}^{(n+1)} &= f_{MR_i}^{(n)} + \frac{\partial f_{MR_i}^{(n)}}{\partial r_j} \Delta r_j + \frac{\partial f_{MR_i}^{(n)}}{\partial X_j} \Delta X_j + \frac{\partial f_{MR_i}^{(n)}}{\partial \theta_j} \Delta \theta_j \\ &\quad + \frac{\partial f_{MR_i}^{(n)}}{\partial \dot{r}_j} \Delta \dot{r}_j + \frac{\partial f_{MR_i}^{(n)}}{\partial \dot{X}_j} \Delta \dot{X}_j + \frac{\partial f_{MR_i}^{(n)}}{\partial \dot{\theta}_j} \Delta \dot{\theta}_j + \ldots \end{aligned} \tag{3.43}$$

By using Adams-Moulton implicit method, the connector force on the end of the line contributed by f_{MR} can be ontained from the integration from $t^{(n)}$ to $t^{(n+1)}$:

$$\int_{t^{(n)}}^{t^{(n+1)}} f_{MR_i} dt = \frac{\Delta t}{2}\left(f_{MR_i}^{(n+1)} + f_{MR_i}^{(n)} \right)$$

$$\approx \frac{\Delta t}{2}\left(\begin{array}{l} \dfrac{\partial f_{MR_i}^{(n)}}{\partial r_j}\Delta r_j + \dfrac{\partial f_{MR_i}^{(n)}}{\partial X_j}\Delta X_j + \dfrac{\partial f_{MR_i}^{(n)}}{\partial \theta_j}\Delta \theta_j \\ + \dfrac{\partial f_{MR_i}^{(n)}}{\partial \dot{r}_j}\Delta \dot{r}_j + \dfrac{\partial f_{MR_i}^{(n)}}{\partial \dot{X}_j}\Delta \dot{X}_j + \dfrac{\partial f_{MR_i}^{(n)}}{\partial \dot{\theta}_j}\Delta \dot{\theta}_j + 2 f_{MR_i}^{(n)} \end{array} \right) \tag{3.44}$$

where the change of velocities are (refer to Eqns. (A.1) - (A.4) in Appendix A):

$$\Delta \dot{X}_j^{(\mathrm{n})} = \frac{\Delta\left(\Delta X_j^{(\mathrm{n})}\right)}{\Delta t^{(\mathrm{n})}}\ ,\ \Delta \dot{r}_j^{(\mathrm{n})} = \frac{\Delta\left(\Delta r_j^{(\mathrm{n})}\right)}{\Delta t^{(\mathrm{n})}}\text{, and } \Delta \dot{\theta}_j^{(\mathrm{n})} = \frac{\Delta\left(\Delta \theta_j^{(\mathrm{n})}\right)}{\Delta t^{(\mathrm{n})}} \tag{3.45}$$

therefore, the Eqn. (3.44) can be rewritten as:

$$\int_{t^{(n)}}^{t^{(n+1)}} f_{MR_i} dt = \frac{\Delta t}{2}\left(\begin{array}{l} \dfrac{\partial f_{MR_i}^{(n)}}{\partial r_j}\Delta r_j + \dfrac{\partial f_{MR_i}^{(n)}}{\partial X_j}\Delta X_j + \dfrac{\partial f_{MR_i}^{(n)}}{\partial \theta_j}\Delta \theta_j + 2 f_{MR_i}^{(n)} + \\ \dfrac{\partial f_{MR_i}^{(n)}}{\partial \dot{r}_j}\dfrac{\Delta\left(\Delta r_j\right)}{\Delta t} + \dfrac{\partial f_{MR_i}^{(n)}}{\partial \dot{X}_j}\dfrac{\Delta\left(\Delta X_j\right)}{\Delta t} + \dfrac{\partial f_{MR_i}^{(n)}}{\partial \dot{\theta}_j}\dfrac{\Delta\left(\Delta \theta_j\right)}{\Delta t} \end{array} \right)$$

$$= \frac{\Delta t}{2}\left(\frac{\partial f_{MR_i}^{(n)}}{\partial r_j}\Delta r_j + \frac{\partial f_{MR_i}^{(n)}}{\partial X_j}\Delta X_j + \frac{\partial f_{MR_i}^{(n)}}{\partial \theta_j}\Delta \theta_j + 2 f_{MR_i}^{(n)} \right)$$

$$+ \frac{1}{2}\left(\frac{\partial f_{MR_i}^{(n)}}{\partial \dot{r}_j}\Delta\left(\Delta r_j^{(\mathrm{n})}\right) + \frac{\partial f_{MR_i}^{(n)}}{\partial \dot{X}_j}\Delta\left(\Delta X_j^{(\mathrm{n})}\right) + \frac{\partial f_{MR_i}^{(n)}}{\partial \dot{\theta}_j}\Delta\left(\Delta \theta_j^{(\mathrm{n})}\right) \right) \tag{3.46}$$

$$\int_{t^{(n)}}^{t^{(n+1)}} f_{MR_i}\,dt = \frac{\Delta t}{2}\left(\frac{\partial f_{MR_i}^{(n)}}{\partial r_j}\Delta r_j + \frac{\partial f_{MR_i}^{(n)}}{\partial X_j}\Delta X_j + \frac{\partial f_{MR_i}^{(n)}}{\partial \theta_j}\Delta\theta_j + 2 f_{MR_i}^{(n)} \right)$$
$$+ \frac{\partial f_{MR_i}^{(n)}}{\partial \dot{r}_j}\left[\frac{1}{2}\left(\Delta r_j^{(n+1)} - \Delta r_j^{(n)}\right)\right] + \frac{\partial f_{MR_i}^{(n)}}{\partial \dot{X}_j}\left[\frac{1}{2}\left(\Delta X_j^{(n+1)} - \Delta X_j^{(n)}\right)\right]$$
$$+ \frac{\partial f_{MR_i}^{(n)}}{\partial \dot{\theta}_j}\left[\frac{1}{2}\left(\Delta\theta_j^{(n+1)} - \Delta\theta_j^{(n)}\right)\right] \tag{3.47}$$

where the tangential stiffness coefficients can be derived as:

$$\frac{\partial f_{MR_i}^{(n)}}{\partial r_j} = \frac{\partial}{\partial r_j}\left\{\begin{matrix} c\left(\dot{X}_i + \dot{\theta}_j C_{ji} - \dot{r}_i\right) + k\left(X_i + p_i + \theta_j C_{ji} - r_i\right) \\ + \alpha\left\{\tan^{-1}\left[\beta\left(\dot{X}_i + \dot{\theta}_j C_{ji} - \dot{r}_i\right) \pm \delta\right]\right\} \end{matrix}\right\} = -k \tag{3.48}$$

$$\frac{\partial f_{MR_i}^{(n)}}{\partial X_j} = \frac{\partial}{\partial X_j}\left\{\begin{matrix} c\left(\dot{X}_i + \dot{\theta}_j C_{ji} - \dot{r}_i\right) + k\left(X_i + p_i + \theta_j C_{ji} - r_i\right) \\ + \alpha\left\{\tan^{-1}\left[\beta\left(\dot{X}_i + \dot{\theta}_j C_{ji} - \dot{r}_i\right) \pm \delta\right]\right\} \end{matrix}\right\} = k \tag{3.49}$$

$$\frac{\partial f_{MR_i}^{(n)}}{\partial \theta_j} = \frac{\partial}{\partial \theta_j}\left\{\begin{matrix} c\left(\dot{X}_i + \dot{\theta}_j C_{ji} - \dot{r}_i\right) + k\left(X_i + p_i + \theta_j C_{ji} - r_i\right) \\ + \alpha\left\{\tan^{-1}\left[\beta\left(\dot{X}_i + \dot{\theta}_j C_{ji} - \dot{r}_i\right) \pm \delta\right]\right\} \end{matrix}\right\} = kC_{ji} \tag{3.50}$$

$$\frac{\partial f_{MR_i}^{(n)}}{\partial \dot{r}_j} = \frac{\partial}{\partial \dot{r}_j}\left\{\begin{matrix} c\left(\dot{X}_i + \dot{\theta}_j C_{ji} - \dot{r}_i\right) + k\left(X_i + p_i + \theta_j C_{ji} - r_i\right) \\ + \alpha\left\{\tan^{-1}\left[\beta\left(\dot{X}_i + \dot{\theta}_j C_{ji} - \dot{r}_i\right) \pm \delta\right]\right\} \end{matrix}\right\}$$
$$= -c - \frac{\alpha\beta}{\left[\beta\left(\dot{X}_i + \dot{\theta}_j C_{ji} - \dot{r}_i\right) \pm \delta\right]^2 + 1} \tag{3.51}$$

$$\frac{\partial f_{MR_i}^{(n)}}{\partial \dot{X}_j} = \frac{\partial}{\partial \dot{X}_j}\left\{\begin{matrix} c\left(\dot{X}_i + \dot{\theta}_j C_{ji} - \dot{r}_i\right) + k\left(X_i + p_i + \theta_j C_{ji} - r_i\right) \\ + \alpha\left\{\tan^{-1}\left[\beta\left(\dot{X}_i + \dot{\theta}_j C_{ji} - \dot{r}_i\right) \pm \delta\right]\right\} \end{matrix}\right\}$$
$$= c + \frac{\alpha\beta}{\left[\beta\left(\dot{X}_i + \dot{\theta}_j C_{ji} - \dot{r}_i\right) \pm \delta\right]^2 + 1} \tag{3.52}$$

$$\frac{\partial f_{MR_i}^{(n)}}{\partial \dot{\theta}_j} = \frac{\partial}{\partial \dot{\theta}_j}\begin{Bmatrix} c\left(\dot{X}_i + \dot{\theta}_j C_{ji} - \dot{r}_i\right) + k\left(X_i + p_i + \theta_j C_{ji} - r_i\right) \\ + \alpha\left\{\tan^{-1}\left[\beta\left(\dot{X}_i + \dot{\theta}_j C_{ji} - \dot{r}_i\right) \pm \delta\right]\right\} \end{Bmatrix}$$

$$= c \cdot C_{ji} + \frac{\alpha\beta C_{ji}}{\left[\beta\left(\dot{X}_i + \dot{\theta}_j C_{ji} - \dot{r}_i\right) \pm \delta\right]^2 + 1} \tag{3.53}$$

$$\text{Let, } \gamma = \frac{\alpha\beta}{\left[\beta\left(\dot{X}_i + \dot{\theta}_j C_{ji} - \dot{r}_i\right) \pm \delta\right]^2 + 1} \tag{3.54}$$

and therefore the tangential stiffness coefficients in the above equations can be simplified as:

$$\frac{\partial f_{MR_i}^{(n)}}{\partial r_j} = -k \; ; \qquad \frac{\partial f_{MR_i}^{(n)}}{\partial X_j} = k \; ; \qquad \frac{\partial f_{MR_i}^{(n)}}{\partial \theta_j} = kC_{ji}$$

$$\frac{\partial f_{MR_i}^{(n)}}{\partial \dot{r}_j} = -c - \gamma \; ; \qquad \frac{\partial f_{MR_i}^{(n)}}{\partial \dot{X}_j} = c + \gamma \; ; \qquad \frac{\partial f_{MR_i}^{(n)}}{\partial \dot{\theta}_j} = \left(c + \gamma\right) \cdot C_{ji} \tag{3.55}$$

Substituting these tangential stiffness coefficients into Eqn. (3.47):

$$\int_{t^{(n)}}^{t^{(n+1)}} f_{MR_i} dt = \frac{\Delta t}{2}\left(-k \cdot \Delta r_j + k \cdot \Delta X_j + k \cdot C_{ij} \cdot \Delta\theta_j + 2 f_{MR_i}^{(n)}\right)$$
$$+ \left(-c - \gamma\right)\left[\frac{1}{2}\left(\Delta r_j^{(n+1)} - \Delta r_j^{(n)}\right)\right] + \left(c + \gamma\right)\left[\frac{1}{2}\left(\Delta X_j^{(n+1)} - \Delta X_j^{(n)}\right)\right]$$
$$+ \left(c + \gamma\right) \cdot C_{ji} \cdot \left[\frac{1}{2}\left(\Delta\theta_j^{(n+1)} - \Delta\theta_j^{(n)}\right)\right] \tag{3.56}$$

$$\int_{t^{(n)}}^{t^{(n+1)}} f_{MR_i} dt = \frac{\Delta t}{2}\left(-k \cdot \Delta r_j + k \cdot \Delta X_j + k \cdot C_{ij} \cdot \Delta\theta_j\right)$$
$$+ \left(-c - \gamma\right)\left[\frac{1}{2}\left(\Delta r_j^{(n+1)} - \Delta r_j^{(n)}\right)\right] + \left(c + \gamma\right)\left[\frac{1}{2}\left(\Delta X_j^{(n+1)} - \Delta X_j^{(n)}\right)\right]$$
$$+ \left(c + \gamma\right) \cdot C_{ji} \cdot \left[\frac{1}{2}\left(\Delta\theta_j^{(n+1)} - \Delta\theta_j^{(n)}\right)\right] + \Delta t \cdot f_{MR_i}^{(n)} \tag{3.57}$$

and examine the term $\Delta t \cdot f_{MR_i}^{(n)}$ on the right hand side of Eqn. (3.57);

$$\begin{aligned}\Delta t \cdot f_{MR_i}^{(n)} &= \Delta t \begin{Bmatrix} c\left(\dot{X}_i + \dot{\theta}_j C_{ji} - \dot{r}_i\right) + k\left(X_i + p_i + \theta_j C_{ji} - r_i\right) \\ + \alpha\left\{\tan^{-1}\left[\beta\left(\dot{X}_i + \dot{\theta}_j C_{ji} - \dot{r}_i\right) \pm \delta\right]\right\} \end{Bmatrix} \\ &= c \cdot \Delta t\left(\frac{\Delta X_i}{\Delta t} + \frac{\Delta \theta_i}{\Delta t} C_{ji} - \frac{\Delta r_i}{\Delta t}\right) + k \cdot \Delta t\left(X_i + p_i + \theta_j C_{ji} - r_i\right) \\ &\quad + \alpha \cdot \Delta t \cdot \tan^{-1}\left[\beta\left(\dot{X}_i + \dot{\theta}_j C_{ji} - \dot{r}_i\right) \pm \delta\right] \end{aligned} \tag{3.58}$$

Rewrite $\Delta t \cdot f_{MR_i}^{(n)}$ in the following form:

$$\begin{aligned}\Delta t \cdot f_{MR_i}^{(n)} &= c \cdot \left(\Delta X_i^{(n)} + \Delta \theta_i^{(n)} C_{ji} - \Delta r_i^{(n)}\right) + k \cdot \Delta t\left(X_i + p_i + \theta_j C_{ji} - r_i\right) \\ &\quad + \alpha \cdot \Delta t \cdot \tan^{-1}\left[\beta\left(\dot{X}_i + \dot{\theta}_j C_{ji} - \dot{r}_i\right) \pm \delta\right] \\ &\quad + \gamma\left(\Delta X_i^{(n)} + \Delta \theta_i^{(n)} C_{ji} - \Delta r_i^{(n)}\right) - \gamma\left(\Delta X_i^{(n)} + \Delta \theta_i^{(n)} C_{ji} - \Delta r_i^{(n)}\right) \\ &= (c + \gamma) \cdot \left(\Delta X_i^{(n)} + \Delta \theta_i^{(n)} C_{ji} - \Delta r_i^{(n)}\right) + k \cdot \Delta t\left(X_i + p_i + \theta_j C_{ji} - r_i\right) \\ &\quad + \alpha \cdot \Delta t \cdot \tan^{-1}\left[\beta\left(\dot{X}_i + \dot{\theta}_j C_{ji} - \dot{r}_i\right) \pm \delta\right] - \gamma\left(\Delta X_i^{(n)} + \Delta \theta_i^{(n)} C_{ji} - \Delta r_i^{(n)}\right) \end{aligned} \tag{3.59}$$

and substituting Eqn. (3.59) into Eqn. (3.57):

$$\begin{aligned}\int_{t^{(n)}}^{t^{(n+1)}} f_{MR_i} dt &= \frac{\Delta t}{2}\left(-k \cdot \Delta r_j + k \cdot \Delta X_j + k \cdot C_{ij} \cdot \Delta \theta_j\right) \\ &\quad + (-c - \gamma)\left[\frac{1}{2}\left(\Delta r_j^{(n+1)} - \Delta r_j^{(n)} + 2\Delta r_j^{(n)}\right)\right] \\ &\quad + (c + \gamma)\left[\frac{1}{2}\left(\Delta X_j^{(n+1)} - \Delta X_j^{(n)} + 2\Delta X_j^{(n)}\right)\right] \\ &\quad + (c + \gamma) \cdot C_{ji} \cdot \left[\frac{1}{2}\left(\Delta \theta_j^{(n+1)} - \Delta \theta_j^{(n)} + 2\Delta \theta_j^{(n)}\right)\right] \\ &\quad + k \cdot \Delta t\left(X_i + p_i + \theta_j C_{ji} - r_i\right) \\ &\quad + \alpha \cdot \Delta t \cdot \tan^{-1}\left[\beta\left(\dot{X}_i + \dot{\theta}_j C_{ji} - \dot{r}_i\right) \pm \delta\right] - \gamma\left(\Delta X_i^{(n)} + \Delta \theta_i^{(n)} C_{ji} - \Delta r_i^{(n)}\right) \end{aligned} \tag{3.60}$$

By approximating the time varying $\Delta r_j, \Delta\theta_j$, and ΔX_j in the time interval $t^{(n+1)} - t^{(n)}$ to be a constant $\Delta r_j^{\left(n+\frac{1}{2}\right)}, \Delta\theta_j^{\left(n+\frac{1}{2}\right)}, X_j^{\left(n+\frac{1}{2}\right)}$ which are the position at time $t^{(n)} + \frac{\Delta t}{2}$, and for: $\Delta r_j^{\left(n+\frac{1}{2}\right)} = \frac{1}{2}\left(\Delta r_j^{(n+1)} + \Delta r_j^{(n)}\right)$, and so on, the Eqn. (3.60) can be approximated as:

$$\begin{aligned}\int_{t^{(n)}}^{t^{(n+1)}} f_{MR_i}\, dt = \frac{\Delta t}{2}\Bigg(& -k\cdot\Delta r_j^{\left(n+\frac{1}{2}\right)} + k\cdot\Delta X_j^{\left(n+\frac{1}{2}\right)} + k\cdot C_{ij}\cdot\Delta\theta_j^{\left(n+\frac{1}{2}\right)} \\ & + \left(-c-\gamma\right)\Delta r_j^{\left(n+\frac{1}{2}\right)} + \left(c+\gamma\right)\Delta X_j^{\left(n+\frac{1}{2}\right)} + \left(c+\gamma\right)\cdot C_{ji}\Delta\theta_j^{\left(n+\frac{1}{2}\right)} \\ & + k\cdot\Delta t\left(X_i + p_i + \theta_j C_{ji} - r_i\right) + \alpha\cdot\Delta t\cdot\tan^{-1}\left[\beta\left(\dot{X}_i + \dot{\theta}_j C_{ji} - \dot{r}_i\right) \pm \delta\right] \\ & - \gamma\left(\Delta X_i^{(n)} + \Delta\theta_i^{(n)} C_{ji} - \Delta r_i^{(n)}\right)\end{aligned} \tag{3.61}$$

where the last term on the right hand side of Eqn. (3.61) can be rewritten as (refer to Eqns. (A.1) to (A.4) in Appendix A):

$$\left(\Delta X_i^{(n)} + \Delta\theta_i^{(n)} C_{ji} - \Delta r_i^{(n)}\right) = \frac{\left(\Delta X_i^{(n)} + \Delta\theta_i^{(n)} C_{ji} - \Delta r_i^{(n)}\right)}{\Delta t}\cdot\Delta t = \left(\dot{X}_i + \dot{\theta}_i C_{ji} - \dot{r}_i\right)^{(n)}\cdot\Delta t \tag{3.62}$$

Therefore, Eqn. (3.61) can be rearranged as:

$$\begin{aligned}\int_{t^{(n)}}^{t^{(n+1)}} f_{MR_i}\, dt \approx \frac{\Delta t}{2}\Bigg(& \left[-k + \frac{2}{\Delta t}\left(-c-\gamma\right)\right]\cdot\Delta r_j^{\left(n+\frac{1}{2}\right)} + \left[k + \frac{2}{\Delta t}\left(c+\gamma\right)\right]\cdot\Delta X_j^{\left(n+\frac{1}{2}\right)} \\ & + \left[k + \frac{2}{\Delta t}\left(c+\gamma\right)\right]\cdot C_{ij}\cdot\Delta\theta_j^{\left(n+\frac{1}{2}\right)}\Bigg) \\ & + \frac{\Delta t}{2}\begin{Bmatrix} 2k\left(X_i + p_i + \theta_j C_{ji} - r_i\right) + 2\alpha\cdot\tan^{-1}\left[\beta\left(\dot{X}_i + \dot{\theta}_j C_{ji} - \dot{r}_i\right) \pm \delta\right] \\ -2\gamma\left(\dot{X}_i + \dot{\theta}_j C_{ji} - \dot{r}_i\right)\end{Bmatrix}\end{aligned} \tag{3.63}$$

$$\int_{t^{(n)}}^{t^{(n+1)}} f_{MR_i}\,dt \approx \frac{\Delta t}{2}\left(\begin{array}{l}\left[-k+\frac{2}{\Delta t}(-c-\gamma)\right]\cdot\Delta r_j^{\left(n+\frac{1}{2}\right)}+\left[k+\frac{2}{\Delta t}(c+\gamma)\right]\cdot\Delta X_j^{\left(n+\frac{1}{2}\right)}\\ +\left[k+\frac{2}{\Delta t}(c+\gamma)\right]\cdot C_{ij}\cdot\Delta\theta_j^{\left(n+\frac{1}{2}\right)}\end{array}\right)$$
$$+\frac{\Delta t}{2}\left\{2\cdot\left[f_{MR}-c\left(\dot{X}_i+\dot{\theta}_j C_{ji}-\dot{r}_i\right)-\ \gamma\left(\dot{X}_i+\dot{\theta}_j C_{ji}-\dot{r}_i\right)\right]\right\} \tag{3.64}$$

$$\int_{t^{(n)}}^{t^{(n+1)}} f_{MR_i}\,dt \approx \frac{\Delta t}{2}\left(\begin{array}{l}\left[-k+\frac{2}{\Delta t}(-c-\gamma)\right]\cdot\Delta r_j^{\left(n+\frac{1}{2}\right)}+\left[k+\frac{2}{\Delta t}(c+\gamma)\right]\cdot\Delta X_j^{\left(n+\frac{1}{2}\right)}\\ +\left[k+\frac{2}{\Delta t}(c+\gamma)\right]\cdot C_{ij}\cdot\Delta\theta_j^{\left(n+\frac{1}{2}\right)}\end{array}\right)$$
$$+\frac{\Delta t}{2}\left\{2\cdot\left[f_{MR}-(c+\gamma)\left(\dot{X}_i+\dot{\theta}_j C_{ji}-\dot{r}_i\right)\right]\right\} \tag{3.65}$$

It can be found that the Eqn. (3.65) can be rearranged in the following form as:

$$\int_{t^{(n)}}^{t^{(n+1)}} f_{MR_i}\,dt = \frac{\Delta t}{2}\left(f_{MR_i}^{(n+1)}+f_{MR_i}^{(n)}\right)$$
$$\approx \frac{\Delta t}{2}\left(\begin{array}{l}\left[-k+\frac{2}{\Delta t}(-c-\gamma)\right]\cdot\Delta r_j^{\left(n+\frac{1}{2}\right)}+\left[k+\frac{2}{\Delta t}(c+\gamma)\right]\cdot\Delta X_j^{\left(n+\frac{1}{2}\right)}\\ +\left[k+\frac{2}{\Delta t}(c+\gamma)\right]\cdot C_{ij}\cdot\Delta\theta_j^{\left(n+\frac{1}{2}\right)}\end{array}\right)$$
$$+\frac{\Delta t}{2}\left\{2\cdot\left[f_{MR}^{(n)}-(c+\gamma)\left(\dot{X}_i+\dot{\theta}_j C_{ji}-\dot{r}_i\right)\right]\right\} \tag{3.66}$$

$$\left(\begin{array}{l}\left[-k+\frac{2}{\Delta t}(-c-\gamma)\right]\cdot\Delta r_j^{\left(n+\frac{1}{2}\right)}\\ +\left[k+\frac{2}{\Delta t}(c+\gamma)\right]\cdot\Delta X_j^{\left(n+\frac{1}{2}\right)}\\ +\left[k+\frac{2}{\Delta t}(c+\gamma)\right]\cdot C_{ij}\cdot\Delta\theta_j^{\left(n+\frac{1}{2}\right)}\end{array}\right)\approx\left(f_{MR_i}^{(n+1)}-f_{MR_i}^{(n)}\right)+2(c+\gamma)\left(\dot{X}_i+\dot{\theta}_j C_{ji}-\dot{r}_i\right) \tag{3.67}$$

which is exactly same in the form of *pseudo dynamic stiffness* and *dynamic force* as in Eqns. (3.40) and (3.41).

Following from the Eqn. (3.65), the tangential stiffness coefficients and the connector force on the end of the line $\int_{t^{(n)}}^{t^{(n+1)}} f_{MR_i}\,dt$ contributed by the MR damper force are:

$$\begin{aligned}\int_{t^{(n)}}^{t^{(n+1)}} f_{MR_i}\,dt \approx{}& \frac{\Delta t}{2}\left(-K_{ij}^{rr}\cdot\Delta r_j^{\left(n+\frac{1}{2}\right)} - K_{ij}^{rX}\cdot\Delta X_j^{\left(n+\frac{1}{2}\right)} - K_{ij}^{r\theta}\cdot\Delta\theta_j^{\left(n+\frac{1}{2}\right)} \right) \\ &+ \frac{\Delta t}{2}\left\{ 2\cdot\left[f_{MR} - (c+\gamma)\left(\dot{X}_i + \dot{\theta}_j C_{ji} - \dot{r}_i \right) \right] \right\}\end{aligned} \tag{3.68}$$

and the connector force on the <u>rigid body</u> $\int_{t^{(n)}}^{t^{(n+1)}} F_{i(MR)}\,dt$ caused by the MR damper force is:

$$\begin{aligned}\int_{t^{(n)}}^{t^{(n+1)}} F_{i(MR)}\,dt ={}& -\int_{t^{(n)}}^{t^{(n+1)}} f_{MR_i}\,dt \\ ={}& \frac{\Delta t}{2}\left(-K_{ij}^{Xr}\cdot\Delta r_j^{\left(n+\frac{1}{2}\right)} - K_{ij}^{XX}\cdot\Delta X_j^{\left(n+\frac{1}{2}\right)} - K_{ij}^{X\theta}\cdot\Delta\theta_j^{\left(n+\frac{1}{2}\right)} \right) \\ &- \frac{\Delta t}{2}\left\{ 2\cdot\left[f_{MR} - (c+\gamma)\left(\dot{X}_i + \dot{\theta}_j C_{ji} - \dot{r}_i \right) \right] \right\}\end{aligned} \tag{3.69}$$

where

$$\begin{aligned} K_{ij}^{rr} &= -K_{ij}^{Xr} = k + \frac{2}{\Delta t}(c+\gamma) \\ K_{ij}^{rX} &= -K_{ij}^{XX} = K_{ij}^{Xr} = -\left[k + \frac{2}{\Delta t}(c+\gamma) \right] \\ K_{ij}^{r\theta} &= -K_{ij}^{X\theta} = -\left[k + \frac{2}{\Delta t}(c+\gamma) \right] C_{ji} \end{aligned}$$

$$K_{ij}^{\theta\theta} = \left(K_i C_{ij} \right)_D C_{ki} + K_i^{\theta} D_{ij} D_{ki}\text{, where } \left(K_i C_{ij} \right)_D = \frac{\partial f_{MR_i}^{(n)}}{\partial \theta_j} = \left[k + \frac{2}{\Delta t}(c+\gamma) \right] C_{ji} \tag{3.70}$$

There can be found that the second term on the right hand side (RHS) of Eqn. (3.68) (for the riser *line*) and Eqn. (3.69) (for the platform *body*), are the residue forcing terms after coupling with the MR damper. Therefore, these terms are to be included into the matrix (R) and (S) in Fig. 2.5, respectively, to modify the forcing terms in Charm3D. The total element tangential stiffness matrix, after considering the MR damper and spring coupling with the platform, on the *end node of the riser* (line), as modified from Eqn. (2.183) is:

$$\frac{\Delta t}{2}\left\{\begin{bmatrix} K_{ij}^{rr} & 0 \\ 0 & K_{ij}^{r'r'} \end{bmatrix}_{LS} + \begin{bmatrix} K_{ij}^{rr} & 0 \\ 0 & 0 \end{bmatrix}_{MR}\right\}\begin{Bmatrix} \Delta r_j \\ \Delta r_j' \end{Bmatrix} = \frac{\Delta t}{2}\begin{Bmatrix} 2N_i \\ 2L_i \end{Bmatrix}_{LS} + \frac{\Delta t}{2}\begin{Bmatrix} 2f_{MR} - 2(c+\gamma)\left(\dot{r}_j\right) \\ 0 \end{Bmatrix}_{MR} \tag{3.71}$$

The element tangential stiffness matrix that needs to be added into the platform *body,* as modified from Eqn. (2.184) is:

$$\frac{\Delta t}{2}\left\{\begin{bmatrix} K_{ij}^{XX} & K_{ij}^{X\theta} \\ K_{ij}^{\theta X} & K_{ij}^{\theta\theta} \end{bmatrix}_{LS} + \begin{bmatrix} K_{ij}^{XX} & K_{ij}^{X\theta} \\ K_{ij}^{X\theta} & K_{ij}^{\theta\theta} \end{bmatrix}_{MR}\right\}\begin{Bmatrix} \Delta X_j \\ \Delta \theta_j \end{Bmatrix} = \frac{\Delta t}{2}\begin{Bmatrix} 2F_i \\ 2M_i \end{Bmatrix}_{LS} + \frac{\Delta t}{2}\begin{Bmatrix} -2f_{MR} + 2(c+\gamma)\left(\dot{X}_j\right) \\ 0 \end{Bmatrix}_{MR} \tag{3.72}$$

and the *coupling* terms of element tangential stiffness matrix that need to be added into the global matrix is:

$$\frac{\Delta t}{2}\left\{\left[\begin{matrix} 0 & 0 & K_{ij}^{rX} & K_{ij}^{r\theta} \\ 0 & 0 & 0 & K_{ij}^{r'\theta} \\ K_{ij}^{Xr} & 0 & 0 & 0 \\ K_{ij}^{\theta r} & K_{ij}^{\theta r'} & 0 & 0 \end{matrix}\right]_{LS} + \left[\begin{matrix} 0 & 0 & K_{ij}^{rX} & K_{ij}^{r\theta} \\ 0 & 0 & 0 & 0 \\ K_{ij}^{Xr} & 0 & 0 & 0 \\ K_{ij}^{\theta r} & 0 & 0 & 0 \end{matrix}\right]_{MR}\right\}\left\{\begin{matrix} \Delta r_j \\ \Delta r_j' \\ \Delta X_j \\ \Delta \theta_j \end{matrix}\right\}$$

$$= \frac{\Delta t}{2}\left\{\begin{matrix} 2N_i \\ 2L_i \\ 2F_i \\ 2M_i \end{matrix}\right\}_{LS} + \frac{\Delta t}{2}\left\{\begin{matrix} 2f_{MR} - 2(c+\gamma)\left(\dot{r}_j\right) \\ 0 \\ -2f_{MR} + 2(c+\gamma)\left(\dot{X}_j\right) \\ 0 \end{matrix}\right\}_{MR} \tag{3.73}$$

4. SEMI-ACTIVE CONTROL SCHEMES

4.1 Introduction and Literature Reviews

The semi-active control schemes is utilized to control the riser tensioner system integrated with MR damper, as proposed in Subsection 3.4 and Subsection 3.5. The versatility and adaptability of active devices and the realiablity of passive devices are offered by semi-active devices (Hurlebaus et al., 2011), such as magneto-rheological (MR) damper. The mechanical properties of these systems may be adjusted based on feedback from the excitation and/or from the measured response, where a controller monitors the feedback measurements and generates an appropriate command signal for the semi-active devices (Symans and Constantinou, 1999). The semi-active control concept involves the use of control theory to augment the damping properties of devices in real time and offers considerable advantages in performance over passive damping elements. On the other hand, semi-active system cannot deliver the level of performance of a fully active system, however, semi-active system requires much less energy than active system (Symans and Constantinou, 1999). As energy can only be dissipated, spillover phenomena are avoided (Hurlebaus and Gaul, 2006). The control forces are developed through appropriate (based on a pre-determined control algorithm) adjustment of the mechanical properties of the semi-active control system. Furthermore, the control forces in many semi-active control systems primarily act to oppose the motion of the structural system and therefore promote the global stability of the structure (Symans and Constantinou, 1999).

The technology of installing MR dampers in land-based building to minimize the structural vibration especially during the earthquake has gained successful results (Duan *et al.,* (2002). Jansen and Dyke (2000) presented the results of a study to evaluate the performance of a number of semi-active control algorithms for use with multiple magneto-rheological (MR) dampers, including the *Lyapunov* controller, decentralized *bang-bang* controller, modulated homogeneous friction algorithm, and clipped-optimal controller. Each algorithm uses measurements of the absolute acceleration and device displacements for determining the control action to ensure that the algorithms could be implemented on a physical structure. Yao et al. (2002) proposed a semi-active control of MR damper in a two degree-of-freedoms system by using a Skyhook control scheme. Kim (2007) developed a multiple autoregressive exogenous inputs-based Takagi-Sugeno fuzzy model, to identify nonlinear behavior of structure-magnetorheological damper systems. It was demonstrated from the numerical simulation that the proposed algorithm is effective to control responses of seismically excited building structures equipped with MR dampers. Bahar *et al.* (2010) proposed an inverse model of an MR damper to overcome the difficulty of commanding the MR damper to output the desired control force. The inverse model of MR dampers consider a hybrid seismic control system for building structures, which combines a class of passive nonlinear base isolator with a semi-active control system. In this application, the damper is used as a semi-active device in which the voltage is updated by a feedback control loop. The management of MR dampers is performed in a hierarchical way according to the desired control force, the actual force of the dampers and its capacity to react.

Bitaraf *et al.* (2010) developed an effective control strategy by utilizing two semi-active control methods for seismic protection of structures using MR dampers. The first method is the Simple Adaptive Control method which tracks the response of the system with desired behavior and deals with the changes that occur in the characteristics of the structure. The second controller is a genetic-based fuzzy control method whose *rule-base* is determined by a multi-objective genetic algorithm to determine the command voltage of MR dampers. The developed controllers was reported can effectively control both displacement and acceleration response of the considered structure. Yu *et al.* (2010) developed a semi-active control strategy by using the Linear Quadratic Regulator (LQR) method to integrate with a modified inverse dynamic model to evaluate the value of evolutionary variable based on the *Bouc-Wen* model (Spencer Jr., et al., 1997) of MR dampers. This control strategy is applied to the dynamic response control of a fixed jacket offshore platform.

4.2 Semi-Active Skyhook Control Strategy

The semi-active *skyhook* control is studied in this Subsection. The input variables to the skyhook control are selected as the velocity of the tensioner ring and the host platform, while the output is the control force of the MR damper as follows (Yao et al., 2002; Yang et al., 2011):

$$\begin{cases} \dot{x}_1\left(\dot{x}_2-\dot{x}_1\right)>0, & F_c=\max \\ \dot{x}_1\left(\dot{x}_2-\dot{x}_1\right)<0, & F_c=\min \end{cases} \tag{4.1}$$

where $\dot{x}_1$ and $\dot{x}_2$ are the velocity of platform and tension ring, respectively, as illustrated in Figs. 3.9 – 3.12, and F_c is the control output force. If the relative velocity $(\dot{x}_2 - \dot{x}_1)$ between the tensioner ring and the platform is in the same direction of the velocity of the platform $\dot{x}_1$, an electric current is applied to the MR damper, otherwise no damping force is required (Yao et al., 2002).

4.3 Fuzzy-Logic Control

The *fuzzy logic* control (FLC) scheme is studied in this Subsection. The input variables to the FLC are selected as the vertical displacement x_2 and velocity $\dot{x}_2$ of the tensioner ring, as refered to the cases in Figs. 3.9 – 3.12, while the output is the command electric current $i(t)$, as stated in Eqns. (3.3) – (3.7), to the MR damper. For the inputs and output *membership functions*, seven identical triangles with 50% overlap are defined on the *normalized universe of discourse* in the range of [-1, 1] as illustrated in Fig. 4.1 (Wang and Song, 2013; Wilson, 2005).

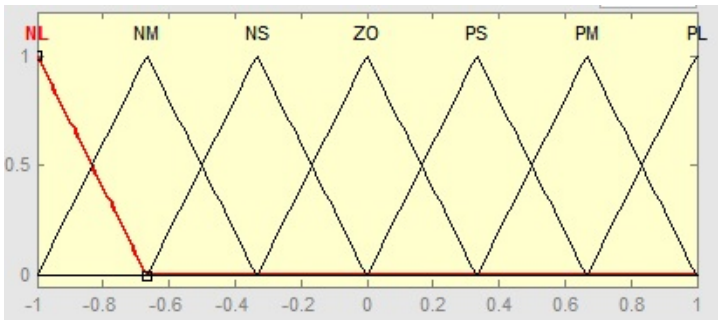

Figure 4.1 Membership functions of inputs (displacement and velocity of tensioner ring) and output (command current).

The linguistic variables of *membership function* are defined as Negative Large (NL), Negative Medium (NM), Negative Small (NS), Zero (ZO), Positive Small (PS), Positive Medium (PS), and Positive Large (PL), respectively. The triangular curve is a function of a vector x and depends on three scalar parameters a, b, c. For example, the *membership function* $f_{\Delta i}$ of triangular for case NL can be determined by (Lewis, 2004):

$$f_{\Delta i}\left(x; a_{NL}, b_{NL}, c_{NL}\right) = \max\left[\min\left(\frac{x - a_{NL}}{b_{NL} - a_{NL}}, \frac{c_{NL} - x}{c_{NL} - b_{NL}}\right), 0\right] \tag{4.2}$$

where

x = normalized input variables (vertical displacement and velocity, respectively)

a_{NL} = lowest value of triangular feet at the degree of membership equals to zero

b_{NL} = value of triangular peak at the degree of membership equals to one

c_{NL} = highest value of triangular feet at the degree of membership equals to zero

The block diagram of fuzzy logic controller is depicted in Fig. 4.2. According to Lewis (2004), a *rule-base* contains a fuzzy logic quantification of the expert's linguistic description of how to achieve good control. The *inference mechanism* emulates the expert's decision making in interpreting and applying knowledge about how best to control the system. The *fuzzification* interface converts controller inputs into information that the inference mechanism can easily use to activate and apply rules while the *defuzzification* interface converts the conclusions of the inference mechanism into actual inputs for the process. The *centroid defuzzification* method is used in this research and is given as (Lewis, 2004):

$$f_i(x) = \frac{\sum_{i=1}^{N} z^i \prod_{j=1}^{n} \mu_{ij}(x_j)}{\sum_{i=1}^{N} \prod_{j=1}^{n} \mu_{ij}(x_j)} \tag{4.3}$$

where

z^i = control representative values

$\mu_{ij}(x_j)$ = membership functions of the components of the n-vector x

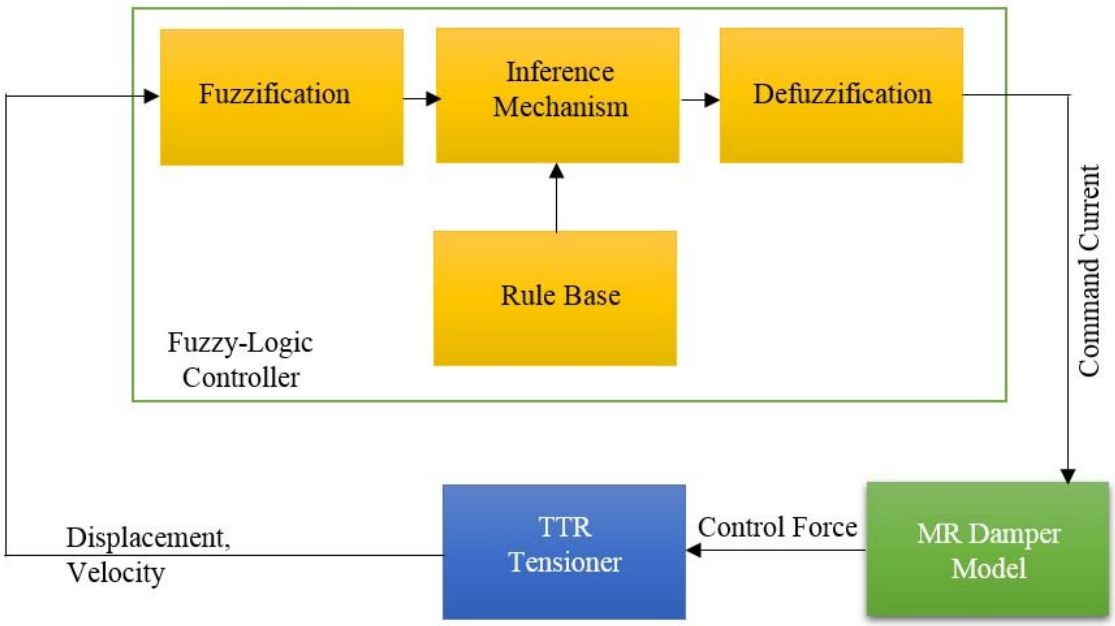

Figure 4.2 Block diagram of fuzzy logic controller.

The *inference rules* for computing the command current $i(t)$ into the MR damper is based on the works of Wang and Song (2013) are listed in Table 4.1. The response surface of fuzzy logic controller based on this inference rules is shown in Fig. 4.3. There is noteworthy that a *negative* command current $-i(t)$ is potential to be produced based on

this inference rules. Nevertheless, the physical nature of MR damper is a device that only provides dissipative damping force, therefore, the *negative* command current is regarded as *zero* current input in this control scheme.

Table 4.1 Control rules base of fuzzy logic controller (Wang and Song, 2013).

		Normalized Displacement						
		NL	**NM**	**NS**	**ZO**	**PS**	**PM**	**PL**
Normalized Velocity	**NL**	NM	NS	NS	NS	ZO	PS	PM
	NM	NM	NM	NM	NS	PS	PM	PM
	NS	NL	NM	NM	NS	PM	PL	PL
	ZO	NL	NL	NM	ZO	PM	PL	PL
	PS	NL	NL	NM	PS	PM	PM	PL
	PM	NM	NM	NS	PS	PM	PM	PM
	PL	NM	NS	ZO	PS	PS	PS	PM

Normalized Command Current

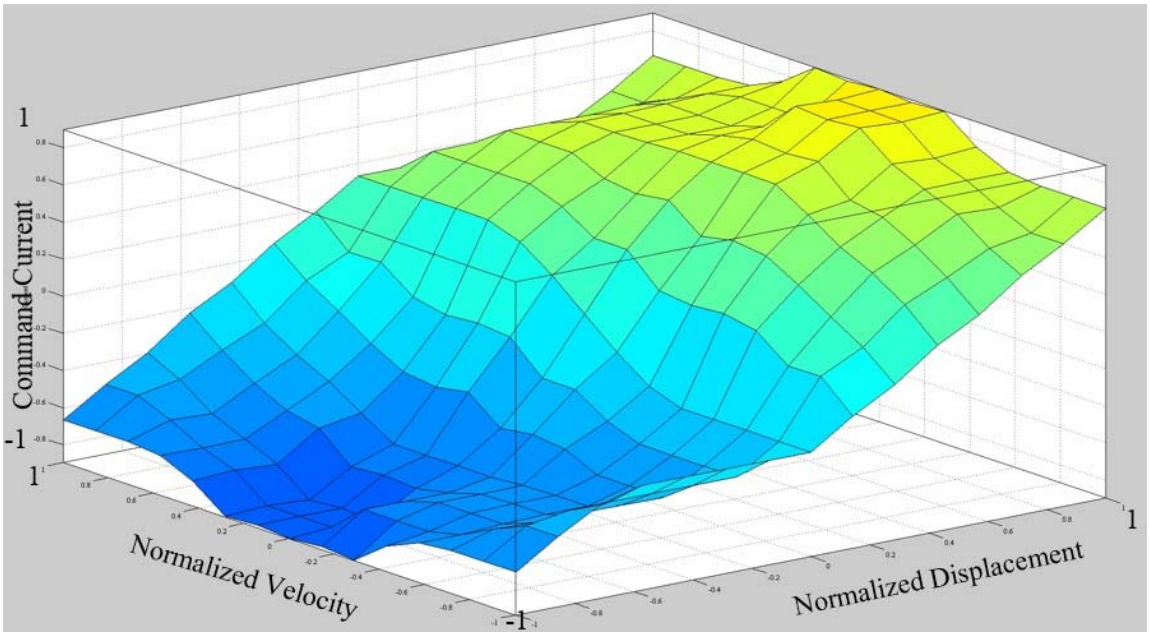

Figure 4.3 Response surface of fuzzy logic control scheme.

4.4 Control Performance Evaluation

The performance of the discussed control schemes were evaluated in this Subsection. The simulation was conducted to examine the dynamic responses of a two-DOFs system, as illustrated in Figs. 3.9 – 3.12. A typical two-DOFs system based on the works of Yao et. al (2002) and Sathishkumar et al. (2014), was studied in this Subsection. The parameters of a *scaled-down* two-DOFs system is modified from the works of Sathishkumar et al. (2014) and tabulated in Table 4.2.

Table 4.2 Parameters for a two-DOFs system.

Sprung mass m_2	290 kg (*19.8713 slug*)
Unsprung mass m_1	60 kg (*4.1113 slug*)
Stiffness k_t	16200 N/m (*1.11 kips/ft*)
Stiffness k_b	39100 N/m (*2.68 kips/ft*)
Damping c_t	1000 Ns/m (*0.0685 kips.s/ft*)
Stiffness k_r	0 N/m (*0 kips/ft*)

There is noteworthy that the *sprung* mass is equivalent to the tensioner ring, and the *unsprung* mass is equivalent to the platform mass, as illustrated in Figs. 3.9 – 3.12. Generally, the mass of the host platform m_1 is much larger than the mass of the tensioner ring m_2. However, since the purpose of this Subsection is to study the effectiveness of each discussed control schemes, therefore, the sprung mass / unsprung mass values were followed identically from the works of Sathishkumar et al. (2014).

The accelecration of the sprung mass is shown in Fig. 4.4. The *passive* control is the case where the motion is restrained by a damper with constant damping coefficient c_t. While the *active* control is the benchmark case when an active force actuator is installed into the two-DOFs system and fully follow the control scheme in Table 4.1, where the *negative* command current was regarding as the non-dissipative active forces to be actively transferred into the system.

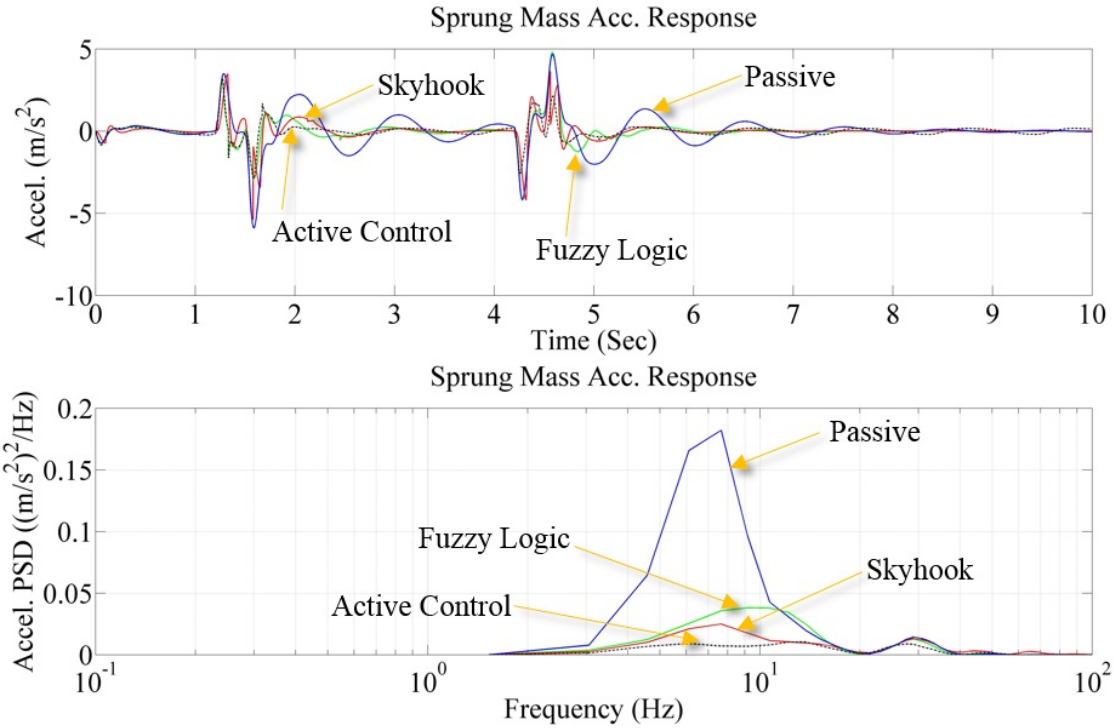

Figure 4.4 Acceleration of the sprung mass by using different types of control scheme.

There can be found that the semi-active control schemes, Skyhook and fuzzy-logic, had significantly reduced the sprung mass responses in the frequency range of body resonance (Yao et. al, 2002) from the uncontrolled passive condition, even though the performance in the reduction of sprung mass motion is not as much as performed by the active control.

The relative stroke response in between the sprung mass and unsprung mass is shown in Fig. 4.5. The semi-active control schemes and active control can significantly reduce the stroke in the body resonance range, however, increase the stroke outside this range.

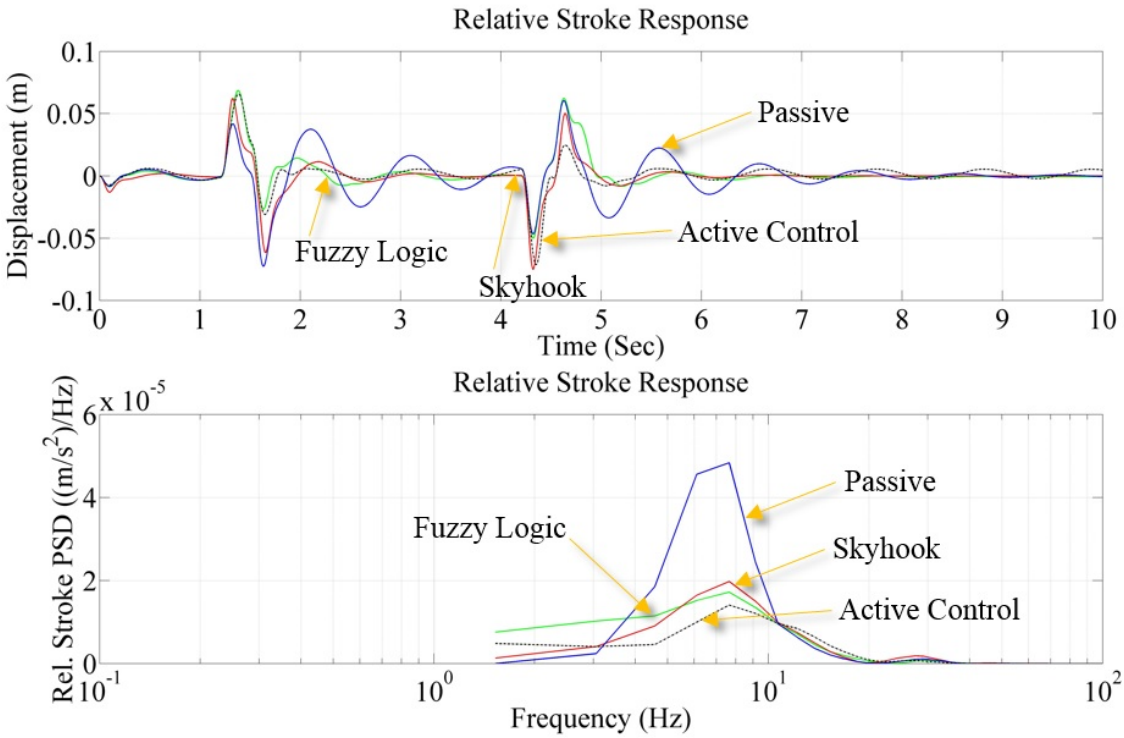

Figure 4.5 Relative stroke response by using different types of control scheme.

The deflection of the unsprung mass $(x_w - x_1)$ is shown in Fig. 4.6. The fuzzy logic control and skyhook control perform better than the active control in the body resonance range. However, the semi-active control schemes generates higher responses in the high-frequency region (second peak).

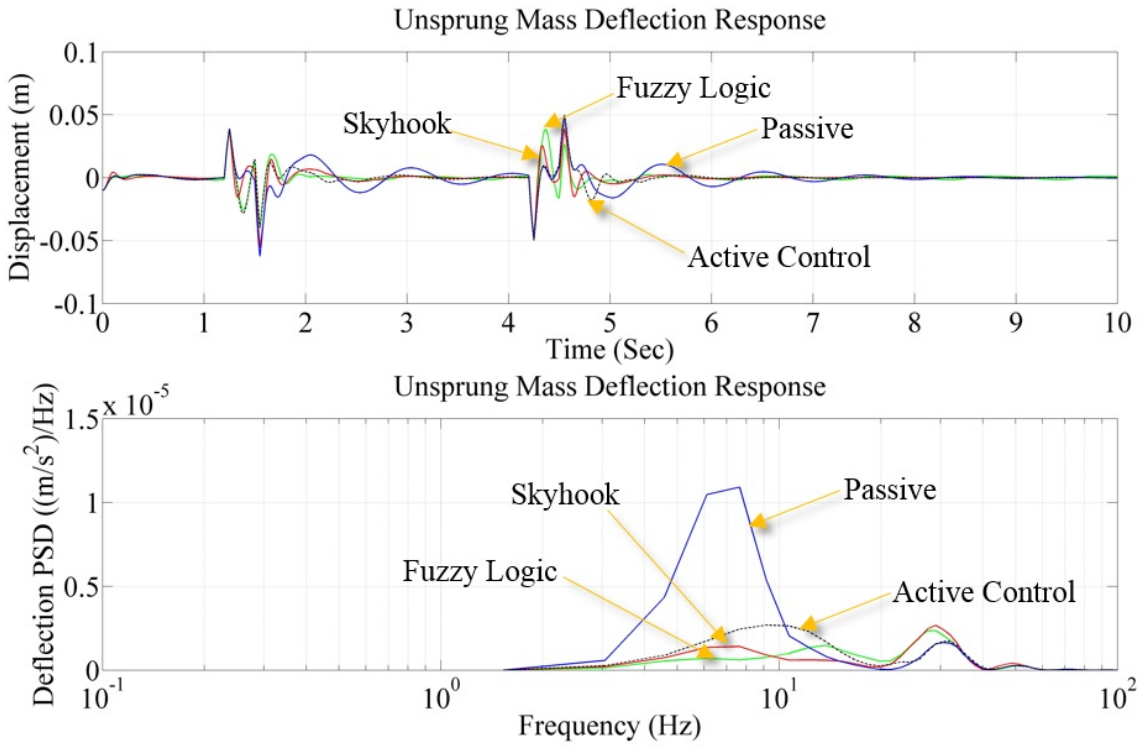

Figure 4.6 Deflection of the unsprung mass by using different types of control scheme.

From the simulation of two-DOFs system, it can be found that the semi-active control provides improved performances compared with the passive control (Yao et. al, 2002). Also, the semi-active control schemes have a comparable performance with the active control scheme, but the semi-active control scheme can reduce the complexity and avoid the spillover phenomena inherent form the active control (Hurlebaus and Gaul, 2006).

The semi-active control schemes of *Skyhook* control and *fuzzy logic* control are further utilized in Section 7 to control the stroke of tensioner ring. On the other hand, an active control scheme, Equivalent Force Compensation Control (EFCC), is conceptually

proposed in Section 5 (refer to Subsection 5.7) to compensate the force deviations in between the actual tensioner ring tension and the desired pretension by using a combination of MR dampers and force actuators.

5. REDUCTION OF FORCE VARIATIONS ON RISER TENSIONER BY USING MAGNETO-RHEOLOGICAL DAMPER

5.1 Introduction

The top tensioned risers (TTR) must have a heave compensator system that maintains a near constant axial tension. However, a near constant tension can only be obtained under very small heave motions and requires for large and sophisticated tensioner system. In real-world sea environments, excessive dynamic axial tension variations can be exerted on the TTR and lead to structural integrity issues. The traditional riser tension variations analysis, however, by using *parametric* formulation is only conditionally valid under certain strict limits and potentially underestimate the total magnitudes of the tension variations. This phenomenon is especially important for the offshore operations where the dynamic axial tension of riser must be closely monitored, such as in the offshore drilling operation and excessive fatigue loads prevention on the connection points in between the riser and *dry-tree* production system. This Section is focusing on the simulations and analysis of tension variations of a TTR, as illustrated in the Fig. 5.1. The TTR is modeled in detailed *component*-level which includes a set of hydraulic and pneumatic components. Moreover, the viscous fluid frictional effect in the hydro-pneumatic (HP) tensioner system is considered in the calculation of tension variations. The exertion of excessive tension variations in the tensioner system leads to the necessity of reduction of tension variations which can be achieved by using magneto-rheological (MR) damper.

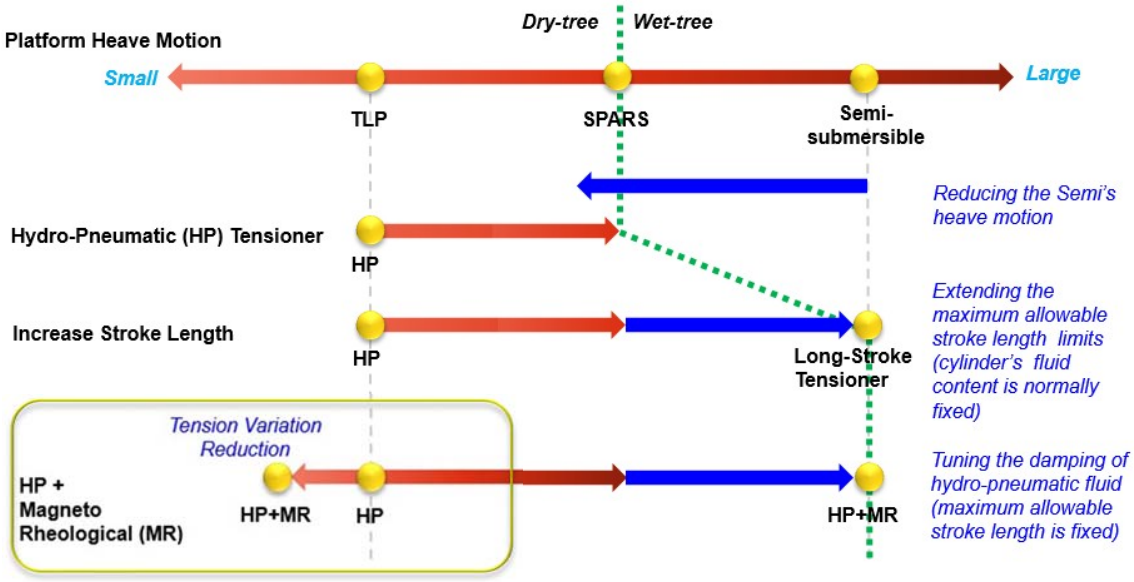

Figure 5.1 Overview of MR damper applications in ocean engineering.

The specific characteristics of MR damper in alternating the damping forces have great potential to interactively suppress the tension variations corresponding to various sea conditions. The main objectives of this Section are:

(i) to develop a detailed tension variations model of the HP tensioner (Subsection 5.3 and Subsection 5.5);

(ii) to identify the deviations in between the *parametric* formulation and *component-level* formulation in the analysis of TTR axial tension (Subsection 5.4);

(iii) to implement the MR damper and its control scheme in order to suppress the riser tension variations (Subsections 5.6 - 5.8).

The formulation and analysis of marine riser tensioning system which includes the hydraulic-pneumatic (HP) tensioner and the effects of magneto-rheological (MR) damper were studied. The tensioner system of a top-tensioned riser (TTR) is designed to maintain a *nearly constant* axial tension on the contact point with the TTR so that the host platform is able to move relatively to the risers. The TTR must be tensioned so that the riser does not buckle under its own weight. Hydro-pneumatic (HP) tensioner systems are a form of riser tensioning mechanism used to support TTRs on various *dry tree* (in which drilling and production equipment is disposed above the waterline) platforms. Conventionally, a plurality of hydraulic cylinders with hydro-pneumatic accumulators are connected between the platform and the riser to provide and maintain the necessary riser tension. Platform responses to environmental conditions, mainly heave and horizontal motions causing hull *set-down* (in the case of TLP), necessitate changes in riser length relative to the platform, which causes the tensioning cylinders to stroke in (up-stroke) and out (down-stroke). The spring effect caused by the gas compression or expansion in the tensioner (accumulator and gas bank) during riser stroke partially isolates the riser from the low heave platform motions while maintaining a nearly constant riser tension. However, when the platform, in case of TLP, takes a significant horizontal offset, the compression of the gas in the tensioner causes increased internal pressure and thus increased riser tension (Crotwell and Yu, 2011).

In this Section, the formulation of riser tensioner is developed to identify the deviations in between the following two approaches in the marine tensioner-riser dynamic analysis:

(i) *parametric* formulation (Yang, 2009), and

(ii) *component-level* formulation, which is the integrated *component-level* effects that considers the total component effects of the HP tensioner (Gallagher et al., 2012; Kozik, 1975; Kozik and Noerager, 1976; Sten et al., 2010).

The effects of dynamic tension variations acting on the TTR based on these two approaches were identified. The tension variations are important in the tensioner fatigue issue (Trent, 2012) and sometimes can potentially be underestimated if only using the conventional *parametric* formulation (Gallagher et al., 2012). Finally, the incorporation of MR dampers into the TTR tensioning system has demonstrated its effectiveness in the reduction of TTR's tension variations.

5.2 Riser Tensioner

There are three most common types of tensioner systems in the offshore industry, as illustrated in Fig. 5.2. The *wire-rope* type had once been popular for decades in the offshore field developments. However, due to the complexity and limited payload ability of the wire-rope type system, the hydro-pneumatic (HP) types have become predominant in the more recent offshore field developments. The direct-acting (DAT, pull-style) tensioner and ram-style (push-style) tensioner can be categorized as the hydro-pneumatic (HP) tensioner.

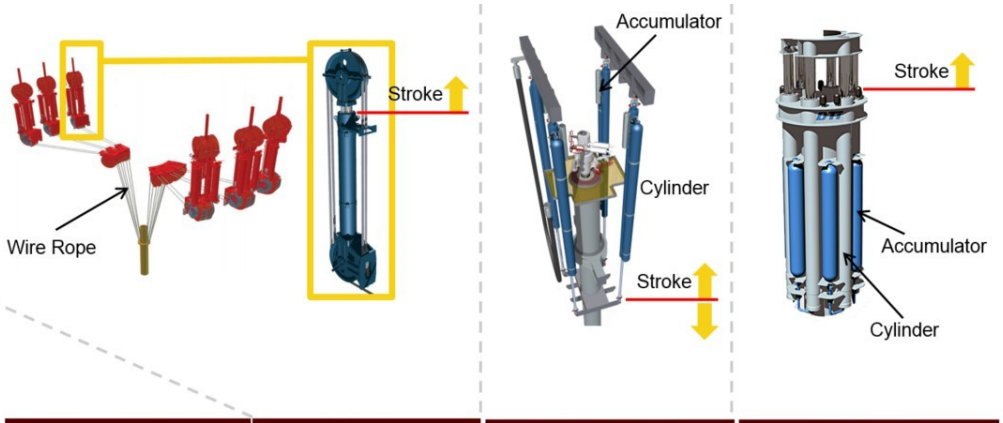

Type of Tensioner	Wire-Rope	Direct Acting (Pull-Style)	Ram-Style (Push-Style)
Load Range	250 kips (~1,100 kN)	2000 kips (~8,900 kN)	2000 kips (~8,900 kN)
Max. Allowable Pressure	3500 psi (~240 bar)	3500 psi (~240 bar)	3500 psi (~240 bar)
Stroke Limits	-	6 to 35-foot (1.8 – 10.7 m)	20 to 40-foot (6.1 – 12.2 m)

* Data from DTI ,LLC

Figure 5.2 The types of riser tensioner (Courtesy of DTI, LLC, USA).

The DAT riser tensioner system is illustrated in Fig. 5.3. The tensioner cylinders are symmetrically mounted under the well deck and angled inboard to riser attachment points on a tensioner ring. The surface production tree or flow control device at the top of the riser on a host floating platform can be mounted closer to the tensioning point of the riser so that the well spacing inside the platform can be reduced. This reduces the bending loads induced in the portion of the riser above the tension point from the dynamic motions of the surface production equipment. Generally, the direct-acting tensioners (DATs) are designed for relatively short strokes and therefore this system is predominately utilized in tension-leg platform (TLP) due to the low heave characteristics of the hull, combined with the relatively small riser length changes associated with small

heave motion and set down due to the parallelogram arrangement formed by the platform, tendons, risers, and the seafloor well pattern (Crotwell and Yu, 2011).

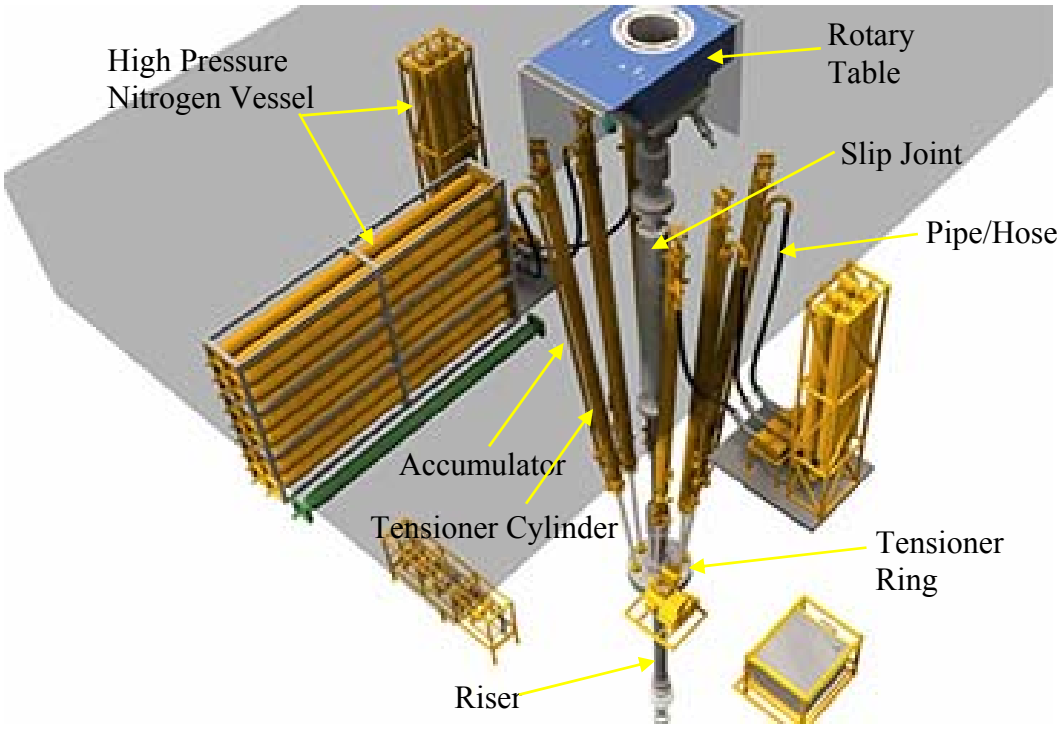

Figure 5.3 The riser tensioner system (Courtesy of National Oilwell Varco, USA).

On the other hand, the ram-style (push style) tensioners with long stroke are to be considered in the newly developed dry-tree Semi-submersible (DTS) concepts (Xiang et al., 2014). There is noteworthy that the discussion of the hydro-pneumatic system of a DAT tensioner can be generalized to the ram-style tensioner as well for the reason that both of these two systems are developed from an identical hydro-pneumatic principle. The main component is the tensioner cylinder that generates a pulling force (or pushing

force in ram-style) on the tensioner ring. The pulling force (or pushing force) is generated by a hydro-pneumatic pressure in a closed volume. The cylinder of each tensioner is fluidly coupled, at its lower end (piston rod side) to a hydraulic fluid reservoir pressurized by a high pressure hydro-pneumatic accumulator, as illustrated in Fig. 5.3. The top manifold is for pressurized nitrogen connected to the low pressure nitrogen pressure vessels (NPVs) (Sten et al., 2010). On the other end, a gas (such as nitrogen or dry air) at relatively high pressure is applied from the high pressure hydro-pneumatic accumulator to hydraulic fluid in the cylinder rod-side chamber, driving the hydraulic fluid to push the piston upwardly in the cylinder to retract the rod, thus pulling up the slip joint through the tensioner ring and, in turn, tensioning the riser (Crotwell and Yu, 2011).

The schematic diagram of hydro-pneumatic (HP) components is shown in Fig. 5.4 for a DAT system. There is noteworthy that the discussion of the hydro-pneumatic system of a DAT tensioner can be directly generalized to the ram-style tensioner for the reason that both of these two systems are developed from an exact basic hydro-pneumatic principle. The main component is the tensioner cylinder that generates a pulling force on the tensioner ring. The pulling force (or pushing force in the case of ram-style tensioner) is generated by a hydro-pneumatic pressure in a closed volume. The cylinder of each tensioner is fluidly coupled, at its lower end (piston rod side) to a hydraulic fluid reservoir pressurized by a high pressure hydro-pneumatic accumulator. The top manifold is for pressurized nitrogen connected to the low pressure nitrogen pressure vessels (NPVs) (Sten et al., 2010). On the other end, a gas (such as nitrogen or

dry air) at relatively high pressure is applied from the high pressure hydro-pneumatic accumulator to hydraulic fluid in the cylinder rod-side chamber, driving the hydraulic fluid to push the piston upwardly in the cylinder to retract the rod, thus pulling up the slip joint through the tensioner ring and, in turn, tensioning the riser (Crotwell and Yu, 2011). The stroke for these cylinders needs to be sufficiently long and the volume of high pressure NPVs must be sufficiently large in order to provide nearly constant riser tension and compensate for relative motions between the platform and the upper riser end (Sten et al., 2010).

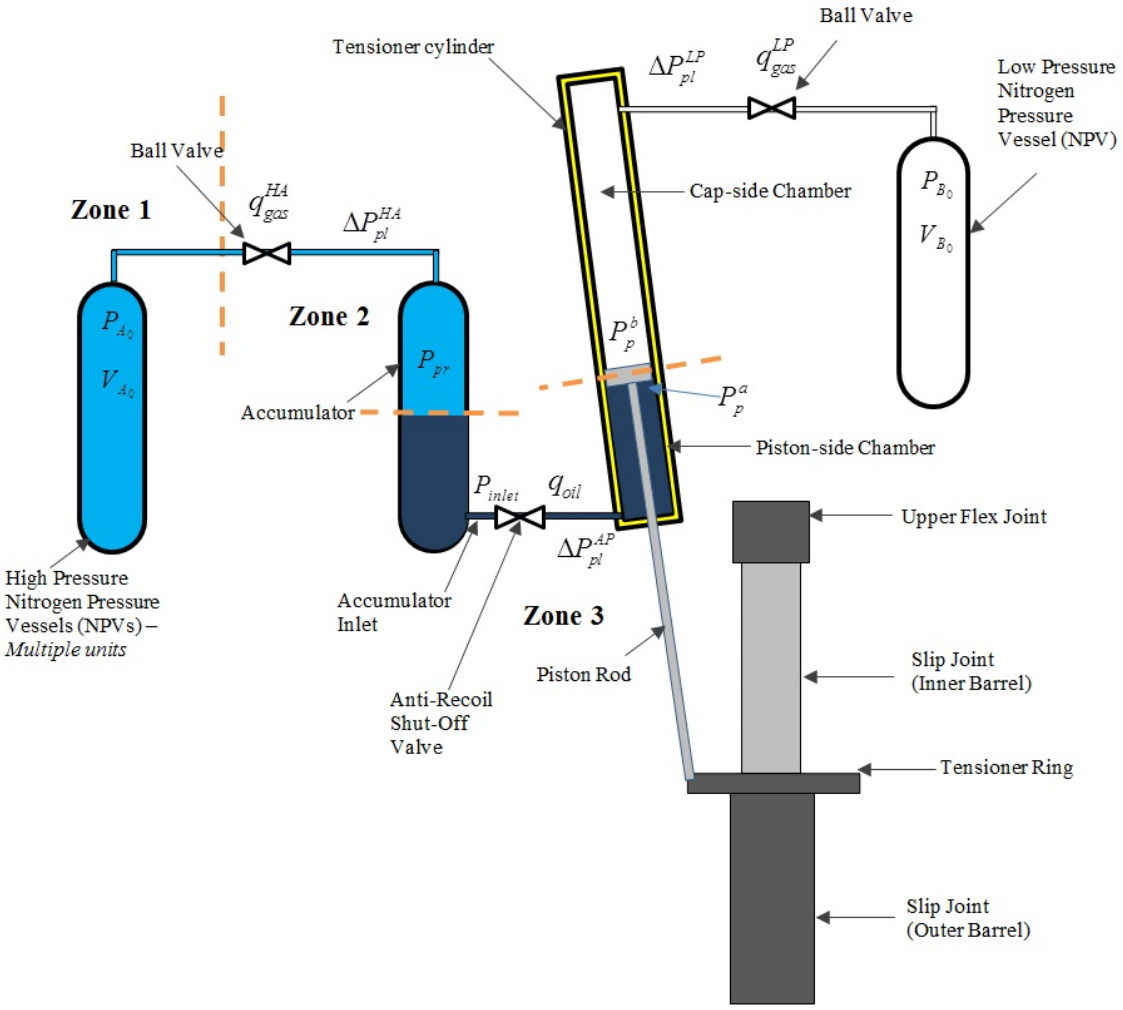

Figure 5.4 The schematic diagram of direct-acting tensioner (DAT) system.

(5.0)

5.3 Formulation of Riser Tension Variations

The high pressure vessels (NPVs), as illustrated in Fig. 5.4, are designed to give the hydraulic cylinder a *nearly constant* force at the required pressure setting. The pressure variations can have a range from few bars to over 100 bars (*1450.38 psi*) (Grønevik, 2013). The relative motion between the floating platform and the riser causes the extension and retraction of the tensioner piston rod. The inflow of hydraulic fluid from the accumulator to the tensioner cylinder causes retraction (up-stroke motion) of the piston rod and therefore exerted pulling force on the tensioner ring. The outflow of hydraulic fluid from the tensioner cylinder to the accumulator during the extension (down-stroke motion) of cylinder exerted large nonlinear air spring force caused by the compression of the air volume in the accumulator and pressure vessels. Due to the large dimensions of the tensioner system, the retracting and extending motion of tensioner cylinder involves large volumes of hydraulic oil flow. Therefore, having large volumes of compressed nitrogen in the pressure vessels will reduce the pressure variations (Sten et al., 2010).

5.3.1 Zone 1: Pressure Variation in the Nitrogen Pressure Vessel (NPV)

The *high*-pressure nitrogen pressure vessels (NPVs) are connected, by using pipes and hoses, to the accumulator under a constant preload pressure P_{A_0} controlled by the nitrogen compressor as shown in **Zone 1** in Fig. 5.4. The ball valves connected on these gas conduits are assumed to be kept open during normal operation to maintain small tension variations (Grønevik, 2013). The total gas volume in the boundary from

the NPV to the gas domain inside the accumulator is regarded as single volume V_{A_0} and the variation of gas volume change is represented by the volume ratio of $\Delta V_A / V_{A_0}$.

The local pressure variation in the high pressure NPV is a function of riser stroke length and that can be calculated when the internal area and initial pressure P_{A_0} at the equilibrium mid-position are known. The upstroke/down-stroke motion of the tensioner rod gives a change of volume in the oil/nitrogen accumulator and NPV. This change of volume ΔV_A is assumed as an adiabatic process (without the change of heat in between the system and its environment) (Grønevik, 2013). The pressure variation ΔP_A in the high pressure gas domain (from NPV to accumulator) due to the variation of gas volume can be represented as (Kozik, 1975):

$$\Delta P_A = P_{A_0}\left(\frac{1}{\left(1-\Delta V_A / V_{A_0}\right)^{\gamma}} - 1\right) \tag{5.1}$$

where P_{A_0} is the initial pressure in the high pressure NPV and γ is adiabatic gas constant, which is 1.4 for adiabatic process (Li et al., 2013) of nitrogen at 15°C. The decrement of volume $-\Delta V_A$ (compression of high pressure NPV gas domain during downstroke motion) leads to the increment of pressure variation ΔP_A in the high pressure NPV (gas bank). the details derivation from the *first law* of thermodynamics of ideal gas can be refered to Appendix C.

5.3.2 Zone 2: Pressure Variations from NPV to Accumulator

The *high*-pressure nitrogen pressure vessels (NPVs) are located at a certain distance away from the accumulator on the production / drilling deck (30-feet (*9.144 m*), for instance (Sten et al., 2010)) and to be connected in gas flow connection through the pipes and valves. The frictional losses ΔP_{pl}^{HA} , as illustrated in Fig. 5.4, can be occurred as fluid (nitrogen in this case) moves through the pipes and conduits at a flow rate q_{gas}^{HA} and lead to the variations in pressure applied by the tensioner system. The pressure variations caused by the flow friction in the pipes and conduits is modeled by using Darcy-Weisbach equation (Manring, 2005). This model is derived with the assumptions that the fluid/gas flow is fully developed along the pipe length and the effects due to the fluid/gas inertia and fluid/gas compressibility are not taken into account, which implies that features such as *water hammer* and the end effects of piping are not considered in this steady state fluid momentum conditions (Mathworks, 2009). In order to account for local resistances, such as bends, fittings, inlet and outlet losses, and so on, all the resistances are converted into their equivalent lengths L_{eq}^{HA}, and then the total length of all the resistances is added to the pipe geometrical length L^{HA}. Therefore, the flow pressure losses ΔP_{pl}^{HA} attributed by the pipes friction, according to Darcy-Weisbach equation, are defined as:

$$\Delta P_{pl}^{HA} = \frac{\rho_{gas} f^{HA}}{2A_{HA}^2}\left(\frac{L^{HA} + L_{eq}^{HA}}{D_{HA}}\right) q_{gas}^{HA} \cdot \left|q_{gas}^{HA}\right| \tag{5.2}$$

where ρ_{gas} is the density of gas, while f^{HA}, A_{HA}, and D_{HA} are the friction factor, cross sectional area, and diameter of the pipe from high pressure NPV (superscript H) to accumulator (superscript A), respectively.

Pressure losses due to friction are proportional to the flow regime-dependable friction factor f^{HA} and the square of the flow rate q_{gas}^{HA}. The friction factor f^{HA} in Eqn. (5.2) can be calculated based on Moody diagram by using the Haaland's approximation (Haaland, 1983; Mathworks, 2009) as shown in the following expression:

$$f^{HA} = \begin{cases} K_S / \mathrm{Re} & \text{for} \quad \mathrm{Re} \le \mathrm{Re}_L \\ f_L + \dfrac{f_T - f_L}{\mathrm{Re}_T - \mathrm{Re}_L}\left(\mathrm{Re} - \mathrm{Re}_L\right) & \text{for} \quad \mathrm{Re}_L < \mathrm{Re} < \mathrm{Re}_T \\ \left\{-1.8 \log_{10}\left(\dfrac{6.9}{\mathrm{Re}} + \left(\dfrac{r_{hHA}}{3.7 D_{HA}}\right)^{1.11}\right)\right\}^{-2} & \text{for} \quad \mathrm{Re} \ge \mathrm{Re}_T \end{cases} \tag{5.3}$$

$$\mathrm{Re} = \frac{q_{gas}^{HA} \cdot D_{HA}}{A_{HA} \nu_{gas}} \tag{5.4}$$

where K_S is the shape factor that characterizes the pipe cross section, Re is the Reynolds number, f_L and f_T are friction factor at laminar border and turbulent border, respectively, Re_L and Re_T are maximum Reynolds number at laminar flow and turbulent flow, respectively, r_{hHA} is the height of the internal surface roughness on the pipe from high pressure NPV (subscript H) to accumulator (subscript A), and ν_{gas} is the kinematic viscosity of gas. Note that the ball valves on the conduits from high pressure NPVs to

accumulator in this study are assumed to be initially fully opened and have the same flow diameter with the pipes in connection during the normal operation.

The *preload pressure* in the accumulator P_{pr} after considered as the total effects of the pressure variation ΔP_A in high pressure NPV and the pressure losses ΔP_{pl}^{HA} due to pipeline and valve flow friction, as represented from the combination of Eqns. (5.1) and (5.2) is stated as:

$$P_{pr} = P_{A_0} + \Delta P_A + \Delta P_{pl}^{HA} \tag{5.5}$$

$$P_{pr} = P_{A_0}\left(\frac{1}{\left(1-\Delta V_A/V_{A_0}\right)^{\gamma}}\right) + \frac{\rho_{gas} f^{HA}}{2A_{HA}^2}\left(\frac{L^{HA}+L_{eq}^{HA}}{D_{HA}}\right) q_{gas}^{HA}\cdot\left|q_{gas}^{HA}\right| \tag{5.6}$$

5.3.3 Zone 3: Pressure Variation from Accumulator to the Piston

In the hydro-pneumatic tensioner system, the accumulator consists of a pre-charged gas domain (connected to the high pressure NPVs) and a fluid domain (connected to the hydraulic part in the tensioner cylinder), as illustrated in Fig. 5.4. If the hydraulic fluid pressure at the accumulator inlet P_{inlet} becomes higher than the preload pressure P_{pr}, which is acting on the gas-oil interface boundary, the hydraulic oil is going to enter the accumulator chamber and compress the gas domain, thus storing hydro-pneumatic energy. On the other hand, a drop in the inlet fluid pressure P_{inlet} during riser up-stroke motion is going to restore the hydraulic oil back into the tensioner cylinder. The flow rate of hydraulic oil q_{oil} flows in / out the accumulator is calculated by using the volumetric of fluid changes induced by the motion of tensioner piston. Note that the

shut-off valve on the conduit from the accumulator to the tensioner cylinder in this study are assumed to be initially fully opened and has the same passage diameter with the pipes in connection during the normal operation. Therefore, the pressure P_p^a at the piston-side chamber after considered the pressure variation in high pressure NPV, pressure variation from high pressure NPV to accumulator ΔP_{pl}^{HA}, and pressure losses ΔP_{pl}^{AP} due to pipes friction and valve flow friction can be represented as:

$$P_p^a = P_{pr} + \Delta P_{pl}^{AP} \tag{5.7}$$

$$P_p^a = P_{A_0} + \Delta P_A + \Delta P_{pl}^{HA} + \Delta P_{pl}^{AP} \tag{5.8}$$

$$P_p^a = P_{A_0}\left(\frac{1}{\left(1-\Delta V_A/V_{A_0}\right)^{\gamma}}\right) + \frac{\rho_{gas} f^{HA}}{2A_{HA}^2}\left(\frac{L^{HA}+L_{eq}^{HA}}{D_{HA}}\right) q_{gas}^{HA}\cdot\left|q_{gas}^{HA}\right| + \frac{\rho_{oil} f^{AP}}{2A_{AP}^2}\left(\frac{L^{AP}+L_{eq}^{AP}}{D_{AP}}\right) q_{oil}\cdot\left|q_{oil}\right| \tag{5.9}$$

where ρ_{oil} is the density of hydraulic oil, q_{oil} is the flow rate of hydraulic oil , f^{AP}, A_{AP}, and D_{AP} are the friction factor, cross sectional area, and diameter of the pipe from the accumulator (superscript A) to the tensioner piston (superscript P), respectively. The method to calculate the oil friction factor f^{AP} is same with finding the gas friction factor f^{HA} in the Eqn. (5.3), by modifying the Reynold number in Eqn. (5.4) to the corresponding hydraulic oil inputs.

In general, the pressure loss ΔP_{pl}^{HA} due to the friction of gas is around three orders of magnitudes smaller than the liquid ΔP_{pl}^{AP}, in the case of nitrogen/oil, due to the

density of the fluid (Van de Ven and Li, 2009). Hence, the Eqn. (5.9) can be simplified, under a reasonable level of accuracy, into:

$$P_p^a \approx P_{A_0}\left(\frac{1}{\left(1-\Delta V_A/V_{A_0}\right)^{\gamma}}\right)+\frac{\rho_{oil} f^{AP}}{2A_{AP}^2}\left(\frac{L^{AP}+L_{eq}^{AP}}{D_{AP}}\right)q_{oil}\cdot|q_{oil}| \tag{5.10}$$

The industrial practices normally assumed that the fictional losses of hydraulic oil in between the accumulator and the tensioner cylinder, which is the second term of the right hand side of Eqn. (5.10), to be neglected (Yang, 2009). Therefore, the Eqn. (5.10) is further approximated, as the *parametric* formulation, into:

$$P_p^a \approx P_{A_0}\left(\frac{1}{\left(1-\Delta V_A/V_{A_0}\right)^{\gamma}}\right) \tag{5.11}$$

The pressure at the piston-side chamber P_p^a is highly dependable with respect to the ratio of volume change in the gas domain $\Delta V_A/V_{A_0}$. The Eqn. (5.11) can be rewritten into the form of tension force T exerted from the tensioner cylinder piston as in the following equation (Yang, 2009) (refer to Appendix C):

$$T = T_0\left(1-\frac{\Delta z}{z_0}\right)^{-\gamma} \tag{5.12}$$

where T_0 is the pretension of tensioner, z_0 is the *equivalent* length of cylinder (which is the ratio of *total fluid volume* to *cylinder piston-side cross-sectional area*). The Δz is the change of platform-riser relative displacement, which is defined as the counterpart of the change of riser stroke, as:

$$\Delta z = -\Delta S_Z \tag{5.13}$$

and the stroke S_Z of tensioner is defined from Eqn. (2.153) as:

$$S_Z = -\left(X_i + p_i + \theta_j C_{ji} - r_i \right) \tag{5.14}$$

where,

Down-stroke motion: $-S_z = \left(X_i + p_i + \theta_j C_{ji} - r_i \right)$ (5.15)

Up-stroke motion: $+S_z = -\left(X_i + p_i + \theta_j C_{ji} - r_i \right)$ (5.16)

which is assumed that the downstroke motion leads to the *compression* of gas and hydraulic oil domain in the high-pressure NPVs and accumulator, and upstroke motion leads to the *extension* of this domain.

The *parametric* formulation (as stated in Eqns. (5.11) and (5.12)) is reasonable if the length of connection pipes L^{AP} is *sufficiently* short (Trent, 2012) or the relative velocity of the riser in the heave direction is sufficiently small, such as in the case of connecting to the TLP host platform. However, it is noteworthy that the hydraulic pressure losses ΔP_{pl}^{AP} through the pipes in between the accumulator and the piston in the second term of RHS of the Eqn. (5.10) must be evaluated if the velocity of riser stroke is *sufficiently* large, such as under the operations of drillship, *dry-tree* semi-submersible, and during the anti-recoiling and disconnection of TTR.

Finally, if the fluid compressibility and leakages inside the tensioner cylinder are assumed to be negligible, the equation of force equilibrium on the both side of tensioner piston F_{ten} in the hydraulic cylinder, from Fig. 5.4, can be represented as:

$$F_{ten} = A_p^a \cdot P_p^a - A_p^b \cdot P_p^b + F_{HS} \tag{5.17}$$

$$\begin{aligned} F_{ten} = {} & A_p^a \cdot P_{A_0} \left(\frac{1}{\left(1 - \Delta V_A / V_{A_0}\right)^{\gamma}} \right) + A_p^a \cdot \frac{\rho_{oil} f^{AP}}{2A_{AP}^2} \left(\frac{L^{AP} + L_{eq}^{AP}}{D_{AP}} \right) q_{oil} \cdot \left| q_{oil} \right| \\ & - A_p^b \cdot P_{B_0} \left(\frac{1}{\left(1 - \Delta V_B / V_{B_0}\right)^{\gamma}} \right) - A_p^b \cdot \frac{\rho_{gas} f^{LP}}{2A_{LP}^2} \left(\frac{L^{LP} + L_{eq}^{LP}}{D_{LP}} \right) q_{gas}^{LP} \cdot \left| q_{gas}^{LP} \right| + F_{HS} \end{aligned} \tag{5.18}$$

After considered the reciprocal relationship of the stroke on the both sides of the piston, where the *stroke-in* to the piston-side is equal to the *stroke-out* from the cap-side, and *vice versa*, the Eqn. (5.18) can be rewritten as:

$$\begin{aligned} F_{ten} = {} & A_p^a \cdot P_{A_0} \left(\frac{1}{\left(1 - \Delta V_A^{(S+)} / V_{A_0}\right)^{\gamma}} \right) + A_p^a \cdot \frac{\rho_{oil} f^{AP}}{2A_{AP}^2} \left(\frac{L^{AP} + L_{eq}^{AP}}{D_{AP}} \right) q_{oil}^{(S+)} \cdot \left| q_{oil}^{(S+)} \right| \\ & - \left\{ A_p^b \cdot P_{B_0} \left(\frac{1}{\left(1 - \Delta V_B^{(S-)} / V_{B_0}\right)^{\gamma}} \right) + A_p^b \cdot \frac{\rho_{gas} f^{LP}}{2A_{LP}^2} \left(\frac{L^{LP} + L_{eq}^{LP}}{D_{LP}} \right) q_{gas}^{LP(S-)} \cdot \left| q_{gas}^{LP(S-)} \right| \right\} \\ & + F_{HS} \end{aligned} \tag{5.19}$$

where the superscript $(S+)$ and $(S-)$ denote the both strokes of opposite directions. The Eqn. (5.19) is further rearranged in the same direction of stroke $(S+)$, as:

$$\begin{aligned} F_{ten} = {} & F_{HP_0}^a \left(1 - \frac{\Delta z}{z_{A0}} \right)^{-\gamma} + A_p^a \cdot \frac{\rho_{oil} f^{AP}}{2A_{AP}^2} \left(\frac{L^{AP} + L_{eq}^{AP}}{D_{AP}} \right) q_{oil} \cdot \left| q_{oil} \right| \\ & - F_{HP_0}^b \left(1 + \frac{\Delta z}{z_{B0}} \right)^{-\gamma} + A_p^b \cdot \frac{\rho_{gas} f^{LP}}{2A_{LP}^2} \left(\frac{L^{LP} + L_{eq}^{LP}}{D_{LP}} \right) q_{gas}^{LP} \cdot \left| q_{gas}^{LP} \right| + F_{HS} \end{aligned} \tag{5.20}$$

where z_{A0} and z_{B0} are the *equivalent* length of tensioner in piston-side and cap-side, respectively, $F_{HP_0}^a$ and $F_{HP_0}^b$ are the initial forces acting on the piston at the piston-side and cap-side, respectively, A_p^a and A_p^b are the cross sectional area of the piston at the

rod-side and cap-side, respectively, A_{LP} and D_{LP} are the cross sectional area and diameter of the pipe, respectively, from the tensioner piston (subscript P) to the low pressure NPV (subscript L). The F_{HS} is the hard-stop force when the piston is approaching very close to the upper/lower limits of the cylinder length, which can be modeled as a cubic spring force (Yang, 2009),

$$F_{HS} = \begin{cases} F_{csp} & \text{for} \quad z \geq z_{upper} \\ 0 & \text{for} \quad z_{lower} < z < z_{upper} \\ F_{csp} & \text{for} \quad z \leq z_{lower} \end{cases} \tag{5.21}$$

where F_{csp} is the cubic spring force, and the z_{upper} and z_{lower} denote the upper and lower limits of the cylinder length, respectively.

Since the density of nitrogen is around three orders of magnitudes smaller than the hydraulic oil (Van de Ven and Li, 2009), the pressure losses due to the friction of gas can be neglected in the Eqn. (5.20) under a reasonable level of accuracy:

$$F_{ten} \approx F^a_{HP_0}\left(1-\frac{\Delta z}{z_{A0}}\right)^{-\gamma} + A^a_p \cdot \frac{\rho_{oil} f^{AP}}{2A^2_{AP}}\left(\frac{L^{AP}+L^{AP}_{eq}}{D_{AP}}\right) q_{oil}\cdot|q_{oil}| - F^b_{HP_0}\left(1+\frac{\Delta z}{z_{B0}}\right)^{-\gamma} + F_{HS} \tag{5.22}$$

There is noteworthy that the third term in the RHS of Eqn. (5.22) is normally acting as an air spring for the up-stroke motion and, in general, the $F^b_{HP_0}$ which is connected to the low-pressure NPV is much smaller than the $F^a_{HP_0}$.

5.4 Simulation of Dynamic Pressure/Tension Variations

In order to identify the deviations in between the *parametric* formulation (Eqn. (5.11) and Eqn. (5.12)) and *component-level* formulation (Eqn. (5.10) and Eqn. (5.22)) in

the analysis of TTR axial tension, the effects of dynamic pressure / tension variations on a numerical model of HP tensioner, as illustrated in Fig. 5.4, were simulated in this Subsection under the following two settings:

(i) a conventional nonlinear hydro-pneumatic (HP) tensioner was simulated under a preset dynamic displacement Δz and velocity inputs (Fig. 5.6);

(ii) the length of hydraulic pipe is varied in order to simulate the pressure variations attributed by the frictional fluid effects (Figs. 5.7~5.9);

The simulation was conducted by using the Simulink software package (Mathworks, 2009). The dimensions and data of the HP tensioner in this simulation are tabulated in Table 5.1.

Table 5.1 Hydraulic-pneumatic tensioner data (Sten et al., 2010).

Pressure at LNPV	10 bar *(145.0 psi)*
Volume of LNPV	4.0 m^3 *(141.3 ft^3)*
Pressure at HNPV	60 bar *(870.2 psi)*
Volume of HNPV	9.0 m^3 *(317.8 ft^3)*
Length of Pipe from LNPV to Cylinder	30.0 m *(98.4 ft)*
Diameter of Pipe from LNPV to Cylinder	0.1 m *(0.328 ft)*
Length of Pipe from HNPV to Accumulator	30.0 m *(98.4 ft)*
Diameter of Pipe from HNPV to Accumulator	0.1 m *(0.328 ft)*
Diameter of Pipe from Accumulator to Cylinder	0.2 m *(0.656 ft)*
Cylinder Inner Diameter	0.560 m *(1.837 ft)*
Piston Rod Diameter	0.230 m *(0.755 ft)*

* Note: LNPV = low pressure nitrogen pressure vessel, HNPV = high pressure nitrogen pressure vessel

The characteristic responses of the hydro-pneumatic (HP) tensioner are shown in Fig. 5.5. The tensioner was excited by a sinusoidal dynamic displacement Δz (from -0.50 m to 4.25 m (*-1.64 ft to 13.94 ft*), positive side is referred to down-stroke motion as indicated in Eqns. (5.13) and (5.15)) and dynamic velocity (from -1.0 m/s to 1.0 m/s (*-3.28 ft/s to 3.28 ft/s*)) in this case. This is noteworthy that the velocity of the HP tensioner piston is normally far below 1.0 m/s (*3.28 ft/s*) when the host platform is the tension-leg platform (TLP). However, the dynamic velocity inputs in this simulation are reasonable for the cases of drillship and *dry-tree* Semi-submersible, in which the

platform heave motion is no longer constrained by the high stiffed tendons, and for the case of instantaneous velocity during the anti-recoiling and TTR disconnection.

The position of piston after taking the overall static loadings into account is at around +2.0 m (*+6.56 ft*) (positive sign is referred to downward direction of tensioner ring from its nominal position, in this case). If the dynamic loadings are included, it can be seen that the piston dynamic displacement and piston velocity are out of phase, with maximum velocity occurring as the piston reaches static equilibrium position, as matched with the findings of Sten *et al.* (2010). The pressure in the piston-side chamber, based on Eqn. (5.9), has the phase in between the piston displacement and piston velocity.

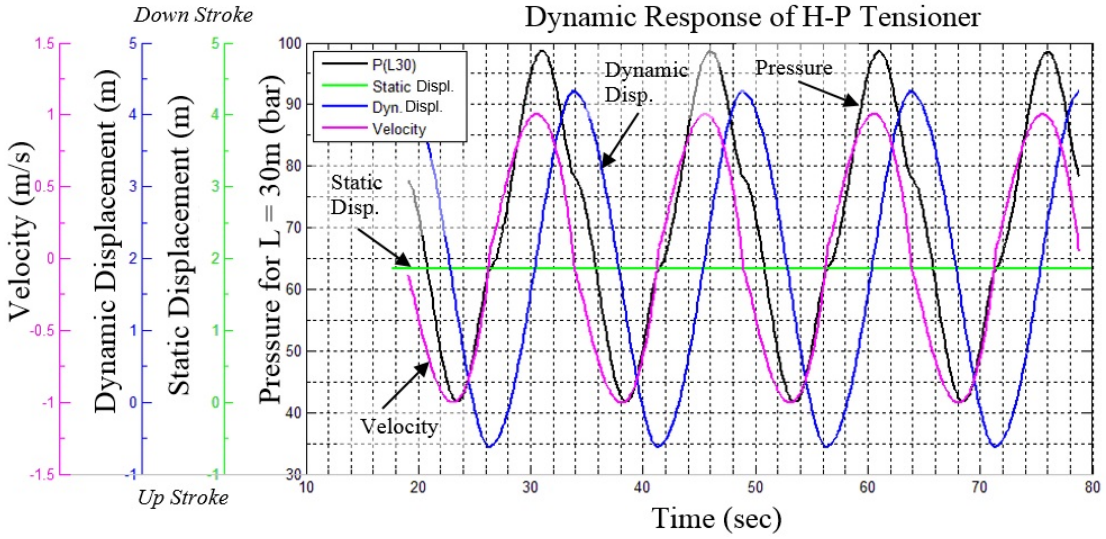

Figure 5.5 Dynamic response of HP tensioner.

The effects on the pressure variations in tensioner cylinder due to the fictional losses in the pipe are shown in Fig. 5.6. The contribution of frictional losses to the pressure variations is stated by the second term of the right hand side of Eqn. (5.10). It can be found that the effects of friction for the 30 m (*98.43 ft*) length L^{AP} *long* pipe is significant compared to the one with 3 m (*9.84 ft*) *short* length L^{AP} pipe. The percentage of dynamic pressure variation for *long* pipe is ~43% while the pressure variations for the *short* pipe is ~11%, with respect to the mean pressure. It can be found that the dynamic pressure (and tension) variation is very sensitive to the length of hydraulic fluid pipe. Therefore, in order to reduce dynamic tension variation, the hydraulic pipe must be designed **as short as possible**, which means that the location of the accumulator and the tensioner cylinder is recommended to be as close as possible.

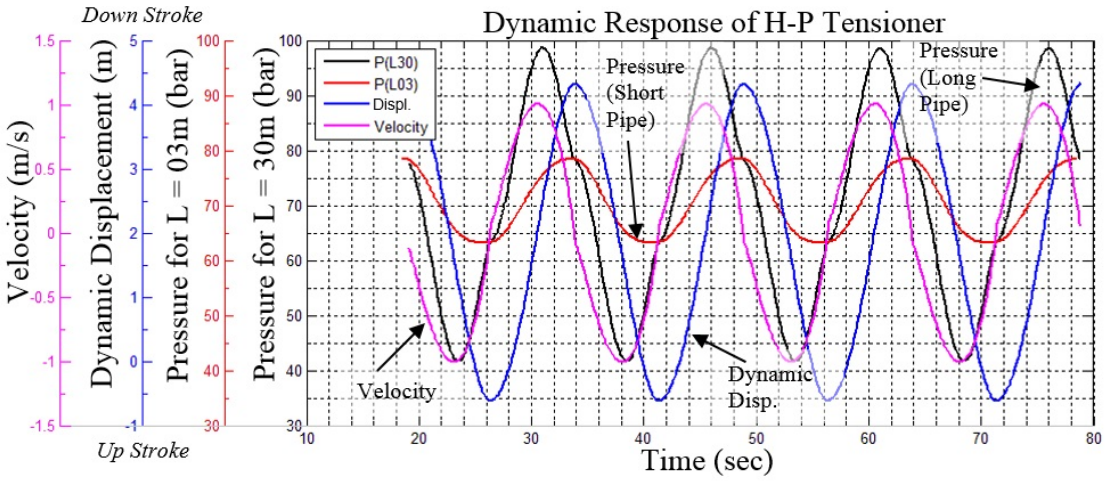

Figure 5.6 Pressure variations due to the fictional losses in the pipe.

The validity and accuracy of the *parametric* formulation of HP tensioner, as stated in Eqn. (5.11) (Yang, 2009; Yang and Kim, 2010), is analyzed and shown in Fig. 5.7. The pressure variations of the 3 m (*9.84 ft*) *short* pipe is compared with the case that the fictional losses of hydraulic oil in between the accumulator and the tensioner cylinder ΔP_{pl}^{AP} to be neglected. It can be found that the simplified *parametric* formulation is **conditionally valid** if the length of connection pipes L^{AP} is sufficiently short (3 m to 0 m (*9.84 ft to 0 ft*)), even though the dynamic velocity is large (~-1.0 m/s to 1.0 m/s (*-3.28 ft/s to 3.28 ft/s*)). Therefore, this is noteworthy that the accuracy of the *parametric* formulation (Eqn. (5.11)), which is a popular riser tension analysis method in the industry, is very dependent on the physical length of the hydraulic pipe L^{AP} of the HP tensioner system. The excessive dynamic tension variation is potentially to be underestimated if the HP tensioner is built with long hydraulic conduits and very long stroke.

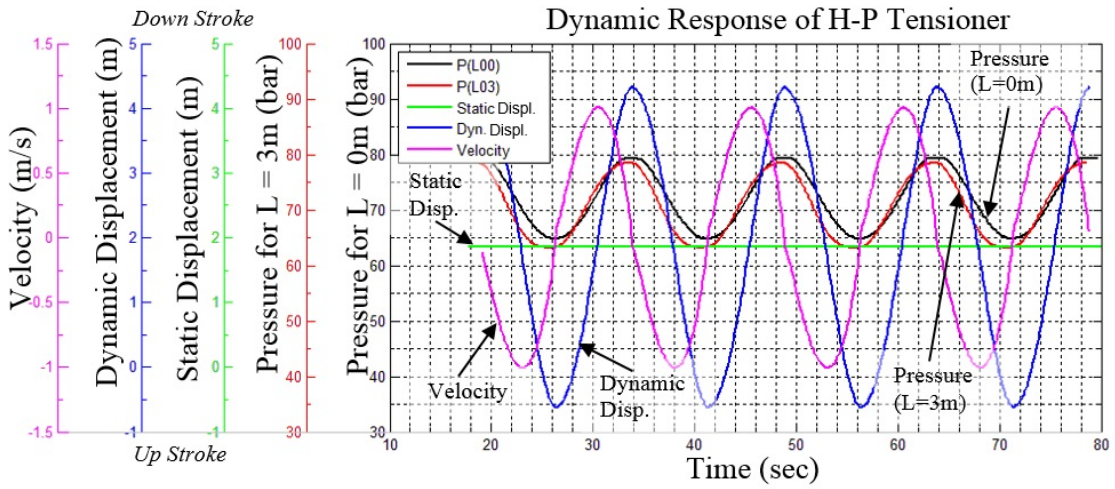

Figure 5.7 Pressure variation due to the frictional pipe length.

The *pressure-displacement* and *pressure-velocity* plot with respect to the different lengths of pipes caused by the effects of fluid friction are shown in Fig. 5.8. It is apparent that the pressure is a function not only of piston displacement but also of the the piston velocity. Throughout the loops (in the clock-wise direction) the pressure is greater when the extension of tensioner cylinder (positive sign is referred to down-stroke motion in this case). The variations of hysteresis are smallest at the displacement amplitude points (at ~-0.50 m (*~-1.64 ft*) and ~4.25 m (*~13.94 ft*), respectively, in this case) and is most pronounced at the static equilibrium point (which is at around +2.0 m (*+6.56 ft*), in this case). It is noteworthy that the pressure variation is very dependable to the frictional length of pipe conduits. If the length of hydraulic flow pipe is sufficiently short and can be neglected (L^{AP} = 0 m (*0 ft*)), as expressed in Eqn. (5.11), the *pressure-displacement* loop is reduced to a *curve* line (the *blue* line in Fig. 5.8), which normally represents the HP tensioner characteristics in the industrial manufacturer manuals.

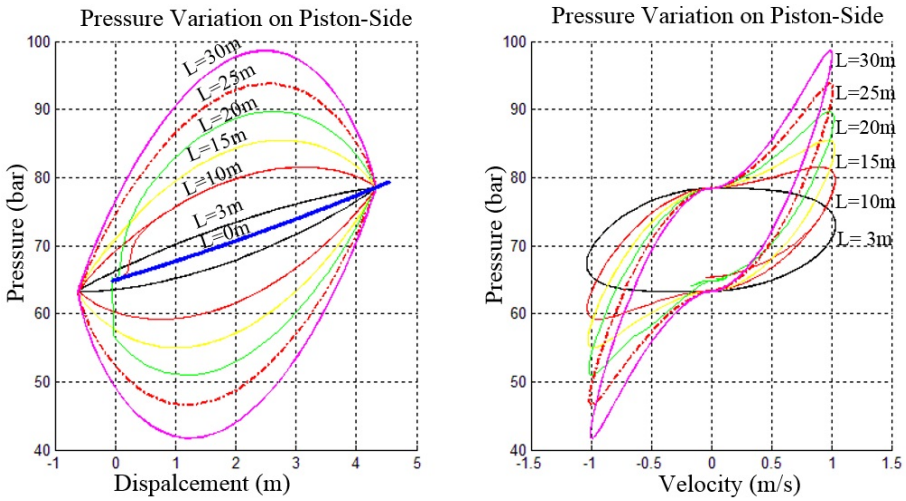

Figure 5.8 Pressure variation in the piston-side chamber, positive displacement is referred to down-stroke motion in this case.

5.5 Finite Element Coupling of Hydro-Pneumatic Tensioner, Platform, and Riser after Considered the Dynamic Tension Variation

In this Subsection, the finite element modeling of the dynamic tension variation is considered into the connection between the risers, hydro-pneumatic (HP) tensioner, and the platform. Recalling from the Eqn. (5.10) and Fig. 5.4, the pressure at the piston-side chamber P_p^a after considered the pressure variation in high pressure NPV, accumulator, and pressure losses due to pipes friction and valve flow friction can be represented, under a reasonable level of accuracy, as:

$$P_p^a = P_{A_0}\left(\frac{1}{\left(1-\Delta V_A/V_{A_0}\right)^{\gamma}}\right)+\frac{\rho_{oil} f^{AP}}{2A_{AP}^2}\left(\frac{L^{AP}+L_{eq}^{AP}}{D_{AP}}\right)q_{oil}\cdot|q_{oil}| \tag{5.10}$$

By assuming the air-spring reaction force on the cap-side is much smaller than the pulling force from the piston-side (this assumption is reasonable when the low-

pressure NPV is much lower pressurized than the high-pressure NPVs), hence, the tension F_{HP} generated by the hydro-pneumatic tensioner (HPT) can be approximated from Eqn. (5.22) as:

$$F_{HP} \approx A_a \cdot P_p^a = A_a \cdot P_{A_0} \left(\frac{1}{\left(1 - \Delta V_A / V_{A_0}\right)^{\gamma}} \right) + A_a \cdot \frac{\rho_{oil} f^{AP}}{2 A_{AP}^2} \left(\frac{L^{AP} + L_{eq}^{AP}}{D_{AP}} \right) q_{oil} \cdot \left| q_{oil} \right| \tag{5.23}$$

$$F_{HP} = F_{HP_0} \left(1 - \frac{\Delta z}{z_0} \right)^{-\gamma} + A_a \cdot \frac{\rho_{oil} f^{AP}}{2} \left(\frac{L^{AP} + L_{eq}^{AP}}{D_{AP}} \right) v_{AP} \cdot \left| v_{AP} \right| \tag{5.24}$$

where the v_{AP} is the fluid velocity in the HPT connector pipe, and

$$v_{AP} \cdot \left| v_{AP} \right| = v_Z \left| v_Z \right| \cdot \left(\frac{A_a}{A_{Ap}} \right)^2 \tag{5.25}$$

where v_Z is the velocity of piston in the HPT cylinder, by considering the Eqn. (5.13) and Eqn. (5.15), which is equal to the first-order time-derivative of the platform-riser relative displacement, $\left(X_i + p_i + \theta_j C_{ji} - r_i \right)$ as the combined effects of the host platform motion and riser tension ring motion, and it is represented as $\left(\dot{X}_i + \dot{\theta}_j C_{ji} - \dot{r}_i \right)$. Hence, the Eqn. (5.24) can be stated as:

$$\begin{aligned} F_{HP} = {} & F_{HP_0} \left(1 - \frac{\Delta \left(X_i + p_i + \theta_j C_{ji} - r_i \right)}{z_0} \right)^{-\gamma} \\ & + A_a \cdot \left(\frac{A_a}{A_{Ap}} \right)^2 \cdot \frac{\rho_{oil} f^{AP}}{2} \left(\frac{L^{AP} + L_{eq}^{AP}}{D_{AP}} \right) \left(\dot{X}_i + \dot{\theta}_j C_{ji} - \dot{r}_i \right) \cdot \left| \left(\dot{X}_i + \dot{\theta}_j C_{ji} - \dot{r}_i \right) \right| \end{aligned} \tag{5.26}$$

The tensioner force F_{HP} can be further divided into the *static* component $F_{HP_{static}}$ and *dynamic* component $F_{HP_{dyn}}$, respectively:

$$F_{HP} = F_{HP_{static}} + F_{HP_{dyn}} \tag{5.27}$$

$$F_{HP_{static}} = F_{HP_0}\left(1 - \frac{\Delta\left(X_i + p_i + \theta_j C_{ji} - r_i\right)}{z_0}\right)^{-\gamma} \tag{5.28}$$

$$F_{HP_{dyn}} = A_a \cdot \left(\frac{A_a}{A_{Ap}}\right)^2 \cdot \frac{\rho_{oil} f^{AP}}{2}\left(\frac{L^{AP} + L_{eq}^{AP}}{D_{AP}}\right)\left(\dot{X}_i + \dot{\theta}_j C_{ji} - \dot{r}_i\right)\cdot\left|\left(\dot{X}_i + \dot{\theta}_j C_{ji} - \dot{r}_i\right)\right| \tag{5.29}$$

The *static* analysis and time domain analysis of *static tension* part $F_{HP_{static}}$ is identical with the derivation of linear spring connector coupling in the Subsection 2.4.5. Once the dynamic part $F_{HP_{dyn}}$ that causes by the frictional effects of the viscous fluid is taken into consideration, the tangential stiffness matrices and total external forcing terms will be modified in the numerical simulation.

In the *time-domain* simulation, the Average Acceleration Method (AAM) (San Andrés, 2008) is used to derive the numerical integration. Since the Eqn. (5.29) is a nonlinear function of the velocity term $\left(\dot{X}_i + \dot{\theta}_j C_{ji} - \dot{r}_i\right)$, the Taylor series expansion of the nonlinear function and *local linearized stiffness* K and *damping coefficients* D must be defined at every time step before being arranged into the forms in Eqns. (3.40) and (3.41). The detailed derivation of AAM for nonlinear function can be refered to Appendix B. The *dynamic tension variation* $F_{HP_{dyn}}$ of HPT is represented by:

$$
\begin{aligned}
F_{HP_{dyn}} &= A_a \cdot \left(\frac{A_a}{A_{Ap}}\right)^2 \frac{\rho_{oil} f^{AP}}{2} \left(\frac{L^{AP} + L_{eq}^{AP}}{D_{AP}}\right) \left(\dot{X}_i + \dot{\theta}_j C_{ji} - \dot{r}_i\right) \cdot \left|\left(\dot{X}_i + \dot{\theta}_j C_{ji} - \dot{r}_i\right)\right| \\
&= A_a \cdot \left(\frac{A_a}{A_{Ap}}\right)^2 \frac{\rho_{oil} f^{AP}}{2} \left(\frac{L^{AP} + L_{eq}^{AP}}{D_{AP}}\right) \left(\dot{X}_i + \dot{\theta}_j C_{ji} - \dot{r}_i\right)^2 \cdot \mathrm{sgn}\left(\dot{X}_i + \dot{\theta}_j C_{ji} - \dot{r}_i\right) \\
&= \alpha_{HP} \beta_{HP} \left(\dot{X}_i + \dot{\theta}_j C_{ji} - \dot{r}_i\right)^2
\end{aligned} \tag{5.30}
$$

where $\alpha_{HP} = A_a \cdot \left(\frac{A_a}{A_{Ap}}\right)^2 \frac{\rho_{oil} f^{AP}}{2}$ and $\beta_{HP} = \left(\frac{L^{AP} + L_{eq}^{AP}}{D_{AP}}\right) \cdot \mathrm{sgn}\left(\dot{X}_i + \dot{\theta}_j C_{ji} - \dot{r}_i\right)$. This is noteworthy that the frictional factor term f^{AP} in α_{HP} is a dependent of the Reynold Number as stated in Eqn. (5.3), in which the Reynold number is defined by the riser velocity $\left(\dot{X}_i + \dot{\theta}_j C_{ji} - \dot{r}_i\right)$ as shown in Eqn. (5.4). In this research, the velocity component in defining the frictional factor term f^{AP} is treated separately from the velocity-square term $\left(\dot{X}_i + \dot{\theta}_j C_{ji} - \dot{r}_i\right)^2$ in the dynamic tension part $F_{HP_{dyn}}$ as stated in Eqn. (5.30). This simplification is reasonable because the riser velocity $\left(\dot{X}_i + \dot{\theta}_j C_{ji} - \dot{r}_i\right)$ in the frictional factor f^{AP} is used in the curve-fitting of the *Moody diagram*, which value is normally not varying significantly in between the two steps of time interval if the time interval is sufficiently small. Moreover, this assumption is compliant with the numerical scheme which has the second-order accuracy.

By using the linear approximation of multivariable Tylor series expansion, the equation for r_i and $\dot{r}_i$ (rod side) is:

$$F_{HP_{dyn}}^{(n+1)} = F_{HP_{dyn}}^{(n)} + \frac{\partial F_{HP_{dyn}}^{(n)}}{\partial \dot{r}_j}\Delta\dot{r}_j + \frac{\partial F_{HP_{dyn}}^{(n)}}{\partial \dot{X}_j}\Delta\dot{X}_j + \frac{\partial F_{HP_{dyn}}^{(n)}}{\partial \dot{\theta}_j}\Delta\dot{\theta}_j + \ldots \tag{5.31}$$

In time-domain analysis, by using Adams-Moulton implicit method, the connector force on the top end of the riser (tension ring) contributed by $F_{HP_{dyn}}^{(n+1)}$ is integration from $t^{(n)}$ to $t^{(n+1)}$ is:

$$\begin{aligned}\int_{t^{(n)}}^{t^{(n+1)}} F_{HP_{dyn}}\,dt &= \frac{\Delta t}{2}\left(F_{HP_{dyn}}^{(n+1)} + F_{HP_{dyn}}^{(n)}\right) \\ &\approx \frac{\Delta t}{2}\left(\frac{\partial F_{HP_{dyn}}^{(n)}}{\partial \dot{r}_j}\Delta\dot{r}_j + \frac{\partial F_{HP_{dyn}}^{(n)}}{\partial \dot{X}_j}\Delta\dot{X}_j + \frac{\partial F_{HP_{dyn}}^{(n)}}{\partial \dot{\theta}_j}\Delta\dot{\theta}_j + 2F_{HP_{dyn}}^{(n)}\right)\end{aligned} \tag{5.32}$$

where the change of velocities are: $\Delta\dot{X}_j = \frac{\Delta\left(\Delta X_j\right)}{\Delta t}$, $\Delta\dot{r}_j = \frac{\Delta\left(\Delta r_j\right)}{\Delta t}$, and $\Delta\dot{\theta}_j = \frac{\Delta\left(\Delta\theta_j\right)}{\Delta t}$;

therefore,

$$\int_{t^{(n)}}^{t^{(n+1)}} F_{HP_{dyn}}\,dt \approx \frac{\Delta t}{2}\left(\frac{\partial F_{HP_{dyn}}^{(n)}}{\partial \dot{r}_j}\frac{\Delta\left(\Delta r_j\right)}{\Delta t} + \frac{\partial F_{HP_{dyn}}^{(n)}}{\partial \dot{X}_j}\frac{\Delta\left(\Delta X_j\right)}{\Delta t} + \frac{\partial F_{HP_{dyn}}^{(n)}}{\partial \dot{\theta}_j}\frac{\Delta\left(\Delta\theta_j\right)}{\Delta t} + 2F_{HP_{dyn}}^{(n)}\right) \tag{5.33}$$

$$\int_{t^{(n)}}^{t^{(n+1)}} F_{HP_{dyn}}\,dt = \frac{1}{2}\left(\begin{array}{l}\dfrac{\partial F_{HP_{dyn}}^{(n)}}{\partial \dot{r}_j}\Delta\left(\Delta r_j^{(\mathrm{n})}\right) + \dfrac{\partial F_{HP_{dyn}}^{(n)}}{\partial \dot{X}_j}\Delta\left(\Delta X_j^{(\mathrm{n})}\right) \\ + \dfrac{\partial F_{HP_{dyn}}^{(n)}}{\partial \dot{\theta}_j}\Delta\left(\Delta\theta_j^{(\mathrm{n})}\right)\end{array}\right) + \frac{\Delta t}{2}\left(2F_{HP_{dyn}}^{(n)}\right) \tag{5.34}$$

By refering to Eqns. (A.1) - (A.4) in Appendix A, the Eqn. (5.34) can be rewritten as:

$$\int_{t^{(n)}}^{t^{(n+1)}} F_{HP_{dyn}}\,dt = \frac{\partial F_{HP_{dyn}}^{(n)}}{\partial \dot{r}_j}\left[\frac{1}{2}\left(\Delta r_j^{(n+1)} - \Delta r_j^{(n)}\right)\right] + \frac{\partial F_{HP_{dyn}}^{(n)}}{\partial \dot{X}_j}\left[\frac{1}{2}\left(\Delta X_j^{(n+1)} - \Delta X_j^{(n)}\right)\right] + \frac{\partial F_{HP_{dyn}}^{(n)}}{\partial \dot{\theta}_j}\left[\frac{1}{2}\left(\Delta \theta_j^{(n+1)} - \Delta \theta_j^{(n)}\right)\right] + \Delta t \cdot F_{HP_{dyn}}^{(n)} \tag{5.35}$$

where the tangential stiffness coefficients in Eqn. (5.35) can be derived as:

$$\frac{\partial F_{HP_{dyn}}^{(n)}}{\partial \dot{r}_j} = \frac{\partial}{\partial \dot{r}_j}\left\{\alpha_{HP}\beta_{HP}\left(\dot{X}_i + \dot{\theta}_j C_{ji} - \dot{r}_i\right)^2\right\} = -2\alpha_{HP}\beta_{HP}\left(\dot{X}_i + \dot{\theta}_j C_{ji} - \dot{r}_i\right) \tag{5.36}$$

$$\frac{\partial F_{HP_{dyn}}^{(n)}}{\partial \dot{X}_j} = \frac{\partial}{\partial \dot{X}_j}\left\{\alpha_{HP}\beta_{HP}\left(\dot{X}_i + \dot{\theta}_j C_{ji} - \dot{r}_i\right)^2\right\} = 2\alpha_{HP}\beta_{HP}\left(\dot{X}_i + \dot{\theta}_j C_{ji} - \dot{r}_i\right) \tag{5.37}$$

$$\frac{\partial F_{HP_{dyn}}^{(n)}}{\partial \dot{\theta}_j} = \frac{\partial}{\partial \dot{\theta}_j}\left\{\alpha_{HP}\beta_{HP}\left(\dot{X}_i + \dot{\theta}_j C_{ji} - \dot{r}_i\right)^2\right\} = 2\alpha_{HP}\beta_{HP}\left(\dot{X}_i + \dot{\theta}_j C_{ji} - \dot{r}_i\right)\cdot C_{ji} \tag{5.38}$$

Examine the term $\Delta t \cdot F_{HP_{dyn}}^{(n)}$ on the right hand side of Eqn. (5.35);

$$\begin{aligned}
\Delta t \cdot F_{HP_{dyn}}^{(n)} &= \Delta t\left\{\alpha_{HP}\beta_{HP}\left(\dot{X}_i + \dot{\theta}_j C_{ji} - \dot{r}_i\right)^2\right\} \\
&= \Delta t\left\{\alpha_{HP}\beta_{HP}\left(\frac{\Delta X_i}{\Delta t} + \frac{\Delta \theta_i}{\Delta t}C_{ji} - \frac{\Delta r_i}{\Delta t}\right)^2\right\} \\
&= \alpha_{HP}\beta_{HP}\left(\frac{\Delta X_i}{\Delta t} + \frac{\Delta \theta_i}{\Delta t}C_{ji} - \frac{\Delta r_i}{\Delta t}\right)\cdot\left(\Delta X_i^{(n)} + \Delta\theta_i^{(n)}C_{ji} - \Delta r_i^{(n)}\right) \\
&= \alpha_{HP}\beta_{HP}\left(\dot{X}_i + \dot{\theta}_j C_{ji} - \dot{r}_i\right)\cdot\left(\Delta X_i^{(n)} + \Delta\theta_i^{(n)}C_{ji} - \Delta r_i^{(n)}\right) \\
&= \alpha_{HP}\beta_{HP}\left(\dot{X}_i + \dot{\theta}_j C_{ji} - \dot{r}_i\right)\cdot\frac{1}{2}\left(2\Delta X_i^{(n)} + 2\Delta\theta_i^{(n)}C_{ji} - 2\Delta r_i^{(n)}\right)
\end{aligned} \tag{5.39}$$

Let $\left(\dot{X}_i + \dot{\theta}_j C_{ji} - \dot{r}_i\right) = v_Z$, (5.40)

Substituting the tangential stiffness coefficients into Eqn. (5.35),

$$\int_{t^{(n)}}^{t^{(n+1)}} F_{HP_{dyn}}\,dt = -2\alpha_{HP}\beta_{HP}v_Z\left[\frac{1}{2}\left(\Delta r_j^{(n+1)} - \Delta r_j^{(n)}\right)\right] + 2\alpha_{HP}\beta_{HP}v_Z\left[\frac{1}{2}\left(\Delta X_j^{(n+1)} - \Delta X_j^{(n)}\right)\right]$$
$$+2\alpha_{HP}\beta_{HP}v_Z\cdot C_{ji}\left[\frac{1}{2}\left(\Delta\theta_j^{(n+1)} - \Delta\theta_j^{(n)}\right)\right]$$
$$+\alpha_{HP}\beta_{HP}v_Z\cdot\frac{1}{2}\left(2\Delta X_i^{(n)} + 2\Delta\theta_i^{(n)}C_{ji} - 2\Delta r_i^{(n)}\right) \tag{5.41}$$

$$\int_{t^{(n)}}^{t^{(n+1)}} F_{HP_{dyn}}\,dt = \left\{\begin{array}{l} -\alpha_{HP}\beta_{HP}v_Z\left[\frac{1}{2}\left(\Delta r_j^{(n+1)} + \Delta r_j^{(n)}\right)\right] + \alpha_{HP}\beta_{HP}v_Z\left[\frac{1}{2}\left(\Delta X_j^{(n+1)} + \Delta X_j^{(n)}\right)\right] \\ +\alpha_{HP}\beta_{HP}v_Z\cdot C_{ji}\left[\frac{1}{2}\left(\Delta\theta_j^{(n+1)} + \Delta\theta_j^{(n)}\right)\right] \end{array}\right\}$$
$$+\left\{\begin{array}{l} -\alpha_{HP}\beta_{HP}v_Z\left[\frac{1}{2}\left(\Delta r_j^{(n+1)} - \Delta r_j^{(n)}\right)\right] + \alpha_{HP}\beta_{HP}v_Z\left[\frac{1}{2}\left(\Delta X_j^{(n+1)} - \Delta X_j^{(n)}\right)\right] \\ +\alpha_{HP}\beta_{HP}v_Z\cdot C_{ji}\left[\frac{1}{2}\left(\Delta\theta_j^{(n+1)} - \Delta\theta_j^{(n)}\right)\right] \end{array}\right\} \tag{5.42}$$

$$\int_{t^{(n)}}^{t^{(n+1)}} F_{HP_{dyn}}\,dt = \left\{\begin{array}{l} +\alpha_{HP}\beta_{HP}v_Z\left(\Delta X_j^{(n+1)}\right) + \alpha_{HP}\beta_{HP}v_Z\cdot C_{ji}\left(\Delta\theta_j^{(n+1)}\right) \\ -\alpha_{HP}\beta_{HP}v_Z\left(\Delta r_j^{(n+1)}\right) \end{array}\right\} \tag{5.43}$$

$$\int_{t^{(n)}}^{t^{(n+1)}} F_{HP_{dyn}}\,dt = \alpha_{HP}\beta_{HP}v_Z\left\{\Delta X_j^{(n+1)} + \Delta\theta_j^{(n+1)}\cdot C_{ji} - \Delta r_j^{(n+1)}\right\} \tag{5.44}$$

By approximating the time varying $\Delta r_j, \Delta\theta_j$, and ΔX_j in the time interval $t^{(n+1)} - t^{(n)}$ to be a constant $\Delta r_j^{\left(n+\frac{1}{2}\right)}, \Delta\theta_j^{\left(n+\frac{1}{2}\right)}, X_j^{\left(n+\frac{1}{2}\right)}$ which are the position at time $t^{(n)} + \frac{\Delta t}{2}$, and for: $\Delta r_j^{\left(n+\frac{1}{2}\right)} = \frac{1}{2}\left(\Delta r_j^{(n+1)} + \Delta r_j^{(n)}\right)$, and so on, the Eqn. (5.44) can be rewritten as:

$$\int_{t^{(n)}}^{t^{(n+1)}} F_{HP_{dyn}}\,dt = 2\alpha_{HP}\beta_{HP}v_Z\left\{\Delta X_j^{\left(n+\frac{1}{2}\right)} + \Delta\theta_j^{\left(n+\frac{1}{2}\right)}\cdot C_{ji} - \Delta r_j^{\left(n+\frac{1}{2}\right)}\right\}$$
$$-\alpha_{HP}\beta_{HP}v_Z\left\{\Delta X_j^{(n)} + \Delta\theta_j^{(n)}\cdot C_{ji} - \Delta r_j^{(n)}\right\} \tag{5.45}$$

It can be found that the Eqn. (5.45) can be rearranged in the following form as:

$$\frac{\Delta t}{2}\left(F_{HP_{dyn}}^{(\mathrm{n}+1)} + F_{HP_{dyn}}^{(\mathrm{n})}\right) = 2\alpha_{HP}\beta_{HP}v_Z\left\{\Delta X_j^{\left(n+\frac{1}{2}\right)} + \Delta\theta_j^{\left(n+\frac{1}{2}\right)}\cdot C_{ji} - \Delta r_j^{\left(n+\frac{1}{2}\right)}\right\}$$
$$-\alpha_{HP}\beta_{HP}v_Z\left\{\Delta X_j^{(n)} + \Delta\theta_j^{(n)}\cdot C_{ji} - \Delta r_j^{(n)}\right\} \tag{5.46}$$

$$\left(F_{HP_{dyn}}^{(\mathrm{n}+1)} + F_{HP_{dyn}}^{(\mathrm{n})}\right) = \frac{2}{\Delta t}\left(2\alpha_{HP}\beta_{HP}v_Z\right)\left\{\Delta X_j^{\left(n+\frac{1}{2}\right)} + \Delta\theta_j^{\left(n+\frac{1}{2}\right)}\cdot C_{ji} - \Delta r_j^{\left(n+\frac{1}{2}\right)}\right\}$$
$$-\left(2\alpha_{HP}\beta_{HP}v_Z\right)\frac{1}{\Delta t}\left\{\Delta X_j^{(n)} + \Delta\theta_j^{(n)}\cdot C_{ji} - \Delta r_j^{(n)}\right\} \tag{5.47}$$

$$\left(F_{HP_{dyn}}^{(\mathrm{n}+1)} + F_{HP_{dyn}}^{(\mathrm{n})}\right) = \frac{2}{\Delta t}\left(2\alpha_{HP}\beta_{HP}v_Z\right)\left\{\Delta X_j^{\left(n+\frac{1}{2}\right)} + \Delta\theta_j^{\left(n+\frac{1}{2}\right)}\cdot C_{ji} - \Delta r_j^{\left(n+\frac{1}{2}\right)}\right\}$$
$$-\left(2\alpha_{HP}\beta_{HP}v_Z\right)\left\{\dot{X}_j^{(n)} + \dot{\theta}_j^{(n)}\cdot C_{ji} - \dot{r}_j^{(n)}\right\} \tag{5.48}$$

$$\left\{\begin{array}{l}\left[\frac{2}{\Delta t}\left(2\alpha_{HP}\beta_{HP}v_Z\right)\right]\Delta X_j^{\left(n+\frac{1}{2}\right)} \\ +\left[\frac{2}{\Delta t}\left(2\alpha_{HP}\beta_{HP}v_Z\right)\right]C_{ji}\cdot\Delta\theta_j^{\left(n+\frac{1}{2}\right)} \\ -\left[\frac{2}{\Delta t}\left(2\alpha_{HP}\beta_{HP}v_Z\right)\right]\Delta r_j^{\left(n+\frac{1}{2}\right)}\end{array}\right\} = \left(F_{HP_{dyn}}^{(\mathrm{n}+1)} + F_{HP_{dyn}}^{(\mathrm{n})}\right)$$
$$+\left(2\alpha_{HP}\beta_{HP}v_Z\right)\left\{\dot{X}_j^{(n)} + \dot{\theta}_j^{(n)}\cdot C_{ji} - \dot{r}_j^{(n)}\right\} \tag{5.49}$$

By referring to the Eqn. (5.30), the RHS of the Eqn. (5.49) can be further rearranged as:

$$\left\{\begin{array}{l}\left[\dfrac{2}{\Delta t}\left(2\alpha_{HP}\beta_{HP}v_Z\right)\right]\Delta X_j^{\left(n+\frac{1}{2}\right)} \\ +\left[\dfrac{2}{\Delta t}\left(2\alpha_{HP}\beta_{HP}v_Z\right)\right]C_{ji}\cdot\Delta\theta_j^{\left(n+\frac{1}{2}\right)} \\ -\left[\dfrac{2}{\Delta t}\left(2\alpha_{HP}\beta_{HP}v_Z\right)\right]\Delta r_j^{\left(n+\frac{1}{2}\right)}\end{array}\right\}=\left(F_{HP_{dyn}}^{(\mathrm{n}+1)}-F_{HP_{dyn}}^{(\mathrm{n})}\right)$$

$$+2\cdot\left(2\alpha_{HP}\beta_{HP}v_Z\right)\left\{\dot{X}_j^{(n)}+\dot{\theta}_j^{(n)}\cdot C_{ji}-\dot{r}_j^{(n)}\right\} \tag{5.50}$$

which is identical to the form of *pseudo dynamic stiffness* and *dynamic force* as stated in Eqns. (3.40) and (3.41).

Following from the Eqns. (5.48), (5.30), and (5.32), the tangential stiffness coefficients and the connector force on the end of the line $\int_{t^{(n)}}^{t^{(n+1)}} F_{HP_{dyn}}\,dt$ contributed by the dynamic tension variation in the tensioner are:

$$\int_{t^{(n)}}^{t^{(n+1)}} F_{HP_{dyn}}\,dt=\frac{\Delta t}{2}\left(\frac{2}{\Delta t}\left(2\alpha_{HP}\beta_{HP}v_Z\right)\left\{\Delta X_j^{\left(n+\frac{1}{2}\right)}+\Delta\theta_j^{\left(n+\frac{1}{2}\right)}\cdot C_{ji}-\Delta r_j^{\left(n+\frac{1}{2}\right)}\right\}\right)$$

$$-\frac{\Delta t}{2}\left(2\alpha_{HP}\beta_{HP}v_Z\right)\left\{\dot{X}_j^{(n)}+\dot{\theta}_j^{(n)}\cdot C_{ji}-\dot{r}_j^{(n)}\right\} \tag{5.51}$$

$$\int_{t^{(n)}}^{t^{(n+1)}} F_{HP_{dyn}}\,dt=\frac{\Delta t}{2}\left(\frac{2}{\Delta t}\left(2\alpha_{HP}\beta_{HP}v_Z\right)\left\{\Delta X_j^{\left(n+\frac{1}{2}\right)}+\Delta\theta_j^{\left(n+\frac{1}{2}\right)}\cdot C_{ji}-\Delta r_j^{\left(n+\frac{1}{2}\right)}\right\}\right)$$

$$-\frac{\Delta t}{2}\left(2\cdot F_{HP_{dyn}}\right) \tag{5.52}$$

The dynamic tension force, after considered the frictional losses effects, generated by the hydro-pneumatic tensioner at the end node of riser from time $t^{(n)}$ to $t^{(n+1)}$ is obtained in Eqn. (5.52). In the *n*-line direct-acting HPT system, the total

dynamic tension variation will be multiplied by the number of cylinders n_{cyn}, therefore the Eqn. (5.52) can be further modified as:

$$n_{cyn}\cdot\int_{t^{(n)}}^{t^{(n+1)}}F_{HP_{dyn}}dt=\frac{\Delta t}{2}\left\{\begin{array}{l}\left(\frac{2}{\Delta t}\left(n_{cyn}\cdot 2\alpha_{HP}\beta_{HP}v_Z\right)\right)\Delta X_j^{\left(n+\frac{1}{2}\right)}\\+\left(\frac{2}{\Delta t}\left(n_{cyn}\cdot 2\alpha_{HP}\beta_{HP}v_Z\right)\right)\Delta\theta_j^{\left(n+\frac{1}{2}\right)}\cdot C_{ji}\\-\left(\frac{2}{\Delta t}\left(n_{cyn}\cdot 2\alpha_{HP}\beta_{HP}v_Z\right)\right)\Delta r_j^{\left(n+\frac{1}{2}\right)}\end{array}\right\}-\frac{\Delta t}{2}\left(2\cdot n_{cyn}\cdot F_{HP_{dyn}}\right) \tag{5.53}$$

$$\begin{aligned}n_{cyn}\cdot\int_{t^{(n)}}^{t^{(n+1)}}F_{HP_{dyn}}dt&=\frac{\Delta t}{2}\left\{-K_{ij}^{rX}\cdot\Delta X_j^{\left(n+\frac{1}{2}\right)}-K_{ij}^{r\theta}\cdot\Delta\theta_j^{\left(n+\frac{1}{2}\right)}-K_{ij}^{rr}\cdot\Delta r_j^{\left(n+\frac{1}{2}\right)}\right\}\\&\quad-\frac{\Delta t}{2}\left(2\cdot n_{cyn}\cdot F_{HP_{dyn}}\right)\end{aligned} \tag{5.54}$$

and the connector force on the rigid *body* $\int_{t^{(n)}}^{t^{(n+1)}}F_{HP_{dyn}}^{Body}dt$ caused by the dynamic tension variation in the tensioner are:

$$\begin{aligned}n_{cyn}\cdot\int_{t^{(n)}}^{t^{(n+1)}}F_{HP_{dyn}}^{Body}dt&=-n_{cyn}\cdot\int_{t^{(n)}}^{t^{(n+1)}}F_{HP_{dyn}}dt\\&=\frac{\Delta t}{2}\left\{-K_{ij}^{XX}\cdot\Delta X_j^{\left(n+\frac{1}{2}\right)}-K_{ij}^{X\theta}\cdot\Delta\theta_j^{\left(n+\frac{1}{2}\right)}-K_{ij}^{Xr}\cdot\Delta r_j^{\left(n+\frac{1}{2}\right)}\right\}\\&\quad+\frac{\Delta t}{2}\left(2\cdot n_{cyn}\cdot F_{HP_{dyn}}\right)\end{aligned} \tag{5.55}$$

where

$$K_{ij}^{rr} = -K_{ij}^{Xr} = \frac{2}{\Delta t}\left(n_{cyn} \cdot 2\alpha_{HP}\beta_{HP}v_Z\right)$$

$$K_{ij}^{rX} = -K_{ij}^{XX} = K_{ij}^{Xr} = -\left[\frac{2}{\Delta t}\left(n_{cyn} \cdot 2\alpha_{HP}\beta_{HP}v_Z\right)\right]$$

$$K_{ij}^{r\theta} = -K_{ij}^{X\theta} = -\left[\frac{2}{\Delta t}\left(n_{cyn} \cdot 2\alpha_{HP}\beta_{HP}v_Z\right)\right]C_{ji}$$

$$K_{ij}^{\theta\theta} = \left(K_i C_{ij}\right)_D C_{ki} + K_i^{\theta} D_{ij} D_{ki} \tag{5.56}$$

where $\left(K_i C_{ij}\right)_D = \dfrac{\partial F_{HP_{dyn}}^{(n)}}{\partial \theta_j} = \left[\dfrac{2}{\Delta t}\left(n_{cyn} \cdot 2\alpha_{HP}\beta_{HP}v_Z\right)\right]C_{ji}$ (5.57)

There can be found that the second term on the right hand side (RHS) of Eqn. (5.54) (for the riser *line*) and Eqn. (5.55) (for the platform *body*), are the residue forcing terms after coupling with the effects of dynamic tension variations in the tensioner. Therefore, these terms are to be included into the matrix (R) and (S) in the Fig. 2.5, respectively, to modify the forcing terms in the CHARM3D. The total element tangential stiffness matrix, after considering the dynamic tension variation, MR damper and spring coupling with the platform, on the *end node of the riser* (line), as modified from Eqn. (2.183) is:

$$\frac{\Delta t}{2}\left\{\begin{bmatrix} K_{ij}^{rr} & 0 \\ 0 & K_{ij}^{r'r'} \end{bmatrix}_{LS} + \begin{bmatrix} K_{ij}^{rr} & 0 \\ 0 & 0 \end{bmatrix}_{TV} + \begin{bmatrix} K_{ij}^{rr} & 0 \\ 0 & 0 \end{bmatrix}_{MR}\right\}\begin{Bmatrix} \Delta r_j \\ \Delta r_j' \end{Bmatrix}$$

$$= \frac{\Delta t}{2}\begin{Bmatrix} 2N_i \\ 2L_i \end{Bmatrix}_{LS} + \frac{\Delta t}{2}\begin{Bmatrix} -2 \cdot n_{cyn} \cdot F_{HP_{dyn}} \\ 0 \end{Bmatrix}_{TV} + \frac{\Delta t}{2}\begin{Bmatrix} 2f_{MR} - 2(c+\gamma)\left(\dot{r}_j\right) \\ 0 \end{Bmatrix}_{MR} \tag{5.58}$$

The element tangential stiffness matrix that needs to be added into the platform *body,* as modified from Eqn. (2.184) is:

$$\frac{\Delta t}{2}\left\{\begin{bmatrix} K_{ij}^{XX} & K_{ij}^{X\theta} \\ K_{ij}^{\theta X} & K_{ij}^{\theta\theta} \end{bmatrix}_{LS} + \begin{bmatrix} K_{ij}^{XX} & K_{ij}^{X\theta} \\ K_{ij}^{X\theta} & K_{ij}^{\theta\theta} \end{bmatrix}_{TV} + \begin{bmatrix} K_{ij}^{XX} & K_{ij}^{X\theta} \\ K_{ij}^{X\theta} & K_{ij}^{\theta\theta} \end{bmatrix}_{MR}\right\}\begin{Bmatrix} \Delta X_j \\ \Delta\theta_j \end{Bmatrix}$$
$$= \frac{\Delta t}{2}\begin{Bmatrix} 2F_i \\ 2M_i \end{Bmatrix}_{LS} + \frac{\Delta t}{2}\begin{Bmatrix} 2\cdot n_{cyn}\cdot F_{HP_{dyn}} \\ 0 \end{Bmatrix}_{TV} + \frac{\Delta t}{2}\begin{Bmatrix} -2f_{MR} + 2(c+\gamma)\left(\dot{X}_j\right) \\ 0 \end{Bmatrix}_{MR} \tag{5.59}$$

and the *coupling* terms of element tangential stiffness matrix that need to be added into the global matrix, as modified from Eqn. (2.185) is:

$$\frac{\Delta t}{2}\left\{\begin{bmatrix} 0 & 0 & K_{ij}^{rX} & K_{ij}^{r\theta} \\ 0 & 0 & 0 & K_{ij}^{r'\theta} \\ K_{ij}^{Xr} & 0 & 0 & 0 \\ K_{ij}^{\theta r} & K_{ij}^{\theta r'} & 0 & 0 \end{bmatrix}_{LS} + \begin{bmatrix} 0 & 0 & K_{ij}^{rX} & K_{ij}^{r\theta} \\ 0 & 0 & 0 & 0 \\ K_{ij}^{Xr} & 0 & 0 & 0 \\ K_{ij}^{\theta r} & 0 & 0 & 0 \end{bmatrix}_{TV} + \begin{bmatrix} 0 & 0 & K_{ij}^{rX} & K_{ij}^{r\theta} \\ 0 & 0 & 0 & 0 \\ K_{ij}^{Xr} & 0 & 0 & 0 \\ K_{ij}^{\theta r} & 0 & 0 & 0 \end{bmatrix}_{MR}\right\}\begin{Bmatrix} \Delta r_j \\ \Delta r_j' \\ \Delta X_j \\ \Delta\theta_j \end{Bmatrix}$$
$$= \frac{\Delta t}{2}\begin{Bmatrix} 2N_i \\ 2L_i \\ 2F_i \\ 2M_i \end{Bmatrix} + \frac{\Delta t}{2}\begin{Bmatrix} -2\cdot n_{cyn}\cdot F_{HP_{dyn}} \\ 0 \\ 2\cdot n_{cyn}\cdot F_{HP_{dyn}} \\ 0 \end{Bmatrix}_{TV} + \frac{\Delta t}{2}\begin{Bmatrix} 2f_{MR} - 2(c+\gamma)\left(\dot{r}_j\right) \\ 0 \\ -2f_{MR} + 2(c+\gamma)\left(\dot{X}_j\right) \\ 0 \end{Bmatrix}_{MR} \tag{5.60}$$

5.6 Reduction of Riser Tensioner Force Variation by Using MR-Damper

The proposed MR damper is acting as a smart-device that works corporately with the conventional hydro-pneumatic (HP) tensioner, as illustrated in Fig. 5.5, and is able to provide controllable damping force to the TTR to reduce the variation of axial tension force. The MR damper is connected to the production deck of the platform in one end and to the tensioner ring on the other end. There is noteworthy that this is a conceptual design, hence, the dimension (length) of the MR damper is assumed here to be commensurate with the size of the HP tensioner. After the tension variation is

compensated with the MR damper force, the tensioner force equilibrium F_{ten} in Eqn. (5.22) can be modified as:

$$F_{ten} = F_{HP_0}^{a}\left(1-\frac{\Delta z}{z_{A0}}\right)^{-\gamma} + A_p^a \cdot \frac{\rho_{oil} f^{AP}}{2A_{AP}^2}\left(\frac{L^{AP}+L_{eq}^{AP}}{D_{AP}}\right) q_{oil}\cdot\left|q_{oil}\right| - F_{HP_0}^{b}\left(1+\frac{\Delta z}{z_{B0}}\right)^{-\gamma} + F_{HS} + f_{MR} \tag{5.61}$$

The free body diagram (FBD) of the settings in Fig. 5.5 can be refered to Fig. 3.9 and Fig. 3.10. A scheme based on the *Gaussian* distribution function, which has the characteristics of high command current signal $i(t)$ near the piston mid-position, and very low command signal at the extremely end-positions is utilized to control the MR damper. The command current $i(t)$ generated by the controller can be represented in the following function:

$$i(t) = \frac{1}{\sigma\sqrt{2\pi}}\exp\left(-\frac{\left(x_{MR}-\mu\right)^2}{2\sigma^2}\right) + d \tag{5.62}$$

where σ is the standard deviation, μ is the mean of position, and d is the offset of the function that can be adjusted to manipulate the performance of the controller. The command current $i(t)$ is tunable with respect to the dynamic displacement x_{MR} of the riser and then to be feedback into the MR damper model to determine the coefficients in Eqns. (3.3)-(3.7) and damping force based on Eqn. (3.1). The idealistic capacity of this numerical MR damper based on the proposed coefficients from Eqns. (3.3) – (3.7) is up to ~4.5 MN (*~1012 kips*) when sinusoidal excitation amplitude is 1.5 m (*4.92 ft*) and input current is 1.0 A. The numerical model of a HP tensioner was simulated by

incorporating the MR damper to identify the effectiveness of the reduction of tension variations. The simulation was conducted by using the Simulink software package (Mathworks, 2009) based on the dimensions and data of HP tensioner as tabulated in Table 5.1.

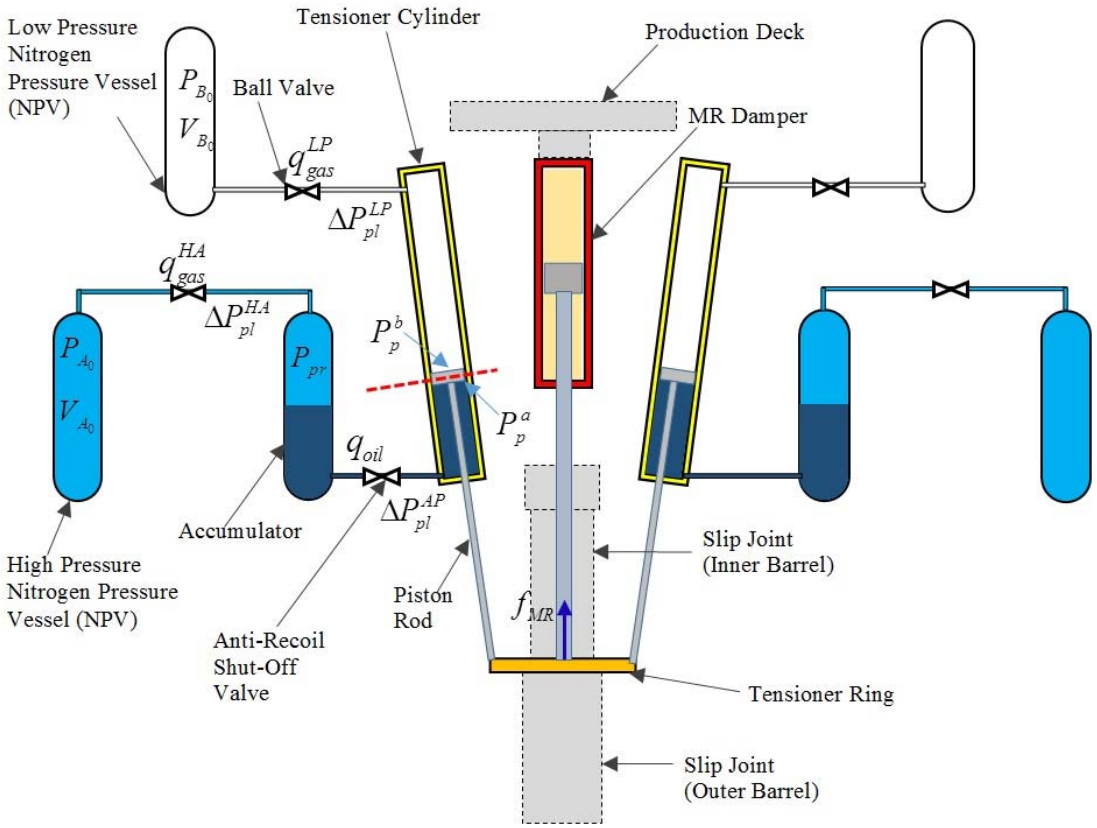

Figure 5.9 The integration of MR damper in the HP tensioner system.

The reduction of the tension variation after the HP tensioner is incorporated with the MR damper, as proposed in Fig. 5.9, is shown in Fig. 5.10. The *green* loop is the *base case* with which is the uncontrolled tension variation of a tensioner system for a long pipe with length L^{AP} = 30 m (*98.43 ft*). The multiple *red* loops are the tension reduction effects achieved by adding different values of fixed damping force. Generally, a larger damping force can reduce the tension variation in the range near the equilibrium mid-position (approximately at +2.0 m (*+6.56 ft*) in this case) but enlarge the tension variation on the extreme end-positions (~ -0.5 m and ~4.25 m (~ *-1.64 ft and ~13.94 ft*), respectively). This phenomenon leads to the necessity of employing a *tunable* damper (such as MR damper) instead of a *fixed* damper for a wide range of dynamic tension reduction control in the TTR tensioner. Finally, the *blue* loop is the result when a controllable MR damper is incorporated into the HP tensioner system. A 'Gaussian' control function, which has the characteristics of *high* command current inputs near the mid-position and *very low* command current inputs at the extremely end-positions, as stated in Eqn. (5.62), is utilized to control the MR damper.

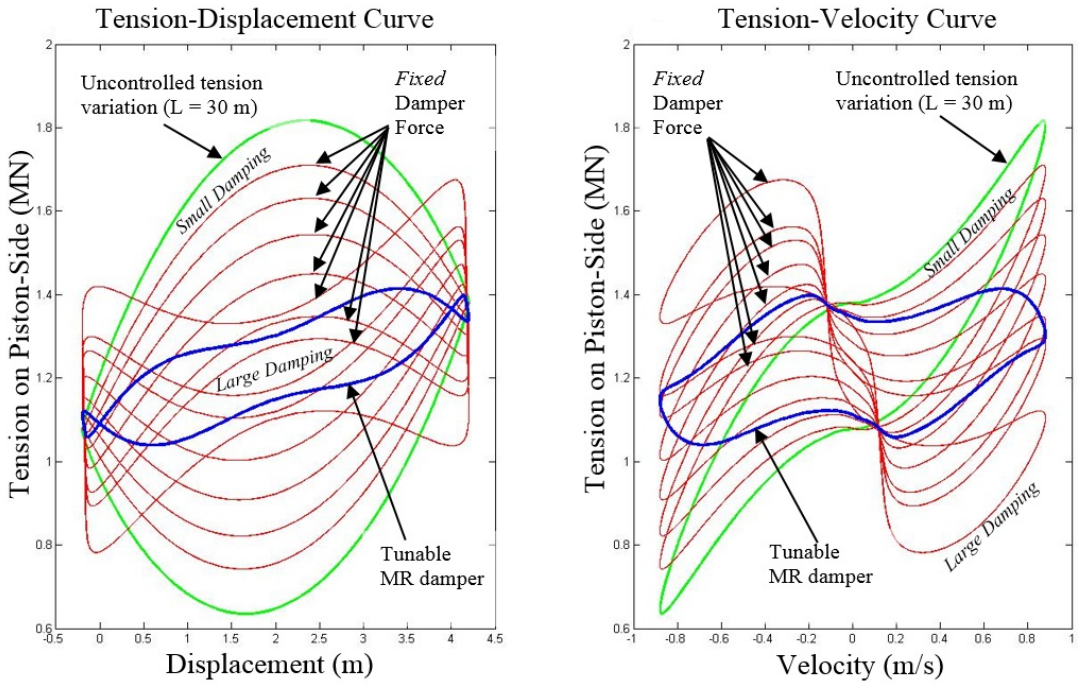

Figure 5.10 Tension reduction (blue line) in the piston-side chamber after the HP tensioner is incorporated with the MR damper.

From the results in Fig. 5.10, there can be further inferred that a controllable MR damper is able to compensate the excessive tension variations that are induced from the following sources:

(i) The hydraulic fluid flow rate q_{oil} which is induced by the velocity of tensioner piston, as stated in Eqn. (5.61). The larger tension variation caused by the larger velocity factor is reasonable for the cases of drillship and *dry-tree* Semi-submersible, where the platform's heave motion is no longer constrained by the high stiffed tendons, and for the cases of instantaneous velocity during anti-recoiling and TTR disconnection.

(ii) The geometrical dimension, especially the length of hydraulic pipe conduits L^{AP}, as stated in Eqn. (5.61). The incorporated of controllable MR damper can be considered as an effective solution to compensate the excessive tension variations when the longer hydraulic fluid travel in between the accumulator and tensioner cylinder is required, such as in the case of *long-stroke* HP tensioner, which is the most popular tensioner solution in the development of the conceptual *dry-tree* Semi-submersible.

(iii) The ratio of gas volume $\Delta V_A / V_{A_0}$ in between the displaced volume and the total gas volume stored in the high pressure NPVs, as stated in the Eqns. (5.10) and (5.11). This volume ratio must be designed as small as possible in order to minimize the dynamic tension variation. Therefore, a very large volume V_{A_0} of high pressure NPVs must be stored nearby the well bay, as illustrated in Fig. 5.4. For the long-stroke HP tensioner to be developed in the *dry-tree* Semi-submersible platform, the required storage of high-pressurized gas volume is even larger. Therefore, the incorporated of controllable MR damper can potentially reduce the total volume of NPVs to be stored on the deck and lead to more flexible well-bay spacing and arrangement.

5.7 Equivalent Force Compensation Control (EFCC)

The Equivalent Force Compensation Control (EFCC) is conceptual scheme to compensate the force deviations in between the actual TTR tension and the desired

pretension by using a combination of MR dampers and force actuators. The working principle of EFCC is shown in Fig. 5.11, and the conceptual system is illustrated in Fig. 5.12. The two pairs of MR damper and force actuator are working in the opposite directions, as shown in the Fig. 5.12. There is noteworthy that this is a conceptual design, hence, the dimension (length) of the MR dampers and force actuators are assumed here to be commensurate with the size of the HP tensioner. The optimization of the equipment sizing, reducancy, and layout are not in the scope of the current study and can be conducted in the future work.

As illustrated in Fig. 5.11, a constant force actuator provides constant force F_{CA} in the same direction of tensioner ring displacement z (where displacement z is opposite in direction with the tensioner cylinder stroke S_Z, as stated in Eqn. (5.13)). The MR damper always provides tunable *resistive* force f_{MR} in the counter-direction of tensioner ring displacement z. The constant force F_{CA} is then to be *fine-tuned* by the combination of MR damper force f_{MR} in the opposite direction to produce a *net* force f_{net} on the tensioner ring. The net force f_{net} is designed to compensate the dynamic axial tension variations ΔT exerted on the tensioner ring, as stated in the second terms on the RHS of Eqn. (5.22), by the HP tensioner with respect to certain given displacement z and velocity $\dot{z}$.

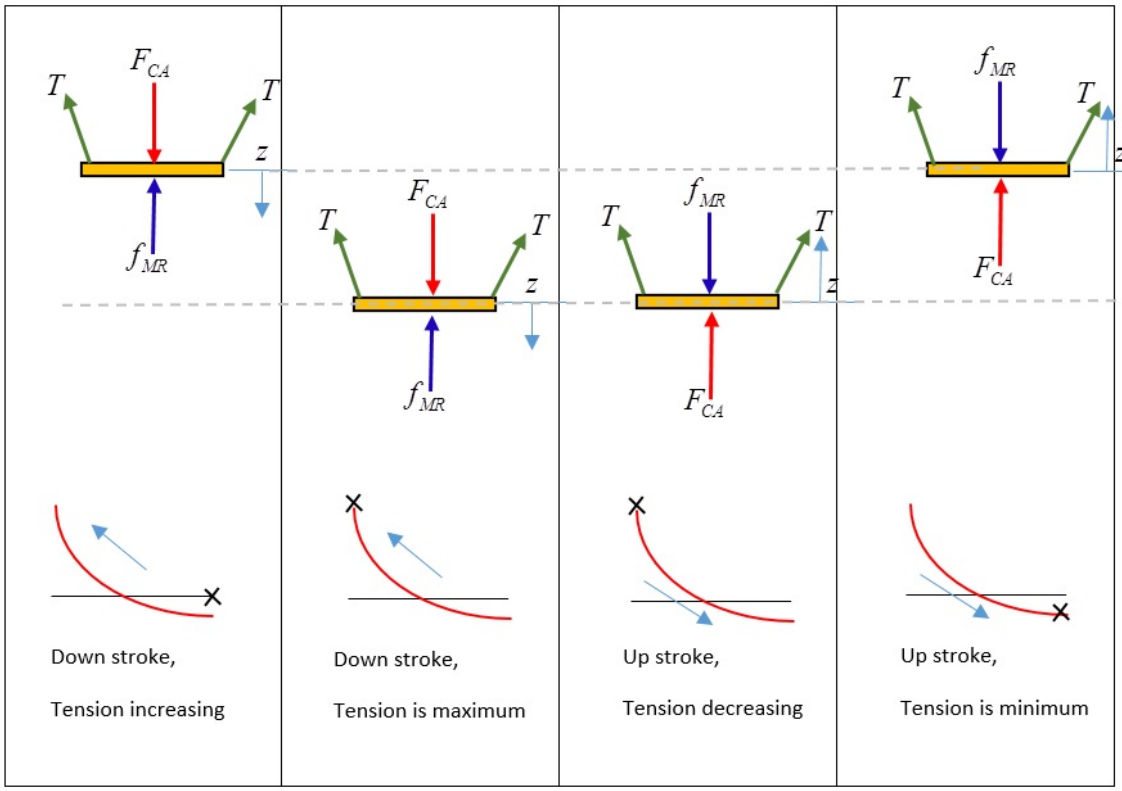

Figure 5.11 Schematic diagram for the working principle of EFCC.

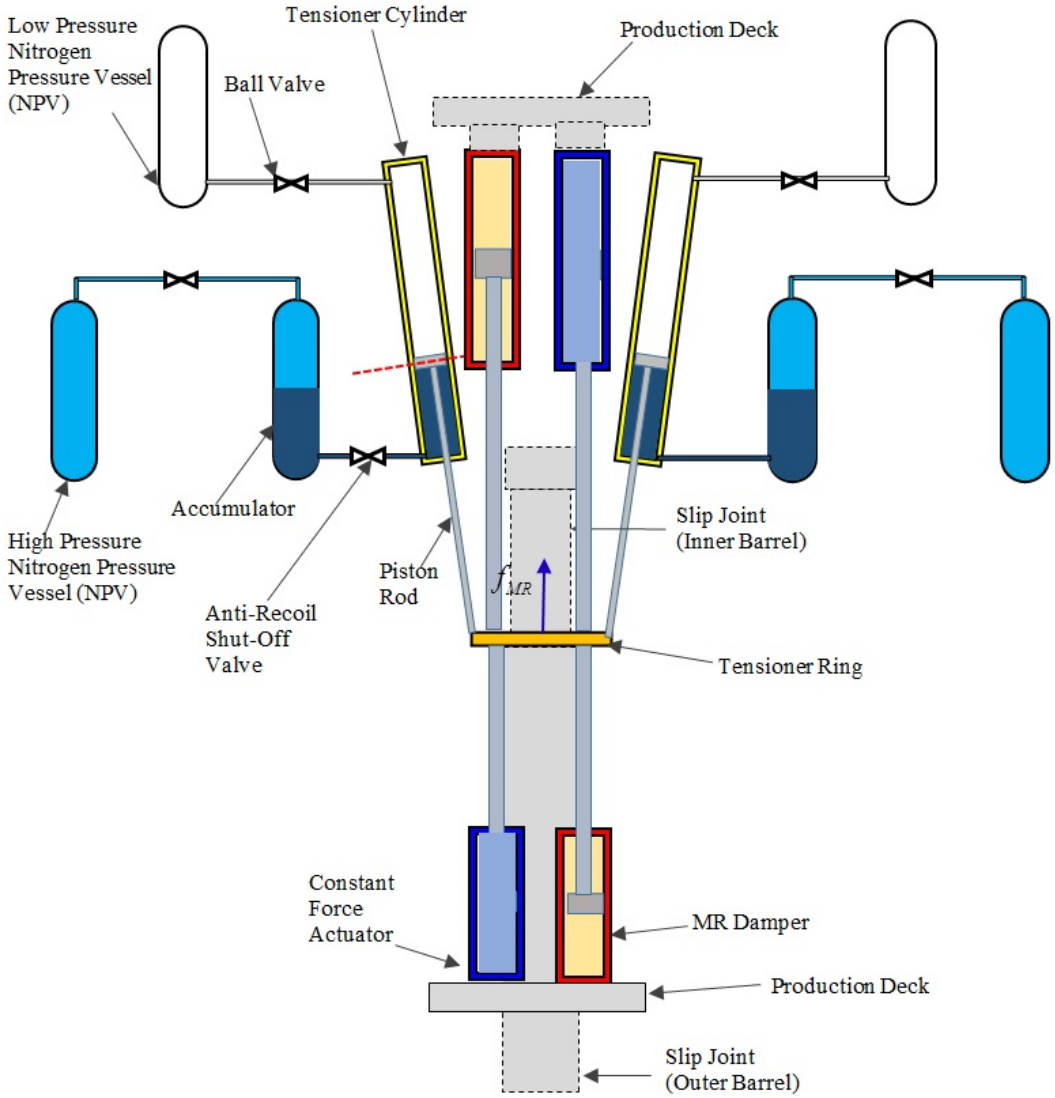

Figure 5.12 Equivalent force compensation control (EFCC). Proposed integration of MR dampers and force actuators in the direct acting tensioner (DAT) system.

The constant force actuator can either be the pneumatic actuator, hydraulic actuator, or any other type of force actuators which force outputs is not required to be in very high precision. The accuracy of net tension f_{net} acting on the tensioner ring is fully adjustable by the MR damper. The reduction of tension variation can be achieved cost effectively, in this method, as an alternative to the high-cost precision active force compensator. Moreover, the capacity for very large compensated force outputs, especially in the offshore applications, is not readily available for precision active force actuators. The MR damper has the advantage to react very fast and therefore it is appropriate to be used in the EFCC.

The relationsip of riser tension, MR damper force, and actuator force in the EFCC is illustrated in Fig. 5.13. If the riser tension is over the threshold value F_{Th} for activating the EFCC, the deviation of the riser tension F_{ten} and pretension T_{pr} is calculated as:

$$F_{net} = F_{ten} - T_{pr} \tag{5.63}$$

The direction of constant actuator force F_{CA} is always in the same direction of the tensioner ring displacement, and is determined by the value of F_{net} in the following equation:

$$F_{CA} = \begin{cases} -F_{CA} & \text{if } F_{net} \geq 0 \\ F_{CA} & \text{if } F_{net} < 0 \end{cases} \tag{5.64}$$

The required force F_{req} to be generated by the MR damper is therefore:

$$F_{req} = -\left(F_{CA} + F_{net}\right) \tag{5.65}$$

The required force F_{req} of the MR damper at any given displacement z and velocity $\dot{z}$ can be determined by identifying the input command current of the *primary* MR damper i_{MR}^{P} and the *secondary* MR damper i_{C}^{S}. The *primary* MR damper is regarded as the one moving in the same direction with the tensioner ring, and the *secondary* MR damper is the one in the opposite direction of the tensioner ring. Therefore, the *primary* and *secondary* MR damper is changing with respect to the stroke motion, in back and forth.

The *iterative bi-section* method is developed to approximate the command current i_{MR}^{P} and i_{C}^{S} to be fed into the *primary* and *secondary* MR dampers, respectively, as stated in Eqns. (3.3)-(3.7). For example, the *iterative bi-section* method for the *primary* MR damper can be represented as:

$$\text{For } F_{MR} < F_{req}: \; i_{L}^{P} = i\big|_{i=\text{mid}} \;;\; i_{U}^{P} = i\big|_{i=\text{max}} \;;\; i_{C}^{P} = \left(i_{L}^{P} + i_{U}^{P}\right)/2 \tag{5.66}$$

$$\text{For } F_{MR} \geq F_{req}: \; i_{L}^{P} = i\big|_{i=\text{min}} \;;\; i_{U}^{P} = i\big|_{i=\text{mid}} \;;\; i_{C}^{P} = \left(i_{L}^{P} + i_{U}^{P}\right)/2 \tag{5.67}$$

where i_{L}^{P}, i_{U}^{P}, and i_{C}^{P} are refered to the lowest current limit, highest current limit, and control current of the primary MR damper, respectively. The $i\big|_{i=\text{min}}$, $i\big|_{i=\text{max}}$, and $i\big|_{i=\text{mid}}$ denote the minimum current input (normally less than 0.001 A), maximum current input (normally less than 3.0 A), and mid-point of these two current inputs, respectively.

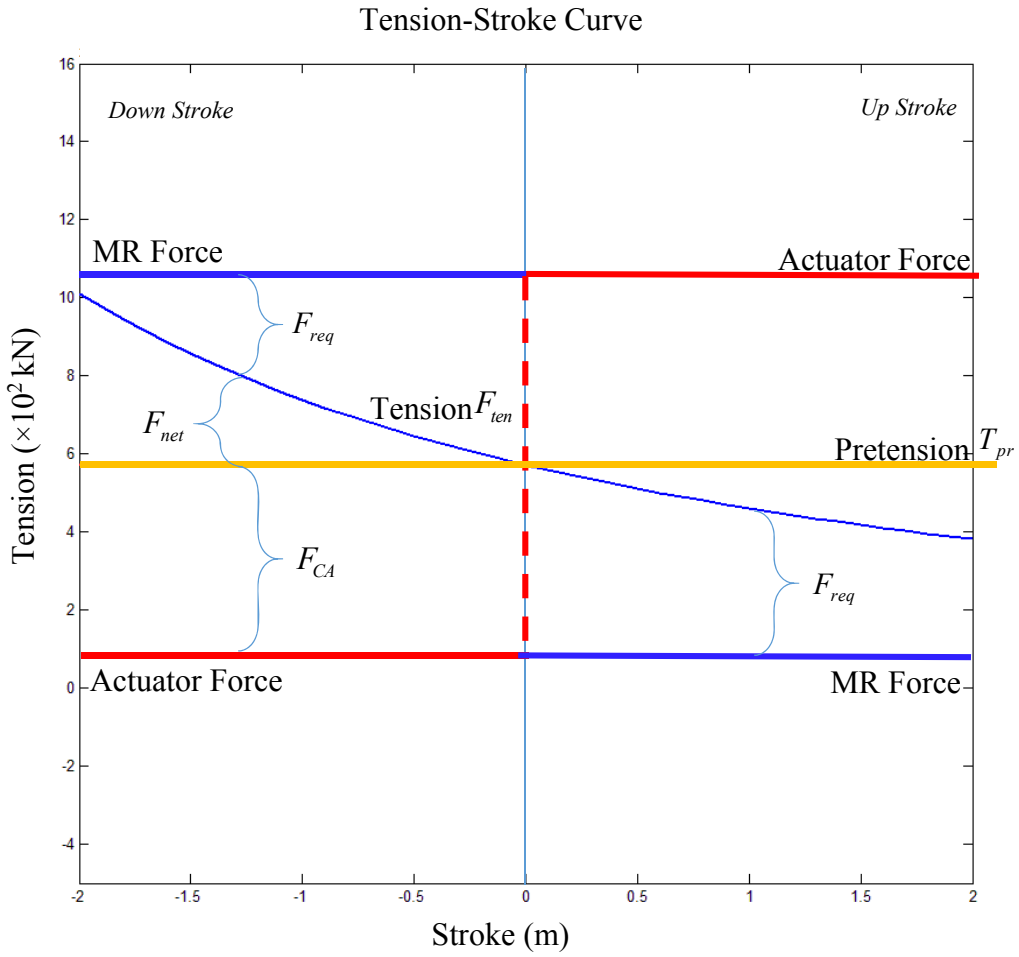

Figure 5.13 Relationship of riser tension, MR damping force, and actuator force.

The criterion of accuracy for the command current input for the primary MR damper is:

$$F_{dev}^{P} = 1.0 - F_{MR} / F_{req} \tag{5.68}$$

and the MR damper force for each iteration is therefore stated as:

$$F_{MR} = F_{MR}^{P}\Big|_{i=X} + \mathrm{sgn}(F_{req}) \cdot \left| \left(F_{MR}^{S}\Big|_{i=0} \right) \right| \tag{5.69}$$

where the F_{MR}^{P} and F_{MR}^{S} are refered to the *primary* and *secondary* MR damper forces, respectively. In this study, the targeting MR damper force f_{MR} is iterated until its deviation from the required force F_{req} is less than two percents.

If the MR damper force from the primary MR damper F_{MR}^{P} is not sufficient to achieve the required force F_{req}, the secondary MR damper will be activated in the similar way and total force will be added to the required force F_{req}. Finally, the total force acting on the tensioner ring F_{TR} can be represented as:

$$F_{TR} = F_{ten} + F_{MR} + F_{CA} \tag{5.70}$$

This total force F_{TR} is comparable with the HP tensioner force F_{ten} by the tension variation has been fine-tuned after taking the F_{MR} and F_{CA} into account. In the ideal condition, the total force acting on the tensioner ring F_{TR} is very close, less than 2% deviation, to the pretension T_{pr} of the riser. There is noteworthy that the pretension T_{pr} is chosen in this study as the targeting force for the simulation. However, the value of targeting force can be customized case-by-case in future works. For example, some cases may require a higher constant tension than the pretension under certain loading conditions.

Since the MR damper force in this EFCC is used to fine-tune the required tension on the tensioner ring, therefore, the large output force is not required in this case. The coefficients of MR damper are modified from Table 3.2, as tabulated in the Table 5.2, are proposed in this simulation. The capacity of this MR damper based on the proposed

coefficients in Table 5.2 is up to ~150 kN (*~33.7 kips*) when at the displacement amplitude of 1.0 m (*0.3048 ft*), frequency at 0.6 rad/s, and displacement offset at -17.0 m (*-5.1816 ft*). The variations of MR damper output forces under different combinations of amplitudes, frequencies, and controlled currents are shown in Figs. 5.14 - 5.19. The *displacement offset* is refered to the adjustment of the nominal position of MR damper with respect to the mean of the tensioner ring dynamic displacement in the particular cases.

Table 5.2 Coefficients of MR damper in EFCC simulation.

Coefficients	i^2	i^1	i^0
c	8500	5400	50
k	0	540	50
α	2500	8100	40
β	0	52.05	2.82
δ	0	2.6	0.25

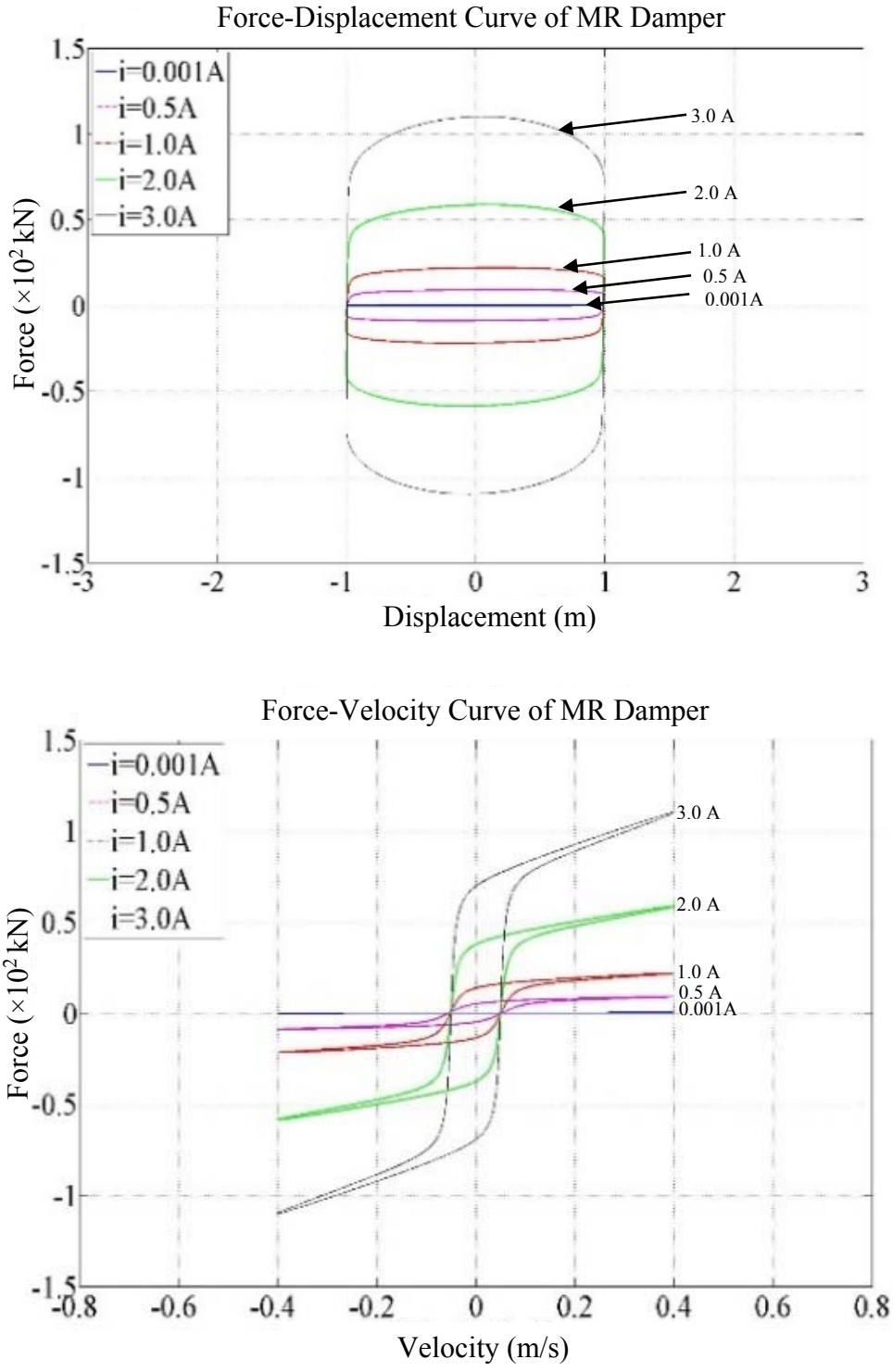

Figure 5.14 Variation of MR damper force at amplitude = 1.0 m (*3.28 ft*), frequency = 0.6 rad/s.

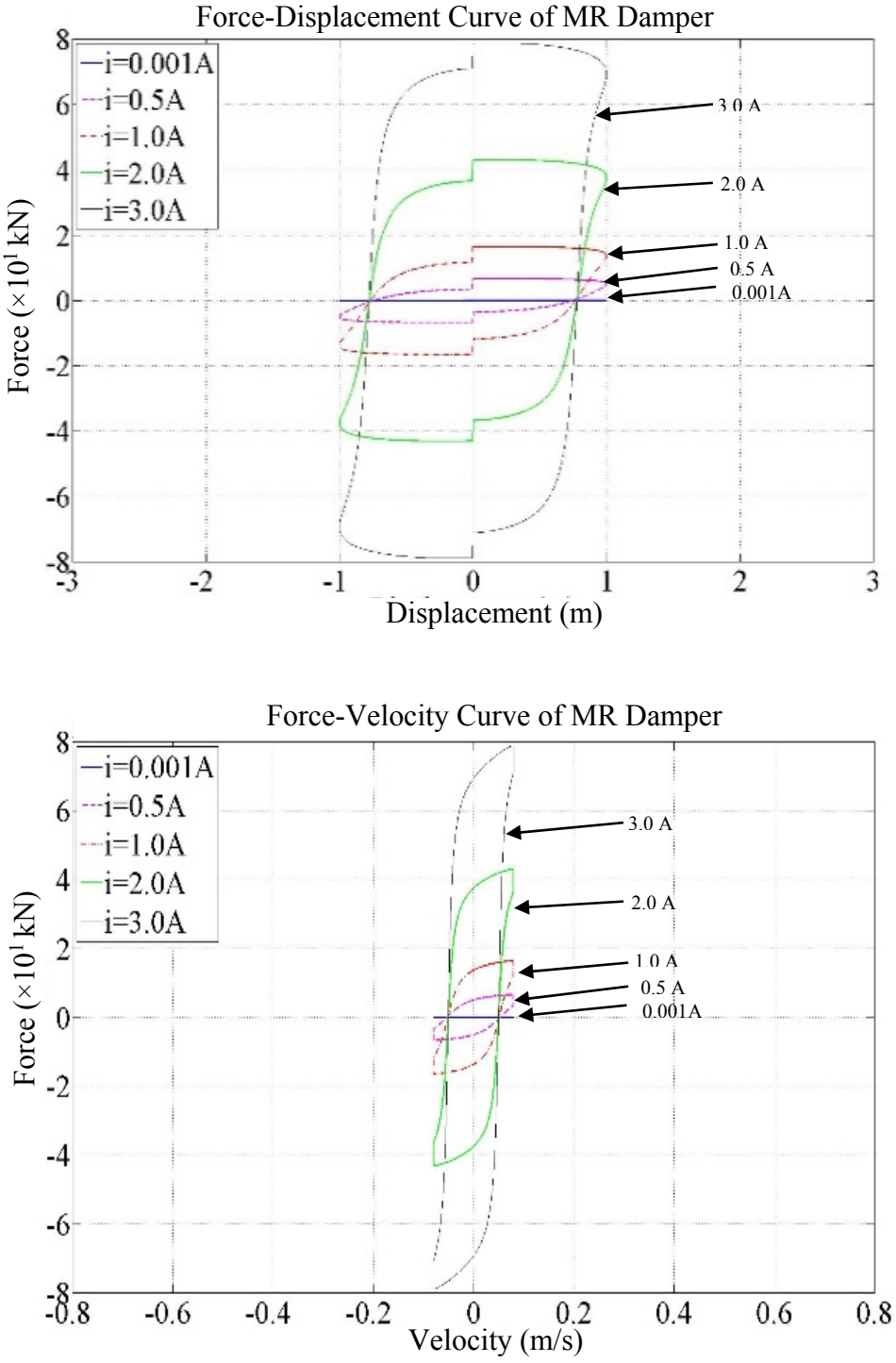

Figure 5.15 Variation of MR damper force at amplitude = 1.0 m (*3.28 ft*), frequency = 0.08 rad/s.

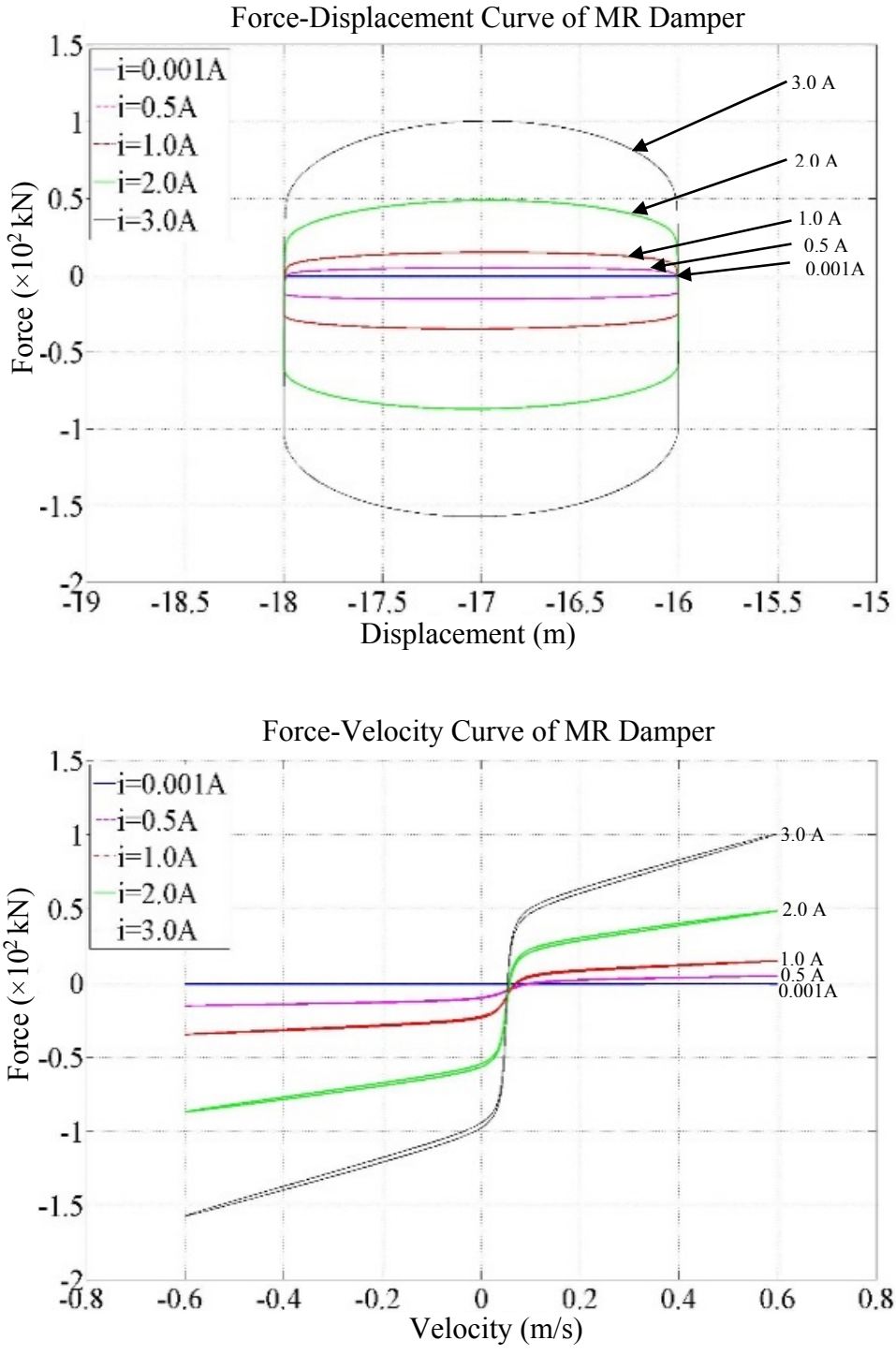

Figure 5.16 Variation of primary MR damper force at amplitude = 1.0 m (*3.28 ft*), frequency = 0.6 rad/s, displacement offset = -17.0 m (*-55.77 ft*).

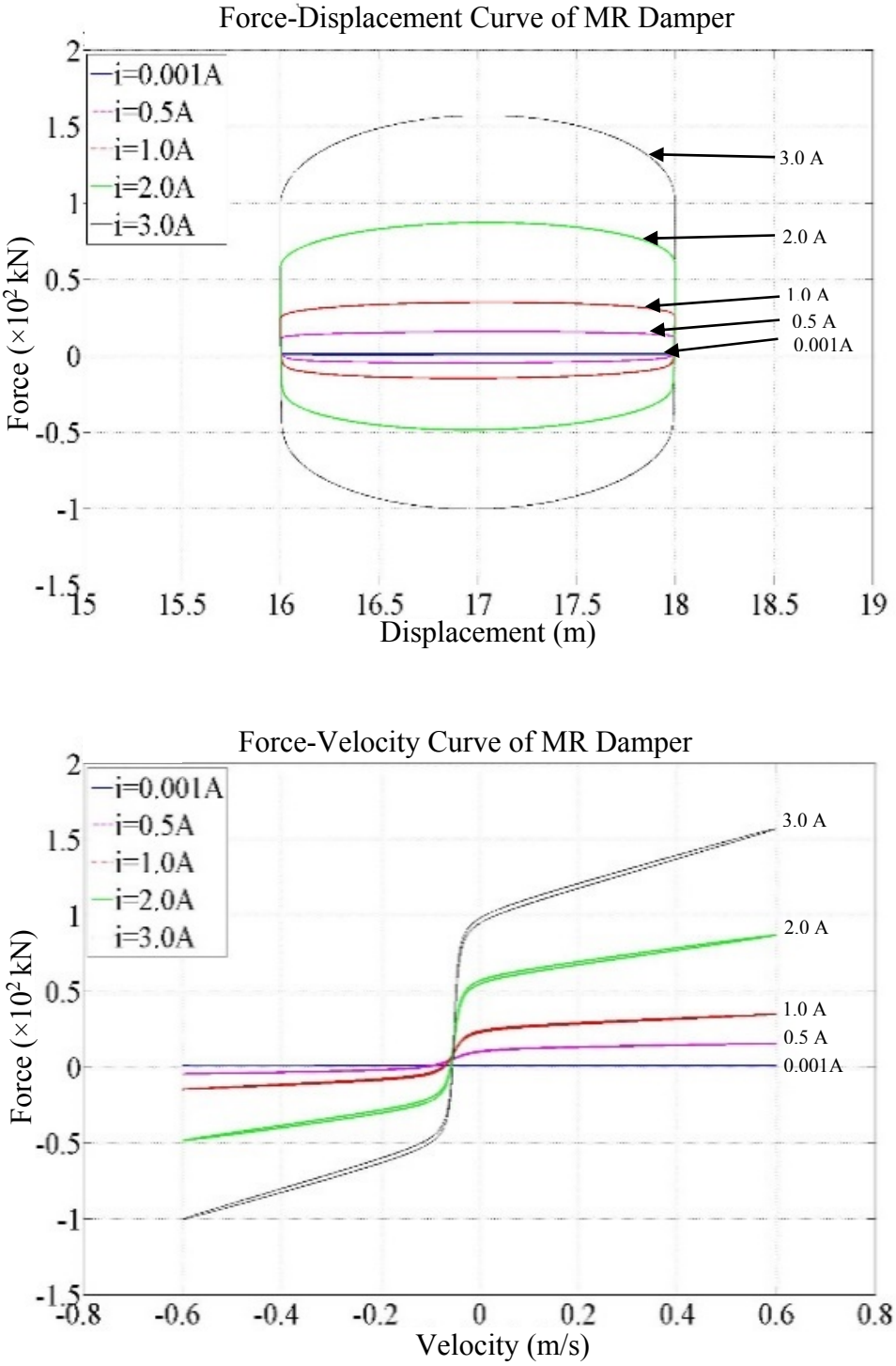

Figure 5.17 Variation of secondary MR damper force at amplitude = 1.0 m (*3.28 ft*), frequency = 0.6 rad/s, displacement offset = +17.0 m (*55.77 ft*).

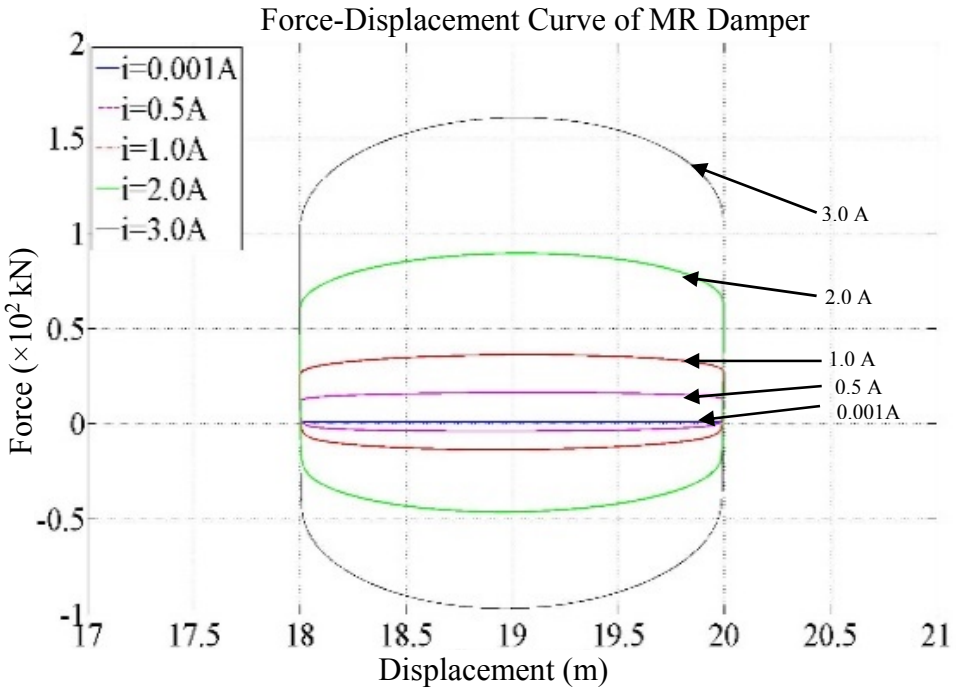

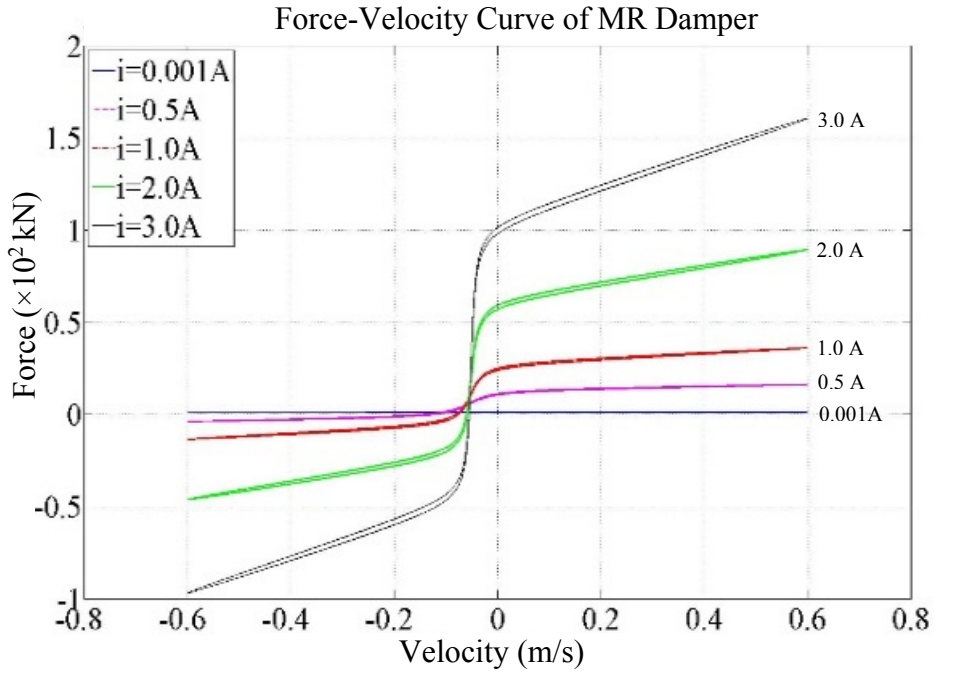

Figure 5.18 Variation of secondary MR damper force at amplitude = 1.0 m (*3.28 ft*), frequency = 0.6 rad/s, displacement offset = +19.0 m (*62.34 ft*).

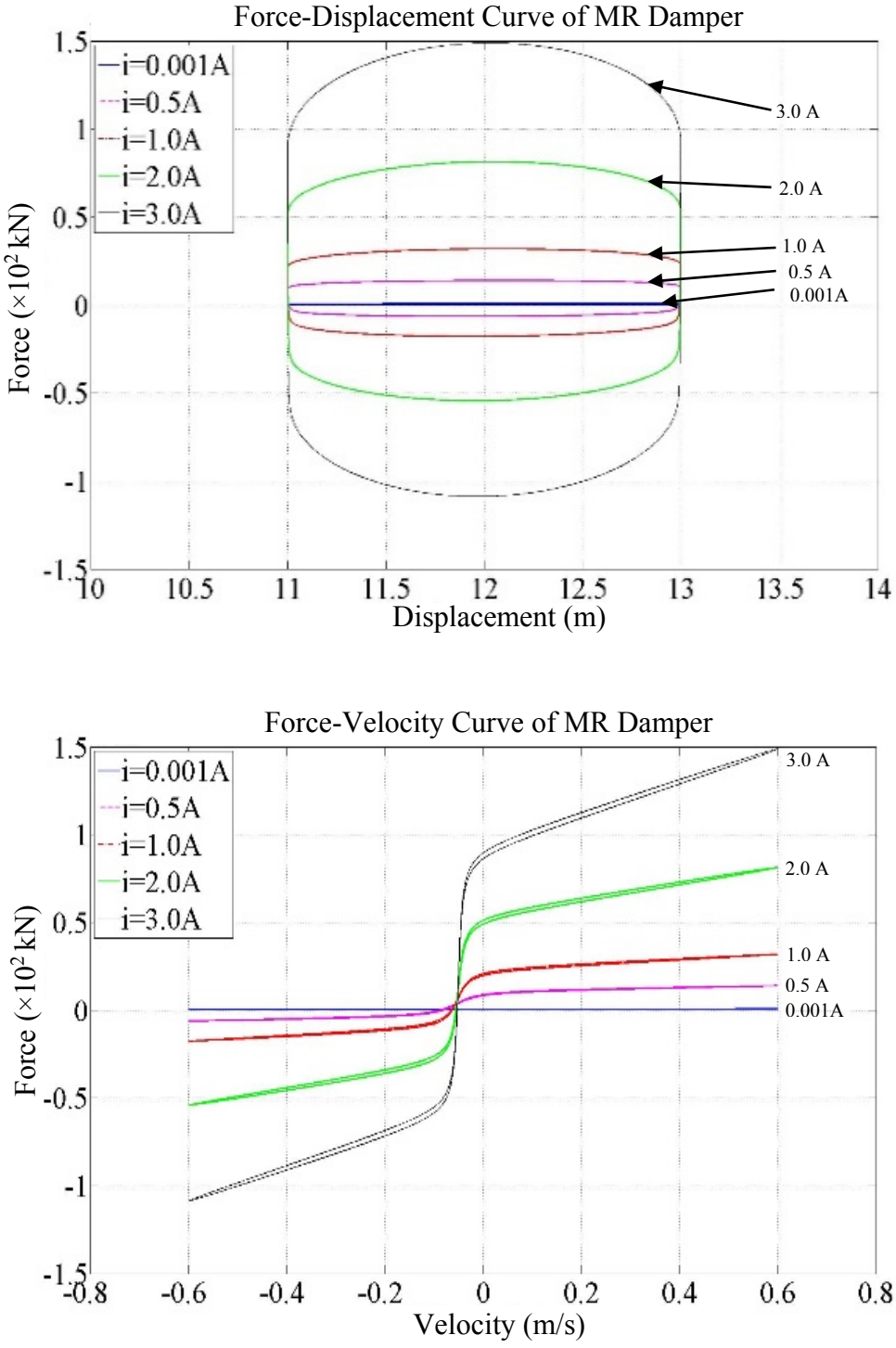

Figure 5.19 Variation of secondary MR damper force at amplitude = 1.0 m (*3.28 ft*), frequency = 0.6 rad/s, displacement offset = +12.0 m (*39.37 ft*).

5.8 Hull-Riser-Tendon Coupled Analysis for EFCC

The coupling of dynamic tension variation and MR damper into the conventional HP tensioner after considered the viscous frictional fluids condition was developed in this Subsection by using the CHARM3D numerical scheme as developed in the Subsection 5.5. The modeling of host platform to be used in this coupling analysis is a *generic* type tension-leg platform (TLP) as illustrated in Fig. 5.20.

The principal dimensions of the TLP platform are tabulated in Table 5.3 (Kim et al., 2001; Yang, 2009) and the hull load condition are listed in Table 5.4 (Yang, 2009). In this research, the FE equations for the line members are coupled with the TLP platform dynamics by using the linear and rotational spring and dashpot (Garrett, 1982) for the eight tendons, hydro-pneumatic riser tensioner (Yang and Kim, 2010) for the seven production TTRs, and single top tensioned drilling riser, as listed in Table 5.5. The MR dampers, with the capacity of single unit is up to ~150 kN (*~33.7 kips*) as proposed in Table 5.2, are working corporately with the drilling riser as conceptually illustrated in the Fig. 5.12.

The hull-riser-tendon coupled analysis for EFCC are conducted are the following settings:

(i) TLP host platform with sinusoidal wave input (as the *base-case*)

(ii) TLP host platform with sea condition input, as tabulated in Table 5.6.

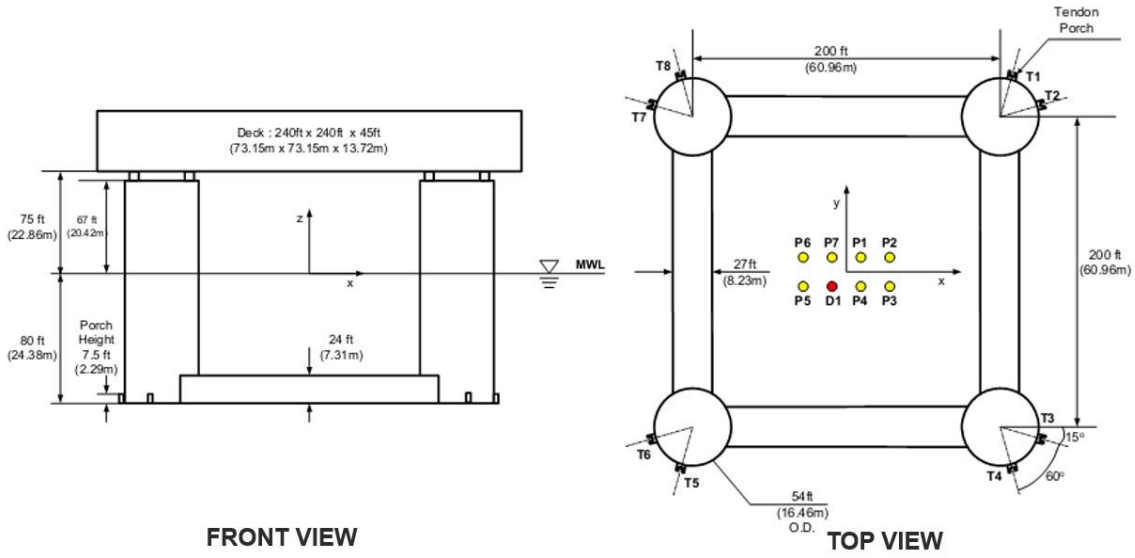

Figure 5.20 The layouts of generic tension leg platform (TLP).

Table 5.3 Principal dimensions of the generic TLP model.

Water Depth	914.36 m *(3000 ft)*
Number of column	4
Column cross section diameter	16.46 m *(54 ft)*
Column center to center distance	60.96 m *(200 ft)*
Column freeboard	20.42 m *(67 ft)*
Pontoon breadth	8.23 m *(27 ft)*
Pontoon height	7.31 m *(24 ft)*
Height of deck bottom from MWL*	22.86 m *(75 ft)*
Deck height	12.19 m *(40 ft)*
Draft	24.38 m *(80 ft)*
Total weight	24,157 MT *(53,257 kips)*

Table 5.3 Continued.

Tendon pretension at the top	7,040 MT *(15,520 kips)*
Riser pretension at the top	1,972 MT *(4,348 kips)*
Displacement	32,775 MT *(72,257 kips)*

*MWL = Mean water level

Table 5.4 Hull load condition at in-place draft.

Vertical center of gravity from MWL	8.56 m *(28.08 ft)*
Vertical center of buoyancy from MWL	-15.18 m *(-49.80 ft)*
Roll radius of gyration	33.19 m *(108.89 ft)*
Pitch radius of gyration	33.19 m *(108.89 ft)*
Yaw radius of gyration	32.40 m *(106.30 ft)*
Wind load coefficient	3.18 kN/(m/sec)^2 *(0.664 kips/(ft/sec)^2)*
Center of pressure from MWL	38.10 m *(125.00 ft)*

Table 5.5 Configurations of the tendons and TTRs.

		Top-end Coordinate			Bottom-end Coordinate			
	No.	X (m) *(ft)*	Y (m) *(ft)*	Z (m) *(ft)*	X (m) *(ft)*	Y (m) *(ft)*	Z (m) *(ft)*	T_o (MT) *(kips)*
Tendon	1	33.01 *(108.3)*	39.90 *(130.9)*	-22.10 *(-72.5)*	33.01 *(108.3)*	39.90 *(130.9)*	-921.26 *(-3022.5)*	880.0 *(1940.0)*
	2	39.90 *(130.9)*	33.01 *(108.3)*	-22.10 *(-72.5)*	39.90 *(130.9)*	33.01 *(108.3)*	-921.26 *(-3022.5)*	880.0 *(1940.0)*
	3	39.90 *(130.9)*	-33.01 *(-108.3)*	-22.10 *(-72.5)*	39.90 *(130.9)*	-33.01 *(-108.3)*	-921.26 *(-3022.5)*	880.0 *(1940.0)*
	4	33.01 *(108.3)*	-39.90 *(-130.9)*	-22.10 *(-72.5)*	33.01 *(108.3)*	-39.90 *(-130.9)*	-921.26 *(-3022.5)*	880.0 *(1940.0)*
	5	-33.01 *(-108.3)*	-39.90 *(-130.9)*	-22.10 *(-72.5)*	-33.01 *(-108.3)*	-39.90 *(-130.9)*	-921.26 *(-3022.5)*	880.0 *(1940.0)*
	6	-39.90 *(-130.9)*	-33.01 *(-108.3)*	-22.10 *(-72.5)*	-39.90 *(-130.9)*	-33.01 *(-108.3)*	-921.26 *(-3022.5)*	880.0 *(1940.0)*
	7	-39.90 *(-130.9)*	33.01 *(108.3)*	-22.10 *(-72.5)*	-39.90 *(-130.9)*	33.01 *(108.3)*	-921.26 *(-3022.5)*	880.0 *(1940.0)*
	8	-33.01 *(-108.3)*	39.90 *(130.9)*	-22.10 *(-72.5)*	-33.01 *(-108.3)*	39.90 *(130.9)*	-921.26 *(-3022.5)*	880.0 *(1940.0)*

Table 5.5 Continued.

		Top-end Coordinate			Bottom-end Coordinate			
	No.	X (m) *(ft)*	Y (m) *(ft)*	Z (m) *(ft)*	X (m) *(ft)*	Y (m) *(ft)*	Z (m) *(ft)*	T_o (MT) *(kips)*
D. Riser*	1	-2.29 *(-7.5)*	-2.29 *(-7.5)*	0.00 *(0.0)*	-2.29 *(-7.5)*	-2.29 *(-7.5)*	-914.36 *(-3000)*	330.7 *(729.0)*
Production Riser	1	2.29 *(7.5)*	2.29 *(7.5)*	0.00 *(0.0)*	2.29 *(7.5)*	2.29 *(7.5)*	-914.36 *(-3000)*	234.5 *(517.0)*
	2	6.86 *(22.5)*	2.29 *(7.5)*	0.00 *(0.0)*	6.86 *(22.5)*	2.29 *(7.5)*	-914.36 *(-3000)*	234.5 *(517.0)*
	3	6.86 *(22.5)*	-2.29 *(-7.5)*	0.00 *(0.0)*	6.86 *(22.5)*	-2.29 *(-7.5)*	-914.36 *(-3000)*	234.5 *(517.0)*
	4	2.29 *(7.5)*	-2.29 *(-7.5)*	0.00 *(0.0)*	2.29 *(7.5)*	-2.29 *(-7.5)*	-914.36 *(-3000)*	234.5 *(517.0)*
	5	-6.86 *(-22.5)*	-2.29 *(-7.5)*	0.00 *(0.0)*	-6.86 *(-22.5)*	-2.29 *(-7.5)*	-914.36 *(-3000)*	234.5 *(517.0)*
	6	-6.86 *(-22.5)*	2.29 *(7.5)*	0.00 *(0.0)*	-6.86 *(-22.5)*	2.29 *(7.5)*	-914.36 *(-3000)*	234.5 *(517.0)*
	7	-2.29 *(-7.5)*	2.29 *(7.5)*	0.00 *(0.0)*	-2.29 *(-7.5)*	2.29 *(7.5)*	-914.36 *(-3000)*	234.5 *(517.0)*

*D. Riser = Drilling Riser

Table 5.6 Wave and current profiles of the extreme condition.

Significant wave height, H_s		15.79 m *(51.8 ft)*
Peak period, T_p		15.4 s
Overshooting parameter, γ		2.4
Main direction of waves		0 deg
Direction of current		0 deg
Current profile	Depth	Velocity
	0 m *(0 ft)*	2.41 m/s *(7.9 ft/s)*
	-50.44 m *(-165.5 ft)*	1.80 m/s *(5.9 ft/s)*
	-100.89 m *(-331.0 ft)*	0.00 m/s *(0.0 ft/s)*
	-914.36 m *(-3000.0 ft)*	0.00 m/s *(0.0 ft/s)*

5.8.1 TLP Hull-Riser-Tendon Coupled Analysis with EFCC under Sinusoidal Wave

The simulated characteristic dynamic responses of the hydro-pneumatic (HP) tensioner with TLP platform are shown in Fig. 5.21. The HP tensioner was excited by a sinusoidal wave loadings input.

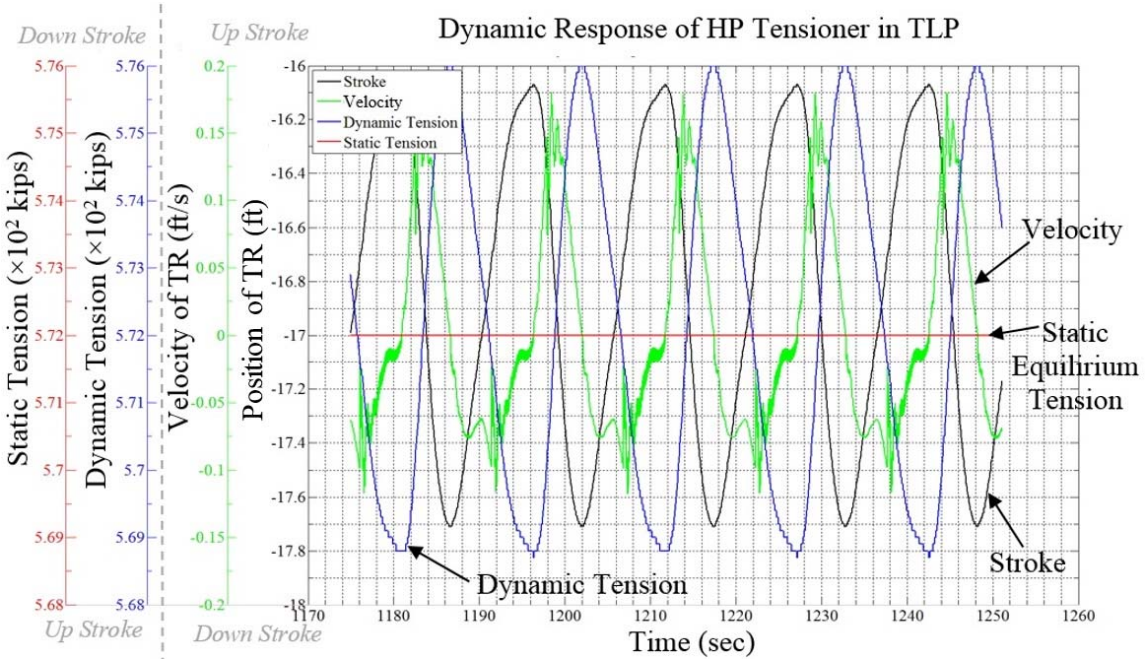

Figure 5.21 The dynamic response of HP tensioner for the case of TLP.

The position of tensioner ring (TR) after achieving the *steady-state* is at around -17.0 ft (*-5.18 m*) (negative sign is referred to that the TR is traveling back-and-forth in the range below the initial mid-point position which is at 0 ft (*0 m*)). The dynamic displacement is from -16.1 ft (*-4.91 m*) to -17.7 ft (*-5.39 m*) and the velocity of tensioner ring is from ~ -0.125 ft/s (~ *-0.038 m/s*) to ~0.175 ft/s (*~0.053 m/s*). It can be found that

the displacement and velocity are out of phase, with the maximum velocities occurring as the tensioner ring reaches its *steady-state equilibrium* position at ~ -17.0 ft (~ *-5.18 m*). There is noteworthy that the velocity of the tensioner ring is far below 1.0 ft/s (*0.305 m/s*) in the tension-leg platform (TLP) for the reason that the platform heave motion is constrained by the highly stiffed tendons.

In this TLP case, the static equilibrium tension is around 572 kips (*2544 kN*), which is lower than the pretension listed in the Table 5.5 because the total weights, payloads, and offset effects have been considered into this static equilibrium tension. The dynamic tension variations (from ~569 kips (*~2531 kN*) to ~576 kips (*~2562 kN*)) is mainly caused by the changing ratio of gas volume $\Delta V_A / V_{A_0}$ in between the displaced volume and the total gas volume stored in the high pressure NPVs, as stated in the Eqn. (5.11).

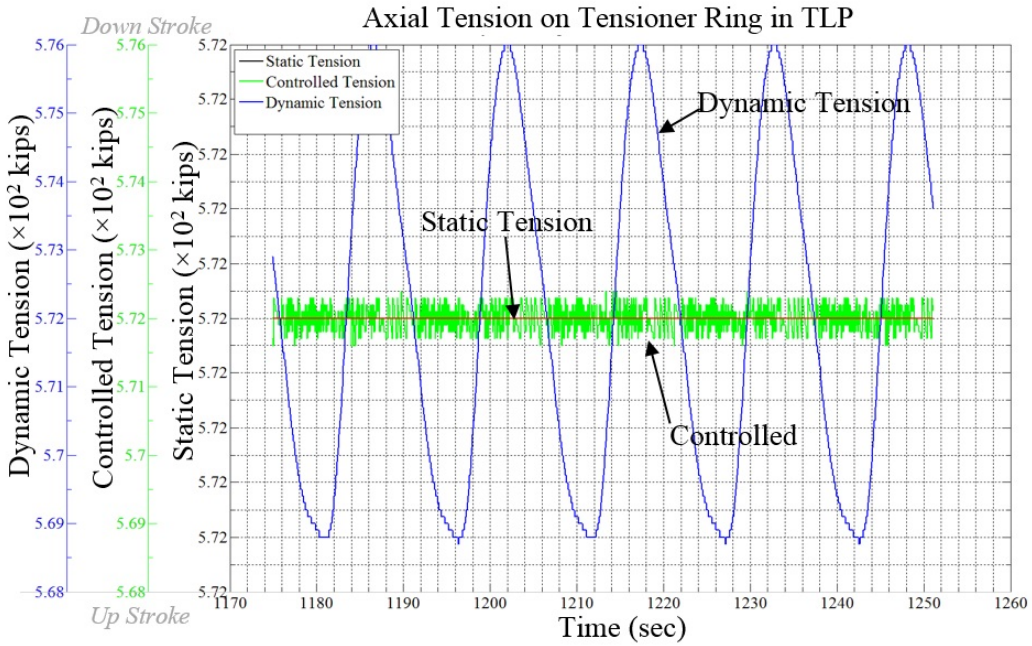

Figure 5.22 Axial Tension on TLP tensioner ring.

It can be found that the dynamic tension variations in the TLP case is minor because the velocity of the tensioner ring is very small, as shown in Fig. 5.21. The EFCC is proposed to further reduce the variations of dynamic tension. The controlled effects on of EFCC scheme on the dynamic tension is shown in Fig. 5.22 and the tension-stroke curve is shown in Fig. 5.23. In this case, the dynamic tension can be suppressed as much as ~88% (tension variation from ~7 kips (*~31.14 kN*) to less than 1 kips (*4.45 kN*)) by using the EFCC scheme.

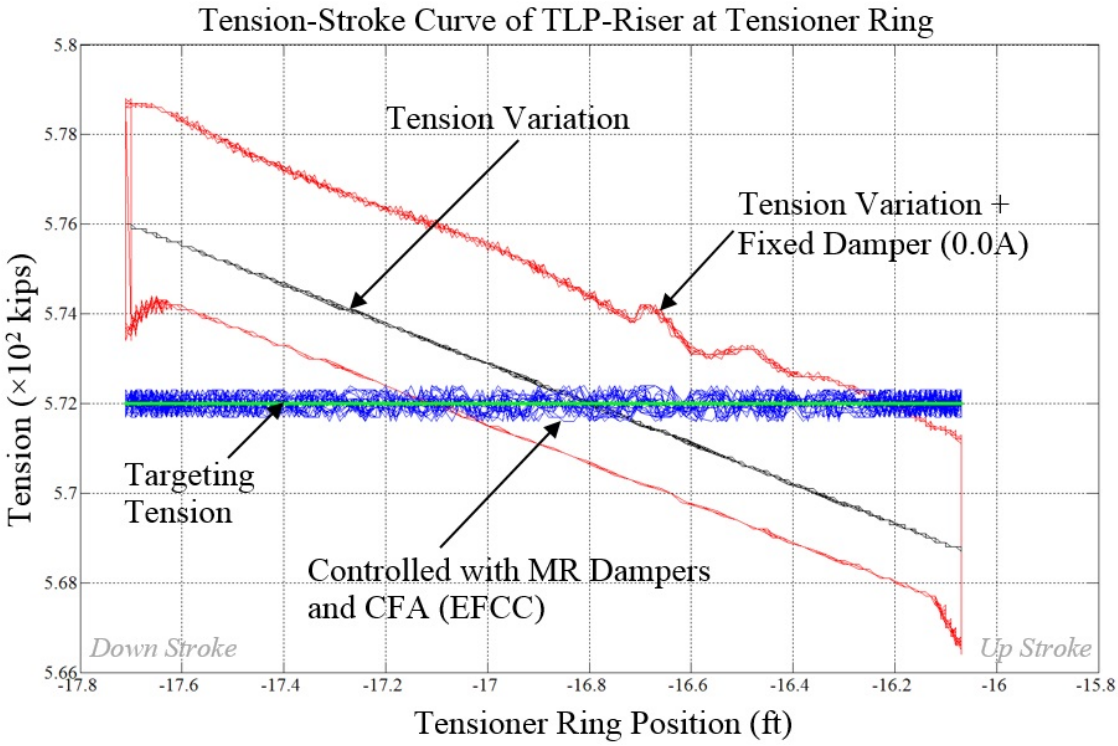

Figure 5.23 Tension-stroke curve of TLP-riser at the tensioner ring under steady-state (for the TR's position range from ~ -16.05 ft (~ *-4.89 m*) to ~ -17.70 ft (~ *-5.39 m*)).

The tension-stroke curve for the simulation started from initial position (transient state) to the steady-state is shown in Fig. 5.24. The EFCC was activated at a threshold value F_{Th}, which is set to the targeting tension in this case. The incorporation of MR dampers with constant force actuators (CFA), as conceptually illustrated in Fig. 5.12, are acting as high-capacity force compensator. Since the EFCC scheme is proposed for precise tension control, therefore it will be activated only under the situation when the axial tension variation must be controlled in very strict limits, such as during the offshore precision drilling. Therefore, a practical EFCC system can be designed as a separated module that can be mounted / dismounted on the conventional HP tensioner.

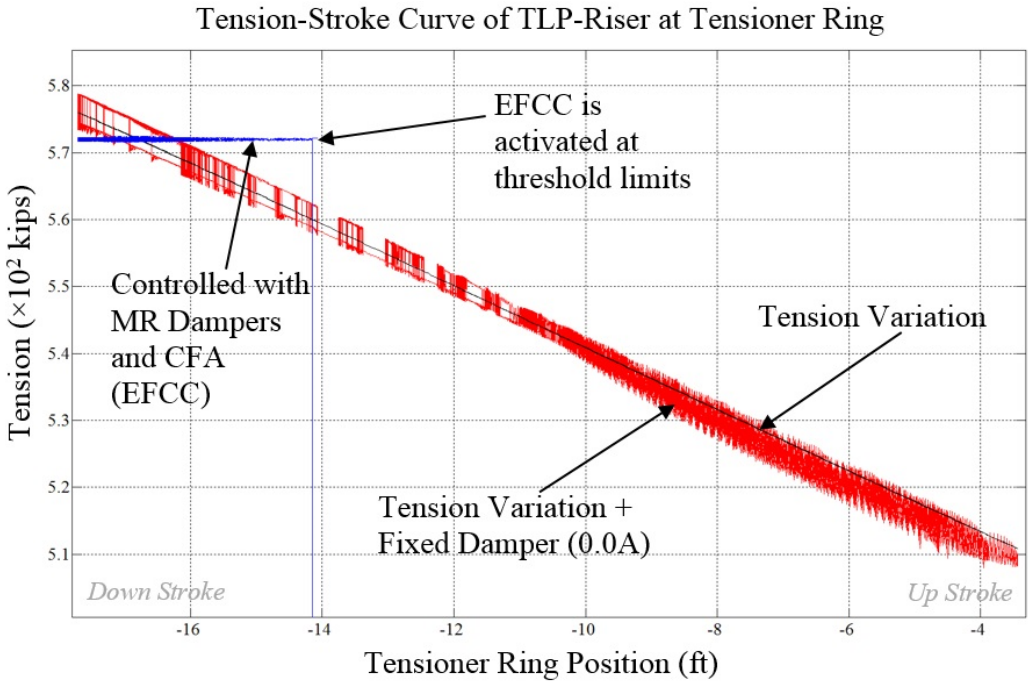

Figure 5.24 Tension-stroke curve of TLP-riser at the tensioner ring from initial condition of simulation.

The required force F_{req} and combined MR damper (MRD) output forces ($F_{MR}^{P} + F_{MR}^{S}$) in time series after the EFCC was activated are shown in Fig. 5.25. A certain range from 1170 sec to 1250 sec is magnified in Fig. 5.26. This can be found that the combined magneto-rheological damper (MRD) forces from *primary* MRD and *secondary* MRD matched with the required force F_{req} with the deviation less than 2%. The combined MRD force is acting in the opposite direction of constant actuator force in order to fine-tune the compensated force to be transfered to the tensioner ring.

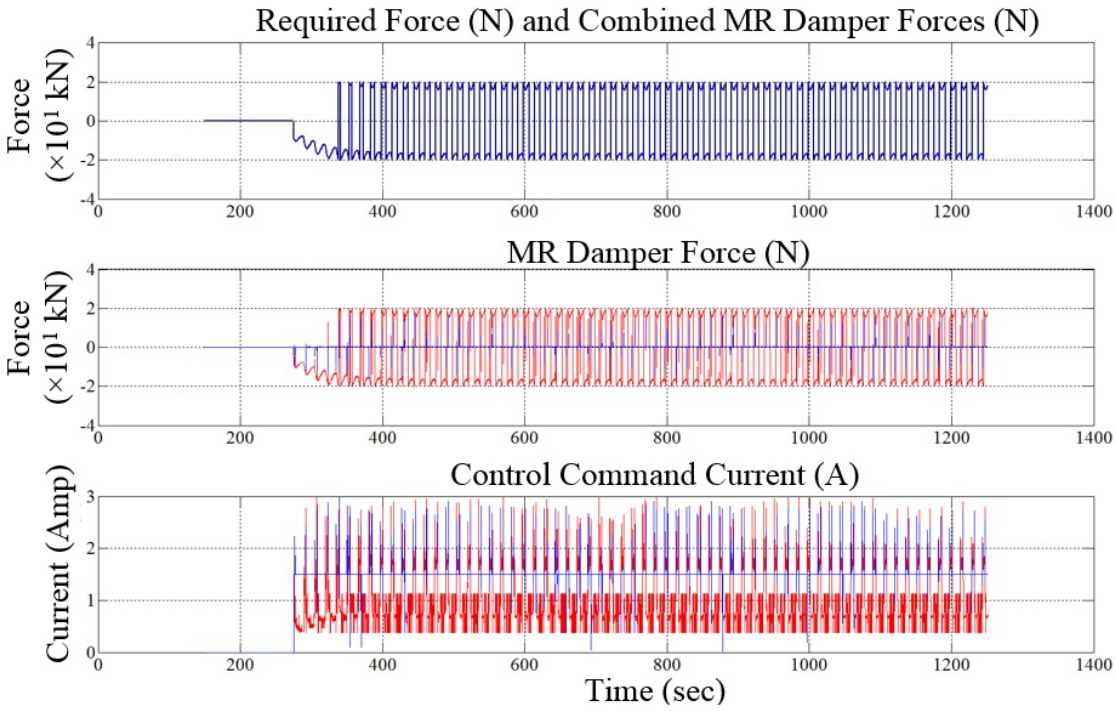

Figure 5.25 Controlled force outputs and control current.

In this case, as shown in Fig. 5.26, the *primary* MRD is the predominant resistive force provider while the *secondary* MRD is activated only if the limitation of primary MRD is met. This is noteworthy that the combined MRD force is a trade-off in between the tensioner properties (force variation), the capacity of the selected MR dampers, the targeting tension, and the characteristics of constant force actuator. Therefore, the combined damping force limits must be identified for each application and the MR dampers with appropriate operational limits.

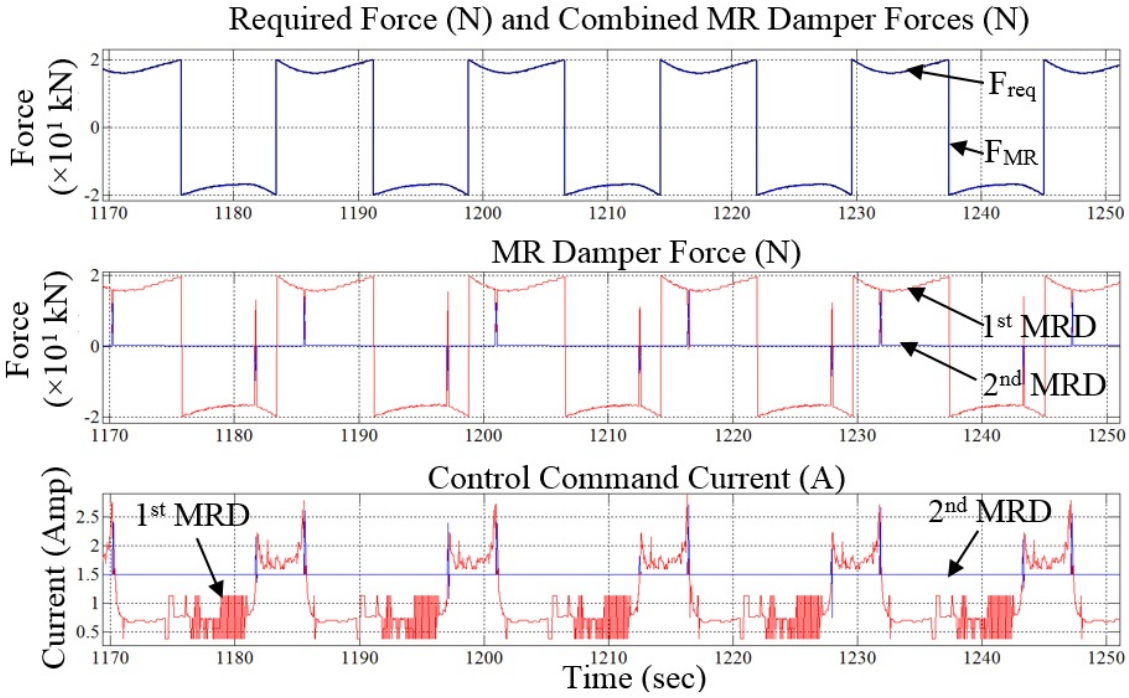

Figure 5.26 Controlled force outputs and control current (for the range from 1170 sec to 1250 sec).

5.8.2 TLP Hull-Riser-Tendon Coupled Analysis with EFCC under Sea-Conditions

The characteristic dynamic responses of the hydro-pneumatic (HP) tensioner with TLP host platform, under the excitation of sea conditions (in Table 5.6), are shown in Fig. 5.27. The position of tensioner ring (TR) was traveling from -16.00 ft (*-4.88 m*) to -12.25 ft (*-3.73 m*) (in the simulation time range from 4520 sec to 4660 sec) and the velocity of tensioner ring was from ~ -0.210 ft/s (~ *-0.064 m/s*) to ~0.175 ft/s (*~0.053 m/s*). It can be found that the position changes and velocity of the tensioner ring were out of phase, with the velocities reach at zero when the tensioner ring reaches its local extrema. The velocity of the tensioner ring is far below 1.0 ft/s (*0.305 m/s*) in the

tension-leg platform (TLP) for the reason that the platform heave motion is constrained by the highly stiffed tendons.

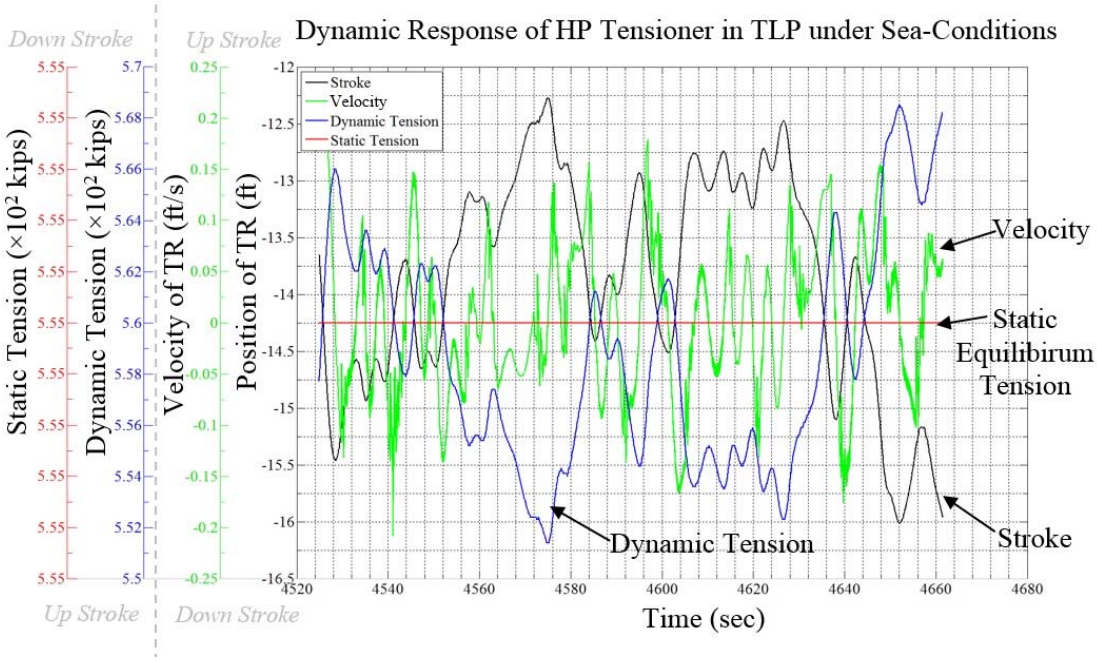

Figure 5.27 Dynamic responses of HP tensioner for the case of TLP under sea-conditions.

In the TLP case, the dynamic tension variations, from ~551 kips (*~2450 kN*) to ~569 kips (*~2531 kN*), (in the time range from 4520 sec to 4660 sec) is mainly caused by the changing ratio of gas volume $\Delta V_A / V_{A_0}$ in between the displaced volume and the total gas volume stored in the high pressure NPVs, as stated in the Eqn. (5.11). The EFCC is proposed to further reduce the variations of dynamic tension. The controlled effects on of EEFC scheme on the dynamic tension is shown in Fig. 5.28 and the

tension-stroke curve is shown in Fig. 5.29. In this case, the dynamic tension can be suppressed as much as ~94%, where the tension variations reduced from ~18 kips (*~80 kN*) to less than 1 kips (*4.45 kN*)) by using the EFCC scheme.

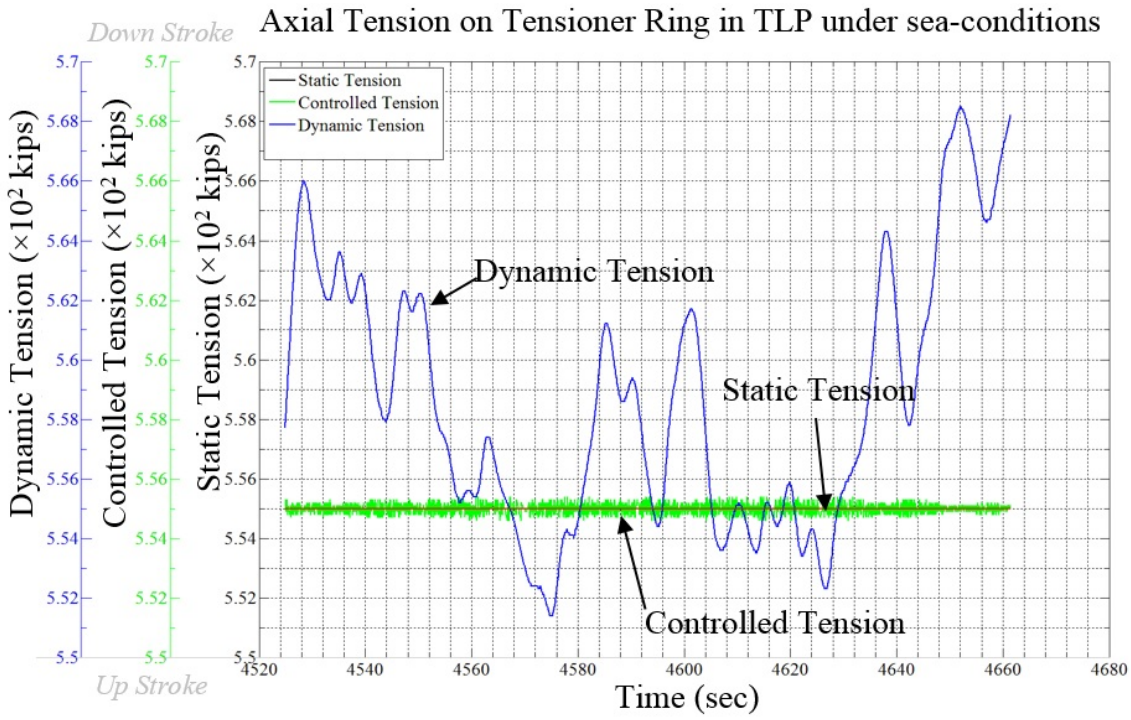

Figure 5.28 Axial tension on TLP tensioner ring under sea-conditions.

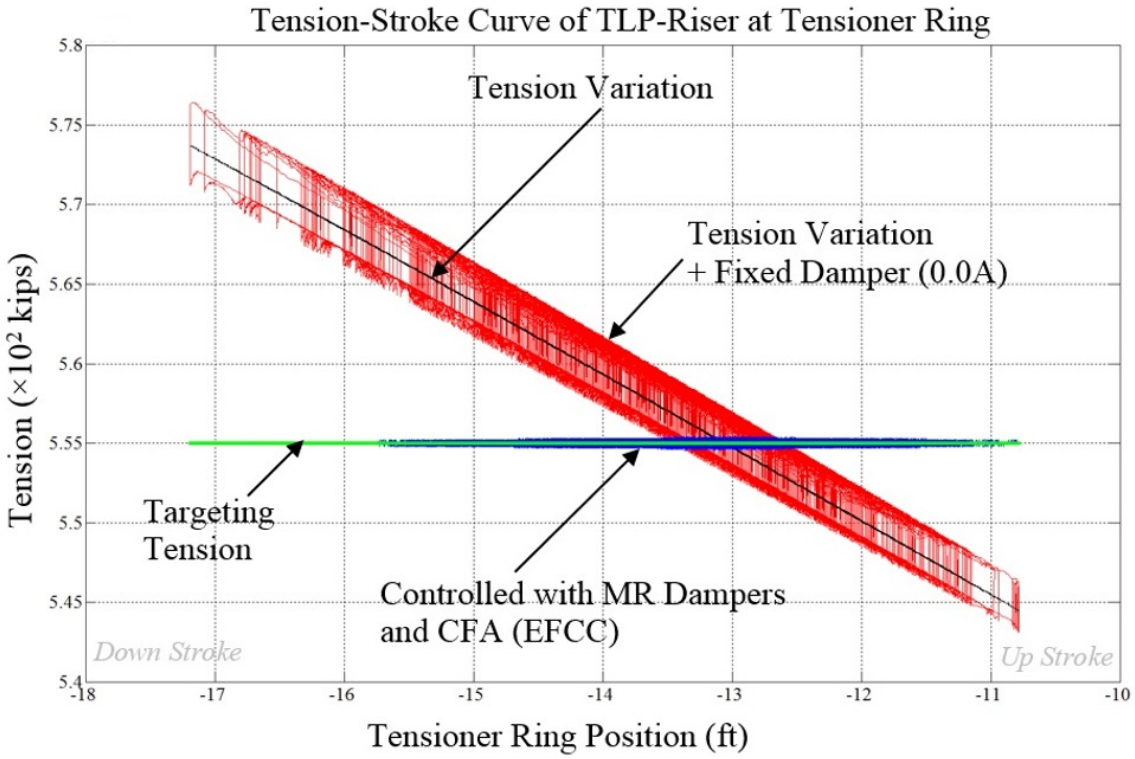

Figure 5.29 Tension-stroke curve of TLP-riser at the tensioner ring under sea conditions.

The tension-stroke curve for the simulation started from the initial position (transient state) to the steady-state is shown in Fig. 5.30. This result implied that the axial tension on the tension ring can be controlled more precisely in the TLP. The EFCC was activated at a threshold value F_{Th}, which is the targeting tension in this case.

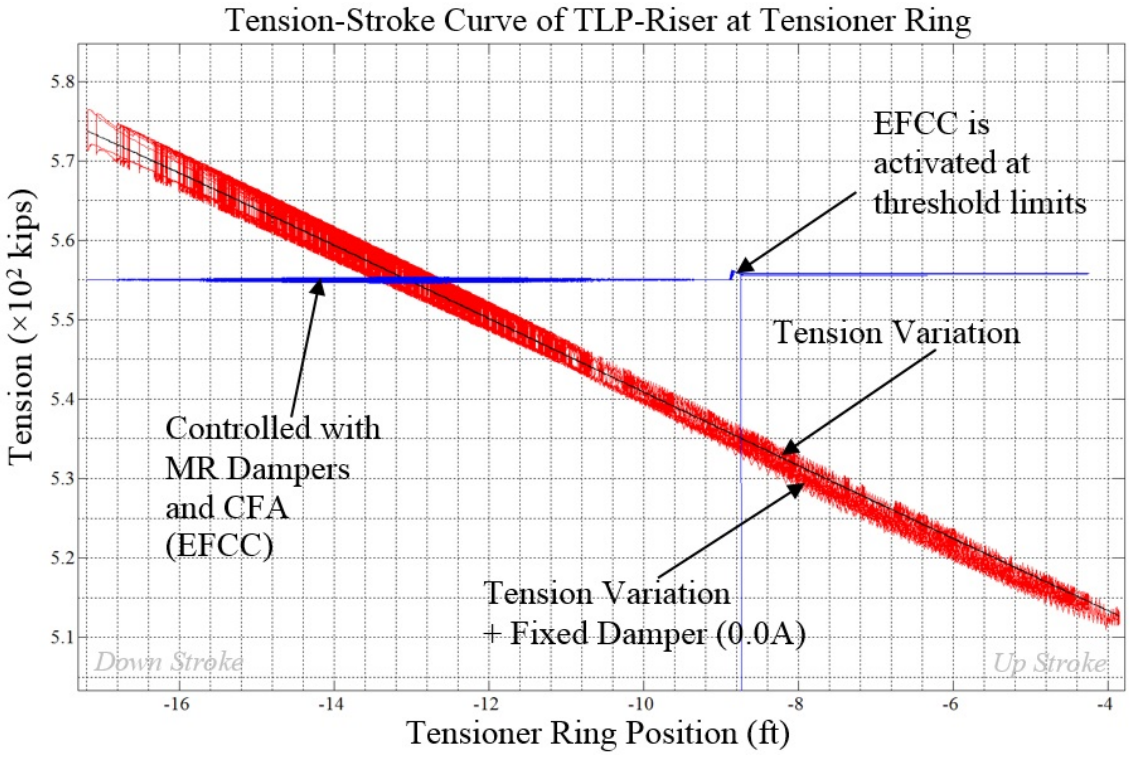

Figure 5.30 Tension-stroke curve of TLP riser at the tensioner ring, under the sea condition, from initial condition.

The required force F_{req} and combined MR damper output forces ($F_{MR}^{P} + F_{MR}^{S}$) in time series after the EFCC was activated are shown in Fig. 5.31. A certain range from 4520 sec to 4660 sec is magnified in Fig. 5.32. It can be found that the combined magneto-rheological damper (MRD) force from *primary* MRD and *secondary* MRD matched with the required force F_{req} with the deviation less than 2%. The combined MRD force is acting in the opposite direction of actuator constant force in order to fine-tune the compensated tension to be transferred to the tensioner ring.

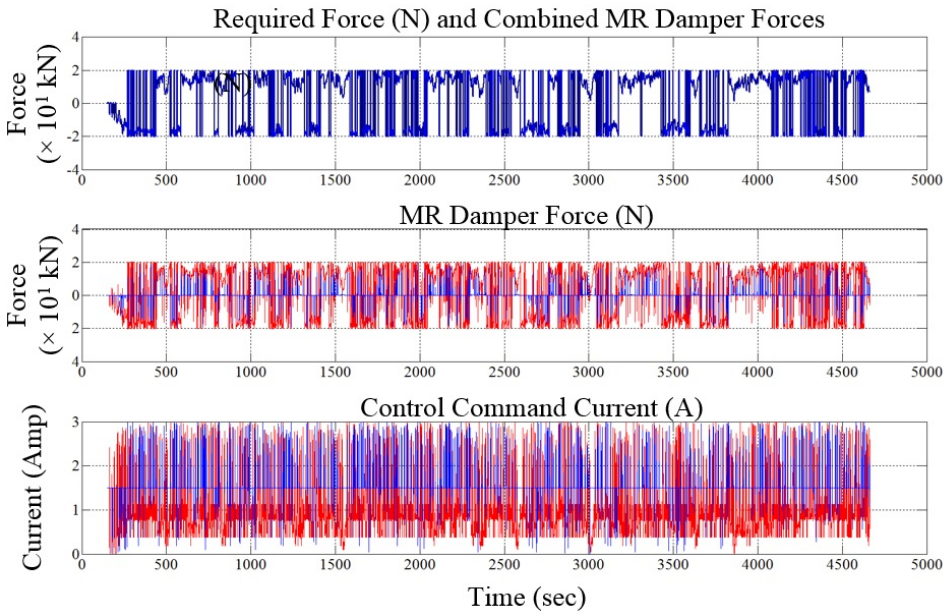

Figure 5.31 Controlled force outputs and control current under the sea conditions.

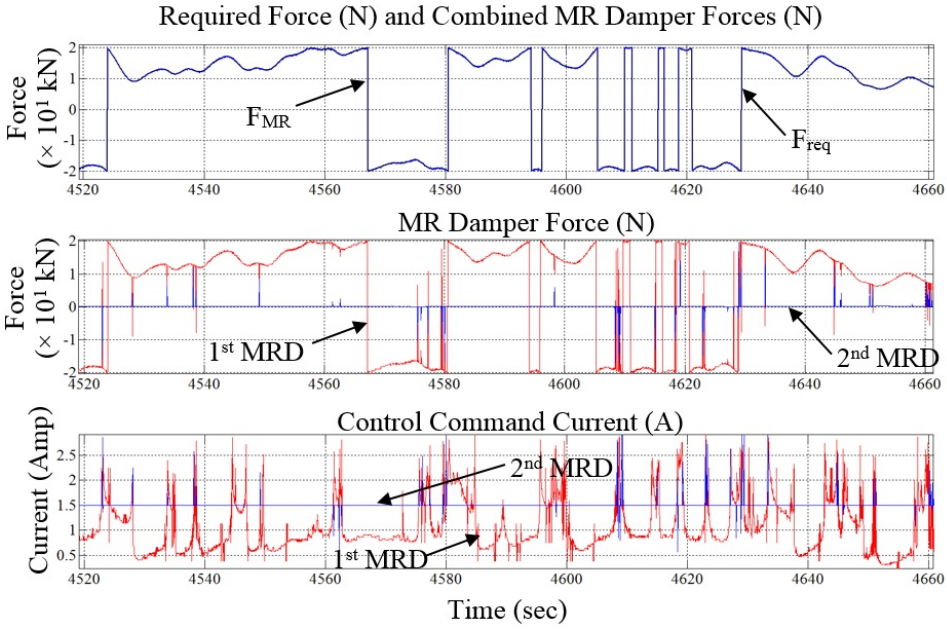

Figure 5.32 Controlled force outputs and control current (for the range from 4520 sec to 4660 sec), under the sea conditions.

6. PARAMETRIC RESONANCE AND STABILITY ANALYSIS OF TOP TENSION RISER

6.1 Introduction

The API RP 2RD suggests that TTRs with relatively stiff tensioning systems may experience tension fluctuations that are significant relative to the mean tension, leading to significant changes in the lateral stiffness (API, 1998; Xiao and Yang, 2014). The parametric resonance occurs when a system is parametrically excited and oscillates at one of its resonant frequencies. Parametric excitation differs from forcing since the action appears as a time varying modification on a system parameter (Radhakrishnan et al., 2007). A small excitation can produce a large response even when the frequency of the excitation is significantly different from the linear natural frequencies of the system (Nayfeh and Balachandran, 2008).

Patel and Park (1991) reported on the investigation in to the dynamics of tethers with reduced pretension to facilitate payload increase over conventional design of a TLP and found that the wave induced time-varying axial tension becomes important in its dynamics when the pretension is reduced. They revealed that the time-varying axial tension variation cause the tether to undergo parametric oscillations described by the Mathieu equation. Simos and Pesce (1997) conducted a dynamic modeling of TLP's tethers considering the tension variation along the length due to the submerged weight. Chatjigeogiou and Mavrakos (2002) studied then nonlinear dynamic response in the transverse direction of long slender structures subjected to parametric excitation at the

top of the host platform. The analytical approach shows that the dynamic lateral response is governed by the effects originated from the coupling of modes in transverse direction.

Mathieu's equation was applied by Zhang et al. (2002) in the investigation of the parametric response excited by the interactions of tension variation and lateral dynamics of tendons. Mathieu's instability could be triggered at a certain model of tendon lateral motion dependent on the magnitude of fluctuation of the tendon tension and damping of tendon transverse motions. Chandrasekaran et al. (2006) studied effects of tension variation due to the increased on water depth on the stability of TLP and found that the increased tendon tension leads to platform stability and also improves the stability due to the increased hydrodynamic loading contributing to added mass. Wang and Zou (2006) discussed the approach of finding the maximum allowable tension variations by using the Mathieu's instability diagram for a robust tendon design in the industry practice. Radhakrishnan et al. (2007) studied the motion of a tethered spherical buoy subjected to incident regular waves in a wave tank. They reported that the parametric instability was observed when the period of the wave generated was close to one-half of the natural period of the buoy. Yang et. al (2013a) studied the parametric resonance of a TTR in irregular waves based on multi-frequency excitation and a more general Hill's equation. They concluded that the single-frequency excitation method, by Mathieu's equation, predicts that the lower vibration mode is more likely to be excited, whereas the multi-frequency excitation method, by Hill's equation, predicted that the higher vibration mode is more likely to fall into an unstable zone.

The main objectives of this Section are:

(i) to study Mathieu's stability diagram and coefficients for the prediction of TTR's stability;

(ii) to identify effects of dynamic tension variation in the stability prediction;

(iii) to determine TTR's stability improvement after implementing the MR damper and its control scheme in order to suppress the riser tension variations.

6.2 Mathieu's Stability Diagram

The Mathieu equation is a special case of Hill's equation that is a linear equation with a periodic coefficient. The standard form for Hill's equation is (Koo et al., 2004):

$$\ddot{z} + \left(a + p\left(t\right)\right)z = 0 \tag{6.1}$$

when $p\left(t\right)$ is periodic, then it is known as Hill's equation. For the special case;

$$p\left(t\right) = b\cos t \tag{6.2}$$

$$\ddot{z} + \left(a + b\cos t\right)z = 0 \tag{6.3}$$

It is referred to as the un-damped Mathieu's equation. A general damped Mathieu's equation is shown as follows:

$$\ddot{z} + c\dot{z} + \left(a + b\cos t\right)z = 0 \tag{6.4}$$

This kind of nonlinear ordinary differential equation (ODE) cannot be solved explicitly. However, by fixing the damping coefficient c, zeros of infinite determinants can be found by specifying a (or b) and searching for the corresponding b (or a) that

gives a set of results sufficiently close to zero. The stability of solution of the Mathieu's equation can be graphically represented in the Mathieu stability diagram (which is also commonly known as the Ince-Strutt diagram) (Moideen, 2010). There are two methods available to find the stability boundaries for the parametric plane. The first is using the perturbation method (Stoker, 1950) and the second is using Hill's infinite determinants method.

By using Hill's infinite determinants, the stability boundaries can be obtained by the complex Fourier series representation of the 2π or 4π periodic solutions to determine the transition values of a and b (Moideen, 2010). For the case of the 2π periodic solution, the response is approximated as:

$$z(\tau) = \sum_{n=0}^{\infty} \left(a_n \cos(n\tau) + b_n \sin(n\tau) \right) \tag{6.5}$$

and for the 4π periodic solution, the response is approximated as:

$$z(\tau) = a_0 + \sum_{\substack{n=0 \\ n=\text{odd}}}^{\infty} \left(a_n \cos\left(\frac{n\tau}{2}\right) + b_n \sin\left(\frac{n\tau}{2}\right) \right) \tag{6.6}$$

After substituting Eqns. (6.5) and (6.6) into the damped Mathieu's equation, Eqn. (6.4), and setting the secular terms to zero, a set of linear homogeneous equations can be obtained in a_n and b_n. The resulting equations can be arranged in matrix form as (Moideen, 2010):

$$[P][A] = 0 \tag{6.7}$$

where $[P]$ is the parametric matrix consisting of parameters a and b, and damping c.

The determinant of $[P]$ is referred to as the Hill's determinant and $[A]$ is the matrix consisted of the Fourier coefficients of response a_n and b_n. This infinite set of homogeneous equations has non-zero solutions if the infinite determinant $[P]$ formed by the coefficients is zero. Hence, the infinite determinants for 2π and 4π are formed as, for 2π (Palazzoro, 2011):

$$\det\begin{vmatrix} a & \frac{b}{2} & 0 & 0 & 0 & 0 & 0 & 0 & 0 & \dots \\ b & a-1 & c & \frac{b}{2} & 0 & 0 & 0 & 0 & 0 & \dots \\ 0 & -c & a-1 & 0 & \frac{b}{2} & 0 & 0 & 0 & 0 & \dots \\ 0 & \frac{b}{2} & 0 & a-4 & 2c & \frac{b}{2} & 0 & 0 & 0 & \dots \\ 0 & 0 & \frac{b}{2} & -2c & a-4 & 0 & \frac{b}{2} & 0 & 0 & \dots \\ 0 & 0 & 0 & \frac{b}{2} & 0 & a-9 & 3c & \frac{b}{2} & 0 & \dots \\ 0 & 0 & 0 & 0 & \frac{b}{2} & -3c & a-9 & 0 & \frac{b}{2} & \dots \\ 0 & 0 & 0 & 0 & 0 & \frac{b}{2} & 0 & a-16 & 4c & \dots \\ 0 & 0 & 0 & 0 & 0 & 0 & \frac{b}{2} & -4c & a-16 & \dots \\ . & . & . & . & . & . & . & . & . & \dots \end{vmatrix} = 0 \tag{6.8}$$

and for 4π :

$$\det\begin{vmatrix} a-\frac{1}{4}+\frac{b}{2} & \frac{c}{2} & \frac{b}{2} & 0 & 0 & 0 & 0 & \dots \\ -\frac{c}{2} & a-\frac{1}{4}-\frac{b}{2} & 0 & \frac{b}{2} & 0 & 0 & 0 & \dots \\ 0 & 0 & a-\frac{9}{4} & \frac{3c}{2} & \frac{b}{2} & 0 & 0 & \dots \\ 0 & \frac{b}{2} & -\frac{3c}{2} & a-\frac{9}{4} & 0 & \frac{b}{2} & 0 & \dots \\ 0 & 0 & \frac{b}{2} & 0 & a-\frac{25}{4} & \frac{5c}{2} & \frac{b}{2} & \dots \\ 0 & 0 & 0 & \frac{b}{2} & -\frac{5c}{2} & a-\frac{25}{4} & 0 & \dots \\ 0 & 0 & 0 & 0 & \frac{b}{2} & 0 & a-\frac{49}{4} & \dots \\ . & . & . & . & . & . & . & \dots \end{vmatrix} = 0 \tag{6.9}$$

A particular characteristic of the Mathieu equation is that it contains a periodically varying coefficient as a special case of the Hill equation. This means that the solutions of the Mathieu equation can be stable or unstable according to the combination of a_n and b_n (Patel and Park, 1991). Thus the approach to the Mathieu equation is to obtain a general solution and stability chart which shows whether the system is in a stable or unstable condition. By setting the Hill's determinants to zero as in the Eqns. (6.8) and (6.9), the implicit relationship between a, b, and c can be obtained. The boundary obtained separates the stable and unstable region. The stability diagram generated by Hill's infinite determinant method for damped Mathieu's equation are obtained by plotting the implicit relationship between the parameters and is shown in Fig. 6.1.

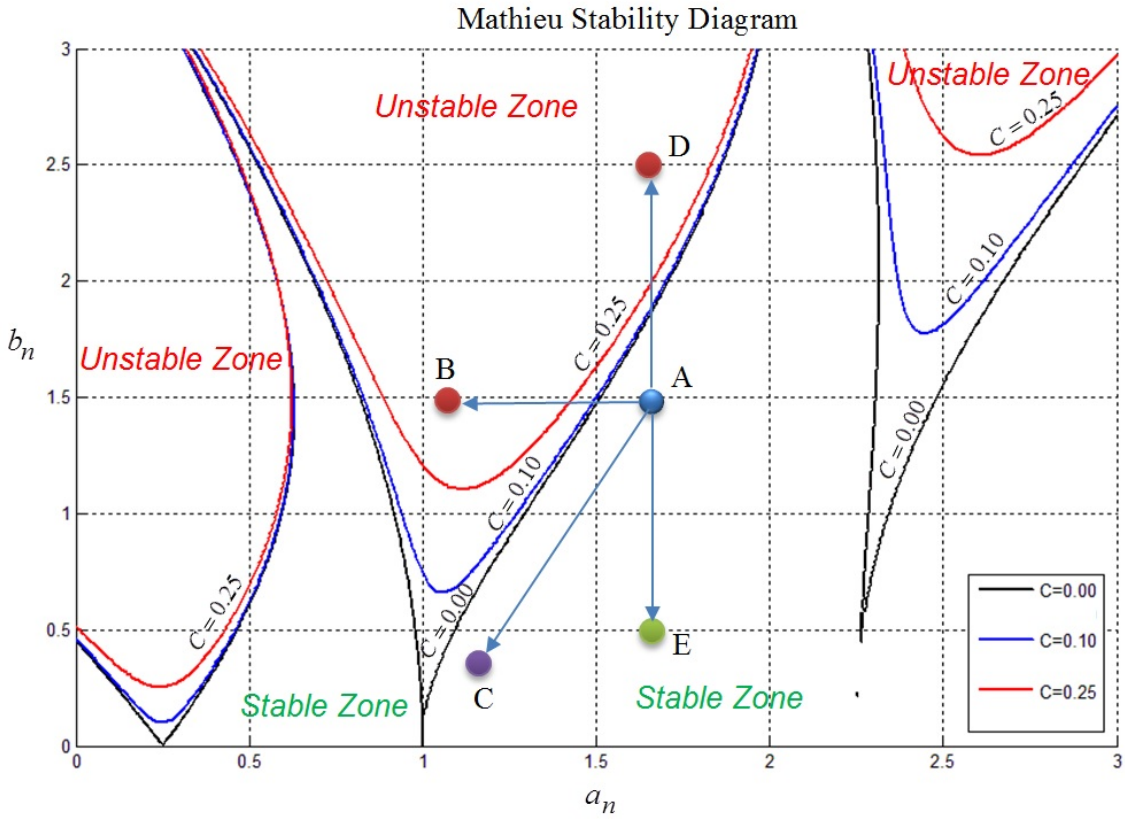

Figure 6.1 Mathieu stability diagram and behaviors of stability condition.

The Fig. 6.1 shows the characteristics of Mathieu stability diagram (MSD). For instance, point A denotes a normal operating condition of a riser (the point's coordinate in Mathieu's diagram is discussed in the next Subsection). If the *pre-tension* of this riser was reduced, the operating point A would shift towards B and encounter the unstable region. Line AC denotes movement of the operating point for increasing riser *length* (or water depth) (Patel and Park, 1991). For longer riser length in deep water, very small values of the parameters a_n and b_n are potential to trigger the lateral vibration of riser. As the riser's length increases, the operation point A in the Mathieu stability chart tends to

the region near its origin (where the a_n and b_n are smaller). The dynamic behavior is very sensitive to small variations in the parameters a_n and b_n in this low mode region. The deep water case is critical concerning riser dynamics, not only due to the common sense fact of being larger the vibration amplitudes as larger is the span, but also because its inherent response instability (Simos and Pesce, 1997). The line DAE indicates the *tension variations* of operating point A. If the tension variation is large, the operating point A would shift towards D and encounter the unstable region. The reduction of dynamic tension variation on the top tension riser can move the operating point A towards E, which provides an important control mechanism to maintain the stability of TTR, even if under the condition of low lateral damping. The second unstable region is more influenced by the damping coefficient, compared to the first unstable region.

6.3 Derivation of Mathieu's Instability Coefficients

The stability of a TTR can be identified by calculating its *location* (the combination of a_n and b_n) on the Mathieu's stability diagram, as in Fig. 6.1, to obtain a general solution which shows whether the system is in a *stable* or *unstable* zone. The location is a sets of Mathieu's coefficients a_n and b_n with respect to the mode n. The derivation of Mathieu's coefficients of a TTR is discussed in this Subsection, based on the following assumptions:

(i) The weight of the TTR is considered, and it is assumed that the axial tension varies linearly along the water depth (Xiao and Yang, 2014);

(ii) the direction of the current propagation is assumed to be fixed, and the velocity varies linearly from the bottom to the surface of the sea (Xiao and Yang, 2014);

(iii) the stiffness and material properties of the TTR are constant and homogenuous along the length of the riser (Xiao and Yang, 2014);

(iv) the top-end of riser do not move in the horizontal direction (Patel and Park, 1991).

The configuration of the TTR and the force distribution of the corresponding infinitesimal element are described in Fig. 6.2,

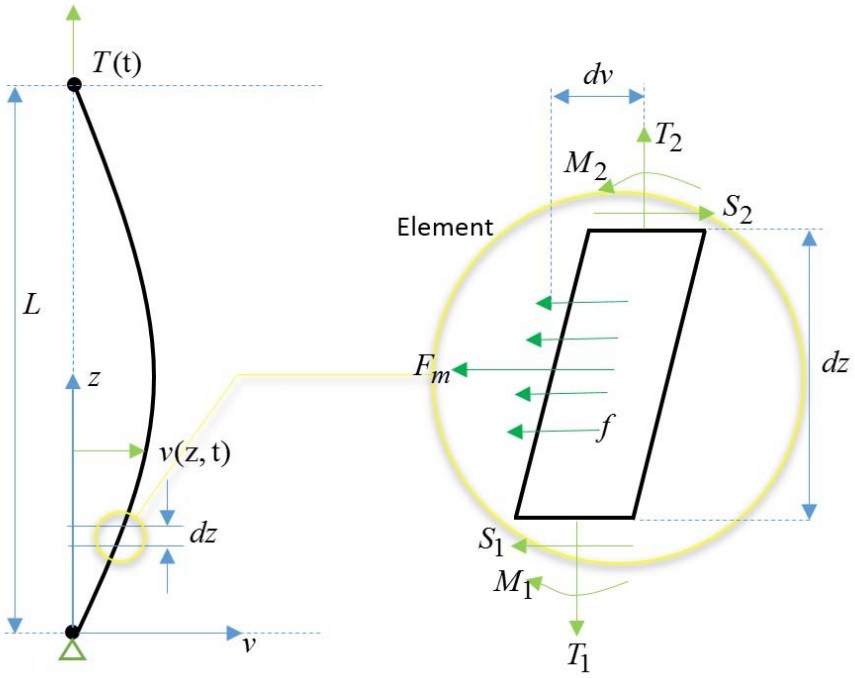

Figure 6.2 Schematic diagram of TTR model with the force distribution of infinitesimal element (Xiao and Yang, 2014).

where v is the horizontal coordinate, z is vertical coordinate, L is the water depth, $T(t)$ is the top tension, $v(z)$ is the lateral motion function, and dz is the length of a finite element.

Considering the horizontal balance of the forces in the infinitesimal element (Xiao and Yang, 2014),

$$S_2 - \left(fdz + Fmdz + S_1 \right) = 0 \tag{6.10}$$

where,

$S_2 = S + \frac{\partial S}{\partial z} dz$, $S_1 = S$ = shear forces, $Fm = \hat{m} \frac{\partial^2 v}{\partial t^2}$ = *inertia* force where the direction of which is opposite to the velocity of lateral motion, $\hat{m} = \pi Dh\rho_s + \frac{1}{4}\pi D^2 \rho_w + \rho_i A_i$ = mass per unit length, D = outer diameter, h = wall thickness, ρ_s = density of steel, ρ_w = density of seawater, ρ_i = density of internal fluid, A_i = internal area, C_d = drag coefficient, and $f = \frac{1}{2} C_d \rho_w D \left| \frac{\partial v}{\partial t} \right| \frac{\partial v}{\partial t}$ = hydrodynamic *drag* force. Therefore, from Eqn. (6.10);

$$\begin{aligned} S_2 - \left(fdz + Fmdz + S_1 \right) &= S_1 + \frac{\partial S}{\partial z} dz - \left(fdz + Fmdz + S_1 \right) \\ &= \frac{\partial S}{\partial z} dz - \left(fdz + Fmdz \right) = \frac{\partial S}{\partial z} - \left(f + Fm \right) \\ &= 0 \end{aligned} \tag{6.11}$$

and $$\frac{\partial S}{\partial z} = \left(f + Fm \right) \tag{6.12}$$

Then, taking into consideration the balance of the bending moments;

$$\left[S_1 dz + M_1\right] - \left[M_2 + T_1 dv\right] = 0 \tag{6.13}$$

where:

$M_2 = M + \frac{\partial M}{\partial z} dz$, $M_1 = M = -EI \frac{\partial^2 v}{\partial z^2}$ = bending moments, $T_2 = T + \frac{\partial T}{\partial z} dz$,

$T_1 = T = T_0 - \left(L - z\right) m_w + \Delta T \delta\left(t\right)$ = tensions in the TTR, $\frac{\partial T}{\partial z} = m_w$ = TTR wet weight per unit length, $dv = \frac{\partial v}{\partial z} dz$ = the difference between the displacements of the upper and lower points of the infinitesimal element dz. From Eqn. (6.13);

$$\begin{aligned}\left[S_1 dz + M_1\right] - \left[M_2 + T_1 dv\right] &= \left[S_1 dz + M_1\right] - \left[M_1 + \frac{\partial M}{\partial z} dz + T_1 dv\right] \\ &= \left[S_1 dz\right] - \left[\frac{\partial M}{\partial z} dz + T_1 \frac{\partial v}{\partial z} dz\right] = \left[S\right] - \left[\frac{\partial M}{\partial z} + T_1 \frac{\partial v}{\partial z}\right] \\ &= 0\end{aligned} \tag{6.14}$$

$$S = \frac{\partial M}{\partial z} + T \frac{\partial v}{\partial z} \tag{6.15}$$

By substituting Eqn. (6.15) into Eqn. (6.12), the coupling equation of the force and moment are:

$$\begin{aligned}&\frac{\partial S}{\partial z} = \left(f + Fm\right) \rightarrow \frac{\partial}{\partial z}\left(\frac{\partial M}{\partial z} + T \frac{\partial v}{\partial z}\right) = \frac{1}{2} C_d \rho_w D \left|\frac{\partial v}{\partial t}\right| \frac{\partial v}{\partial t} + \hat{m} \frac{\partial^2 v}{\partial t^2} \\ &= \hat{m} \frac{\partial^2 v}{\partial t^2} - \frac{\partial}{\partial z}\left(\frac{\partial M}{\partial z} + T \frac{\partial v}{\partial z}\right) + \frac{1}{2} C_d \rho_w D \left|\frac{\partial v}{\partial t}\right| \frac{\partial v}{\partial t} = 0 \\ &\rightarrow \hat{m} \frac{\partial^2 v}{\partial t^2} + \frac{\partial^2}{\partial z^2}\left(EI \frac{\partial^2 v}{\partial z^2}\right) - \frac{\partial}{\partial z}\left(T \frac{\partial v}{\partial z}\right) + \frac{1}{2} C_d \rho_w D \left|\frac{\partial v}{\partial t}\right| \frac{\partial v}{\partial t} = 0\end{aligned} \tag{6.16}$$

and Eqn. (6.16) can be further rearranged as:

$$\hat{m}\frac{\partial^2 v}{\partial t^2}+\frac{1}{2}C_d\rho_w D\left|\frac{\partial v}{\partial t}\right|\frac{\partial v}{\partial t}+EI\frac{\partial^4 v}{\partial z^4}-\frac{\partial}{\partial z}\left(\left[T_0-\left(L-z\right)m_w+\Delta T\delta\left(t\right)\right]\frac{\partial v}{\partial z}\right)=0 \tag{6.17}$$

$$\hat{m}\frac{\partial^2 v}{\partial t^2}+\frac{1}{2}C_d\rho_w D\left|\frac{\partial v}{\partial t}\right|\frac{\partial v}{\partial t}+EI\frac{\partial^4 v}{\partial z^4}-T\frac{\partial^2 v}{\partial z^2}-m_w\frac{\partial v}{\partial z}=0 \tag{6.18}$$

The time varying axial tension causes the TTR to undergo parametric oscillations. However, even if it is in an unstable condition, the quadratic fluid damping force limits the amplitude of the lateral motion (Patel and Park, 1991). The variation of the axial tension is modeled by the following irregular process:

$$\delta\left(t\right)=\sum_{n=0}^{\infty}a_n\cos\left(\omega_n t+\varepsilon_n\right) \tag{6.19}$$

The *wave induced axial tension* is assumed to be *sinusoidal*. This assumption is based on the fact that even if ocean waves are irregular, the time-varying axial tension become more regular (that is a more narrow banded spectrum) due to the transfer function from wave action to TTR forces. Despite irregular incident waves, the inertia of a TLP can cause the resultant TTR axial tension to tend towards near sinusoidal oscillations (Patel and Park, 1991). The riser tension can therefore be defined as:

$$\begin{aligned}T&=T_0-\left(L-z\right)m_w+\Delta T\delta\left(t\right)\\&=T_0-\left(L-z\right)m_w+\Delta T\sum_{n=0}^{\infty}a_n\cos\left(\omega_n t+\varepsilon_n\right)\end{aligned} \tag{6.20}$$

where T_0 = top pretension of the TTR, and ΔT = amplitude of the tension variation

Taking the fundamental mode (the largest amplitude mode of the model) only and using the method of separation of variables (Patel and Park, 1991), according to the Nayfeh and Mook (1977), the expansion of each linear vibration mode is:

$$v(z,t)=\sum_m \phi_m(t)u_m(z) \tag{6.21}$$

By substituting Eqn. (6.21) into Eqn. (6.18);

$$\hat{m}\frac{\partial^2 v}{\partial t^2}+\frac{1}{2}C_d\rho_w D\left|\frac{\partial v}{\partial t}\right|\frac{\partial v}{\partial t}+EI\frac{\partial^4 v}{\partial z^4}-T\frac{\partial^2 v}{\partial z^2}-m_w\frac{\partial v}{\partial z}=0 \tag{6.22}$$

$$\hat{m}\frac{\partial^2 \sum_m \phi_m(t)u_m(z)}{\partial t^2}+\frac{1}{2}C_d\rho_w D\left|\frac{\partial \sum_m \phi_m(t)u_m(z)}{\partial t}\right|\frac{\partial \sum_m \phi_m(t)u_m(z)}{\partial t}+EI\frac{\partial^4 \sum_m \phi_m(t)u_m(z)}{\partial z^4}$$
$$-T\frac{\partial^2 \sum_m \phi_m(t)u_m(z)}{\partial z^2}-m_w\frac{\partial \sum_m \phi_m(t)u_m(z)}{\partial z}=0 \tag{6.23}$$

$$\sum_m\left\{\begin{array}{l}\hat{m}\phi_m''(t)u_m(z)+\frac{1}{2}C_d\rho_w D\left|\phi_m'(t)u_m(z)\right|\phi_m'(t)u_m(z)\\ +EI\phi_m(t)u_m^{(4)}(z)-T\phi_m(t)u_m''(z)-m_w\phi_m(t)u_m'(z)\end{array}\right\}=0 \tag{6.24}$$

Considering that the boundary conditions of both ends are assumed to be pinned-pinned connection (Xiao and Yang, 2014), the special function that satisfies the boundary conditions is:

$$u_m(z)=\sin\left(\frac{n\pi}{L}z\right) \tag{6.25}$$

Because of u_m is mutually orthogonal when m varies, by applying Galerkin's method on Eqn. (6.24) (Brugmans, 2005):

$$\int_0^L\sum_m\left\{\begin{array}{l}\hat{m}\phi_m''(t)u_m(z)+\frac{1}{2}C_d\rho_w D\left|\phi_m'(t)u_m(z)\right|\phi_m'(t)u_m(z)\\ +EI\phi_m(t)u_m^{(4)}(z)-T\phi_m(t)u_m''(z)-m_w\phi_m(t)u_m'(z)\end{array}\right\}\cdot u_n dz=0 \tag{6.26}$$

$$\int_0^L \sum_m \left\{ \hat{m}\phi_m''(t) u_m(z) \right\} \cdot u_n dz + \int_0^L \sum_m \left\{ \frac{1}{2} C_d \rho_w D \left| \phi_m'(t) u_m(z) \right| \phi_m'(t) u_m(z) \right\} \cdot u_n dz +$$
$$\int_0^L \sum_m \left\{ EI \phi_m(t) u_m^{(4)}(z) \right\} \cdot u_n dz - \int_0^L \sum_m \left\{ T \phi_m(t) u_m''(z) \right\} \cdot u_n dz - \int_0^L \sum_m \left\{ m_w \phi_m(t) u_m'(z) \right\} \cdot u_n dz = 0 \tag{6.27}$$

$$\hat{m}\phi_n''(t) \int_0^L u_n^2 dz + \frac{1}{2} C_d \rho_w D \left| \phi_n'(t) \right| \phi_n'(t) \int_0^L |u_n| u_n^2 dz + EI \phi_n(t) \int_0^L u_n^{(4)} \cdot u_n dz$$
$$- \phi_n(t) \int_0^L T u_n'' \cdot u_n dz - m_w \phi_n(t) \int_0^L u_n' \cdot u_n dz = 0 \tag{6.28}$$

$$\hat{m} \int_0^L u_n^2 dz \phi_n''(t) + \frac{1}{2} C_d \rho_w D \int_0^L |u_n| u_n^2 dz \left| \phi_n'(t) \right| \phi_n'(t)$$
$$+ \begin{pmatrix} EI \int_0^L u_n^{(4)} \cdot u_n dz - \int_0^L T u_n'' \cdot u_n dz \\ - m_w \int_0^L u_n' \cdot u_n dz \end{pmatrix} \phi_n(t) = 0 \tag{6.29}$$

$$\phi_n''(t) + \frac{\frac{1}{2} C_d \rho_w D \int_0^L |u_n| u_n^2 dz}{\hat{m} \int_0^L u_n^2 dz} \left| \phi_n'(t) \right| \phi_n'(t) + \frac{\begin{pmatrix} EI \int_0^L u_n^{(4)} \cdot u_n dz - \int_0^L T u_n'' \cdot u_n dz \\ - m_w \int_0^L u_n' \cdot u_n dz \end{pmatrix}}{\hat{m} \int_0^L u_n^2 dz} \phi_n(t) = 0 \tag{6.30}$$

It is convenient to introduce a dimensionless time variable, $\tau = \omega t$ (Xiao and Yang, 2014), therefore,

$$\phi_n''(\tau) + \frac{\frac{1}{2} C_d \rho_w D \int_0^L |u_n| u_n^2 dz}{\hat{m} \int_0^L u_n^2 dz \cdot \omega} \left| \phi_n'(\tau) \right| \phi_n'(\tau) + \frac{\begin{pmatrix} EI \int_0^L u_n^{(4)} \cdot u_n dz - \int_0^L T u_n'' \cdot u_n dz \\ - m_w \int_0^L u_n' \cdot u_n dz \end{pmatrix}}{\hat{m} \int_0^L u_n^2 dz \cdot \omega^2} \phi_n(\tau) = 0 \tag{6.31}$$

The Eqn. (6.31) can be rewritten in the following form in order to determine the Mathieu's coefficients a_n, b_n, C;

$$\phi_n''(\tau)+C\phi_n'(\tau)+\left[\boldsymbol{a_n}+\boldsymbol{b_n}\sum_{\boldsymbol{n}=0}^{\infty}\boldsymbol{a_n}\cos\left(\frac{\boldsymbol{\omega_n}}{\boldsymbol{\omega}}\boldsymbol{\tau}+\boldsymbol{\varepsilon_n}\right)\right]\phi_n(\tau)=0 \tag{6.32}$$

where $n=1,2,3\ldots.$

Therefore, the damping coefficient C in Eqn. (6.32) can be derived as (Patel and Park, 1991):

$$C=\frac{\frac{1}{2}C_d\rho_w D\int_0^L|u_n|u_n^2dz}{\hat{m}\int_0^L u_n^2dz\cdot\omega}\cdot\left|\phi_n'(\tau)\right|=\frac{C_d\rho_w D}{2\hat{m}}\cdot\frac{8}{3\pi}\cdot\frac{1}{\omega}\cdot\left|\phi_n'(\tau)\right|=\frac{4C_d\rho_w D}{3\pi\hat{m}\omega}\cdot\left|\phi_n'(\tau)\right| \tag{6.33}$$

and the stiffness term in Eqns. (6.31) and (6.32) can be further derived as:

$$\begin{aligned}&\frac{\left(EI\int_0^L u_n^{(4)}\cdot u_n dz-\int_0^L Tu_n''\cdot u_n dz-m_w\int_0^L u_n'\cdot u_n dz\right)}{\hat{m}\int_0^L u_n^2dz\cdot\omega^2}\\&=\frac{EI\int_0^L u_n^{(4)}\cdot u_n dz}{\hat{m}\int_0^L u_n^2dz\cdot\omega^2}-\frac{\int_0^L Tu_n''\cdot u_n dz}{\hat{m}\int_0^L u_n^2dz\cdot\omega^2}-\frac{m_w\int_0^L u_n'\cdot u_n dz}{\hat{m}\int_0^L u_n^2dz\cdot\omega^2}\end{aligned} \tag{6.34}$$

By using the following derivative of special function in Eqn. (6.25):

$$u_n(z)=\sin\left(\frac{n\pi}{L}z\right);\quad u_n'(z)=\left(\frac{n\pi}{L}\right)\cos\left(\frac{n\pi}{L}z\right);\quad u_n''(z)=-\left(\frac{n\pi}{L}\right)^2\sin\left(\frac{n\pi}{L}z\right);$$

$$u_n^{(3)}(z)=-\left(\frac{n\pi}{L}\right)^3\cos\left(\frac{n\pi}{L}z\right);\quad u_n^{(4)}(z)=\left(\frac{n\pi}{L}\right)^4\sin\left(\frac{n\pi}{L}z\right) \tag{6.35}$$

Substituting into the coefficients in Eqn. (6.34), we obtain:

$$\int_0^L u_n^{(4)} \cdot u_n dz = \int_0^L \left(\frac{n\pi}{L}\right)^4 \sin\left(\frac{n\pi}{L}z\right) \cdot \sin\left(\frac{n\pi}{L}z\right) dz = \left(\frac{n\pi}{L}\right)^4 \int_0^L \sin^2\left(\frac{n\pi}{L}z\right) dz$$

$$= \left(\frac{n\pi}{L}\right)^4 \left\{ \left[\frac{z}{2} - \frac{L}{4n\pi} \sin\left(\frac{2n\pi}{L}z\right) \right] \Big|_0^L \right\}$$

$$= \left(\frac{n\pi}{L}\right)^4 \left\{ \left[\frac{L}{2} - \frac{L}{4n\pi} \sin\left(2n\pi\right) \right] - \left[0 - 0\right] \right\}$$

$$= \left(\frac{n\pi}{L}\right)^4 \left(\frac{L}{2}\right) \tag{6.36}$$

$$\int_0^L u_n^2 dz = \int_0^L \sin^2\left(\frac{n\pi}{L}z\right) dz = \frac{L}{2} \tag{6.37}$$

The first term on RHS of Eqn. (6.34),

$$\frac{EI\int_0^L u_n^{(4)} \cdot u_n dz}{\hat{m}\int_0^L u_n^2 dz \cdot \omega^2} = \frac{EI\left(\frac{n\pi}{L}\right)^4 \left(\frac{L}{2}\right)}{\hat{m}\left(\frac{L}{2}\right)} \cdot \frac{1}{\omega^2} = \frac{EI\left(\frac{n\pi}{L}\right)^4}{\hat{m}\omega^2} \tag{6.38}$$

For the second term on RHS of Eqn. (6.34),

$$\frac{\int_0^L T u_n'' \cdot u_n dz}{\hat{m}\int_0^L u_n^2 dz \cdot \omega^2} = \frac{\int_0^L \left(T_0 - \left(L - z\right) m_w + \Delta T \delta\left(t\right)\right) u_n'' \cdot u_n dz}{\hat{m}\int_0^L u_n^2 dz \cdot \omega^2}$$

$$= \frac{\int_0^L T_0 u_n'' \cdot u_n dz}{\hat{m}\int_0^L u_n^2 dz \cdot \omega^2} - \frac{\int_0^L m_w L \cdot u_n'' \cdot u_n dz}{\hat{m}\int_0^L u_n^2 dz \cdot \omega^2} + \frac{\int_0^L m_w z \cdot u_n'' \cdot u_n dz}{\hat{m}\int_0^L u_n^2 dz \cdot \omega^2} + \frac{\int_0^L \Delta T \delta\left(t\right) \cdot u_n'' \cdot u_n dz}{\hat{m}\int_0^L u_n^2 dz \cdot \omega^2}$$

$$= \frac{T_0 \int_0^L u_n'' \cdot u_n dz}{\hat{m}\int_0^L u_n^2 dz \cdot \omega^2} - \frac{m_w L \int_0^L u_n'' \cdot u_n dz}{\hat{m}\int_0^L u_n^2 dz \cdot \omega^2} + \frac{m_w \int_0^L z \cdot u_n'' \cdot u_n dz}{\hat{m}\int_0^L u_n^2 dz \cdot \omega^2} + \frac{\Delta T \delta\left(t\right) \int_0^L u_n'' \cdot u_n dz}{\hat{m}\int_0^L u_n^2 dz \cdot \omega^2} \tag{6.39}$$

where

$$\int_0^L u_n'' \cdot u_n dz = -\left(\frac{n\pi}{L}\right)^2 \int_0^L \sin\left(\frac{n\pi}{L}z\right) \cdot \sin\left(\frac{n\pi}{L}z\right) dz$$
$$= -\left(\frac{n\pi}{L}\right)^2 \int_0^L \sin^2\left(\frac{n\pi}{L}z\right) dz = -\left(\frac{n\pi}{L}\right)^2 \left(\frac{L}{2}\right) \tag{6.40}$$

$$\int_0^L z \cdot u_n'' \cdot u_n dz = -\left(\frac{n\pi}{L}\right)^2 \int_0^L z \cdot \sin^2\left(\frac{n\pi}{L}z\right) dz$$
$$= -\left(\frac{n\pi}{L}\right)^2 \left\{\left[\frac{z^2}{4} - \frac{zL}{4n\pi}\sin\left(\frac{2n\pi}{L}z\right) - \frac{L^2}{8n^2\pi^2}\cos\left(\frac{2n\pi}{L}z\right)\right]_0^L\right\}$$
$$= -\left(\frac{n\pi}{L}\right)^2 \left\{\begin{array}{l}\left[\frac{L^2}{4} - \frac{L^2}{4n\pi}\sin(2n\pi) - \frac{L^2}{8n^2\pi^2}\cos(2n\pi)\right] \\ -\left[\frac{0}{4} - \frac{0}{4n\pi}\sin\left(\frac{2n\pi}{L}z\right) - \frac{L^2}{8n^2\pi^2}\cos(0)\right]\end{array}\right\}$$
$$= -\left(\frac{n\pi}{L}\right)^2 \left\{\left[\frac{L^2}{4} - 0 - \frac{L^2}{8n^2\pi^2}\right] - \left[0 - 0 - \frac{L^2}{8n^2\pi^2}\right]\right\} = -\left(\frac{n\pi}{L}\right)^2 \left\{\frac{L^2}{4}\right\}$$
$$= -\left(\frac{n\pi}{L}\right)^2 \left(\frac{L}{2}\right)^2 \tag{6.41}$$

Therefore, Eqn. (6.39) can be rearranged as:

$$\frac{T_0 \int_0^L u_n'' \cdot u_n dz}{\hat{m}\int_0^L u_n^2 dz \cdot \omega^2} - \frac{m_w L \int_0^L u_n'' \cdot u_n dz}{\hat{m}\int_0^L u_n^2 dz \cdot \omega^2} + \frac{m_w \int_0^L z \cdot u_n'' \cdot u_n dz}{\hat{m}\int_0^L u_n^2 dz \cdot \omega^2} + \frac{\Delta T \delta(t) \int_0^L u_n'' \cdot u_n dz}{\hat{m}\int_0^L u_n^2 dz \cdot \omega^2}$$
$$= -\frac{T_0\left(\frac{n\pi}{L}\right)^2\left(\frac{L}{2}\right)}{\hat{m}\left(\frac{L}{2}\right)\cdot\omega^2} + \frac{m_w L\left(\frac{n\pi}{L}\right)^2\left(\frac{L}{2}\right)}{\hat{m}\left(\frac{L}{2}\right)\cdot\omega^2} - \frac{m_w\left(\frac{n\pi}{L}\right)^2\left(\frac{L}{2}\right)^2}{\hat{m}\left(\frac{L}{2}\right)\cdot\omega^2} - \frac{\Delta T\delta(t)\left(\frac{n\pi}{L}\right)^2\left(\frac{L}{2}\right)}{\hat{m}\left(\frac{L}{2}\right)\cdot\omega^2}$$
$$= -\frac{T_0\left(\frac{n\pi}{L}\right)^2}{\hat{m}\cdot\omega^2} + \frac{m_w L\left(\frac{n\pi}{L}\right)^2}{\hat{m}\cdot\omega^2} - \frac{m_w\left(\frac{n\pi}{L}\right)^2\left(\frac{L}{2}\right)}{\hat{m}\cdot\omega^2} - \frac{\Delta T\delta(t)\left(\frac{n\pi}{L}\right)^2}{\hat{m}\cdot\omega^2}$$
$$= -\frac{T_0\left(\frac{n\pi}{L}\right)^2}{\hat{m}\omega^2} + \frac{\frac{1}{2}m_w L\left(\frac{n\pi}{L}\right)^2}{\hat{m}\omega^2} - \frac{\Delta T\delta(t)\left(\frac{n\pi}{L}\right)^2}{\hat{m}\omega^2} \tag{6.42}$$

The second term on RHS of Eqn. (6.34) is:

$$-\frac{\int_0^L Tu_n'' \cdot u_n dz}{\hat{m}\int_0^L u_n^2 dz \cdot \omega^2} = \frac{T_0\left(\frac{n\pi}{L}\right)^2}{\hat{m}\omega^2} - \frac{\frac{1}{2}m_w L\left(\frac{n\pi}{L}\right)^2}{\hat{m}\omega^2} + \frac{\Delta T\delta(t)\left(\frac{n\pi}{L}\right)^2}{\hat{m}\omega^2} \tag{6.43}$$

For the third term on RHS of Eqn. (6.34),

$$\frac{m_w\int_0^L u_n' \cdot u_n dz}{\hat{m}\int_0^L u_n^2 dz \cdot \omega^2} = 0 \tag{6.44}$$

since

$$\begin{aligned}
\int_0^L u_n' \cdot u_n dz &= \int_0^L \left(\frac{n\pi}{L}\right)\cos\left(\frac{n\pi}{L}z\right) \cdot \sin\left(\frac{n\pi}{L}z\right) dz \\
&= \left(\frac{n\pi}{L}\right)\left\{\int_0^L \cos\left(\frac{n\pi}{L}z\right) \cdot \sin\left(\frac{n\pi}{L}z\right) dz\right\} \\
&= \left(\frac{n\pi}{L}\right)\left\{\left[-\frac{L}{2n\pi}\cos^2\left(\frac{n\pi}{L}z\right)\right]_0^L\right\} \\
&= \left(\frac{n\pi}{L}\right)\left\{\left[-\frac{L}{2n\pi}\cos^2(n\pi)\right] - \left[-\frac{L}{2n\pi}\cos^2(0)\right]\right\} \\
&= 0
\end{aligned} \tag{6.45}$$

The *stiffness* term in Eqn. (6.34) can be rewritten as:

$$\frac{\left(EI\int_0^L u_n^{(4)}\cdot u_n dz-\int_0^L Tu_n''\cdot u_n dz-m_w\int_0^L u_n'\cdot u_n dz\right)}{\hat{m}\int_0^L u_n^2 dz\cdot\omega^2}$$

$$=\frac{EI\int_0^L u_n^{(4)}\cdot u_n dz}{\hat{m}\int_0^L u_n^2 dz\cdot\omega^2}-\frac{\int_0^L Tu_n''\cdot u_n dz}{\hat{m}\int_0^L u_n^2 dz\cdot\omega^2}-\frac{m_w\int_0^L u_n'\cdot u_n dz}{\hat{m}\int_0^L u_n^2 dz\cdot\omega^2}$$

$$=\frac{EI\left(\frac{n\pi}{L}\right)^4}{\hat{m}\omega^2}+\frac{T_0\left(\frac{n\pi}{L}\right)^2}{\hat{m}\omega^2}-\frac{\frac{1}{2}m_wL\left(\frac{n\pi}{L}\right)^2}{\hat{m}\omega^2}+\frac{\Delta T\delta(t)\left(\frac{n\pi}{L}\right)^2}{\hat{m}\omega^2}-0$$

$$=\frac{EI\left(\frac{n\pi}{L}\right)^4+T_0\left(\frac{n\pi}{L}\right)^2-\frac{1}{2}m_wL\left(\frac{n\pi}{L}\right)^2}{\hat{m}\omega^2}+\frac{\Delta T\left(\frac{n\pi}{L}\right)^2\delta(t)}{\hat{m}\omega^2}$$

$$=\frac{EI\left(\frac{n\pi}{L}\right)^4+T_0\left(\frac{n\pi}{L}\right)^2-\frac{1}{2}m_wL\left(\frac{n\pi}{L}\right)^2}{\hat{m}\omega^2}+\frac{\Delta T\left(\frac{n\pi}{L}\right)^2\sum_{n=0}^{\infty}a_n\cos(\omega_n t+\varepsilon_n)}{\hat{m}\omega^2} \tag{6.46}$$

By compared to Eqn. (6.32), the Mathieu's coefficient a_n is:

$$a_n=\frac{EI\left(\frac{n\pi}{L}\right)^4+T_0\left(\frac{n\pi}{L}\right)^2-\frac{1}{2}m_wL\left(\frac{n\pi}{L}\right)^2}{\hat{m}\omega^2}=\frac{\omega_n^2}{\omega^2}=\left(\frac{\omega_n}{\omega}\right)^2 \tag{6.47}$$

where

$$\omega_n=\left(\frac{n\pi}{L}\right)\sqrt{\frac{EI\left(\frac{n\pi}{L}\right)^2+T_0-\frac{1}{2}m_wL}{\hat{m}}} \tag{6.48}$$

where the ω_n is the natural frequency of the lateral vibration of the riser, and ω is the basic frequency of the outer excitation (1st mode of free vibration of a loaded riser). Also, the Mathieu's coefficient b_n is:

$$b_n = \frac{\Delta T\left(\frac{n\pi}{L}\right)^2}{\hat{m}\omega^2} \tag{6.49}$$

In summary, the Mathieu's coefficients of top tension riser (TTR), as a slender rod based on Euler-Bernoulli theory, are:

$$\ddot{x} + C\dot{x} + \left[\boldsymbol{a_n} + \boldsymbol{b_n}\sum_{\boldsymbol{n}=0}^{\infty}\boldsymbol{a_n}\cos\left(\frac{\boldsymbol{\omega_n}}{\boldsymbol{\omega}}\boldsymbol{\tau} + \boldsymbol{\varepsilon_n}\right)\right]x = 0 \tag{6.50}$$

$$a_n = \left(\frac{\omega_n}{\omega}\right)^2 \tag{6.51}$$

$$b_n = \frac{\Delta T\left(\frac{n\pi}{L}\right)^2}{\hat{m}\omega^2} \tag{6.52}$$

$$C = \frac{4C_d\rho_w D|\dot{x}|}{3\pi\hat{m}\omega} = \frac{4C_d\rho_w D\cdot v_{\max}}{3\pi\hat{m}\omega} \tag{6.53}$$

$$\omega_n = \left(\frac{n\pi}{L}\right)\sqrt{\frac{EI\left(\frac{n\pi}{L}\right)^2 + T_0 - \frac{1}{2}m_w L}{\hat{m}}} \tag{6.54}$$

The damping coefficient C is dependent of the maximum velocity of the riser in transverse motion $v_{\max}$ (Wang and Zou, 2006).

6.4 Mathieu's Instability Prediction for TTR

The prediction of Mathieu stability was conducted for single top-tension riser as discussed in the Subsection 5.8.2. The configuration of the particular drilling TTR is

tabulated in the Table 6.1. The prediction of stability was conducted under a hull-riser-tendon coupled analysis in the following settings:

(i) TLP was excited with a regular wave loading input (as in the *base-case*);

(ii) the sensitivity tests of pretension, riser length, and tension variation were conducted by calculating the Mathieu's coefficients, as in Eqns. (6.51) and (6.52) for each variation case, as tabulated in Table 6.2, respectively.

Table 6.1 Configuration of a single top-tension riser.

Design water depth	914.36 m (*3000 ft*)
Top pretension (T_0)	330.67 MT (*729.0 kips*)
Riser outer diameter	0.3508 m (*1.1509 ft*)
Riser wall thickness	0.01905 m (*0.625 ft*)
Riser length (L)	914.36 m (*3000 ft*)
Riser wet weight	124.096 MT (*273.58 kips*)
Wet weight per unit length (m_w)	0.1357 MT/m (*0.0912 kips/ft*)
Mass per unit length of riser ($\hat{m}$)	320.2 kg/m (*0.2152 kips/ft*)
Bending stiffness (EI)	5.79E+03 MT.m^2 (*1.32E+05 kips-ft^2*)
Excitation frequency (ω)	0.4080 rad/s
Density of steel	7.86 MT/m^3 (*15.25 slug/ft^3*)
Density of Sea water	1.025 MT/m^3 (*1.99 slug/ft^3*)

Table 6.2 Sensitivity test of Mathieu stability for TTR.

	Variations of Sensitivity Test				
Top pretension (T_0) (MT) *(kips)*	200 (*440.9*)	250 (*551.2*)	330.67* (*729.0*)	500 (*1102.3*)	1000 (*2204.6*)
Riser length (*L*) (m) *(ft)*	200 *(656.2)*	500 *(1640.2)*	914.36* *(3000.0)*	1500 *(4921.3)*	3000 *(9842.5)*
Ten. var. (ΔT)[!] (kN) *(kips)*	500 *(112.4)*	3,000 *(674.4)*	5,500* *(1236.4)*	8,000 *(1798.5)*	10,000 *(2248.1)*

** Base-case values; [!] Ten. var. = Tension variations.*

The Fig. 6.3 shows the characteristics of Mathieu stability diagram (MSD) for the TTR with variations of pretension. The first two vibration modes which have larger amplitudes (Wang and Zou, 2008) were studied by using the Mathieu stability diagram, which predicts more conservative results in the lower modes than the Hill's equation (Yang et al., 2013a). It can be found that the pretension T_o of the top tension riser must be examined nearby the *first* unstable zone. Starting from the *base-case* (where the pretension T_o = 330.67 MT (*3242 kN, 728.8 kips*)), if the pretension of the riser was reduced, the operating point would shift towards the *first* unstable zone on the left-hand side. Neverthelss, if the pretension was increased, the operating point would potentially

shift towards the *second* unstable zone on the right-hand side. There is noteworthy that a slight damping coefficient ($C = 0.10$, for instance) on the *second* unstable zone can transform the unstable condition to a stable condition. This is reasonable for the riser to be more stable when it is affected by the hydrodynamic damping in the water. However, the *first* unstable zone is less influenced by the damping coefficient, compared to the *second* unstable region, a very large damping coefficient is needed to change the unstable condition on the *first* unstable zone. Therefore, this can be concluded that, in general, smaller pretension T_o increases the tendency of instability for the TTR.

There is noteworthy that the damping coefficient C is dependent of the maximum velocity $v_{\max}$ of the riser in the transverse motion (Wang and Zou, 2006). The parameters that can be controlled by the riser designer to adjust the damping coefficient C are riser drag coefficient C_d, riser diameter D, and mass per unit length $\hat{m}$ as shown in the Eqn. (6.53) (Yang et al., 2013a). The damping coefficient C for the riser as tabulated in Table 6.1 is $C = 1.17 C_d \cdot v_{\max}$, where it is highly influenced by the drag coefficient C_d and maximum lateral velocity $v_{\max}$ of the riser. For instance, if the drag coefficient of the riser is in the range of [0.7, 1.2], the range of damping coefficient C is from $0.82 v_{\max}$ to $1.40 v_{\max}$. Hence, maximum velocity $v_{\max}$ must be at least 0.305 m/s (*1.000 ft/s*) and 0.178 m/s (*0.584 ft/s*), for $C_d = 0.7$ and $C_d = 1.2$ respectively, in order to have the damping coefficient $C = 0.25$.

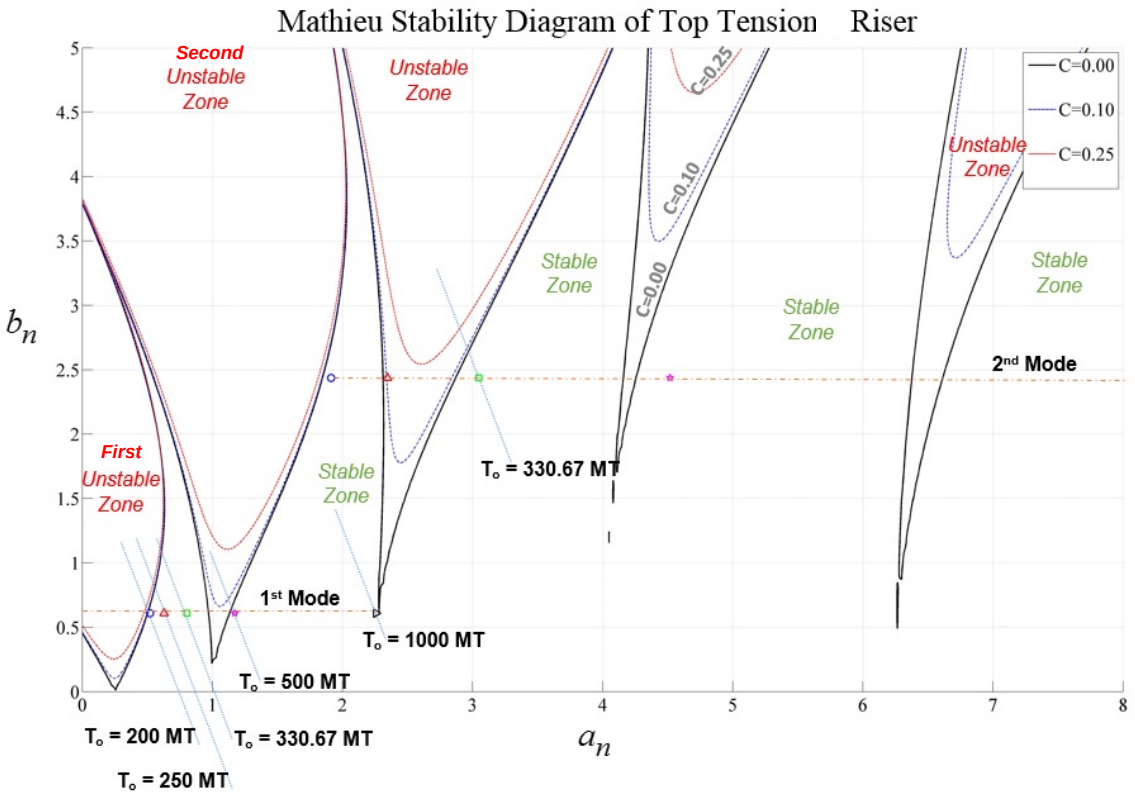

Figure 6.3 Mathieu stability assessment of a single TTR with variations of pretension.

The Mathieu stability assessment of single TTR with the variations of riser length is shown in Fig. 6.4. For longer riser length in deep water, very small values of the parameters a_n and b_n are potential to trigger the lateral vibration of riser. As the riser's length increases, the operation point in the Mathieu stability diagram tends to the region near its origin (where the a_n and b_n are smaller). The dynamic behavior is very sensitive to small variations in the parameters a_n and b_n in this low mode region.

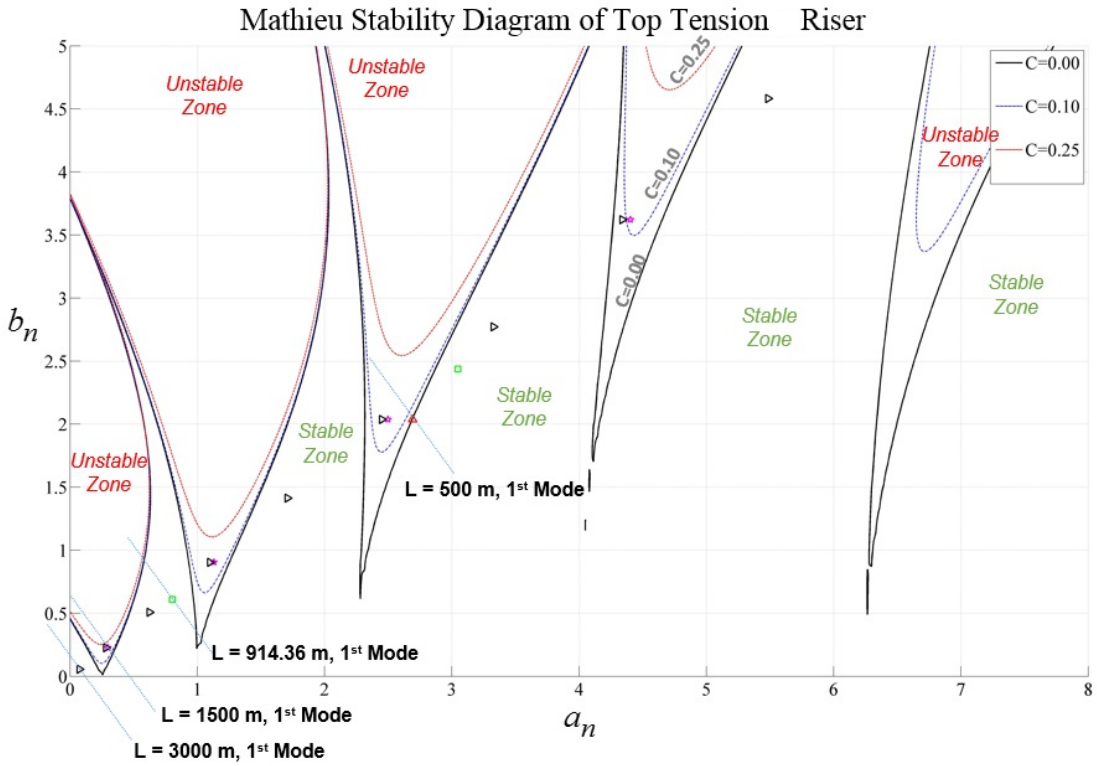

Figure 6.4 Mathieu stability assessment of a single TTR with variations of riser length.

The Mathieu stability assessment of single TTR with dynamic tension variations ΔT is shown in Fig. 6.5, and the results of first nine vibration modes is tabulated in Table 6.3. From the second mode as illustarated in the Fig. 6.5, if the tension variation ΔT is larger, the operating point would shift towards the unstable zone. Most importantly, the reduction of dynamic tension variation ΔT on the top tension riser can move the operating point towards a stable zone. This finding provides an important control mechanism to maintain the stability of TTR, even if the lateral damping is low.

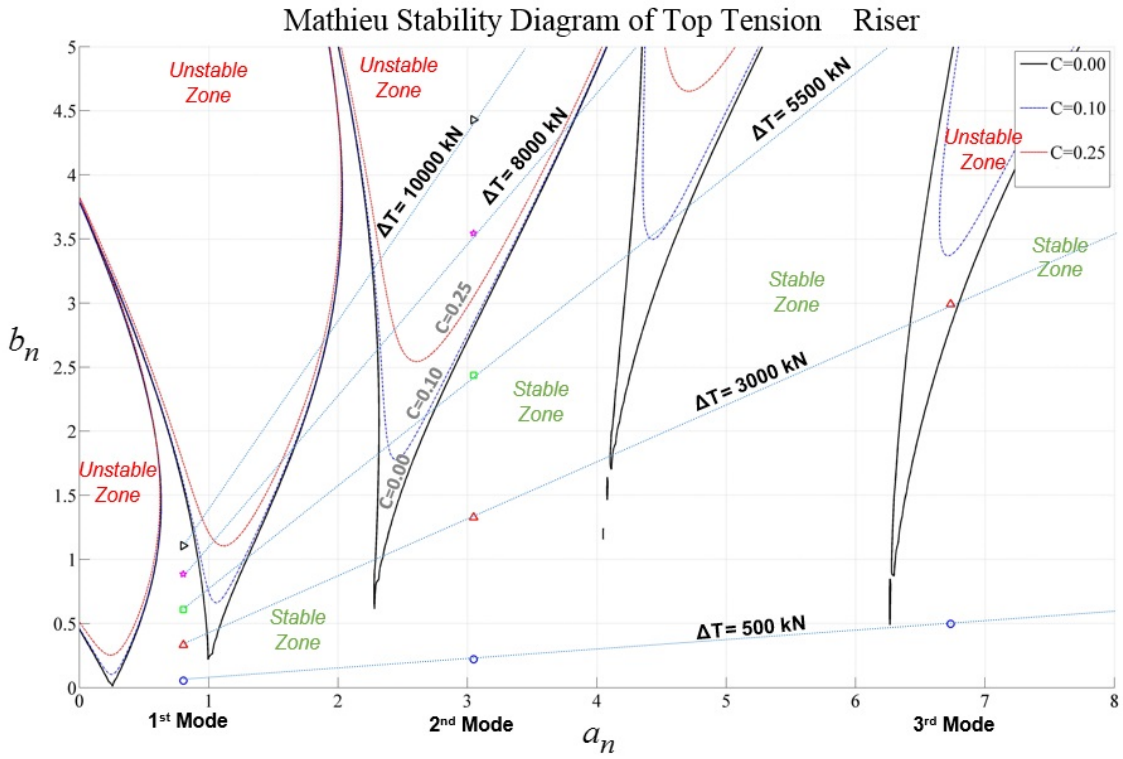

Figure 6.5 Mathieu stability assessment of a single TTR with variations of tension.

Table 6.3 First nine vibration modes of a single TTR with tension variations.

		Tension variations, ΔT				
		500 kN *(112.4 kips)*	3,000 kN *(674.4 kips)*	5,500 kN *(1236.4 kips)*	8,000 kN *(1798.5 kips)*	10,000 kN *(2248.1 kips)*
ω_n (rad/s)	**a_n**	**b_n**				
0.366	0.804	0.055	0.332	0.609	0.886	1.107
0.712	3.047	0.221	1.329	2.436	3.544	4.430
1.059	6.734	0.498	2.990	5.482	7.973	9.966
1.406	11.873	0.886	5.315	9.745	14.174	17.718
1.754	18.478	1.384	8.305	15.226	22.148	27.685
2.103	26.564	1.993	11.960	21.926	31.893	39.866
2.453	36.152	2.713	16.278	29.844	43.409	54.262
2.805	47.263	3.544	21.262	38.980	56.698	70.872
3.158	59.925	4.485	26.909	49.334	71.758	89.698

Since the Mathieu instability for riser is significant in lower order instability zones and most of a system's vibration energy is distributed in the first few vibration modes (Xiao and Yang, 2014), the present study considers only the first two vibration modes on the Mathieu's stability diagram.

There is noteworthy that the analysis of the Mathieu instability of top tension riser is more important when the host platform has larger motion, such as in the cases of drillship and dry-tree semisubmersible (DTS).

For the TLP host platform coupled with TTR, the dynamic tension variation ΔT is generally small due to the small vertical velocity of the platform motion. Followed the TLP-riser case in the Subsection 5.8.2, the uncontrolled *base-case* dynamic tension variation ΔT is 7 kips (*31.1376 kN*), and the reduction of dynamic tension variation by activating the EFCC is until 1 kips (*4.4482 kN*). The Mathieu stability assessment of the case in Subsection 5.8.2 is shown in Fig. 6.6, and the results of first nine vibration modes are tabulated in Table 6.4. This can be found that the first two vibration modes of TTR were far below the unstable zones. Moreover, the reduction of dynamic tension variation by using EFCC can further reduce the values of b_n, which leads to the stability of TTR.

Table 6.4 First nine vibration modes of a single top tension riser in TLP host platform with EFCC control scheme.

Tension variation, ΔT = 31.1376 kN *(7 kips)*			Tension variation, ΔT = 4.4482 kN *(1 kips)*		
ω_n	a_n	b_n	ω_n	a_n	b_n
0.366	0.804	0.003	0.366	0.804	0.000
0.712	3.047	0.014	0.712	3.047	0.002
1.059	6.733	0.031	1.059	6.733	0.004
1.406	11.872	0.055	1.406	11.872	0.008
1.754	18.477	0.086	1.754	18.477	0.012
2.103	26.562	0.124	2.103	26.562	0.018
2.453	36.148	0.169	2.453	36.148	0.024
2.805	47.259	0.221	2.805	47.259	0.032
3.158	59.919	0.279	3.158	59.919	0.040

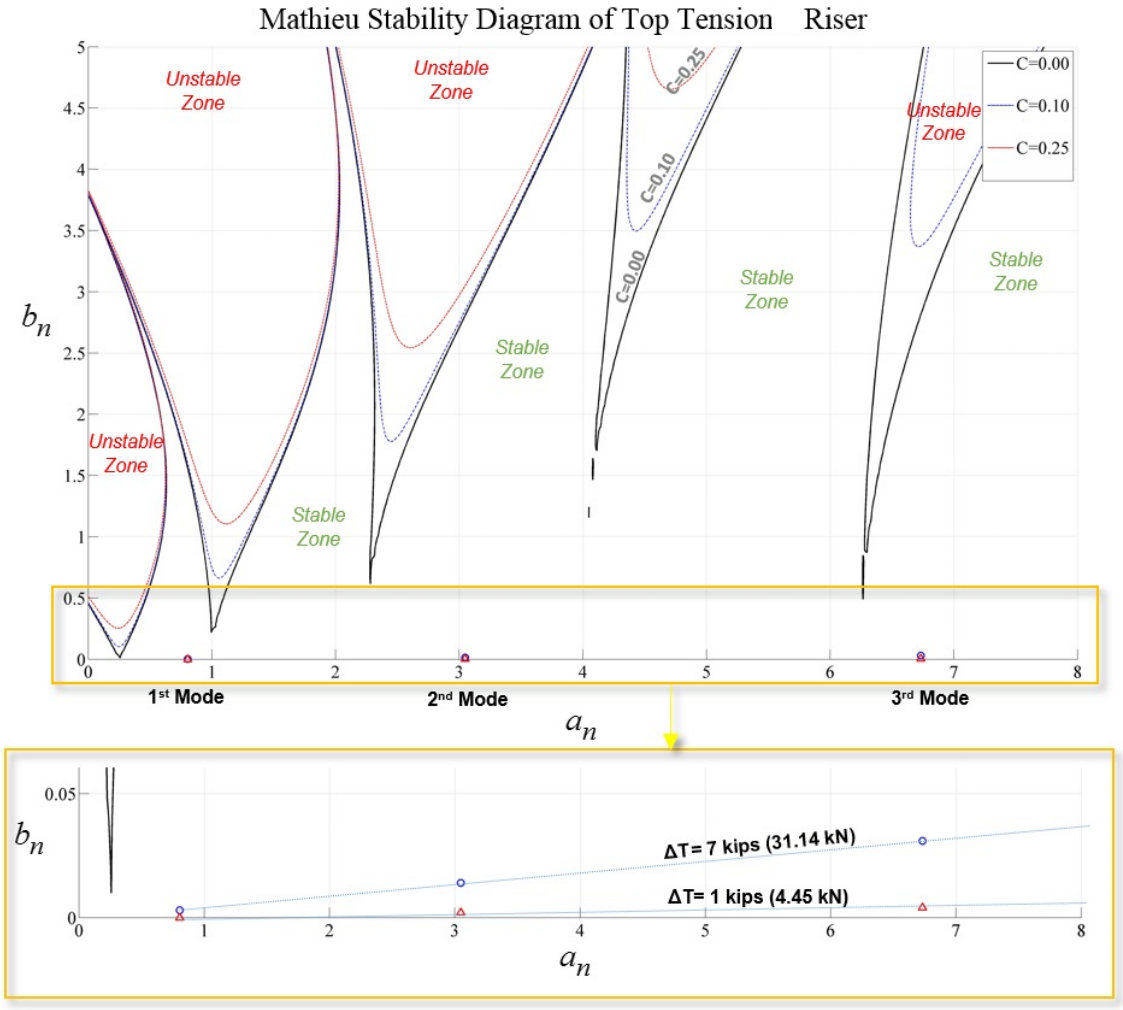

Figure 6.6 Mathieu stability assessment of a single TTR in the TLP host platform with EFCC control scheme.

7. SEMI-SUBMERSIBLE DRY-TREE INTERFACE BY USING MAGNETO-RHEOLOGICAL DAMPER

7.1 Introduction

There is an increasing trend for drilling with high-pressure risers and surface BOPs from semi-submersible (knowned as *Semi*) platform units (Zeng et al., 2013), this concept is named as Dry-Tree Semisubmersible (DTS). The DTS has the advantages of (1) easy access to production tree for operations, maintenance and inspections, (2) direct vertical access for drilling, completion and workover operation, (3) improved recovery of hydrocarbons (Poll et al. 2013). Xiang et al. (2014) presented the overall design of a TTR system for a DTS interface including ram style tensioner, riser conductor, and riser top assembly design with keel joint. Zeng et al. (2013) discussed the development of DTS by addressing the total value and efficiency of the integrated system during entire life cycle of the product, including design, construction, integration, and installation, operation, and decommission, as well as component reliably and safety.

The motions of typical Semi-submersibles are not compatible with existing dry tree systems. All dry tree support system must allow the TTR to move vertically relative to the hull within the allowable stroke limits. The amount of required stroke depends on the platform heave motion, offset, set-down, thermal growth of the risers, pressure growth across the riser wall, draft changes of the hull, deflection of the riser in the water column, and so on (Poll et al., 2013). Therefore, there are two main directions in the developments of technology readiness of the DTS as follows:

(i) Improving the Semisubmersible hull characteristics so that its heave motion can be reduced within the range of technology well-proven tensioner stroke length;

(ii) Increasing the manufacturing ability and technological maturity of longer stroke TTR tensioner so that the tensioner can support for larger heave motion sea conditions.

The latest development trend includes both directions and trade-off in between the Semi heave motion and riser stroke limits. However, the solution will be more complex when it involved the integration of these two systems (a deeper draft Semi and a longer stroke tensioner) into a fully coupled system. As riser tensioners increase in stroke length and capacity to accommodate high riser loads, well bay configurations and tensioner interfaces have a significant impact on the design of the Semi platform (Koos, 2013). The DTS hulls were configured considering the balance between the tensioner stroke-load characteristic, larger vessel offsets, platform heave displacements, hull draft, well-bay arrangement, quayside integration, transportation, installation, and updated Regulatory requirements for survival conditions (Koos, 2013; Xiang et al., 2014). The DTS heave motion is predominantly governed by its hull draft. An increase in the hull draft causes a commensurate reduction in heave motion and required tensioner stroke range (Zeng et al., 2013). As illustrated in Fig. 7.1, Zeng et al. (2013) proposed a deep draft DTS comprises a two-axis symmetrical hull with draft in the range of 100 ft (*30.48 m*) to 155 ft (*47.24 m*) to accommodate the tensioner stroke in the range of 35 ft (*10.67 m*) to 45 ft (*13.72 m*). Poll et al. (2013) designed a Paired-Column Semisubmersible Hull

(PC-Semi) with draft of 175 ft (*53.34 m*) to accommodate the tensioner stroke of 28 ft (*8.53 m*). In addition, Bian and Xiang (2013) also suggested a DTS hull with the draft of 150 ft (*45.72 m*) to support the tensioner stroke within 35 ft (*10.67 m*), all under the Central GOM 1000-year survival condition with *allowable* occasional tensioner bottom out.

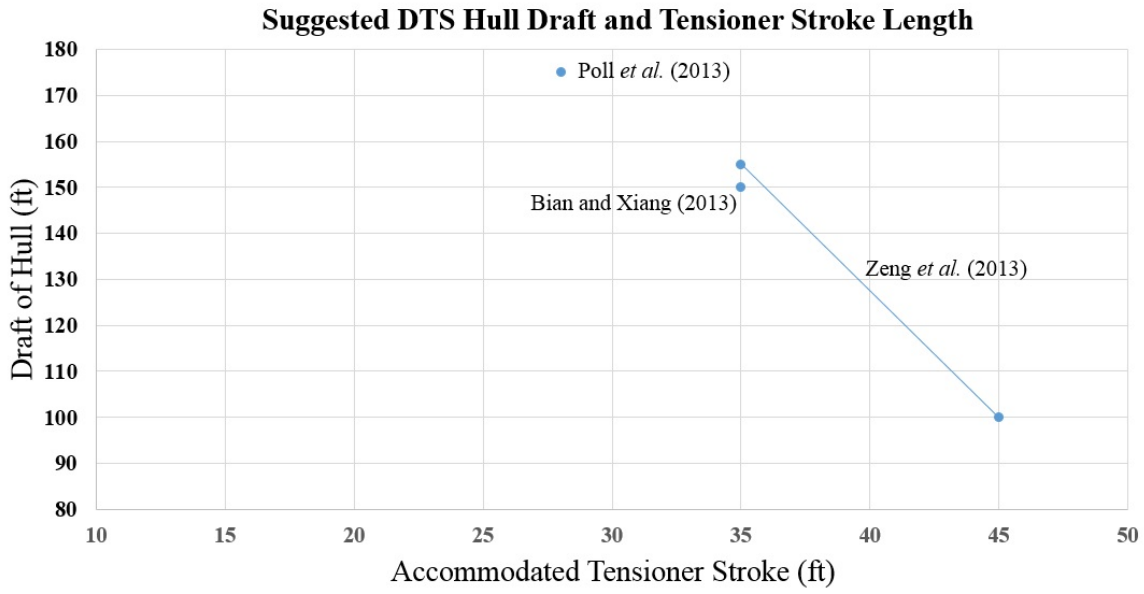

Figure 7.1 Proposed DTS hull draft and accommodated tensioner stroke length.

The interface between the platform and TTR is further complicated by the changes of vertical stiffness. The addition of TTRs' vertical stiffness to the global system of TLP, which is assumed as a beneficial factor in TLP design experience is no longer valid in the integrated design of TTR and DTS. The heave natural period of Semisubmersible is typically larger than the peak wave natural period. Therefore,

additional TTR stiffness into the Semi system will reduce the overall DTS system heave natural period toward the peak wave natural period and potentially trigger heave resonance of the DTS (Poll et al., 2013). The heave natural period of the platform is recommended to be maintained with a range of 5 sec to 8 sec longer than a peak period of the predetermined governing design storm with all riser installed (Zeng et al., 2013). Also, the TTRs with push or pull tensioners of suggested with a combined vertical stiffness less than 30% - 35% of the host platform water plane stiffness (Zou, 2008; Zeng et al., 2013).

Therefore, it can be found that the main challenges in the integration of DTS with TTR system are:

(i) Larger stroke requirements increase the complexity of the DTS technology readiness. Access to the dry tree equipment is more challenging because larger relative motion of mechanical equipment in the deck which may cause potential personnel safety issue. Also, longer stroke may affect deck spacing and arrangement. In addition, the design of flexible jumpers that required for production fluids, power and control are more challenging when the stroke is longer (Poll et al., 2013).

(ii) The combined tensioner system stiffness is limited so that the heave natural period is sufficiently longer than the dominant wave energy periods (Zeng et al., 2013).

The objectives in this Section are:

(i) A numerical analysis of hull/risers/mooring lines coupled motion of a conventional *generic* Semisubmersible will be conducted as the *Base case*; the hydro-pneumatic TTR system was added to a conventional (normal-draft) semi-submersible in order to simulate the dynamic responses of DTS. In this case, the geometrical data, includes draft, of the Semi hull will not be modified. The required TTR tensioner stroke will be determined under the 100-year extreme condition and 1000-year Central GOM survival condition;

(ii) The tension variation effects on the long-stroke tensioner interfaced with the DTS is studied;

(iii) The MR damper is incorporated with the long stroke tensioner in order to (a) provide a damped and deformed contact in between the tensioner ring and MR dampers during bottoming-out motion, (b) redistribute the high tension which in the tensioner cylinders during bottoming-out, and (c) further optimize the total stroke length needed for the DTS.

7.2 Coupled Hull-Mooring Lines-Risers Analysis of Dry-Tree Interface in a Generic Type Conventional Draft Semi-submersible (Base Case)

A coupled hull-mooring lines-risers analysis was carried out for conventional (normal-draft) semisubmersible with dry-tree interface to study the dynamic behaviors and maximum required riser stroke for the DTS. A generic type of DTS model, as illustrated in Fig. 7.2, with 12 chain-polyester-chain mooring lines, 4 steel catenary

risers (SCRs), 2 dual-barrier top tension risers (TTRs) with top tension factor 1.34 is selected for the numerical analyses of tension variations in irregular sea condition. The principal dimensions, displacement and weight distributions of the DTS platform and topside modules are tabulated in Table 7.1 and Table 7.2. In the development of deep-draft semi-submersible, the platform unit may be configured such that a pontoon to platform total displacement ratio is maintained in a range in between 0.3 to 0.5 (Zeng et al., 2013). The deck vertical layout, quayside / in-place stability and hull dynamic motions are important for DTS configuration design iterations (Bian and Xiang, 2013). The large topside and riser payload requires a larger hull than typical wet tree applications. The primary trend in the design is an increased draft to reduce the heave motion to the point that market ready tensioners can be used (Bian and Xiang, 2013). In this numerical case, as illustrated in Fig. 7.3, two top-tensioned risers (TTRs) are proposed to be installed from the DTS symmetrically from the platform geometrical origin with locations of (-5, 0) m (*-16.40 ft, 0 ft*) (labeled as Leg #17) and (5, 0) m (*16.40 ft, 0 ft*) (labeled as Leg #18), respectively. The TTRs are connected to HP-tensioner and simulated with parametric equation, in this *base-case*, as stated in Eqn. (5.12):

$$T = T_0 \left(1 - \frac{\Delta z}{z_0} \right)^{-\gamma} \tag{5.12}$$

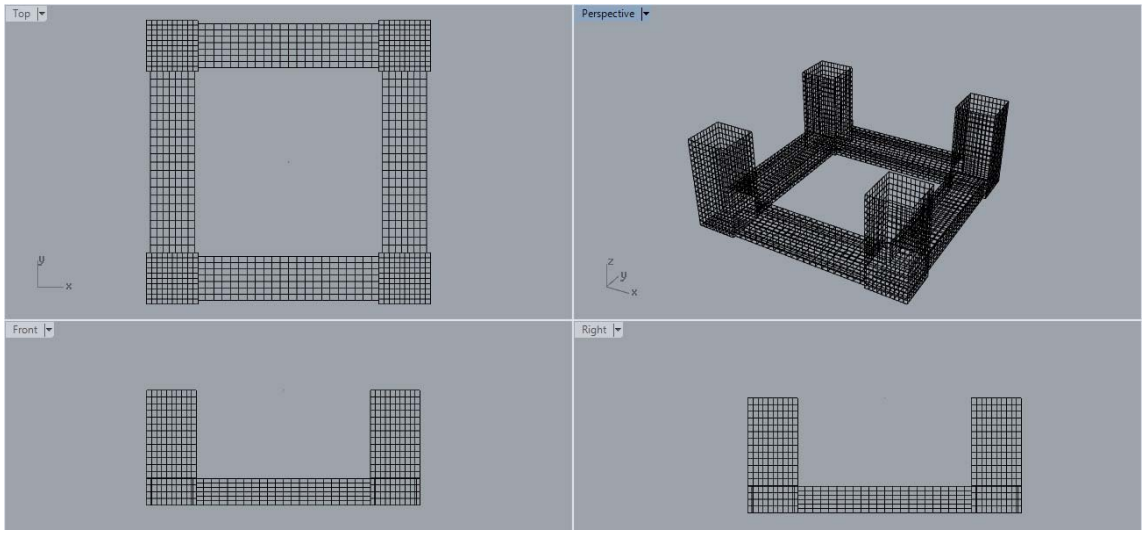

Figure 7.2 Model of generic type DTS platform.

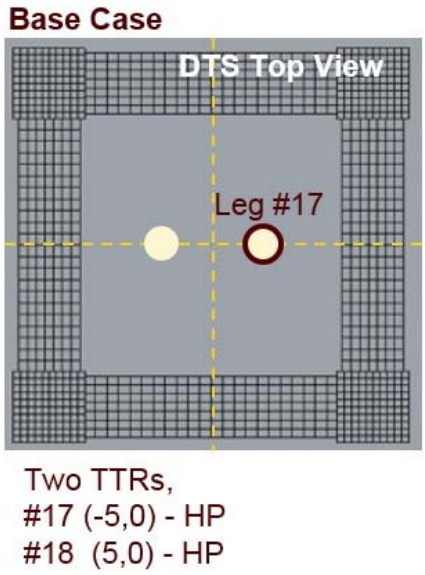

Figure 7.3 Locations of proposed top-tensioned risers in DTS platform.

Table 7.1 Principal dimensions of the generic semi-submersible model.

	SI Unit	**British Unit**
Water depth	1,219.2 m	*4000 ft*
Number of column	4	4
Number of pontoon	4	4
Draft	28.96 m	*95 ft*
Total weight	29,840 ST (265,470 kN)	*59,680 kips*
Hull group	10,928 ST (97,220 kN)	*21,856 kips*
Deck facility	10,000 ST (88,964 kN)	*20,000 kips*
Drilling group	3,000 ST (26,689 kN)	*6,000 kips*
Riser pretension at the top	2,216 ST (19,715 kN)	*4,432 kips*
Mooring load	3,624 ST (32,241 kN)	*7,248 kips*
Single BOP tree weight	10 ST (88.96 kN)	*20 kips*
Displacement	34,810 MT (309,685 kN)	*76,743 kips*

Table 7.2 Principal geometries of generic semi-submersible model*.

		SI Unit	**British Unit**
Pontoon	Width	10.67 m	*35.0 ft*
	Height	6.72 m	*22.1 ft*
	Length	43.89 m	*114.0 ft*
Column	Width	12.50 m	*41.0 ft*
	Height	28.96 m	*95.0 ft*
	Length	12.50 m	*41.0 ft*
Draft		28.96 m	*95.0 ft*
Volume	Pontoon	3,148 m^3	*111,170 ft^3*
	Column	4,524 m^3	*159,764 ft^3*
	Total Pontoon	12,591 m^3	*444,647 ft^3*
	Total Column	18,098 m^3	*639,125 ft^3*
	Hull (under MWL)	30,689 m^3	*1,083,772 ft^3*
Total displacement		**34,810 ST**	***69,620 kips***
Hull group		10,928 ST	*21,856 kips*
Deck facility		10,000 ST	*20,000 kips*
Drilling group		3,000 ST	*6,000 kips*
Total TTR tension		2,216 ST	*4,432 kips*
Mooring load		3,624 ST	*7,248 kips*
Total weight		**29,840 ST**	***59,680 kips***

*Data from estimation and not related to any well-existed dry-tree semi-submersible.

The DTS can support for large payloads, however, its vertical motion is relatively large compared to Spar and TLP, thus requiring longer stroke tensioners to support the vertical TTRs. The tensioner stroke is identified as one of the most dominant design factor to determine the deck layout, hull form, mooring system and the overall floater configuration (Bian and Xiang, 2013). The common material properties of TTR for varying steel grades are listed in Table 7.3. The proposed steel to be used in the TTR is P110 in this case study. Higher grade steel, such as Q125, is suggested for the condition where higher tension is required especially during the bottoming-out period of the tensioner cylinder.

Table 7.3 TTRs and material properties.

			Q125	**P110**	**L80**	**M65**
Elastic modulus		MPa *(ksi)*	2.07E+05 *(30,022)*	2.07E+05 *(30,022)*	2.07E+05 *(30,022)*	2.07E+05 *(30,022)*
Area	Outer casing	m^2 *(ft^2)*	0.0199 *(0.2142)*	0.0199 *(0.2142)*	0.0199 *(0.2142)*	0.0199 *(0.2142)*
	Inner casing	m^2 *(ft^2)*	0.0149 *(0.1604)*	0.0149 *(0.1604)*	0.0149 *(0.1604)*	0.0149 *(0.1604)*
	Tubing	m^2 *(ft^2)*	0.0067 *(0. 0721)*	0.0067 *(0. 0721)*	0.0067 *(0. 0721)*	0.0067 *(0. 0721)*
Yield strength		MPa *(ksi)*	862 *(125)*	758 *(110)*	552 *(80)*	448 *(65)*

Table 7.3 Continued.

			Q125	P110	L80	M65
Stretching stiffness (EA)	Outer casing	N *(kips)*	4.11E+09 *(923,964)*	4.11E+09 *(923,964)*	4.11E+09 *(923,964)*	4.11E+09 *(923,964)*
	Inner casing	N *(kips)*	3.08E+09 *(692,411)*	3.08E+09 *(692,411)*	3.08E+09 *(692,411)*	3.08E+09 *(692,411)*
	Tubing	N *(kips)*	1.39E+09 *(312,484)*	1.39E+09 *(312,484)*	1.39E+09 *(312,484)*	1.39E+09 *(312,484)*
	Total	N *(kips)*	8.59E+09 *(1.93E+06)*	8.59E+09 *(1.93E+06)*	8.59E+09 *(1.93E+06)*	8.59E+09 *(1.93E+06)*
Area moment of inertia, I	Outer casing	m^4 *(ft^4)*	0.00027 *(2.33E-06)*	0.00027 *(2.33E-06)*	0.00027 *(2.33E-06)*	0.00027 *(2.33E-06)*
	Inner casing	m^4 *(ft^4)*	0.00012 *(1.04E-06)*	0.00012 *(1.04E-06)*	0.00012 *(1.04E-06)*	0.00012 *(1.04E-06)*
	Tubing	m^4 *(ft^4)*	0.00001 *(8.63E-08)*	0.00001 *(8.63E-08)*	0.00001 *(8.63E-08)*	0.00001 *(8.63E-08)*
Bending stiffness (EI)	Outer casing	Nm^2 *($kips.ft^2$)*	5.67E+07 *(1.37E+05)*	5.67E+07 *(1.37E+05)*	5.67E+07 *(1.37E+05)*	5.67E+07 *(1.37E+05)*
	Inner casing	Nm^2 *($kips.ft^2$)*	2.51E+07 *(6.07E+04)*	2.51E+07 *(6.07E+04)*	2.51E+07 *(6.07E+04)*	2.51E+07 *(6.07E+04)*
	Tubing	Nm^2 *($kips.ft^2$)*	2.65E+06 *(6.41E+03)*	2.65E+06 *(6.41E+03)*	2.65E+06 *(6.41E+03)*	2.65E+06 *(6.41E+03)*

Table 7.3 Continued**.**

			Q125	P110	L80	M65
Density of steel		kg/m^3 *(slug/ft^3)*	7860 *(15.25)*	7860 *(15.25)*	7860 *(15.25)*	7860 *(15.25)*
Mass per unit length	Outer casing	kg/m *(slug/ft)*	1.56E+02 *(3.26)*	1.56E+02 *(3.26)*	1.56E+02 *(3.26)*	1.56E+02 *(3.26)*
	Inner casing	kg/m *(slug/ft)*	1.17E+02 *(2.44)*	1.17E+02 *(2.44)*	1.17E+02 *(2.44)*	1.17E+02 *(2.44)*
	Tubing	kg/m *(slug/ft)*	5.28E+01 *(1.10)*	5.28E+01 *(1.10)*	5.28E+01 *(1.10)*	5.28E+01 *(1.10)*
Density of seawater		kg/m^3 *(slug/ft^3)*	1025 *(1.99)*	1025 *(1.99)*	1025 *(1.99)*	1025 *(1.99)*
Density of nitrogen gas		kg/m^3 *(slug/ft^3)*	23.965285 *(0.0465)*	23.965285 *(0.0465)*	23.965285 *(0.0465)*	23.965285 *(0.0465)*
Displaced mass per unit length	Outer casing	kg/m *(slug/ft)*	20.35 *(0.425)*	20.35 *(0.425)*	20.35 *(0.425)*	20.35 *(0.425)*
	Inner casing	kg/m *(slug/ft)*	0.36 *(7.52E-03)*	0.36 *(7.52E-03)*	0.36 *(7.52E-03)*	0.36 *(7.52E-03)*
	Tubing	kg/m *(slug/ft)*	0.16 *(3.34E-03)*	0.16 *(3.34E-03)*	0.16 *(3.34E-03)*	0.16 *(3.34E-03)*
Inertial force coef.	Outer casing	N/m-acc.	198.18	198.18	198.18	198.18

Table 7.3 Continued**.**

			Q125	**P110**	**L80**	**M65**
Drag force coef.	Outer casing	N/m-vel.	215.77	215.77	215.77	215.77
C_d	Outer casing		1.2	1.2	1.2	1.2
Section area	Outer casing	m^2 *(ft^2)*	0.0199 *(0.2142)*	0.0199 *(0.2142)*	0.0199 *(0.2142)*	0.0199 *(0.2142)*
Break line tension	Outer casing	N *(kips)*	1.00E+10 *(2.25E+06)*	1.00E+10 *(2.25E+06)*	1.00E+10 *(2.25E+06)*	1.00E+10 *(2.25E+06)*

Three-hour time-simulations were carried out in a Central Gulf of Mexico (GOM) 100-year extreme environmental condition, and GOM 1000-year survival condition, where the metocean profiles are listed in Table 7.4. Wave, wind, and current are collinear with a 180° of incident angle. The time series and spectrum density of wave elevation are shown in Fig. 7.4.

Table 7.4 Wave, current, and wind profiles of the central-GOM 100-year and 1000-year return period (RP) conditions in *base case* simulation.

		100-RP	**1000-RP**
Significant wave height, H_s		15.8 m *(51.84 ft)*	19.8 m *(64.96 ft)*
Peak period, T_p		15.4 sec	17.2 sec
Overshooting parameter, γ		2.40	2.40
Main direction of waves		180 deg	180 deg
Direction of current		180 deg	180 deg
Current profile	Surface speed	2.40 m/s *(7.874 ft/s)*	3.00 m/s *(9.843 ft/s)*
	Speed at mid-profile	1.80 m/s *(5.906 ft/s)*	2.25 m/s *(7.382 ft/s)*
	Zero-speed depth	100.80 m *(330.71 ft)*	126.00 m *(413.39 ft)*
Wind	10 m elevation (1 hour mean speed)	48.00 m/s *(157.48 ft/s)*	60.00 m/s *(196.85 ft/s)*

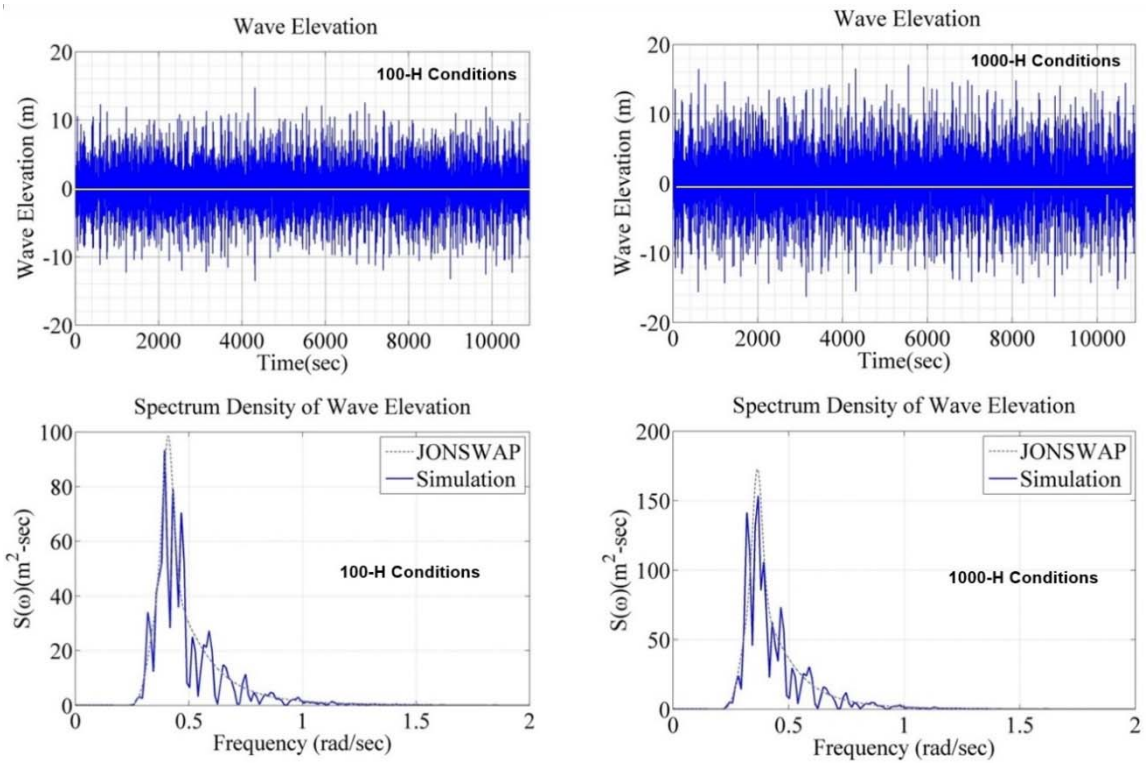

Figure 7.4 The wave elevation of central GOM condition for (a) 100-year return period; and (b) 1000-year return period.

The finite element (FE) model of the nonlinear hydro-pneumatic tensioner and the hull motion is implemented in CHARM3D, a fully-coupled time-domain dynamic-analysis program for floating bodies, mooring lines/tendons, and risers (Ran, 2000; Kang et al., 2014). The DTS platform motions are shown in frequency domain in Fig 7.5 and time domain in Fig. 7.6. These results are compared with the platform motions of conventional semi-submersible (SEMI) settings, where the TTRs are not installed on the platform. It can be found that the motions of DTS are generally smaller than the motions of SEMI. Also, the responses of 1000-year return period (1000-H) is large than the responses of 100-year return period (100-H) in the wave frequency (WF) and low

frequency (LF) regions but there are not apparent differences for both conditions in the high-frequency (HF, low period) region.

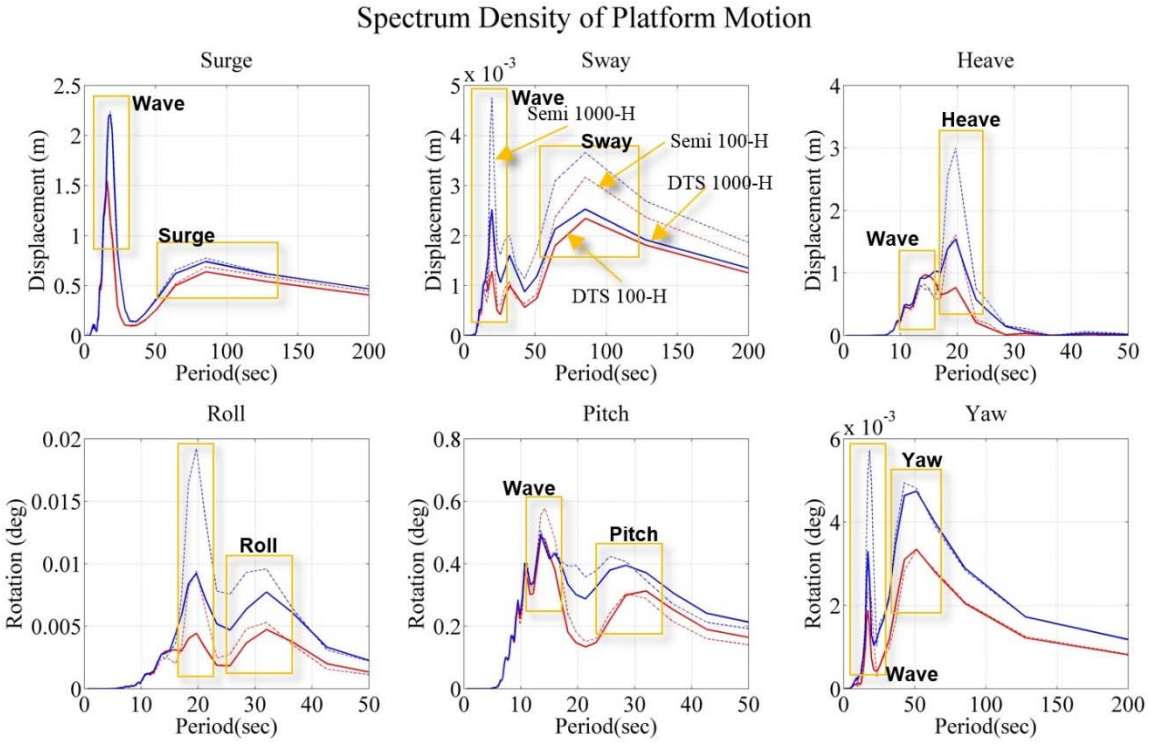

Figure 7.5 Platform motions in frequency domain.

The main concern is the characteristics of dynamic *heave* responses (in Fig. 7.5) where there are two major peaks in its amplitude spectrum: one is around the period of 15 sec which is near the wave peak period, and the other is around the period of 19 sec which is near the platform heave natural period. Similar multi-peaks spectrums are found in the motions of other directions where roll/pitch motion at around the period of 30 sec and surge/sway motion at around the period of 85 sec. Since the platform heave natural

period and wave peak period is very close, the increased vertical stiffness associated with the additional TTRs must be validated robustly because this change reduces the heave period of the semi-submersible closer to the dominant wave period and induces heave resonance (Poll et al., 2013, Bian and Xiang, 2013).

The extreme factor distributions for 100-H and 1000-H conditions are shown in Fig. 7.7. The extreme factor is calculated as the ratio of extrema with respect to the standard deviation of the data series. It can be found that the *heave* extreme factor distribution agrees well with the Gaussian distribution, which means typical Gaussian characteristics containing almost all wave frequency components in the time series (Zou, 2008).

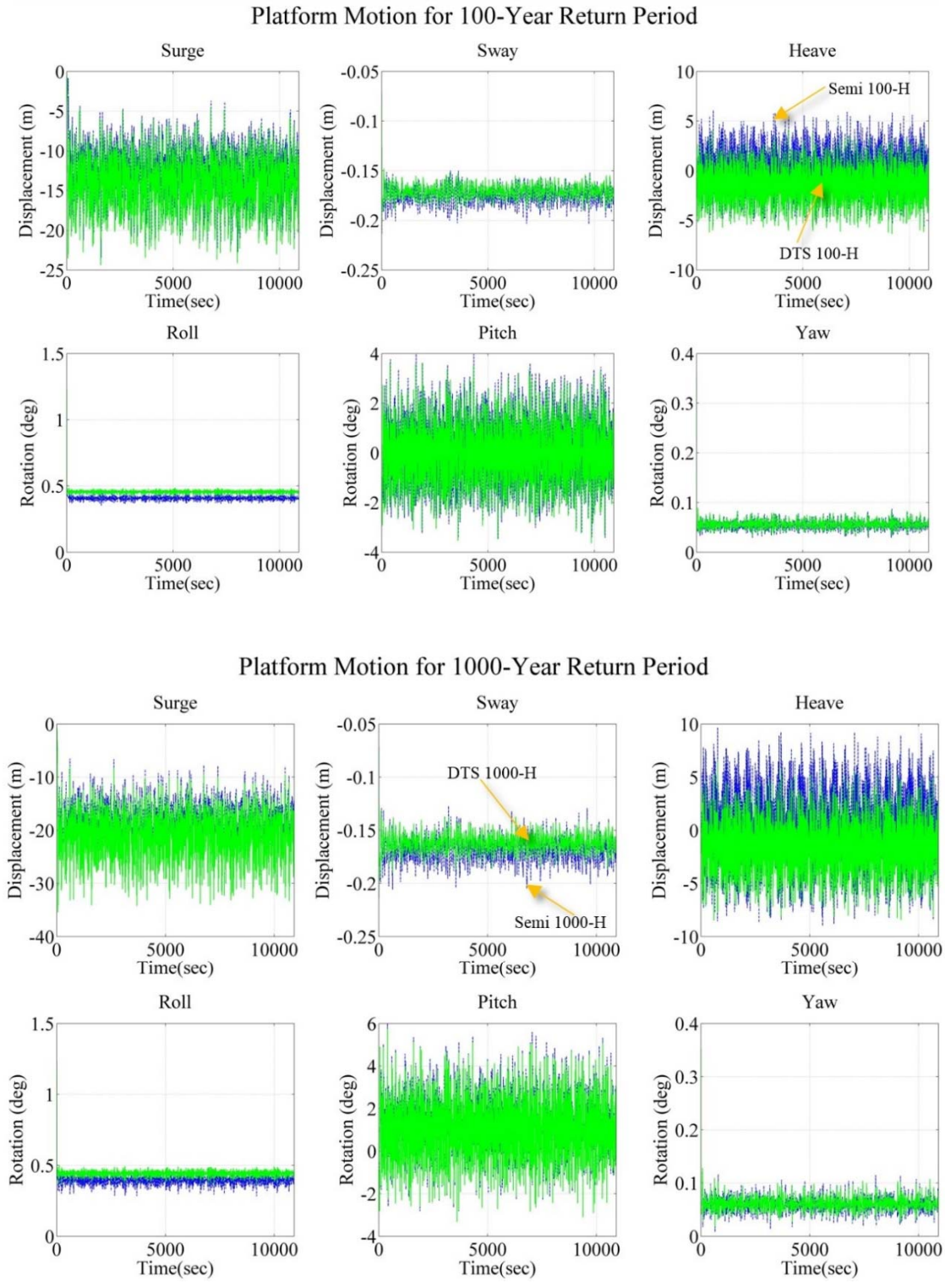

Figure 7.6 Platform motions in time domain.

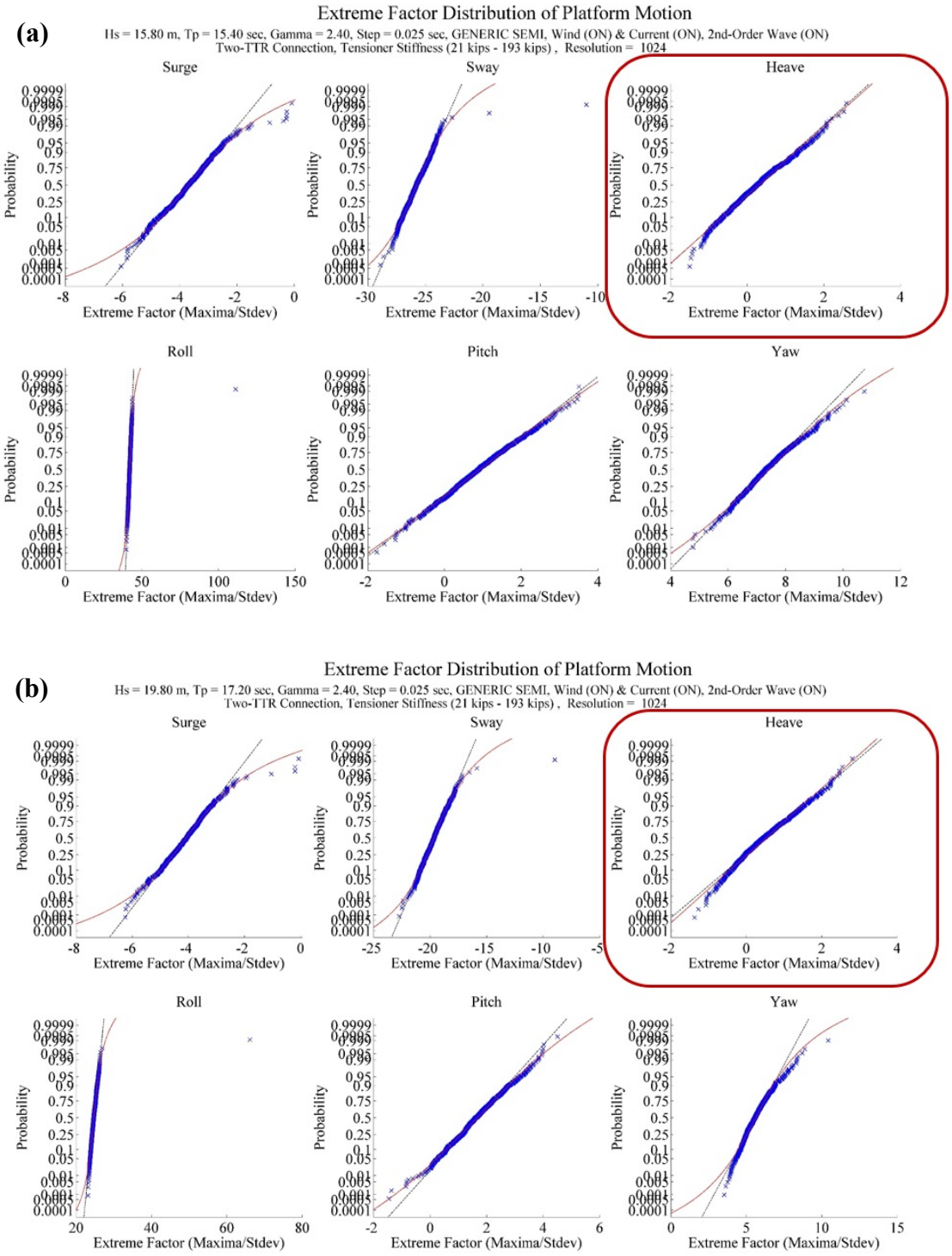

Figure 7.7 Extreme factor distribution of DTS platform motions for (a) 100-year return period, and (b) 1000-year return period.

The response amplitude operators (RAO) of DTS platform and SEMI platform in this case study are shown in Fig. 7.8. In the RAO of heave motion, the cancellation period DTS is located at ~17.5 sec The RAO in heave direction is very sensitive to the additional tensioner stiffness after the top-tensioner risers are incorporated into the system. A softer tensioner (lower stiffness) is better for overall platform heave natural period and global motions. However, the trade-off to increase the softness is by increasing the size of accumulators and NPVs in the hydro-pneumatic system, as illustrated in Fig. 5.3, which increases overall equipment size, complexity and cost (Poll et al., 2013).

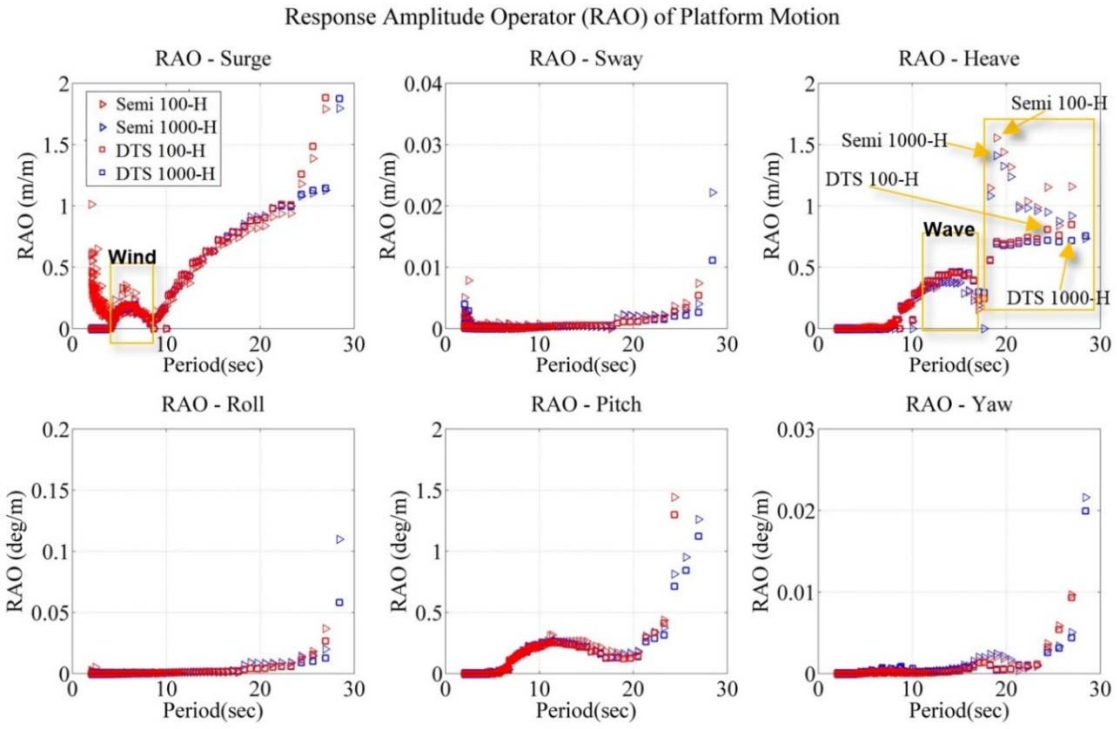

Figure 7.8 RAO of platform motions.

The RAO of DTS platform heave motions for variations of tensioner stiffness is studied in more detailed in Fig. 7.9 and compared to the findings of Bian and Xiang (2013). A higher tensioner stiffness (where the *equivalent* length of cylinder, z_0 in Eqn. 5.12 is shorter) causes slightly increment of RAO in the first peak (coincident with wave peak) and reduces the RAO in the second peak (which after the cancellation period at ~ 17.5 sec, in this case). There is noteworthy that in this numerical analysis, the mass matrix of semi-submersible is remained unchanged in order to observe the effects contributed only by the variations of tensioner stiffness. It can be achieved, in real practice, by rearranging the topside modules payload after considered the additional payloads caused by the higher tensioner stiffness so that the total payload is remained unchanged.

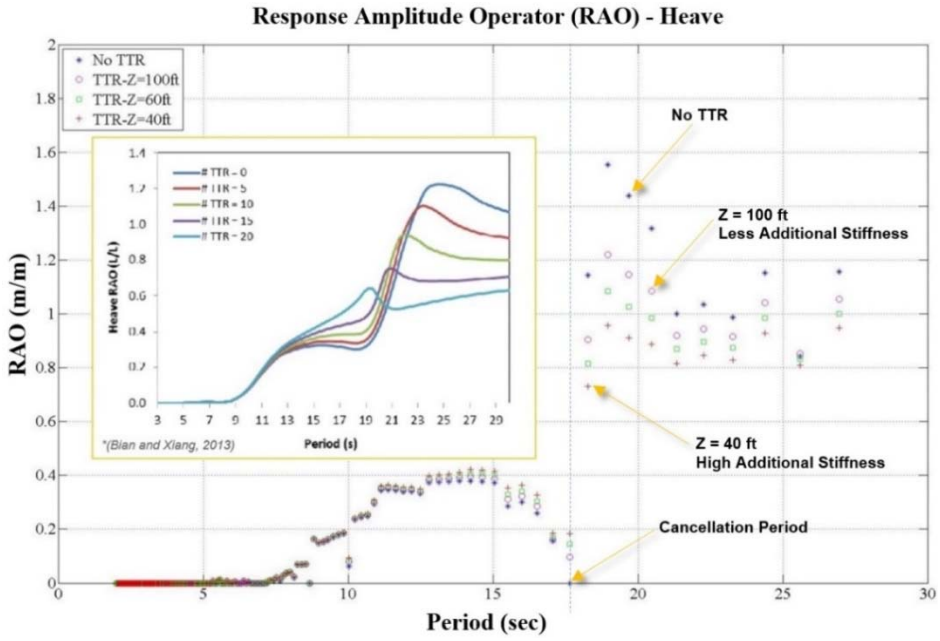

Figure 7.9 RAO of DTS platform motions for variations of tensioner stiffness.

The trajectories of DTS in surge-heave direction are shown in Fig. 7.10. It can be found that the maximum horizontal offset under collinear (from direction of 180°) wave-wind-current condition is ~26 m (*~85.30 ft*) and ~36 m (*~118.11 ft*) for 100-H and 1000-H return period conditions, respectively. The range of platform heave motion is [~ + 4.2 m, - 6.5 m] (*~13.78 ft to -21.33 ft*) for 100-H return period and [~ + 6.5 m, - 8.5 m] (~ *21.33 ft to -27.88 ft*) for 1000-H return period. However, it can also be observed from the probability density spectrum of the DTS motion trajectory in Fig. 7.10 that the probability of extreme positions are very low; the high occurrences are happened in a short range nearby its static equilibrium position. Nevertheless, the *envelopes* of platform motion are important for the calculation of the required TTR stroke lengths in the 100-H and 1000-H return period conditions.

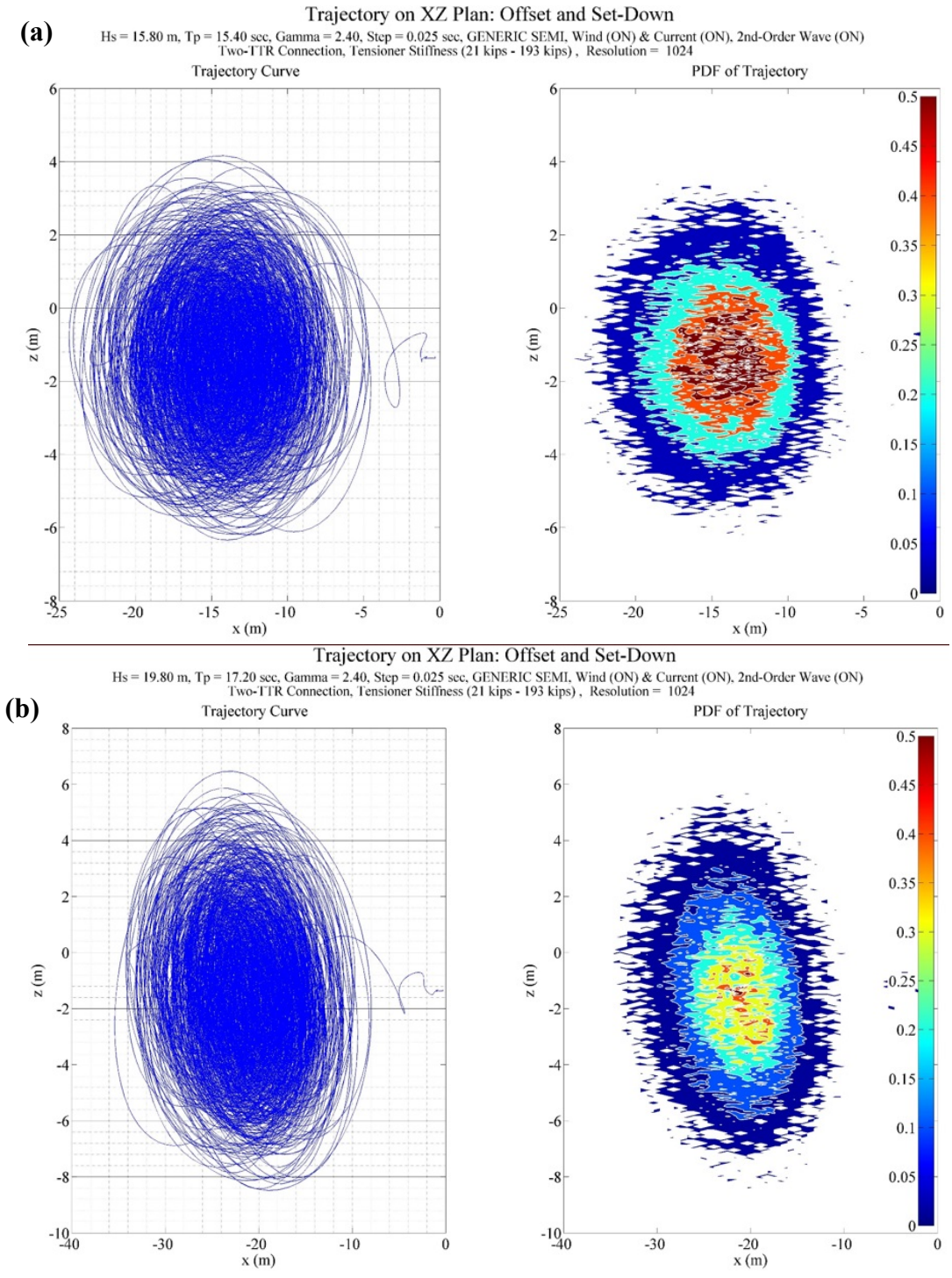

Figure 7.10 Trajectory of DTS platform motions in X-Z plan for (a) 100-year return period, and (b) 1000-year return period.

The dynamic riser strokes for *unbounded* limits of TTR tensioner are illustrated in Fig. 7.11 (frequency domain) and Fig. 7.12 (time domain). The riser stroke in 1000-H condition is large than the stroke in 100-H return period condition in the wave frequency (WF) and low frequency (LF) regions but there are not apparent differences for both conditions in the high-frequency (HF) region.

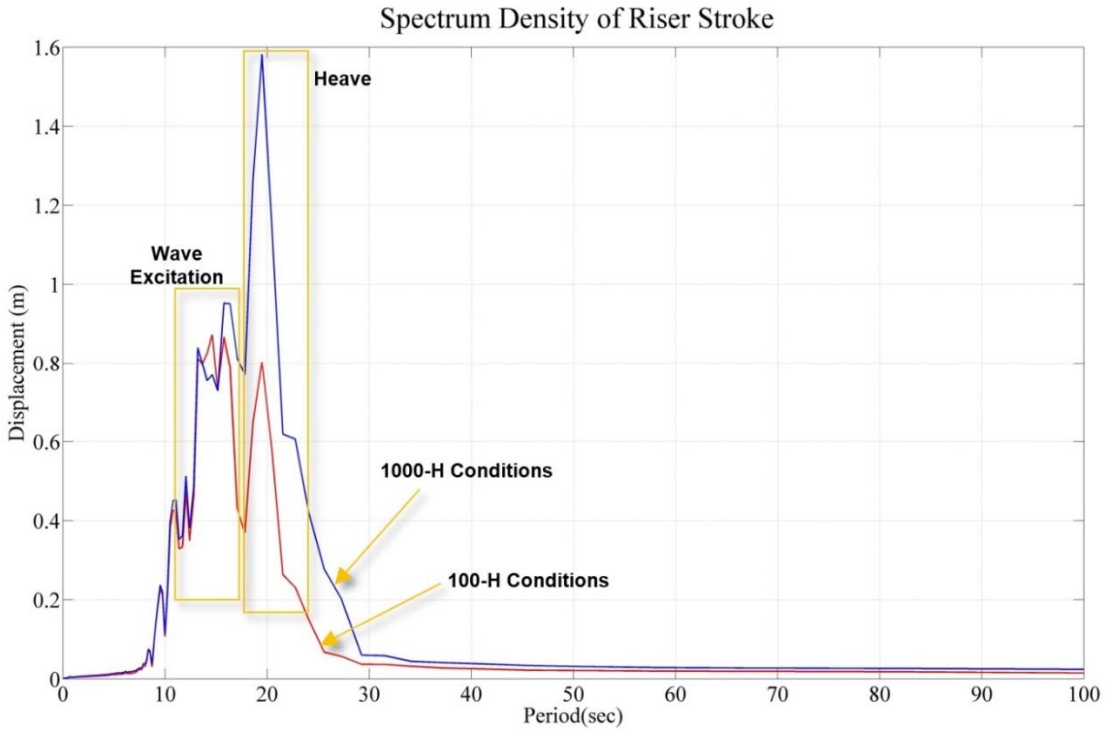

Figure 7.11 Spectrum density of stroke of TTR interface in DTS platform for (a) 100-year return period, and (b) 1000-year return period.

For 100-H extreme condition, the maximum required riser stroke length in this case study is 9.727 m (~ *32 ft*), as shown in the Fig. 7.12, and the heave peak period is around 19 sec. For 1000-H; the maximum required riser stroke length is 13.342 m (~ *44*

ft) and the heave peak period is around 19 sec. There is noteworthy that the dynamic stroke value will be further enlarged after considered the mean offset (sagging) and tidal height effects that are assumed to contribute nearly additional 50% of stroke, *majority in down-stroke*, during the survival condition (Bian and Xiang, 2013).

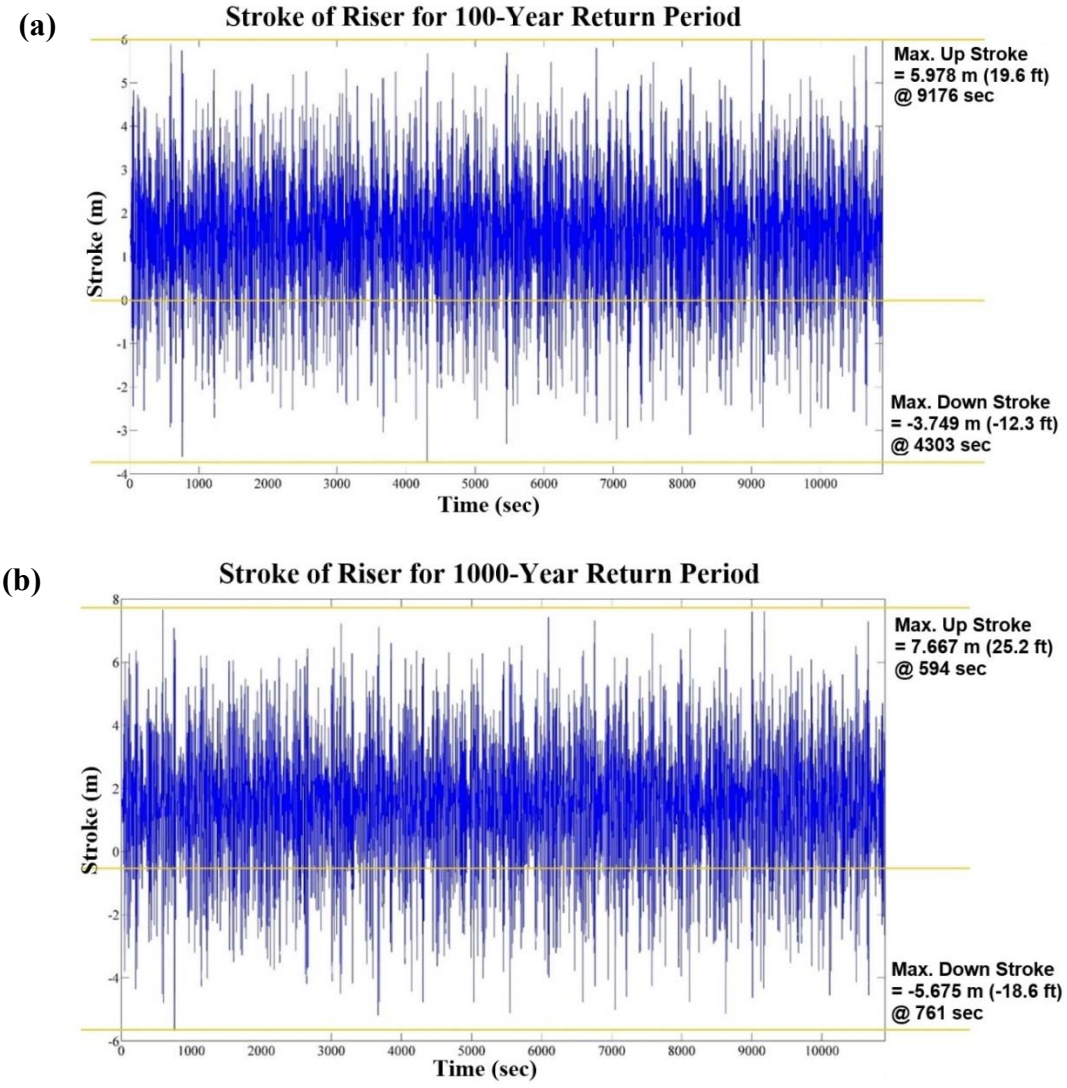

Figure 7.12 Stroke of TTR interface in DTS platform in time domain for (a) 100-year return period, and (b) 1000-year return period.

The top-tension of TTR interface in DTS platform with respect to the variations of strokes and velocities are shown in Fig. 7.13 for 100-H condition and Fig. 7.14 for 1000-H condition. The top-tension acting on the tensioner ring are ranged in [~2.75 MN to ~8.25 MN] (*~618.22 kips to ~1854.67 kips*) and [~2.50 MN to ~11.80 MN] (*~562.02 kips to ~2652.75 kips*) for 100-H and 1000-H return period conditions, respectively. The velocities of riser stroke interfaced with the DTS are from ~ -2.3 m/s (~ *-7.55 ft/s*) to ~ +2.0 m/s (~ *+6.56 ft/s*) for 100-H return period and from ~ -2.5 m/s (~ *-8.20 ft/s*) to ~ +2.6 m/s (~ *+8.53 ft/s*) for 1000-H return period. It can also be found from the probability density spectrum contours of tension-velocity that the probabilities of extreme velocities are in the low occurrences.

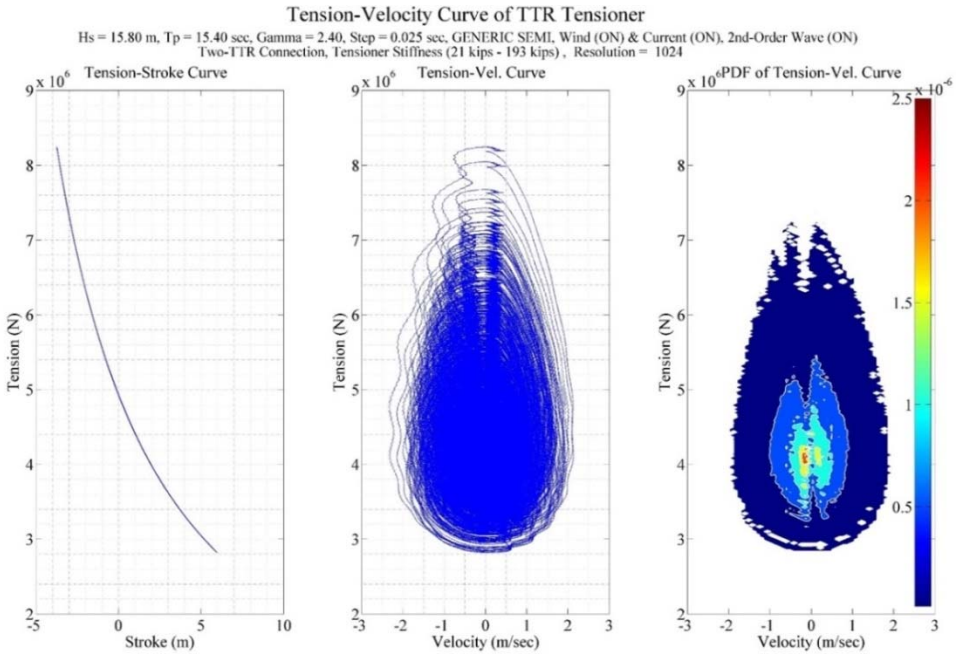

Figure 7.13 Top-tension of TTR interface in DTS platform with respect to the variations of strokes and velocities for 100-year return period.

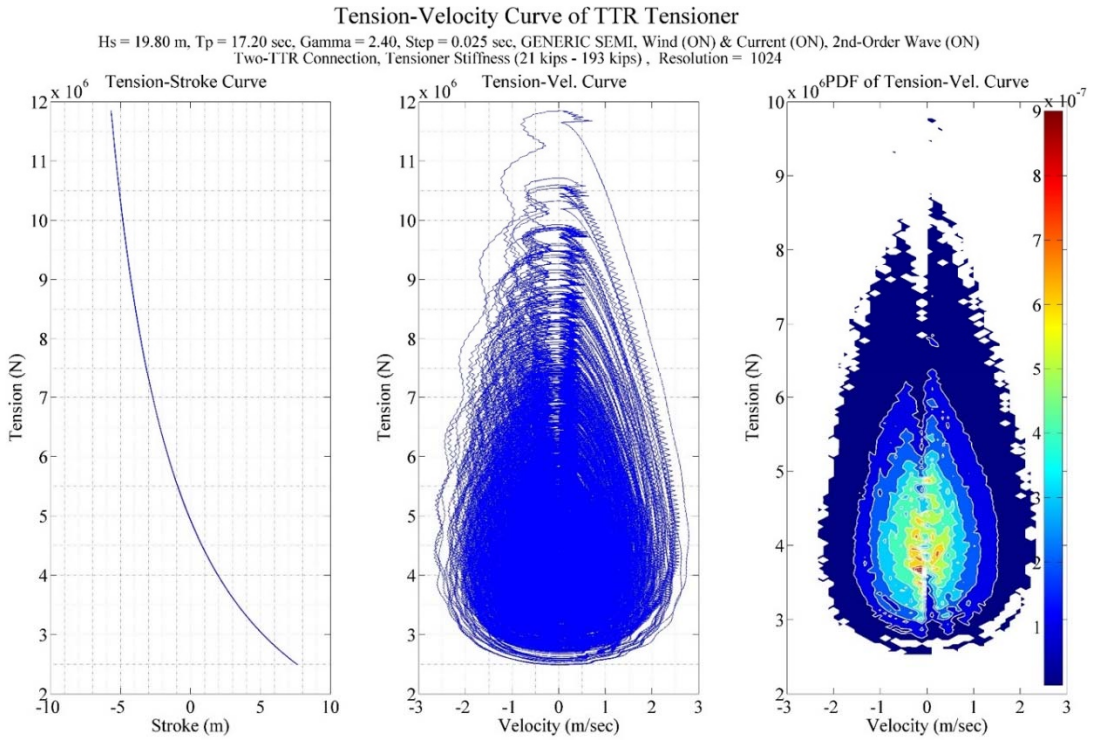

Figure 7.14 Top-tension of TTR interface in DTS platform with respect to the variations of strokes and velocities for 1000-year return period.

The extreme dynamic profiles of TTR upstroke and down-stroke are shown in Fig. 7.15 for 100-H condition and Fig. 7.16 for 1000-H condition. The maximum inclination occurred at the location of tension ring (top-end node) for this case study where the keel guide is not installed. There is noteworthy that the scales in x- and z-directions in the plots in Figs. 7.15 - 7.16 are different in order to clearly represent the deflections of the riser. The segments in the yellow-boxes are located inside the zone of DTS, which are spanned from the tensioner ring (top-end node) to the location at the bottom of platform's hull pontoons. The segments from tensioner ring to the bottom of ram-style tensioner are lined linearly because these nodes are restrained by the structure

of tensioner. The maximum horizontal-deflections inside the DTS platform are ~1.5 m (*~4.92 ft*) for 100-H condition and ~3.0 m (*~9.84 ft*) for 1000-H condition, respectively. This values are significant in the determination of well-spacing in order to prevent collision with neighboring riser. For the overall length of riser, the maximum offset of riser segments are 1.8% WD (water depth) and 2.5% WD, for 100-H and 1000-H conditions respectively.

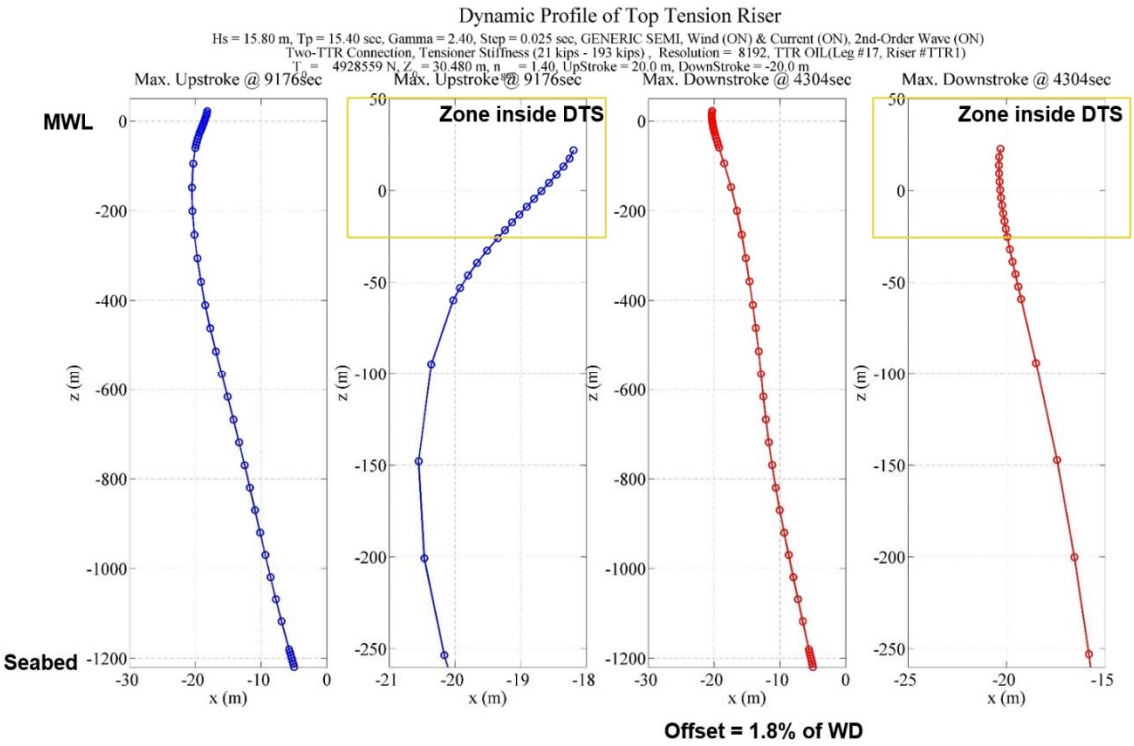

Figure 7.15 Extreme dynamic profiles of TTR in DTS platform for 100-year return period.

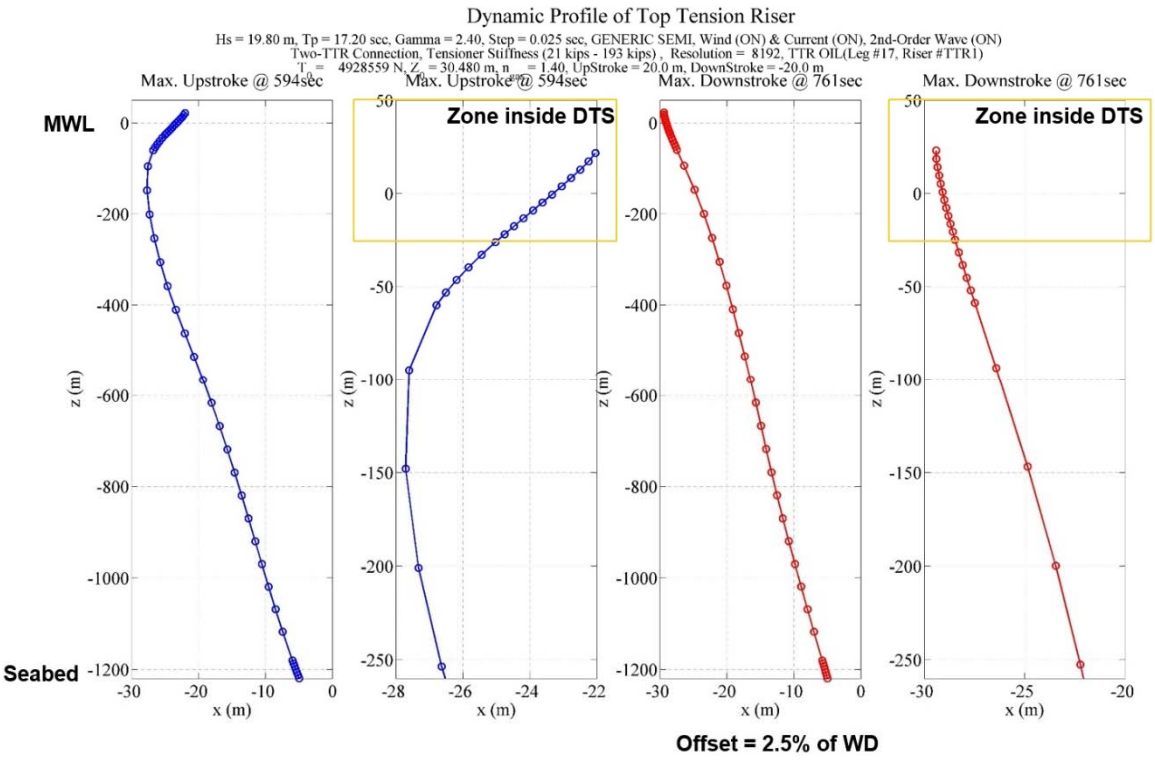

Figure 7.16 Extreme dynamic profiles of TTR in DTS platform for 1000-year return period.

The *envelopes* of axial tension, bending moments, and von-Mises stress of the TTR in the 100-H condition and 1000-H condition are shown in Fig. 7.17. The axial tension is increased proportionally from the bottom of riser to the tensioner ring. The maximum bending moment is found in the location of tension ring (top-end node) where the maximum inclination was occurred. The von-Mises stresses are within the limits (~0.75 utilization for 100-H condition, and ~0.85 utilization for 1000-H condition) for the case of steel grade P110.

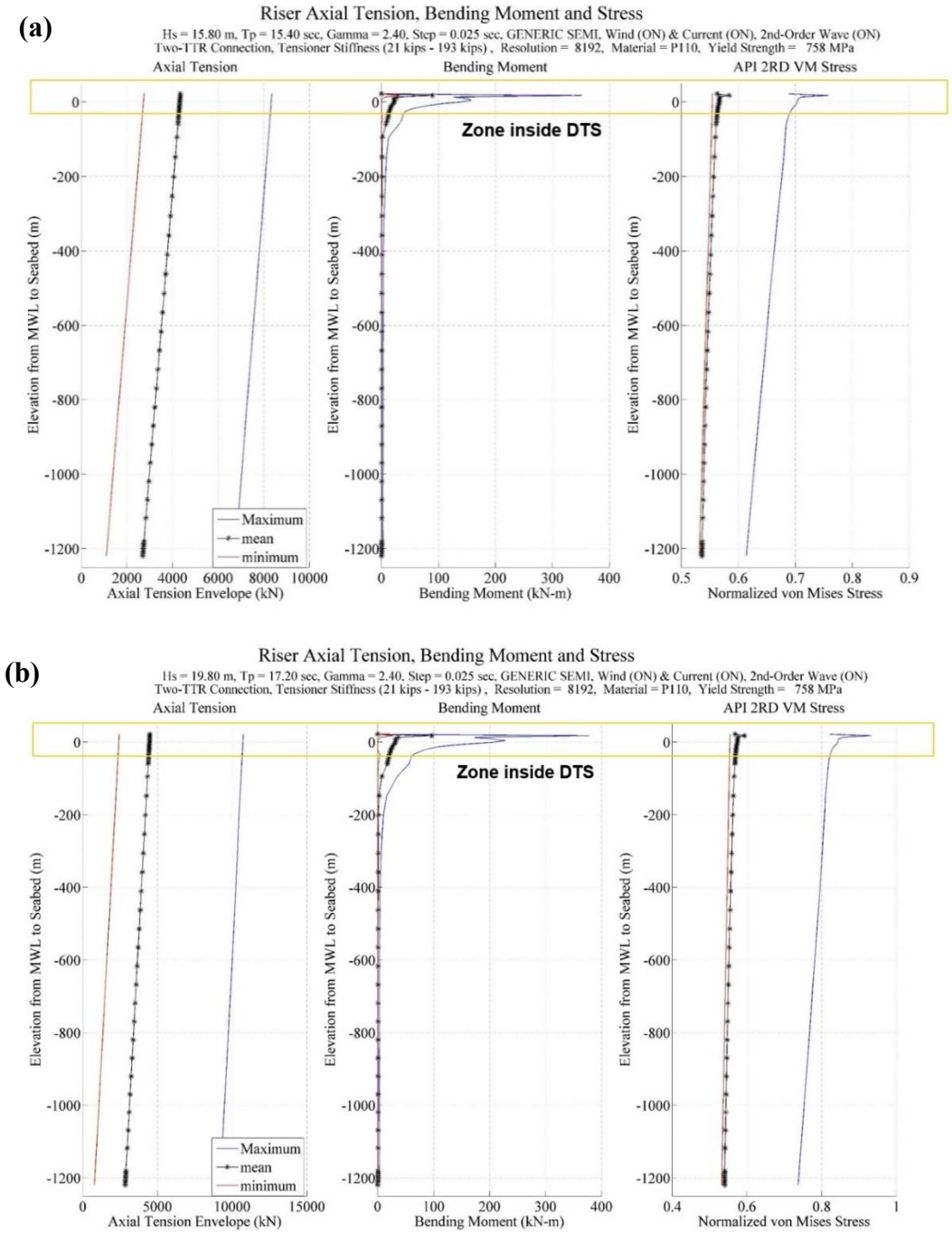

Figure 7.17 Axial tension, bending moment and von-Mises stress of TTR (Leg #17) interfaced with DTS platform for (a) 100-year return period, and (b) 1000-year return period.

The statistical analysis of top-tension for TTRs, SCRs, and mooring lines of DTS platform for 100-year return period, and 1000-year return period is shown in Fig. 7.18. There are 12 mooring lines (4 column × 3 lines/column). Under the collinear wave, wind, and current from 180° of incident angle, the upstream catenary mooring lines (#1 to #6) experiences higher axial tension force and higher tension variations than the downstream counterparts (#7 to #12). The 4 SCRs (#13 for water injection, #14 for oil production, #15 for gas production, and #16 for flow line) are inherited from a conventional type of semi-submersible platform design. It can be found that the axial tension in gas production riser is the lowest, which is around ~0.5 MN (*~112.40 kips*).

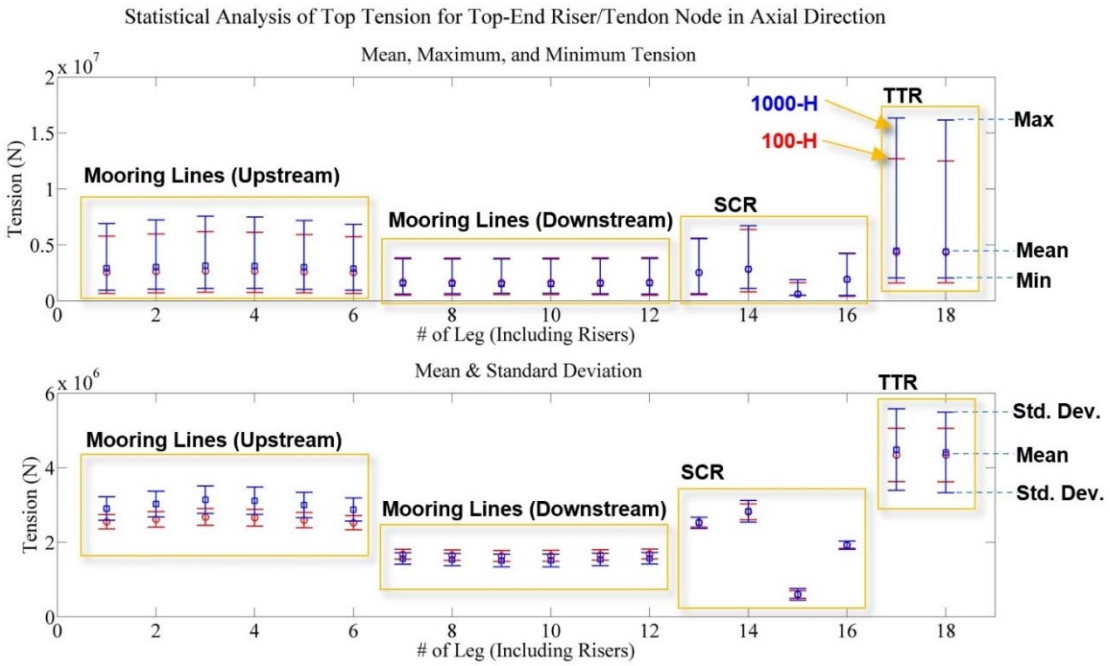

Figure 7.18 Statistical analysis of top-tension for TTRs, SCRs, and mooring lines of DTS platform motions for (a) 100-year return period, and (b) 1000-year return period.

The additions of two TTRs generated highest top-tension, as shown in Fig. 7.18. These two risers are supported by tensioners, instead of in natural catenary form. The inclusion of single TTR can contribute the axial tension exertion of nearly two upstream mooring lines, equivalently, in this case study. The Mathieu stability for the first two modes of the TTR was studied and the results are shown in Fig. 7.19. It was found that the TTR first mode for both 100-H and 1000-H cases are in the stable zone and the second mode for 100-H condition are close to the marginal zone. However, it can be inferred that the second mode for 100-H condition is stable as well because the existence of slight lateral damping, which normally above zero in the wet-condition, can significantly enlarge stable zone in the Mathieu diagram.

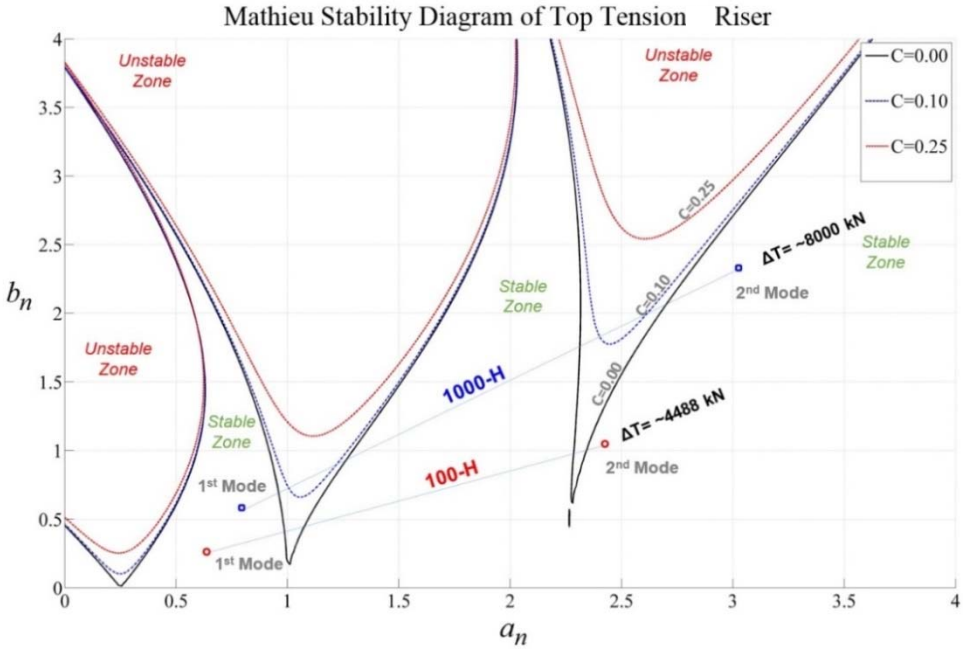

Figure 7.19 Mathieu stability analysis of TTR (Leg #17) interfaced with DTS platform.

7.3 Tension Variations of Hydro-Pneumatic Tensioner (HPT) for Dry-Tree Interface in Semi-submersible

From the numerical analyses in the regular wave condition in Subsection 5.6, it can be found that the tension variations of HPT is a dependent of the length of hydraulic fluid traveling per cycle, and the relative velocity in between the platform and TTR. These two factors contribute minor effects in the TLP because the tensioners in TLP are short stroke with typically in the range from 6 ft (*1.829 m*) to 10 ft (*3.048 m*) (Leverette et al., 2013), hence the maximum allowable traveling length per cycle is small. Moreover, the relative vertical velocity of TLP-TTR is much smaller than one in the semisubmersible platform. These two key factors in tension variations, however, become very significant in the developments of *dry-tree* interface in the semi-submersible. The heave motion of industrially proposed dry-tree semisubmersible (DTS) is large and long stroke tensioner is required to compensate this heave motion. Zeng et al. (2013) proposed a deep draft DTS comprises a two-axis symmetrical hull with draft in the range of 100 ft (*30.48 m*) to 155 ft (*47.24 m*) to accommodate the tensioner stroke in the range of 35 ft (*10.67 m*) to 45 ft (*13.72 m*). Poll et al. (2013) designed a Paired-Column Semisubmersible Hull (PC-Semi) with draft of 175 ft (*53.34 m*) to accommodate the tensioner stroke of 28 ft (*8.53 m*). In addition, Bian and Xiang (2013) also suggested a DTS hull with the draft of 150 ft (*45.72 m*) to support the tensioner stroke within 35 ft (*10.67 m*), as illustrated in Fig. 7.1. From these reported data of the long stroke tensioner to be installed in the DTS, even if the accumulator is designed to be located just beside

the cylinder (Trent, 2012), the hydraulic fluid is allowed to flow at least from 8.53 m (*28 ft*) to 13.72 m (*45 ft*) inside the length of tensioner cylinder.

The dimensions and data of HPT has been modified from Table 5.1 to customize the DTS setting where the stiffness of long-stroke tensioner at zero-displacement is 40 kips/ft (*54 kN/m*) and are tabulated in Table 7.5. There is noteworthy that two different settings with different volume sizes of NPVs were studied. The option **TV-A** has relatively smaller volume of low-pressure NPV and larger high-pressure NPV than option **TV-B**.

Three-hour time-simulations were carried out in a Central Gulf of Mexico (GOM) 100-year extreme environmental condition, and GOM 1000-year survival condition, where the metocean profiles are listed in Table 7.6. Wave, wind, and current are collinear with a 180° of incident angle.

Table 7.5 Hydraulic-pneumatic tensioner data for DTS.

Total Number of Cylinders		6
Pressure at LNPV		8.30 bar *(120.4 psi)*
Pressure at HNPV		49.3 bar *(715.04 psi)*
Length of Pipe from LNPV to Cylinder*		0.1 m *(0.3281 ft)*
Diameter of Pipe from LNPV to Cylinder		0.1524 m *(0.5000 ft)*
Length of Pipe from HNPV to Accumulator*		0.1 m *(0.3281 ft)*
Diameter of Pipe from HNPV to Accumulator		0.1524 m *(0.5000 ft)*
Length of Pipe from Accumulator to Piston		10.0 m *(32.81 ft)*
Diameter of Pipe from Accumulator to Cylinder		0.1524 m *(0.5000 ft)*
Cross-sectional Area of Cylinder		0.2463 m^2 *(2.6512 ft^2)*
Hydraulic Fluid Area of Piston-Side		0.2048 m^2 *(2.2044 ft^2)*
Density of hydraulic oil		850 kg/m^3 *(1.649 $slug/ft^3$)*
Viscosity of hydraulic oil		84.2416 cSt ($\times 10^{-6}$ m^2/s) *(906.77 $\times 10^{-6}$ ft^2/s)*
	Option A (TV-A)	**Option B (TV-B)**
Volume of LNPV	2.5 m^3 *(88.3 ft^3)*	8.0 m^3 *(282.5 ft^3)*
Volume of HNPV	8.0 m^3 *(282.5 ft^3)*	2.5 m^3 *(88.3 ft^3)*

* Note: to be negligible in long-stroke tensioner case

Table 7.6 Wave, current, and wind profiles of the central-GOM 100-year and 1000-year return period (RP) conditions in tension variations simulation.

		100-RP	**1000-RP**
Significant wave height, H_s		15.8 m *(51.84 ft)*	19.8 m *(64.96 ft)*
Peak period, T_p		15.4 sec	17.2 sec
Overshooting parameter, γ		2.40	2.40
Main direction of waves		180 deg	180 deg
Direction of current		180 deg	180 deg
Current profile	Surface speed	2.40 m/s *(7.874 ft/s)*	3.00 m/s *(9.843 ft/s)*
	Speed at mid-profile	1.80 m/s *(5.906 ft/s)*	2.25 m/s *(7.382 ft/s)*
	Zero-speed depth	100.80 m *(330.71 ft)*	126.00 m *(413.39 ft)*
Wind	10 m elevation (1 hour mean speed)	48.00 m/s *(157.48 ft/s)*	60.00 m/s *(196.85 ft/s)*

The tension-stroke curve of *single* cylinder at piston side chamber under 100-H condition, in Fig. 7.20, and 1000-H condition, in Fig. 7.21, respectively, are simulated for option A (TV-A, lower pressure-NPV is smaller) and option B (TV-B lower pressure-NPV is larger). The maximum allowable traveling length of the long-stroke tensioner is set to 10 m (*32.8 ft*) for the case of DTS under irregular sea, extreme (100-H), and survival (1000-H) environmental conditions. There is noteworthy that the negative sign in the DTS case is referred to the *down-stroke* motion.

The tension acting in a *single* cylinder at piston side chamber are ranged in [~0.84 MN to ~1.17 MN] (*~188.83 kips to ~263.03 kips*) (in TV-A) and [~0.60 MN to ~1.70 MN] *(~134.89 kips to ~382.18 kips)* (in TV-B) for 100-H, and [~0.65 MN to ~1.30 MN] (*~146.13 kips to ~292.25 kips*) (in TV-A) and [~0.55 MN to ~2.30 MN] (*~123.64 kips to ~515.06 kips*) (in TV-B) for 1000-H, respectively. This can be found that if the volume size of low-pressure NPV is small, the *total* acting tension on the tensioner ring (after considered all of the six cylinders) is in compression and potentially causes the buckling on the riser, as illustrated in Fig. 7.22. The *total* force balance (the first and third terms in Eqn. 5.22) on the tensioner ring (without considered the tension variation) is [<0 MN to ~7.20 MN] (*<0 kips to ~1618.63 kips*) (in TV-A) and [~1.50 MN to ~12.50 MN] (*~337.21 kips to ~2810.11 kips*) (in TV-B) for 1000-H. Therefore, the option **TV-A** which has smaller volume size settings in low-pressure NPV must be verified robustly, with respect to its volume, pressure, and stiffness changes, in the real-world application.

The tension exerted in *single* HPT cylinder piston side (which is equaled to the tension at TTR's tension ring per each cylinder) for setting **TV-B** varies from -9.0 % to 11.0 % for 100-H condition (as shown in Fig. 7.23), and from -13% to +13 % for 1000-H condition (as shown in Fig. 7.24), with respect to the parametric formulation results after taking the hydraulic effects (the second term in Eqn. 5.22) into account.

From the results in Figs. 7.20 – 7.24, there can be further inferred that the excessive tension variations are induced from the following sources and the effects to the DTS:

(i) The hydraulic fluid flow rate q_{oil} which is induced by the velocity of tensioner piston, as stated in Eqn. 5.22. The larger tension variations caused by the larger velocity factor are reasonable for the cases of DTS, where the platforms heave motion are no longer constrained by the high stiffed tendons.

(ii) The geometrical dimension, especially the length of hydraulic pipe conduits L^{AP}, as stated in Eqn. 5.22. The excessive tension variations is exerted when the longer hydraulic fluid travel in between the accumulator and tensioner cylinder is required, such as in the case of long-stroke tensioner.

(iii) The ratio of gas volume $\Delta V_A / V_{A_0}$ in between the displaced volume and the total gas volume stored in the high pressure NPVs, as stated in the Eqn. 5.18. This volume ratio must be designed as small as possible in order to minimize the dynamic tension variations. Therefore, a very large volume

V_{A_0} of high pressure NPVs must be stored nearby the well bay. For the long-stroke tensioner to be developed in the dry-tree Semi-submersible platform, the required storage of high-pressurized gas volume is even larger.

(iv) The volume size and initial pressure of the low-pressure NPV is equivalently important in the DTS. The *improper* setting can cause the *total* tension acting on the tensioner ring become too low during the extreme up-stroke motion. If the compression (*negative* tension) is found in the segment of the riser, the buckling on the riser structure is a critical issue (Sparks, 2007).

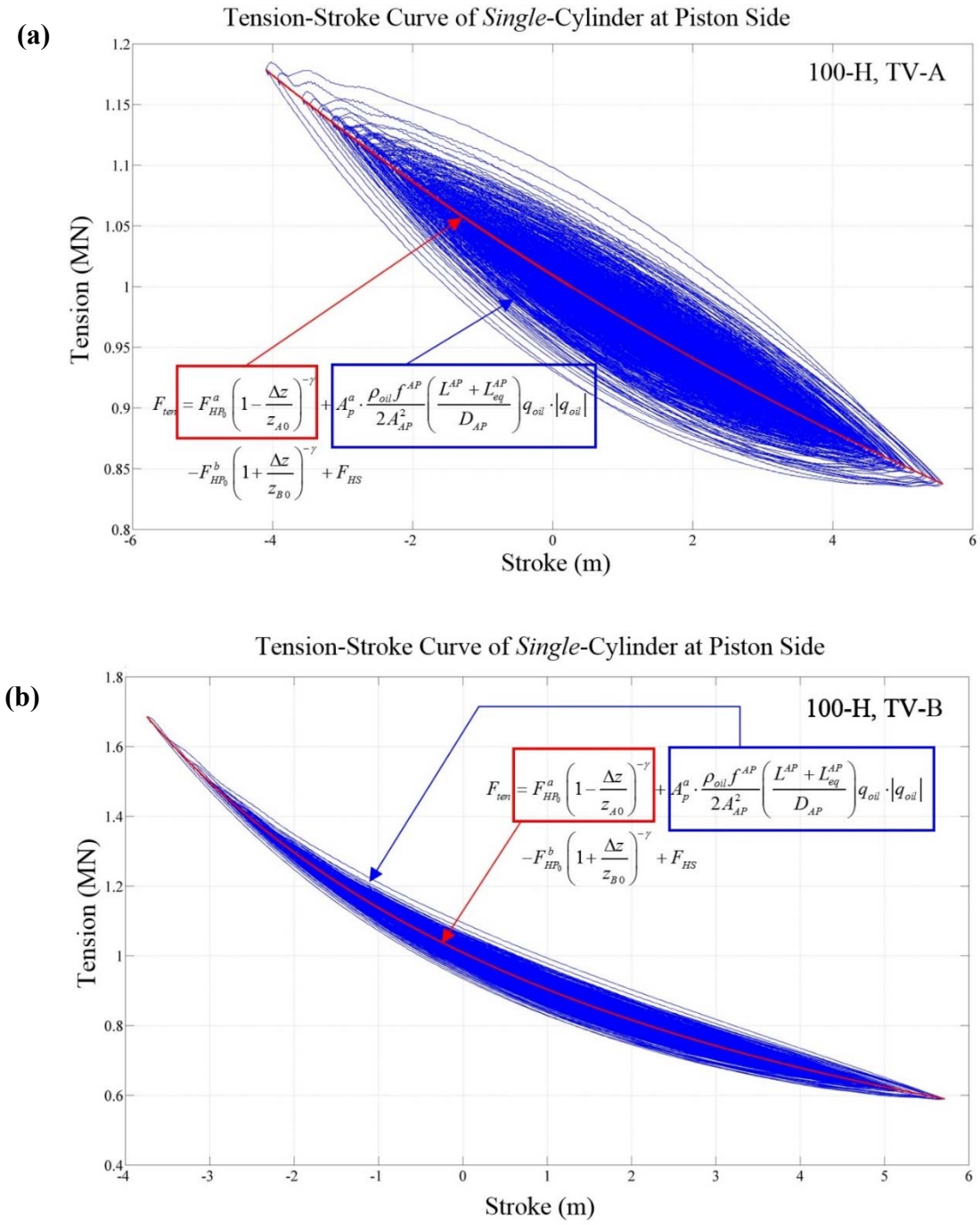

Figure 7.20 Tension-stroke curve of single cylinder at piston side under 100-H condition for (a) high pressure-NPV is larger (TV-A), and (b) low pressure-NPV is larger (TV-B).

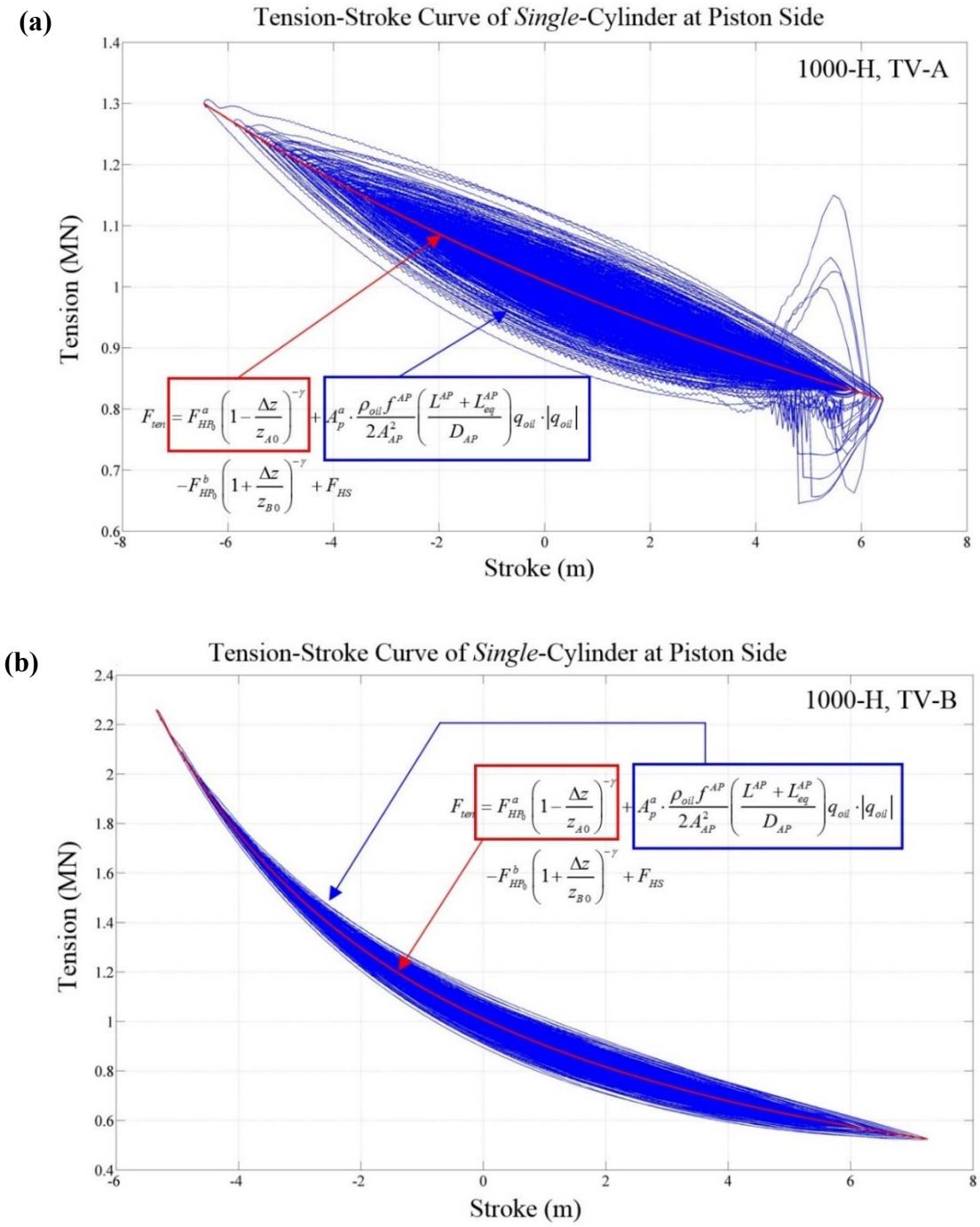

Figure 7.21 Tension-stroke curve of single cylinder at piston side under 1000-H condition for (a) high pressure-NPV is larger (TV-A), and (b) low pressure-NPV is larger (TV-B).

(a)

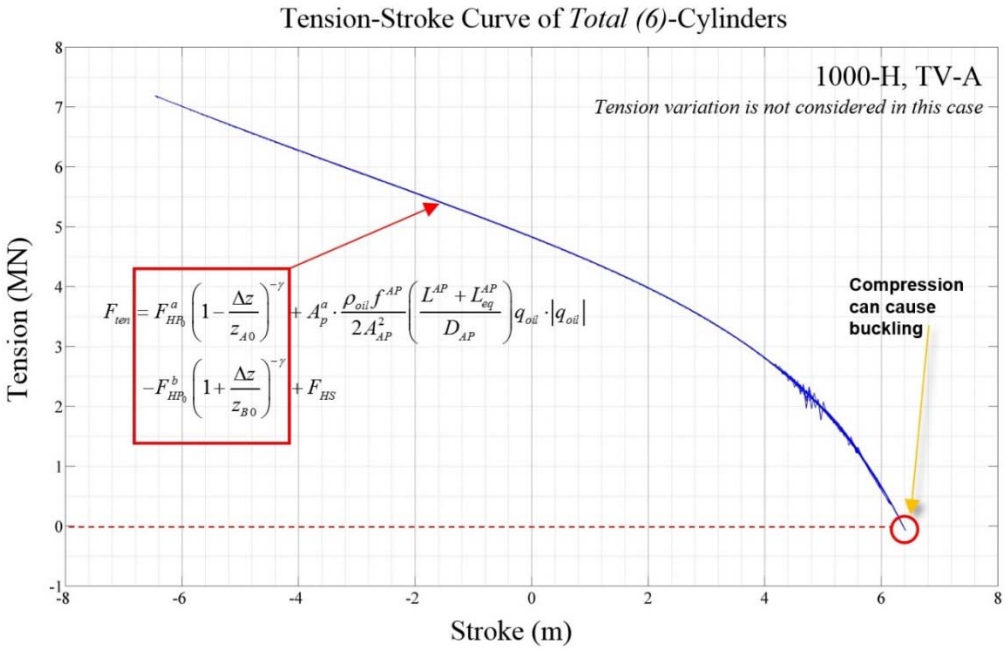

(b)

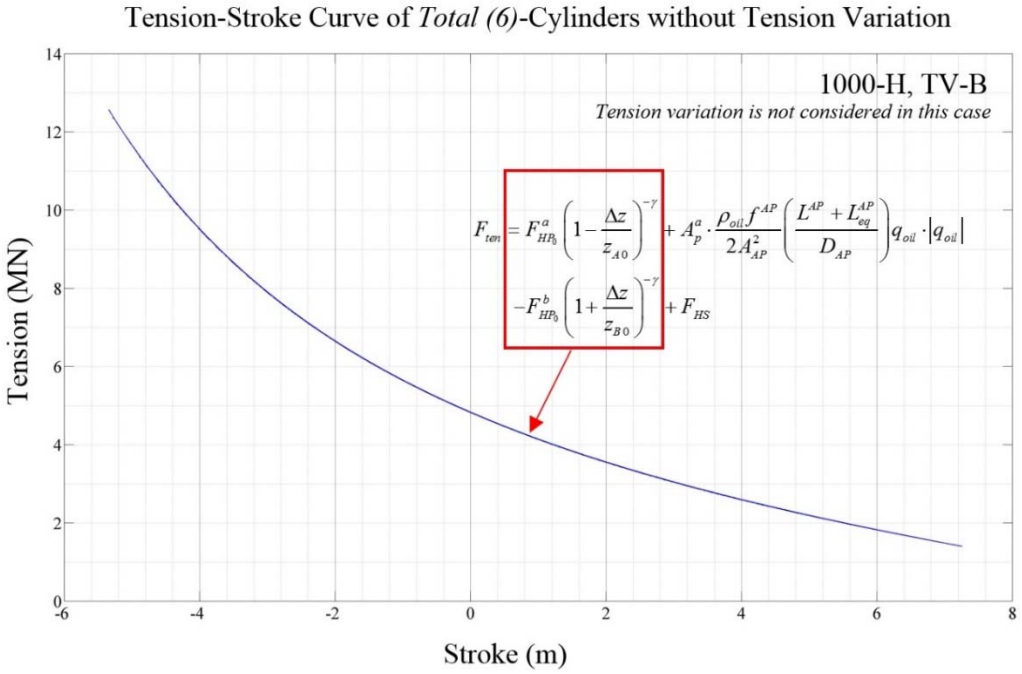

Figure 7.22 Tension-stroke curve of total six cylinders at tensioner-ring under 1000-H condition for (a) high pressure-NPV is larger (TV-A), and (b) low pressure-NPV is larger (TV-B).

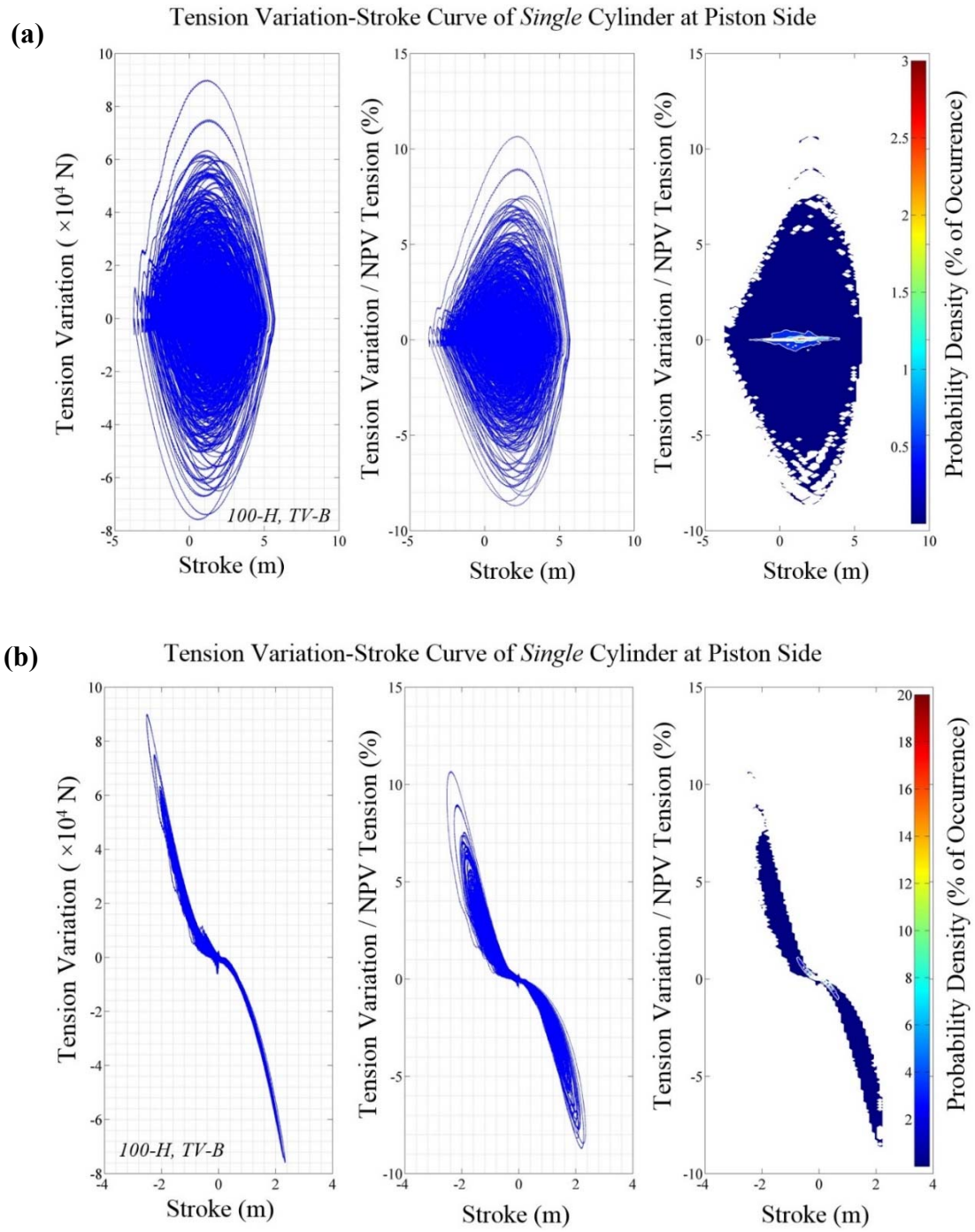

Figure 7.23 Tension variations (TV-B) in the piston-side chamber for single cylinder in the long-stroke tensioner (L=10 m (*32.8 ft*)) for dry-tree semisubmersible case, under condition 100-H, with respect to (a) variations of stroke; (b) variations of velocity.

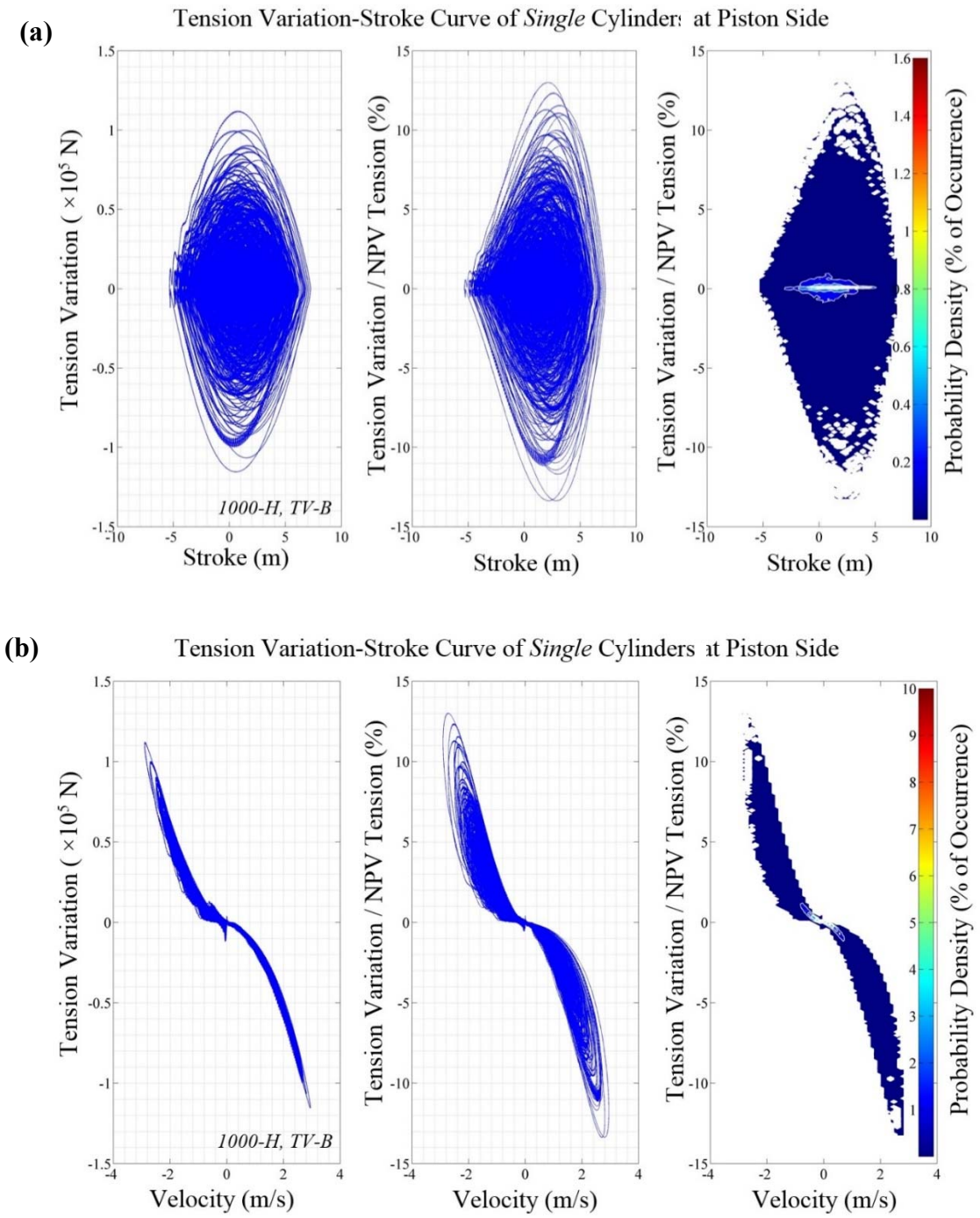

Figure 7.24 Tension variations (TV-B) in the piston-side chamber for single cylinder in the long-stroke tensioner (L=10 m (*32.8 ft*)) for dry-tree semisubmersible case, under condition 1000-H, with respect to (a) variations of stroke; (b) variations of velocity.

The extreme dynamic profiles of TTR, and *envelopes* of axial tension, bending moments, and von-Mises stress are shown in Figs. 7.25 – 7.28. The maximum inclination occurred at the location of tension ring (top-end node) for this case study where the keel guide is not installed. There is noteworthy that the scales in x- and z-directions in the plots in Figs. 7.25 - 7.28 are different in order to clearly represent the deflections of the riser. The segments from tensioner ring to the bottom of ram-style tensioner are lined linearly because these nodes are restrained by the structure of tensioner. The maximum horizontal-deflections *inside the DTS platform* are ~1.5 m (*~4.92 ft*) (TV-A) and ~1.5 m (*~4.92 ft*) (TV-B) for 100-H condition, and ~5.0 m (*~16.40 ft*) (TV-A) and ~4.1 m (*~13.45 ft*) (TV-B) for 1000-H condition, respectively. This values are significant in the determination of well-spacing in order to prevent collision with neighboring riser. For the overall length of riser, the maximum offset of riser segments are 1.39% WD (water depth) (TV-A) and 1.23% WD (TV-B) for 100-H condition, and 2.13% WD (TV-A) and 2.03% WD (TV-B)for 1000-H condition, respectively. The bottom segments in the case of 1000-H for **TV-A** is in bended mode, Fig. 7.28, and potential in buckling. The axial tension is increased proportionally from the bottom of riser to the tensioner ring. The maximum bending moment are found in the location of tension ring (top-end node) in these cases except for the 1000-H TV-A, where high bending moment is found on the segments nearby the bottom of the TTR. The von-Mises stresses are ~0.66 utilization (TV-A) and ~0.70 utilization (TV-B), for 100-H condition, and ~1.65 utilization (TV-A) and ~0.85 utilization (TV-B) for 1000-H condition, for the case of steel grade Q125.

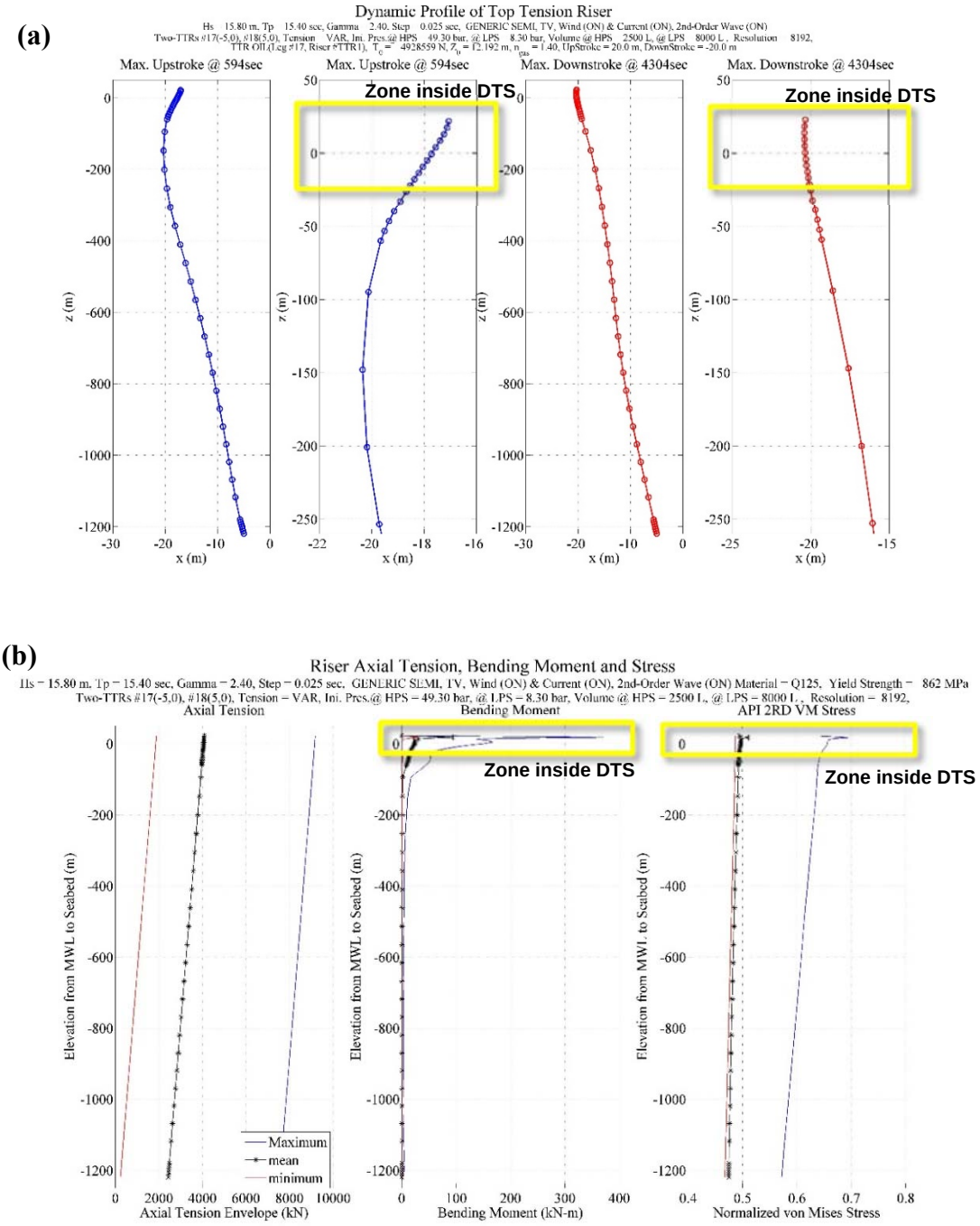

Figure 7.25 TTR (Leg #17) with dynamic tension variation (TV-B) interfaced with DTS platform for 100-year return period for (a) extreme dynamic profiles of TTR, and (b) axial tension, bending moment and von-Mises stress.

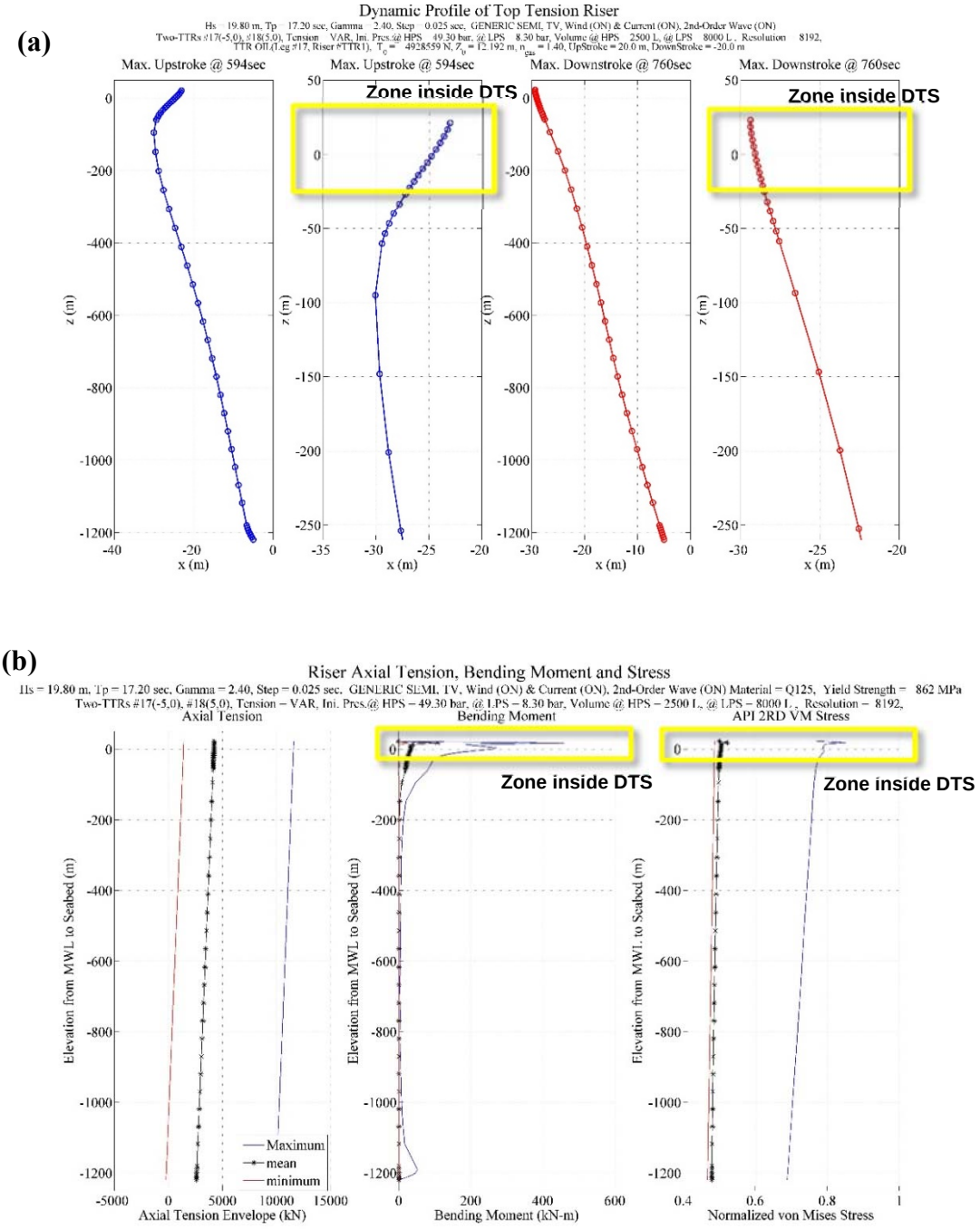

Figure 7.26 TTR (Leg #17) with dynamic tension variation (TV-B) interfaced with DTS platform for 1000-year return period for (a) extreme dynamic profiles of TTR, and (b) axial tension, bending moment and von-Mises stress.

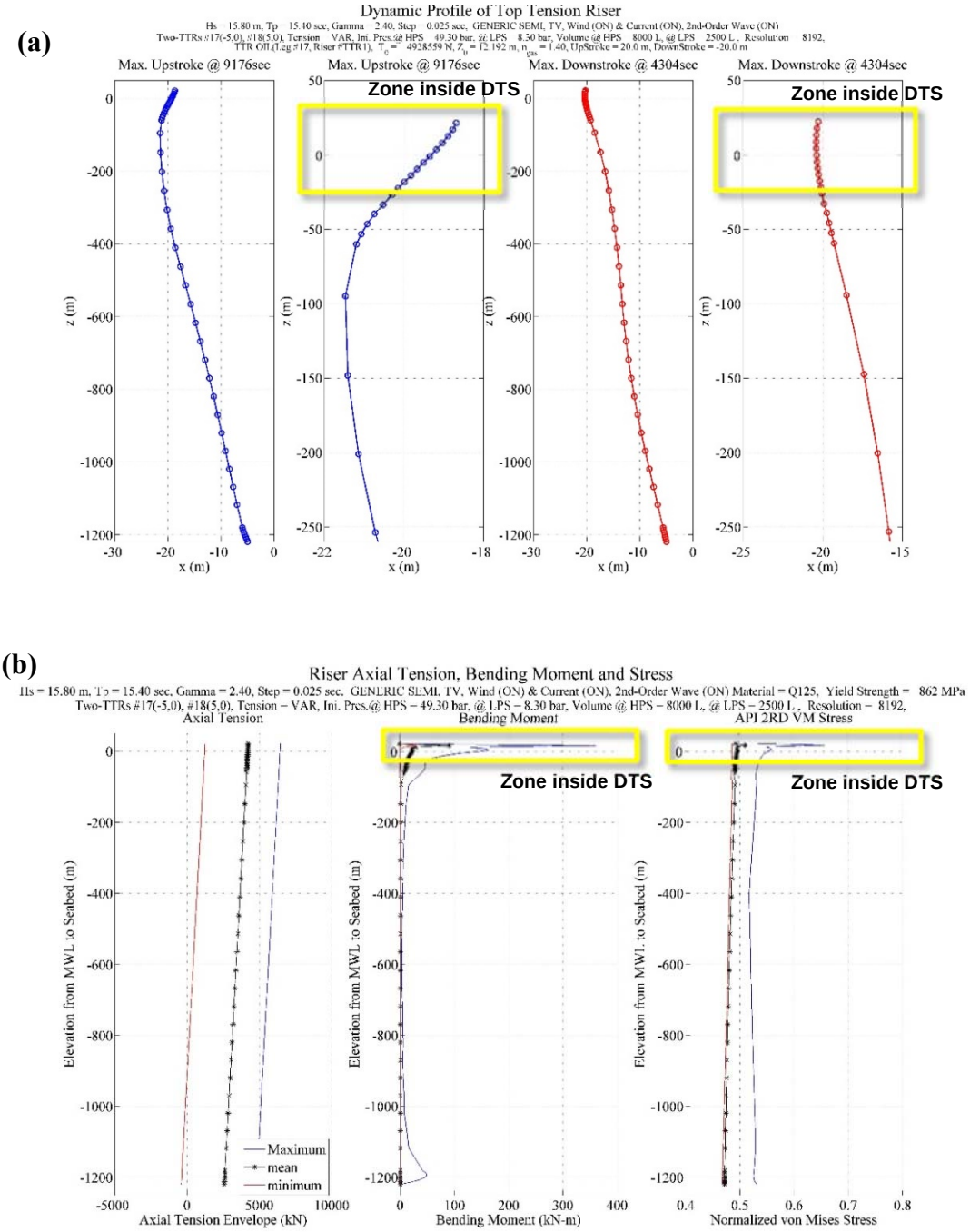

Figure 7.27 TTR (Leg #17) with dynamic tension variation (TV-A) interfaced with DTS platform for 100-year return period for (a) extreme dynamic profiles of TTR, and (b) axial tension, bending moment and von-Mises stress.

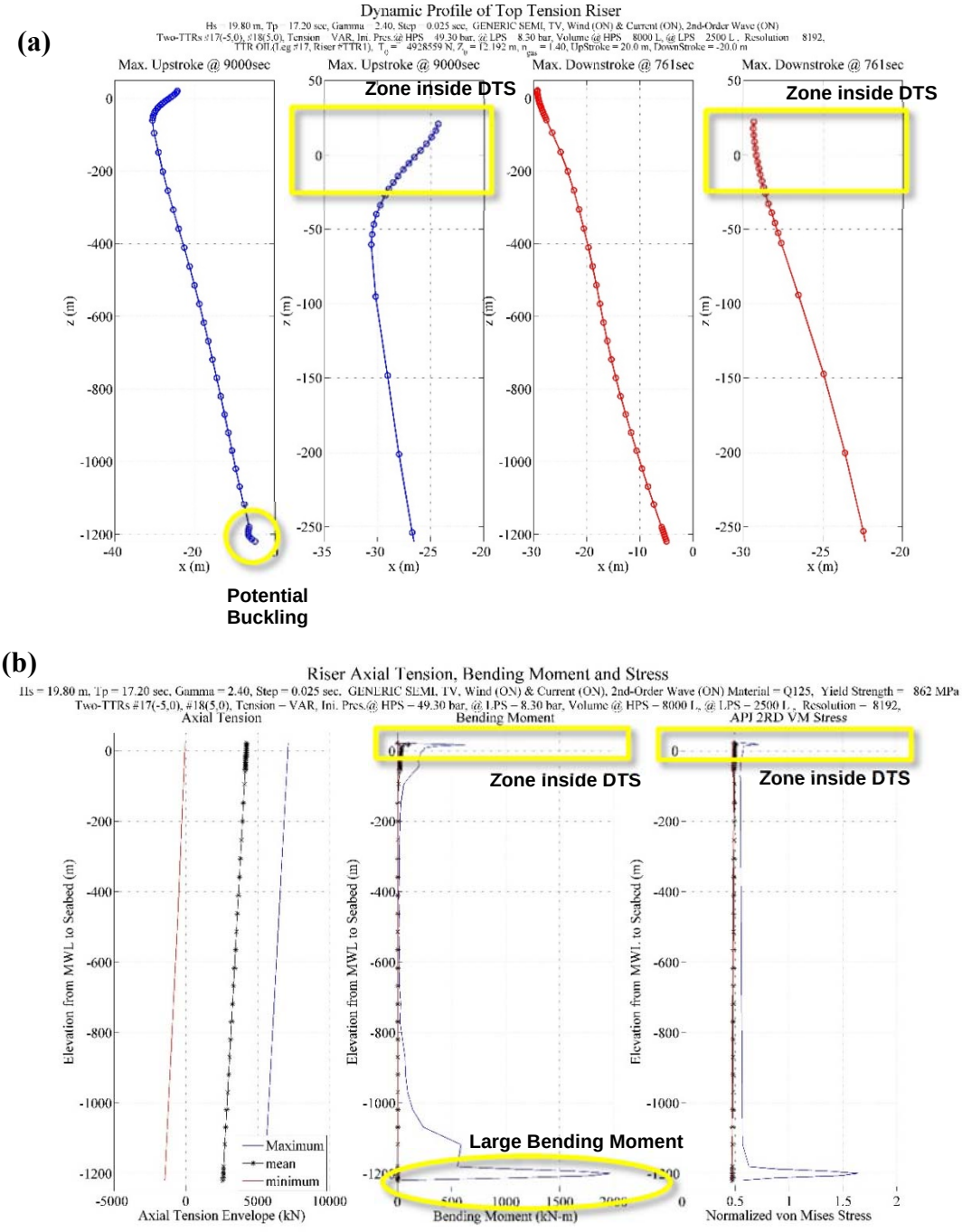

Figure 7.28 TTR (Leg #17) with dynamic tension variation (TV-A) interfaced with DTS platform for 1000-year return period for (a) extreme dynamic profiles of TTR, and (b) axial tension, bending moment and von-Mises stress.

The Mathieu stability for the first two modes of the TTR, with dynamic tension variation, was studied and the results are shown in Fig. 7.29. The TTR first mode for both 100-H and 1000-H cases are in the stable zone and the second mode for the case **TV-B** are in the unstable zone due to the large tension variation. However, the second mode for TV-B can be stabilized if the lateral damping ratio is larger than 0.25, in the case of 1000-H condition.

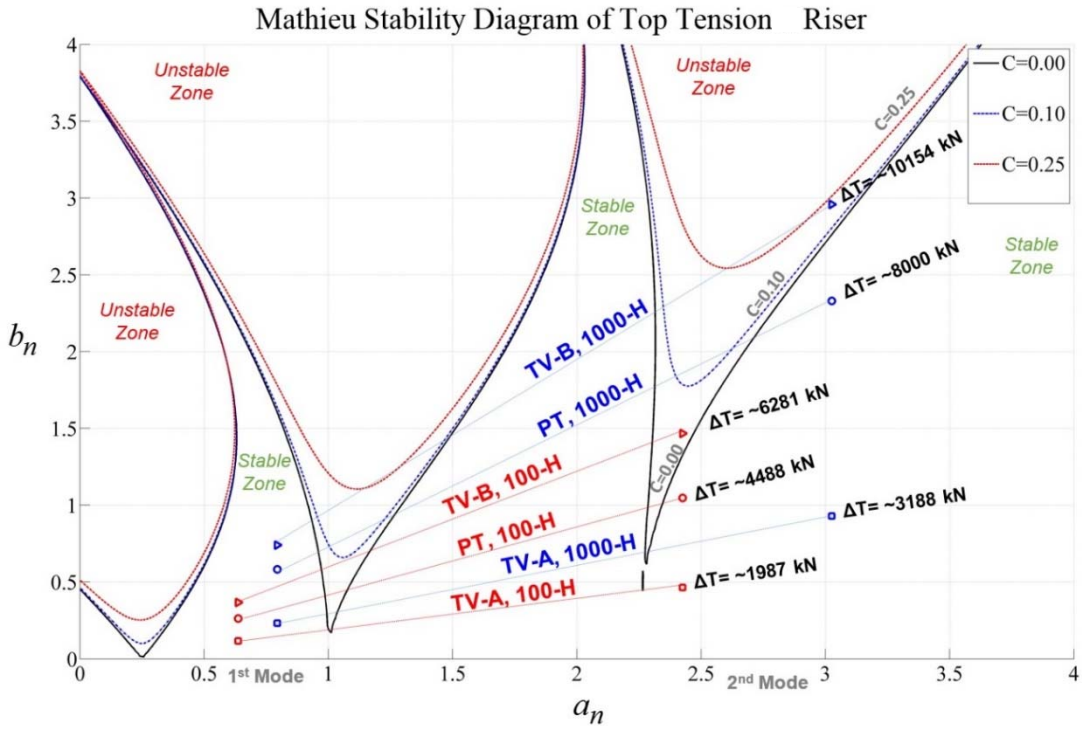

Figure 7.29 Mathieu stability analysis of TTR (Leg #17, integrated with TTR dynamic tension variations) interfaced with DTS platform.

The dynamic riser strokes, with dynamic tension variations, for *unbounded* limits of TTR tensioner are depicted in frequency domain in Fig. 7.30. The riser stroke in

1000-H condition is larger than the stroke in 100-H return period condition in the wave frequency (WF) and low frequency (LF) regions but there are not apparent differences for both conditions in the high-frequency (HF) region. The responses of TV-A is almost identical with the case without taking the dynamic tension variations into account (labeled as **PT**). The response of TV-B is smaller than the others in the frequency range of heave resonance peak.

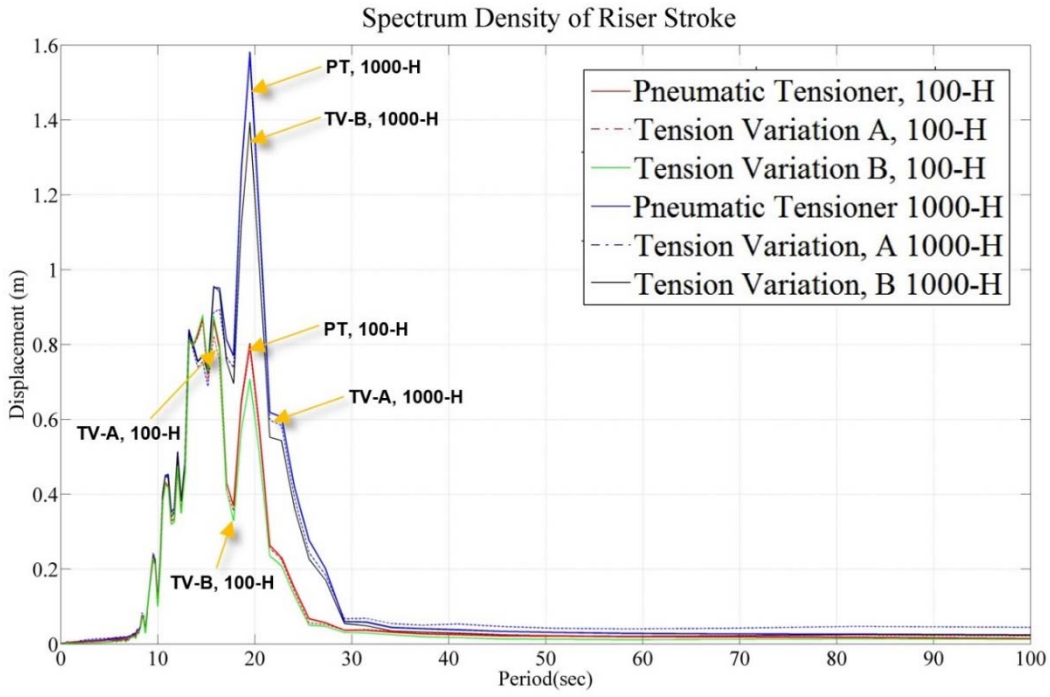

Figure 7.30 Spectrum density of stroke of TTR interface (integrated with dynamic tension variations) in DTS platform.

The maximum up stroke, maximum down stroke, and required riser stroke length for the cases with dynamic tension variations are compared to the *base-case* without the

dynamic tension variation (labeled as **PT**), as tabulated in Table 7.7. The time series of TTR stroke are shown in Figs. 7.31 – 7.32. There is noteworthy that the existence of dynamic tension variation is able to reduce the total required stroke length as much as 0.27 m (*0.886 ft*) in 100-H condition, and 0.74 m (*2.428 ft*) in 1000-H condition. The reason is that the hydraulic friction in the conduit pipes of HP tensioner acting as additional damping effects. Also, the setting TV-B can reduce *more* of the total required riser stroke length than the setting TV-A.

Table 7.7 Maximum upstroke, maximum down stroke, and required riser stroke length.

		PT	**TV-A**	**TV-B**
100-H	Maximum upstroke	5.978 m *(19.6 ft)*	5.573 m *(18.24 ft)*	5.712 m *(18.73 ft)*
	Maximum down stroke	-3.749 m *(-12.3 ft)*	-4.098 m *(-13.33 ft)*	-3.746 m *(-12.29 ft)*
	Total required stroke length	9.727 m *(31.91 ft)*	9.671 m *(31.73 ft)*	9.458 m *(31.03 ft)*
1000-H	Maximum upstroke	7.667 m *(25.2 ft)*	6.413 m *(21.04 ft)*	7.257 m *(23.81 ft)*
	Maximum down stroke	-5.675 m *(-18.6 ft)*	-6.464 m *(-21.21 ft)*	-5.345 m *(-17.54 ft)*
	Total required stroke length	13.342 m *(43.77 ft)*	12.877 m *(42.25 ft)*	12.602 m *(41.35 ft)*

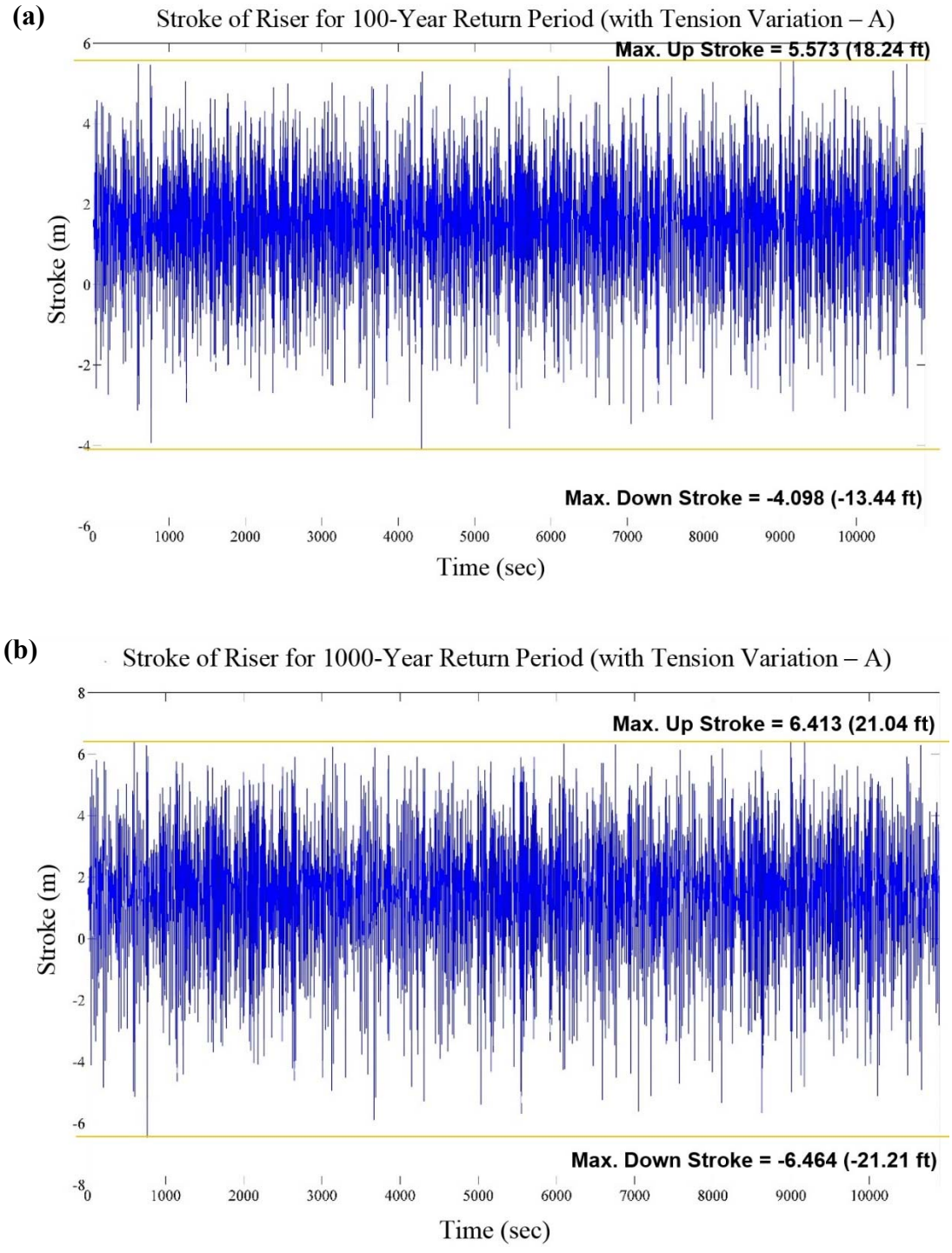

Figure 7.31 Stroke of TTR interface (with dynamic tension variation, TV-A) in DTS platform in time domain for (a) 100-year return period, and (b) 1000-year return period.

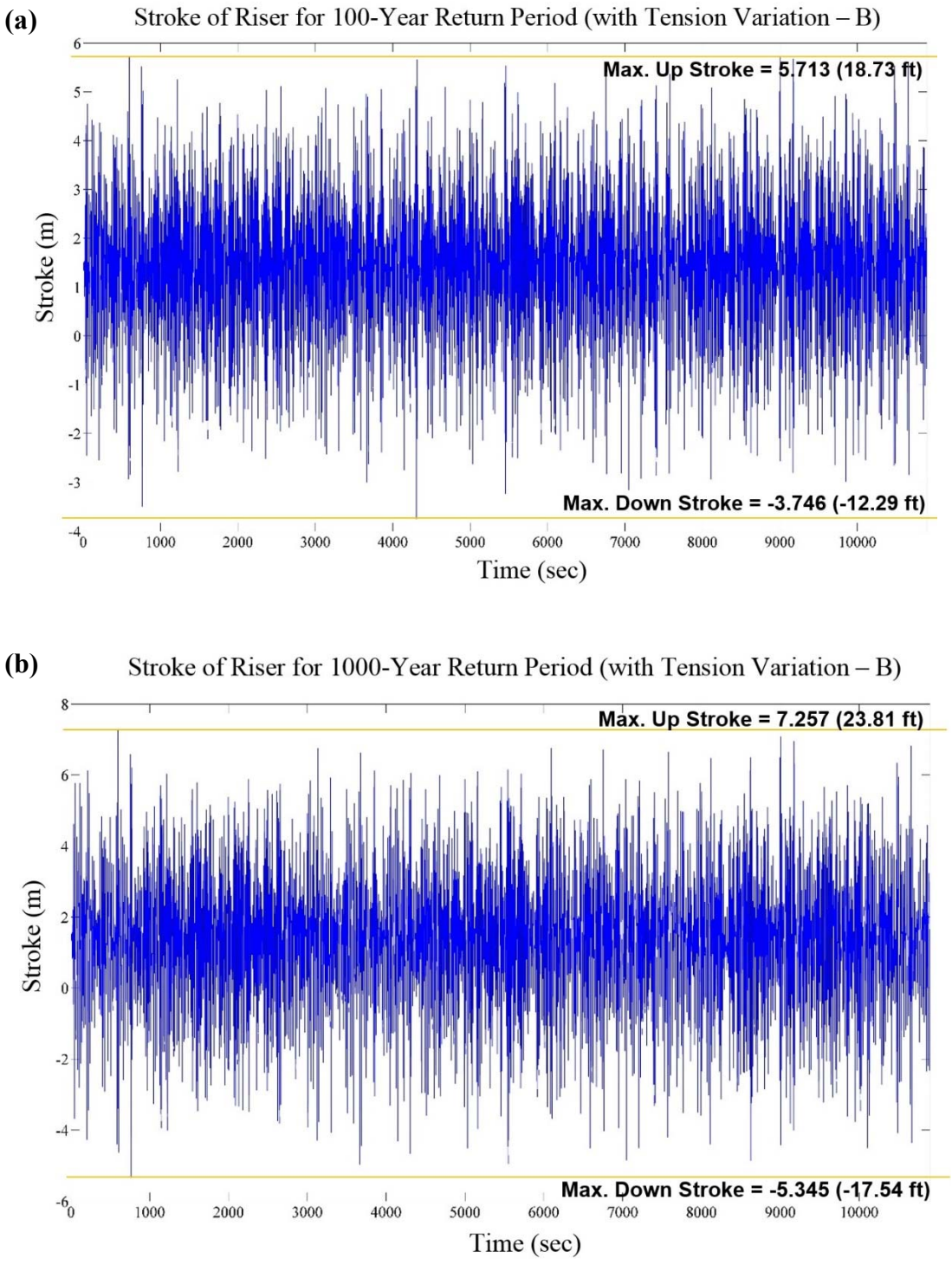

Figure 7.32 Stroke of TTR interface (with dynamic tension variation, TV-B) in DTS platform in time domain for (a) 100-year return period, and (b) 1000-year return period.

The effects of dynamic tension variation on the platform global motion are studied in Figs. 7.33 – 7.34. The DTS platform motions are shown in frequency domain in Fig 7.33. It can be found that the motions of DTS are slightly affected by the dynamic tension variation (in setting **TV-B**), where the amplitude of heave resonance peak is reduced, in Fig. 7.33. Besides, there are not apparent differences for both conditions (with- and without dynamic tension variations) in the high-frequency (HF, low period) region.

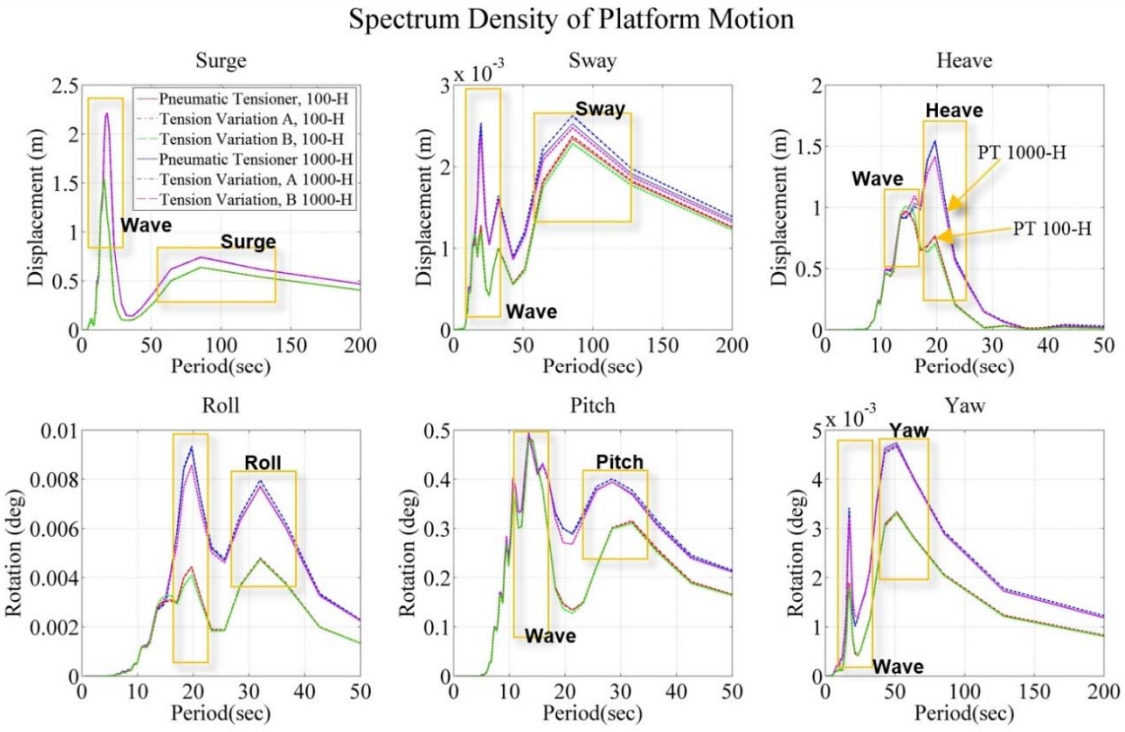

Figure 7.33 Platform motions (integrated with TTR dynamic tension variations) in frequency domain.

The response amplitude operators (RAO) of DTS platform, with- and without dynamic tension variations, in this case study are shown in Fig. 7.34. In the RAO of heave motion, the cancellation period DTS is located at ~17.5 sec. The RAO in heave direction is very sensitive to the additional tensioner stiffness. The setting of **TV-B** reduces the second peak of heave RAO.

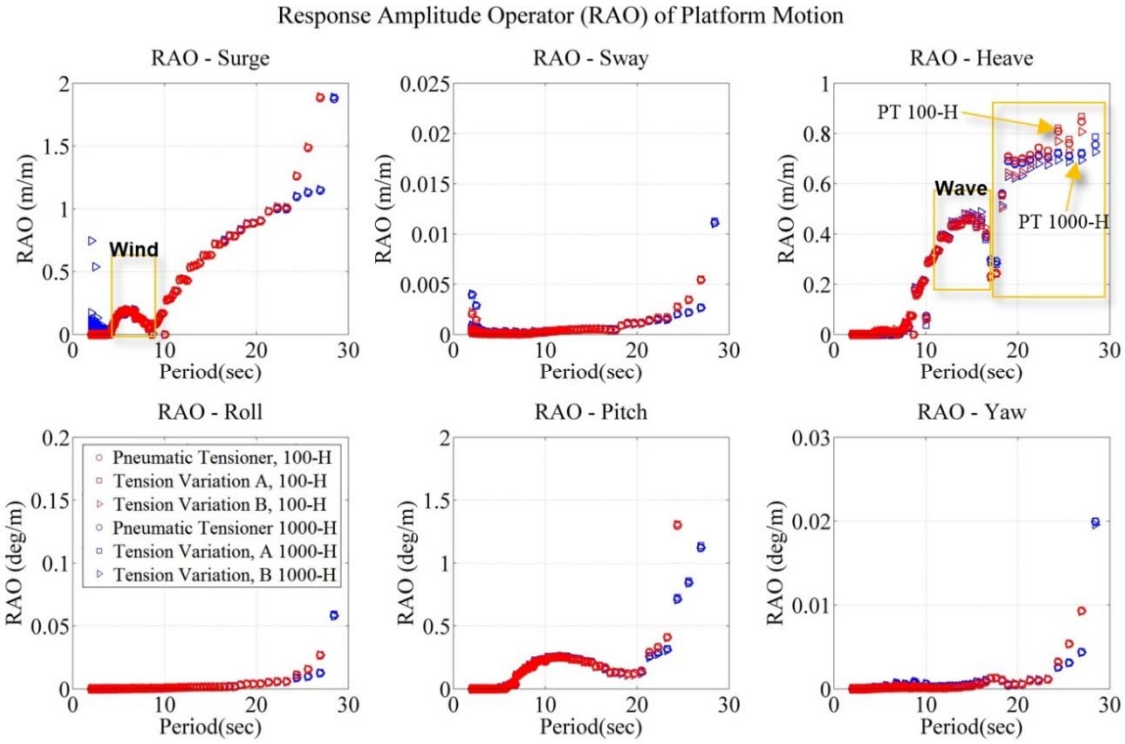

Figure 7.34 RAO (integrated with TTR dynamic tension variations) of platform motions.

7.4 Long Stroke Ram Style (LSRS) Tensioner with MR Dampers

A typical ram style tensioner with a total range of 28 ft and the stiffness is non-linear over the stroke range, as shown in Fig. 7.35 is suggested by Poll et al. (2013) for the use of a deep-draft DTS. The tensioner is incorporated with a hard-stop at upper-end (~ +11 ft, *+3.353 m*) and bottom-end (~ -17 ft, *-5.182 m*) that can be simulated in the performance curve as an abrupt change in stiffness. In the development of DTS, the piston of ram tensioner to hit the cylinder bottom wall (named as **bottom-out**) is allowable in the 1000-year return period extreme environment conditions (Bian and Xiang, 2013). However, the bottoming out scenario is a trade-off to minimize the total required stroke length with the cost of *occasionally* hard-contact (Koos, 2013). Tensioner bottom-out can generates very large tension loads at the tensioner ring and consequently at the wellhead near the sea floor as well (Yu et al., 2008). It can be found from Fig. 7.35, during bottom-out as stroke moves below -17 ft (*-5.182 m*), the stiffness increases abruptly so that the tensioner cylinders and tensioner ring experience a large increment of tension change. The change in riser stiffness can be up to ten times from the normal operation stiffness of a riser (Koos, 2013). This phenomenon causes the axial tension of riser increases significantly so that the stress and strength of riser must be verified to be within the allowable limits. On the other hand, when the tensioner piston **top-out** at stroke nearly +11 ft (*+3.353 m*), the tension exerted by tensioner cylinders decreases significantly far below the nominal tension and this is potential for buckling at the riser lower end (Spark, 2007).

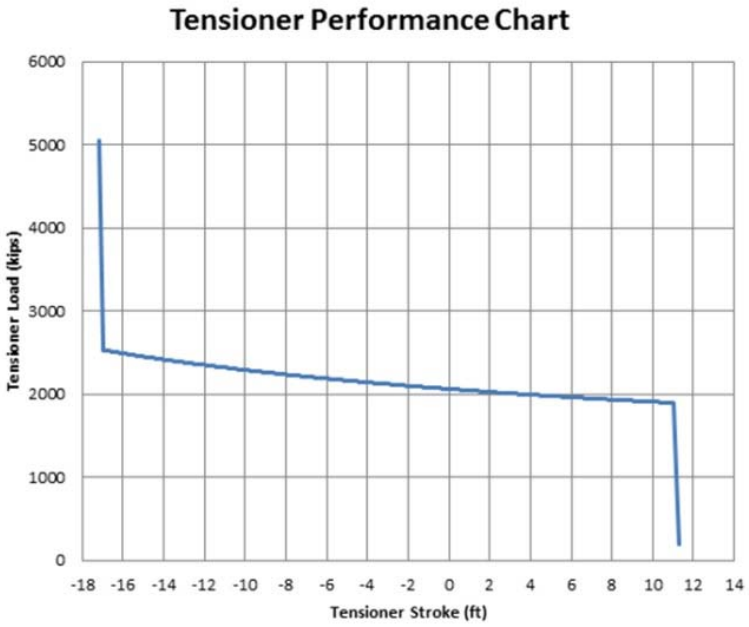

Figure 7.35 Tensioner performance curve (Poll et al., 2013).

Since tensioner **bottom-out** is a very critical progress, especially to the structural health and integrity, and it has not been considered as one criterion in the experience of TLP-TTR applications, the tensioner cylinders must be fully protected from mechanical failures after the experiencing of bottom-out. One of the proposed precautions (Koos, 2013) is to incorporate hydraulic *cushion* in the bottom of the tensioner cylinder to decelerate the riser and tensioner when the piston approaches to its fully down-stroke limit (near the cylinder bottom end-wall). In addition, a fixed support deck structure is proposed (Koos, 2013) to isolate the cylinder piston rod from excessive buckling stress by rigidly restraining the tensioner ring prior to the cylinder rod contacting the cylinder bottom end-wall. The suggestions from Koos (2013) lead to an important direction to

extend the safety margin of long-stroke tensioners bottom-out in DTS while there are several further considerations must be taken into account:

(i) the nearly rigid contact behaviors in between the tensioner ring and a fixed support deck structure (which acts as a hard-stopper) during bottom-out exerts very sheer increment of impact load on the tensioner ring and riser-end; the energy dissipation is fully relied on the deceleration caused by cylinders cushioning and, eventually, the clash in between two rigid hard surfaces (tensioner ring and hard stopper). This solution is not considered as favorable from the structural health and integrity point of view because it can cause the damage of the tensioner ring and piston rod;

(ii) the tensioner need to experience a nearly fully bottom-out condition where large tension force will be exerted in between the piston and cylinder blind-end wall during cushioning. The change in riser stiffness can be up to ten times from the normal operation stiffness of a riser (Koos, 2013). The significant sheer changes of tensioner tension have potential detrimental effects to the cylinder wall structures, seals, bearings and alignment. Also, the very high loads acting on the tensioner piston rod during bottom-out can causes buckling on the piston rod.

After considered the challenges as mentioned above, a long stroke ram-style (LSRS) tensioner incorporated with an innovative type of protector which is consisted of MR dampers is proposed here in order to provide effective solutions to the bottom-out in

DTS. The proposed LSRS-MR system is illustrated in Figure 7.36. A group of magnate-rheological (MR) dampers is installed to replace the fixed-rigid support deck structure. The MR dampers can:

(i) perform as a *Kelvin-Voigt* model when the down-stroke position is lower than the threshold limit in order to provide a damped and deformed contact (instead of rigid and hard contact) in between the tensioner ring and MR dampers, and to dissipate energy caused by the tensioner cylinder bottom-out motion, as illustrated in Fig. 7.37(c)-(d);

(ii) redistribute the high tension which originally to be withheld solely by the tensioner cylinders during bottom-out by adding the total MR dampers' stiffness and damping forces to the tensioner ring. Therefore, a major part of the required tension to be generated by tensioner cylinders can be transferred to the MR dampers. The tensioner cylinders can be protected from extreme cushioning and excessive tension increment, as illustrated in Fig. 7.37(d);

(iii) further optimize the total stroke length needed for the DTS. The down-stroke limits of LSRS tensioner can be fine-tuned by MR dampers to reduce the total required stroke length by the tensioner. There is noteworthy that this optimization is a trade-off in between the riser tension/stress and the piston/tensioner ring position. As long as the stress and strength is within the allowable limits, the MR dampers are able to

enhance the flexibility of the platform designer in sizing the draft of the DTS.

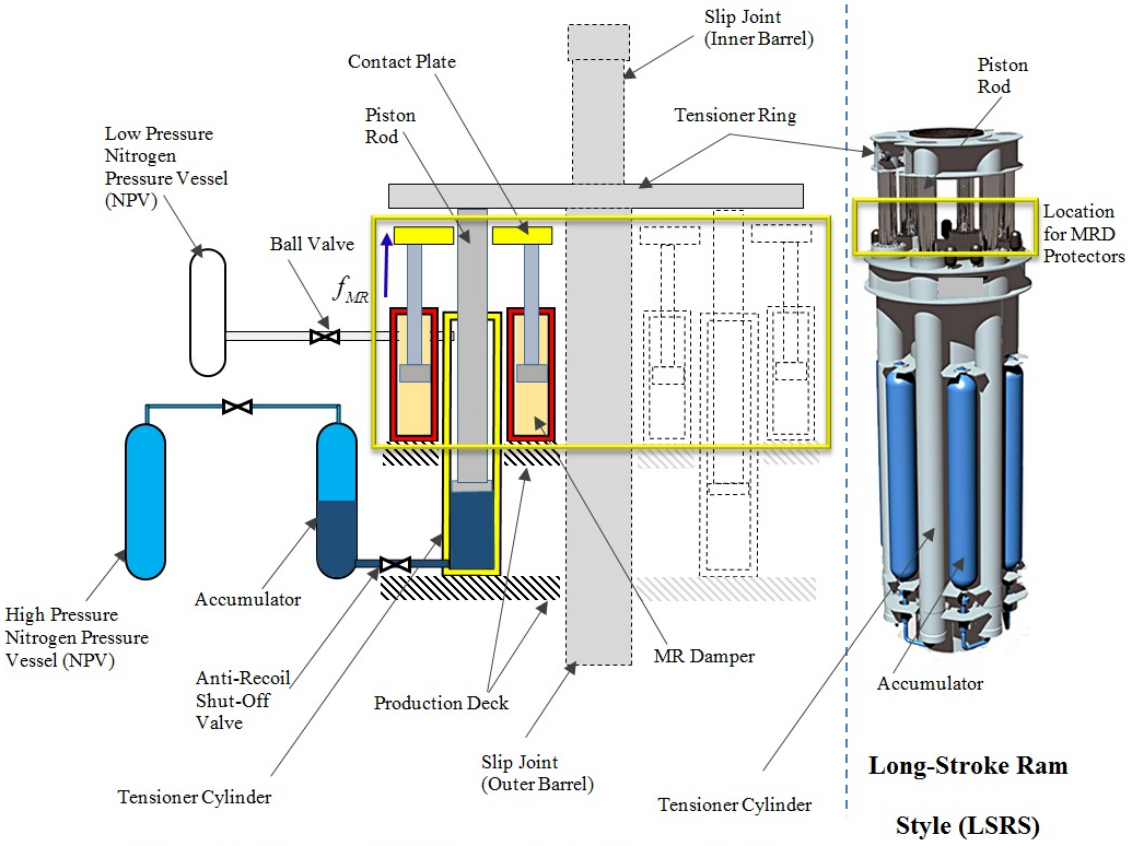

Figure 7.36 LSRS tensioner incorporated with MR dampers as protector.

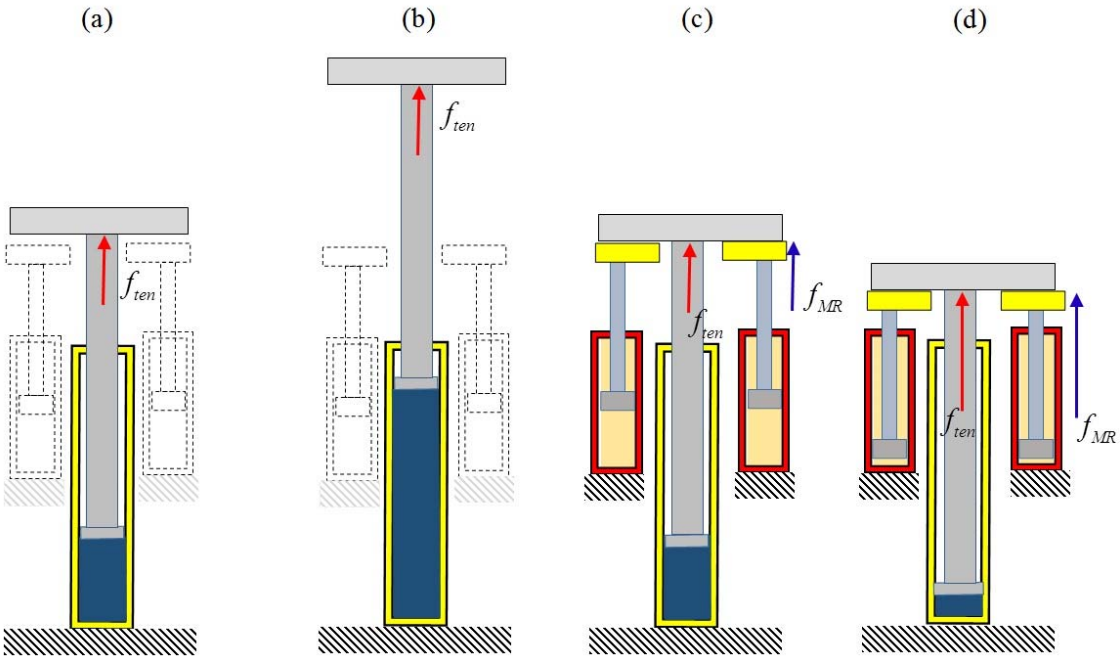

Figure 7.37 Mechanism of MR damper (MRD) tensioner protector. The MRD is in idle condition when the long stroke tensioner operating in the allowable stroke ranges, as shown in (a) and (b); the MRD tensioner protector are activated to dissipate additional energy caused by the TTR's bottom-out motion and prevent high impact load exerted directly in the tensioner cylinders when the piston compressing the cylinder's bottom end-wall, as shown in (c) and (d).

7.5 Numerical Simulation of LSRS-Tensioner with MRD Protector

A numerical simulation for long stroke ram-style (LSRS) tensioner with MR dampers was conducted to study the behaviors of this proposed system. This simulation follows exactly the data as listed in Tables 7.1 – 7.6, with focusing on the setting of **TV-B** (tension variation with low-pressure NPV has larger volume), and 1000-year return period survival condition (**1000-H**). The *base-case* in this simulation is the 1000-H case with tension variation as per discussed in Subsection 7.3. The MR damper, as proposed in Table 7.8, is simulated under (i) passive mode, (ii) semi-active Skyhook control (Subsection 4.2), (iii) semi-active fuzzy logic control (Subsection 4.3), respectively. The threshold limit to activate the MR damper is set as **-2.0 m** (*-6.5617 ft*) of the tensioner ring position.

Table 7.8 Coefficients of MR damper in LSRS-MRD simulation.

Coefficients	i^2	i^1	i^0
c	8.5×10^5	1.44×10^8	2.0×10^4
k	0	1.2×10^6	6.8×10^4
α	2.571×10^4	4.11×10^4	1.2058×10^6
β	0	22.05	17.82
δ	0	2.6	2.3

The tension-stroke curve on the tensioner ring are illustrated in Figs. 7.38 – 7.40. The additional tension exerted by the MRD when the riser strokes were below -2.0 m (-*6.5617 ft*). The tension exerted by the total HP tensioner cylinders are restrained below ~12.5 MN (*~2810.11 kips*) in these three controlled cases. It can be found that the passive mode generates unintentional tension while the Skyhook scheme requires larger MR damper force than the fuzzy logic scheme.

The spectrum density of total tension acting on tensioner ring under different control schemes is shown in Fig. 7.41. The control schemes are effective in the wave frequency (WF) and heave resonance peak region. The time series results of the total tension on tensioner ring are shown in Figs. 7.42 - 7.43.

In a conventional LSRS tensioner system, the high tension is withheld solely by the tensioner cylinders when the piston is approaching the cylinder bottom-limit, as shown in Fig. 7.37. From the tension-stroke curves in Figs. 7.38 – 7.40, the additions of tension exerted by the MRD were acting on the tensioner ring after the threshold values had been reached. Since the cylinders of LSRS tensioner are very complex system that sensitive to the structure integrity and alignment, very large abrupt tension increment (the *red* dash line) during cushioning is an unfavorable factor to the tensioner cylinders' integrity management. The *spikes* of tension are exerted by the MRD to replace and/or redistribute the *spike* that need to be generated by tensioner cylinders during the cushioning, as shown in Fig. 7.37(c)-(d), to protect the structural integrity of LSRS tensioner. The threshold stroke limits can be further determined by the platform designer according to the *trade-off* in between the maximum allowable stroke length and the

maximum allowable tension exerted on the tensioner ring. Asymmetric up and down stroke can be mitigated by resetting the tensioner nominal position in order to make the best use of the tension capacity and it requires careful analysis of the load cases to be robust (Bian and Xiang, 2013).

The total MR damper force output under different control schemes are illustrated in Figs. 7.44 – 7.45. The *passive* mode requires the largest MR damper output force while the fuzzy logic is good in the required output force control. This is an important factor during identifying the capacity and size of MR damper that can support in the purposed system. This result implies that a relatively smaller scale MR damper with fuzzy-logic controller is comparable , in performance, to a larger scale MR damper with the Skyhook controller. The command current inputs to MR damper is shown in Fig. 7.46. The Skyhook control scheme is activated with 0.5 A while the command current by fuzzy logic controller is inferred interactively with respect to the displacement and velocity of tensioner ring and platform.

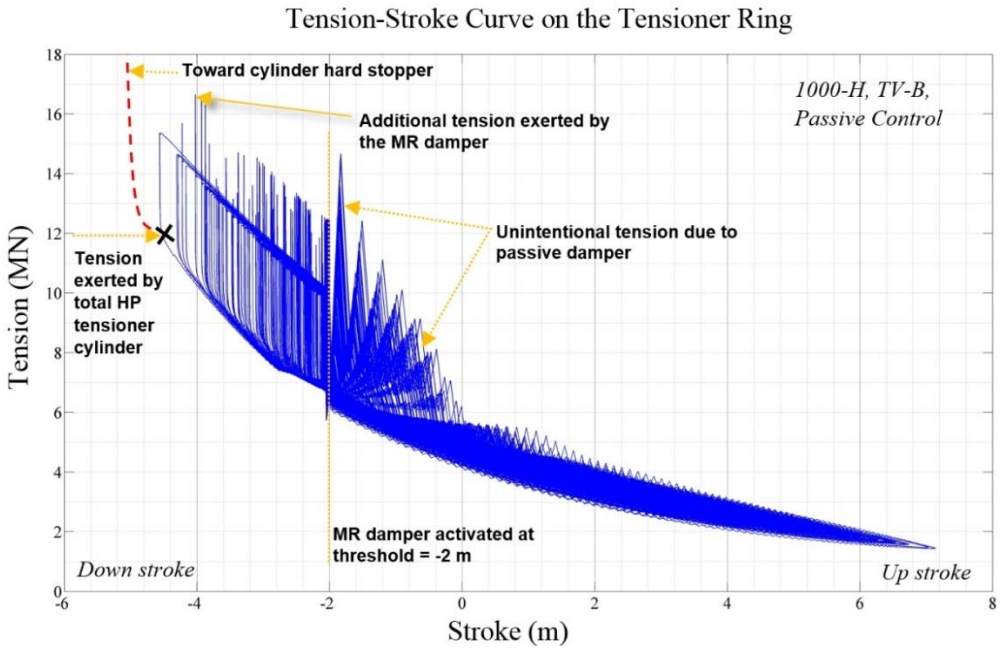

Figure 7.38 Tension-stroke curve on tensioner ring for passive control.

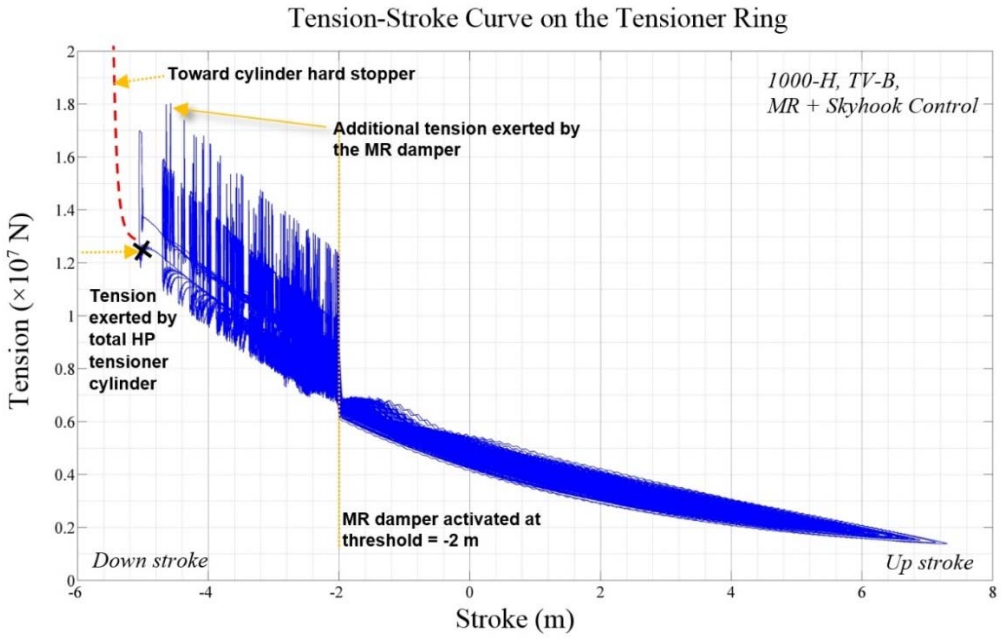

Figure 7.39 Tension-stroke curve on tensioner ring for semi-active Skyhook control.

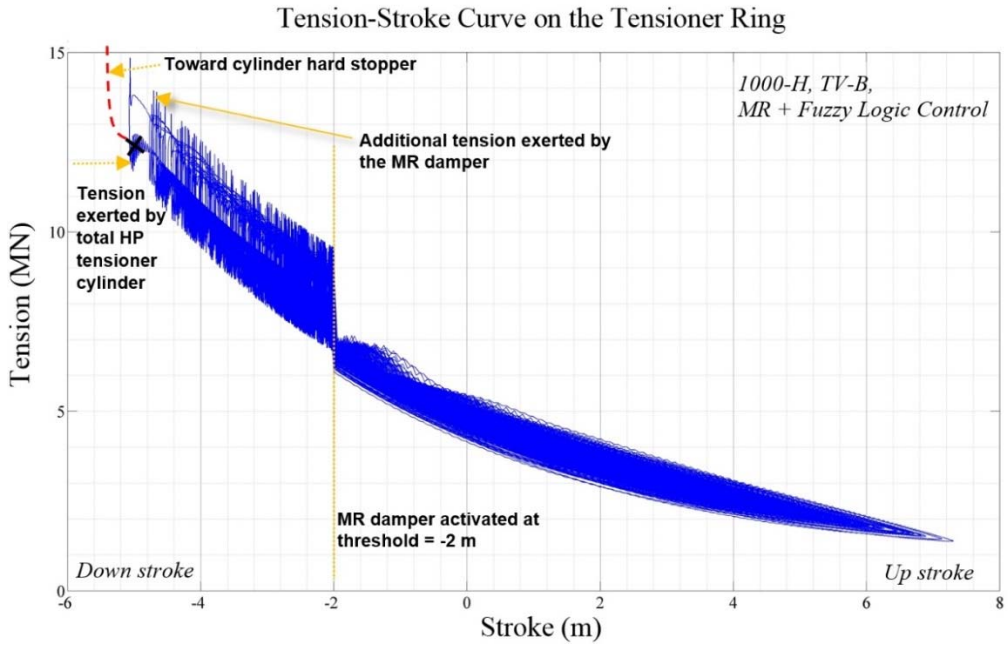

Figure 7.40 Tension-stroke curve on tensioner ring for semi-active fuzzy logic control.

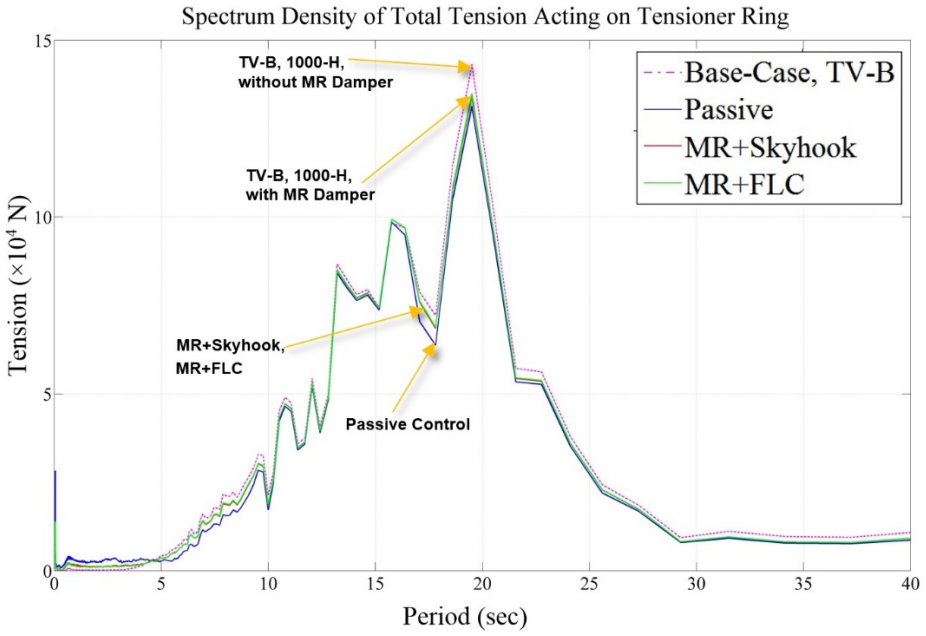

Figure 7.41 Spectrum density of total tension acting on tensioner ring under different control schemes.

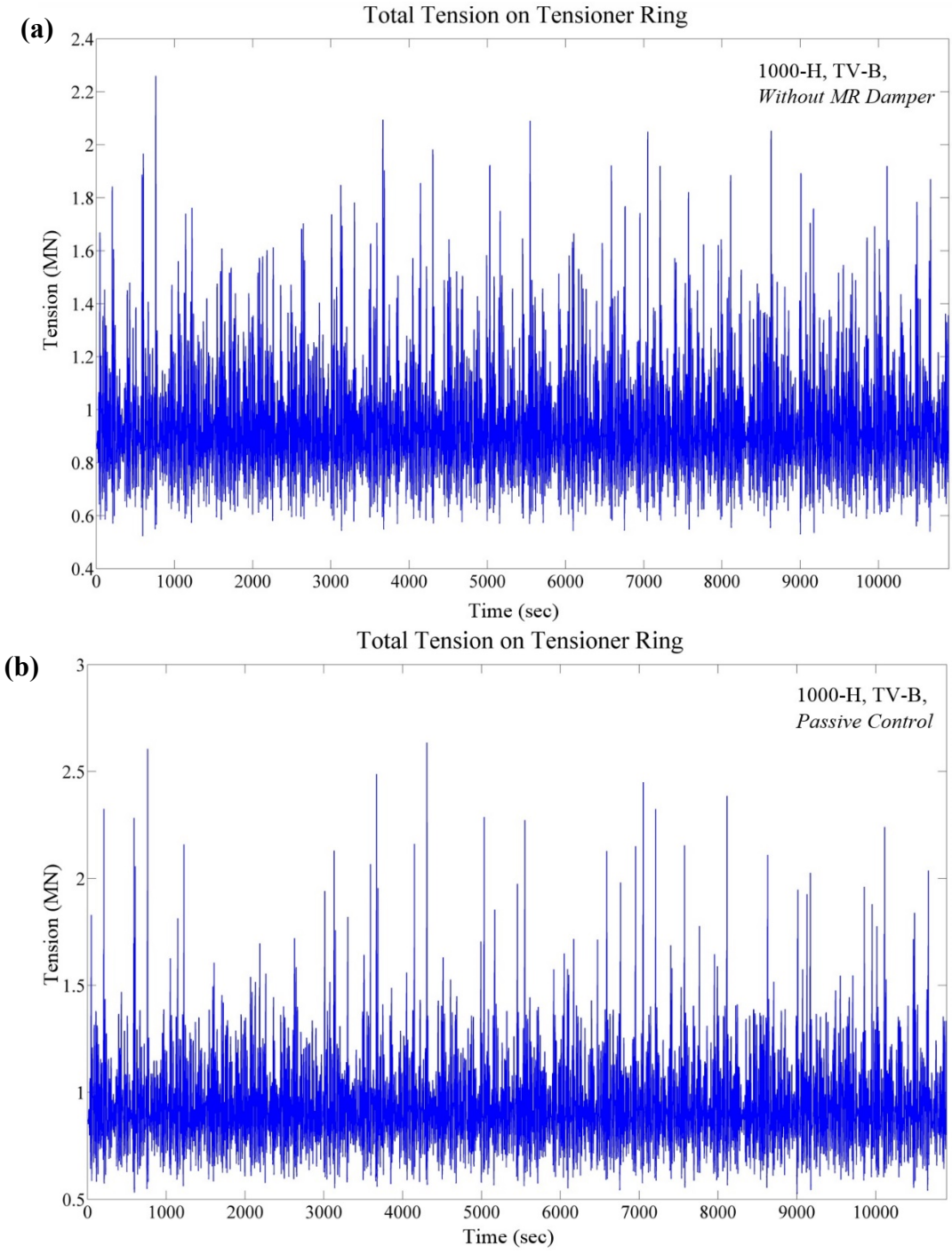

Figure 7.42 Total tension acting on tensioner ring for (a) uncontrolled base-case, (b) passive control mode.

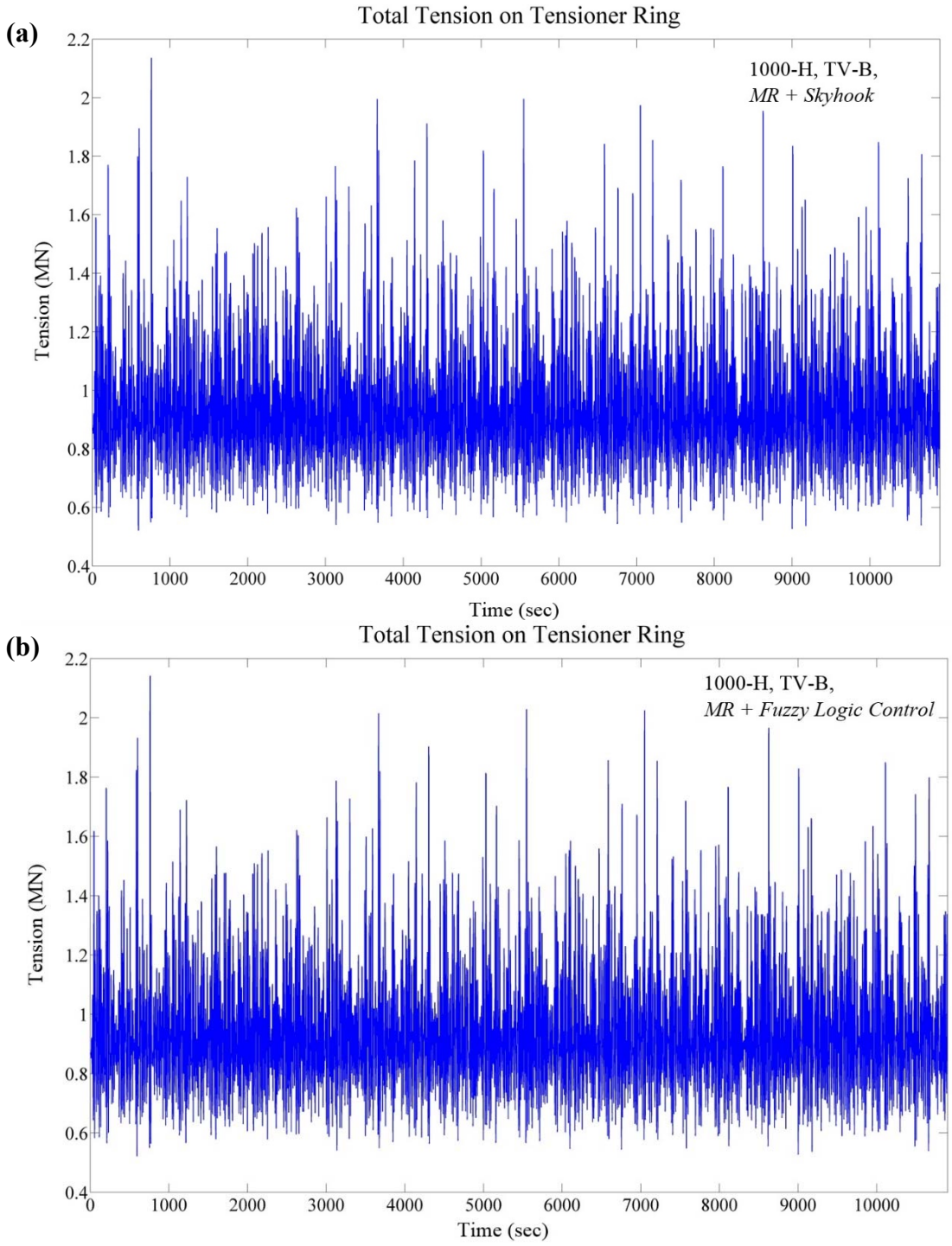

Figure 7.43 Total tension acting on tensioner ring for (a) semi-active Skyhook control mode, (b) semi-active fuzzy logic control mode.

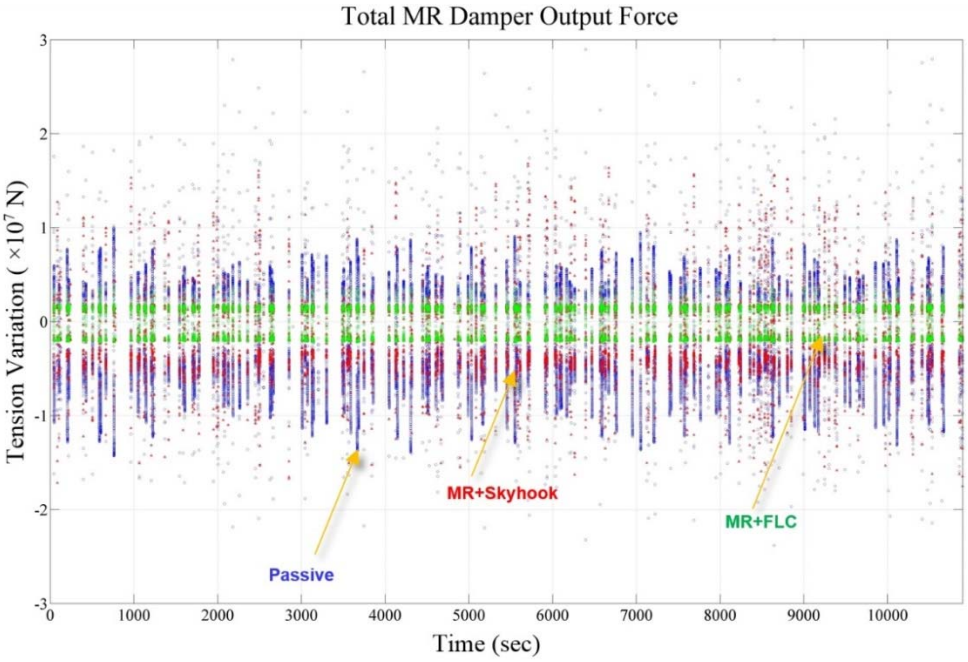

Figure 7.44 Total MR damper force output under different control schemes.

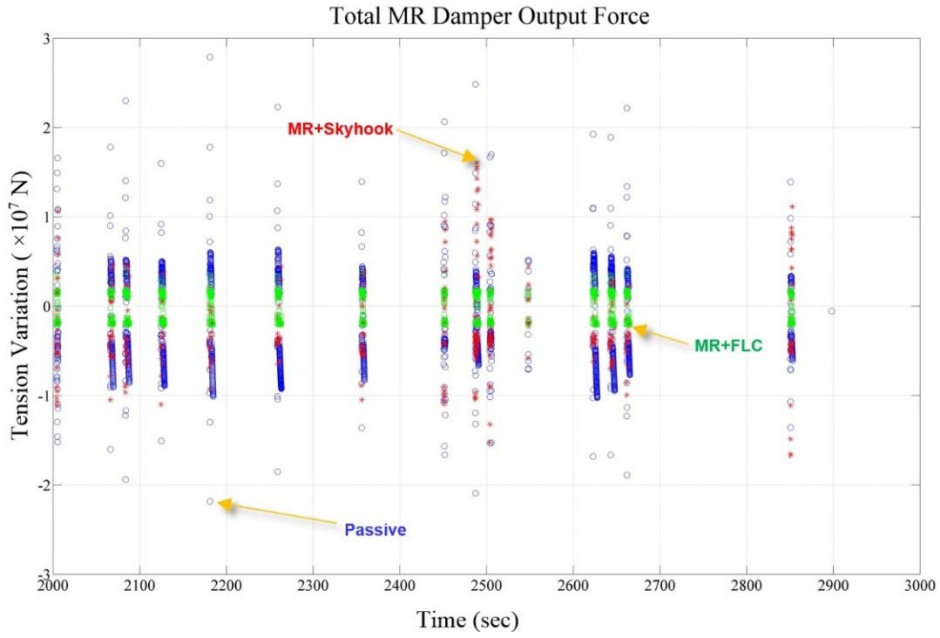

Figure 7.45 Total MR damper force output under different control schemes (from 2000 sec to 3000 sec).

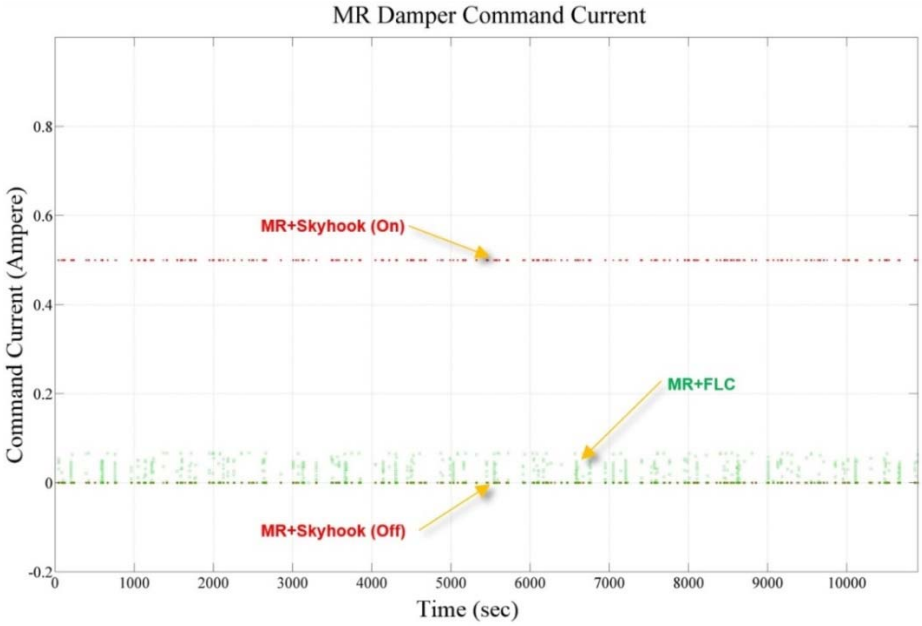

Figure 7.46 Command current inputs to MR damper under different control schemes.

The strokes of TTR after incorporated with MRD protector are shown in frequency domain (Fig. 7.47) and time domain (Figs. 7.48 – 7.49) for different control scchemes. The MRD responses as a damped and deformed contact (instead of rigid hard stopper) in between the tensioner ring and MR dampers so that the tensioner ring was allowed to further compress the MR dampers in more gradual form of energy dissipation cycles. There is noteworthy that the total required stroke length has been reduced as much as 0.963 m *(3.16 ft)*, from 13.342 m (*43.77 ft*) to 12.379 m (*40.61 ft*), in the **fuzzy logic** control scheme as tabulated in Table 7.9. In the frequency domain as shown in Fig. 7.47, the heave displacement for *heave* resonance period at around 19 sec were reduced from ~1.4 m (*~4.59 ft*) in the *base-case* to ~1.3 m (*~4.27 ft*) in by using the MR dampers,

while the heave displacement for the wave peak period is remained unchanged at around 1.0 m (*3.28 ft*).

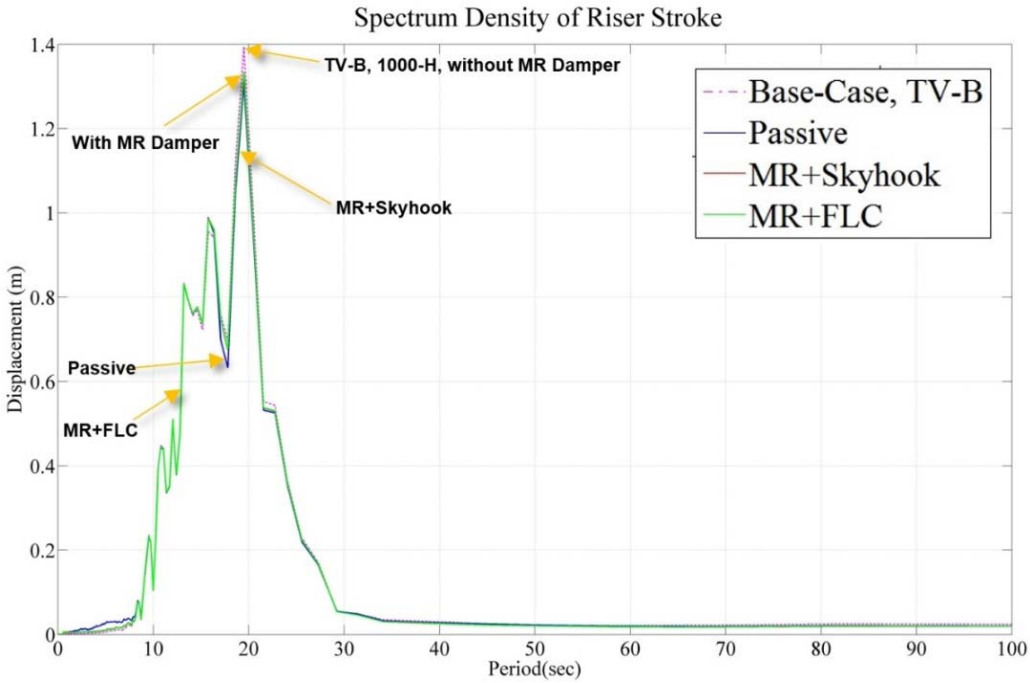

Figure 7.47 Spectrum density of TTR stroke under different control schemes.

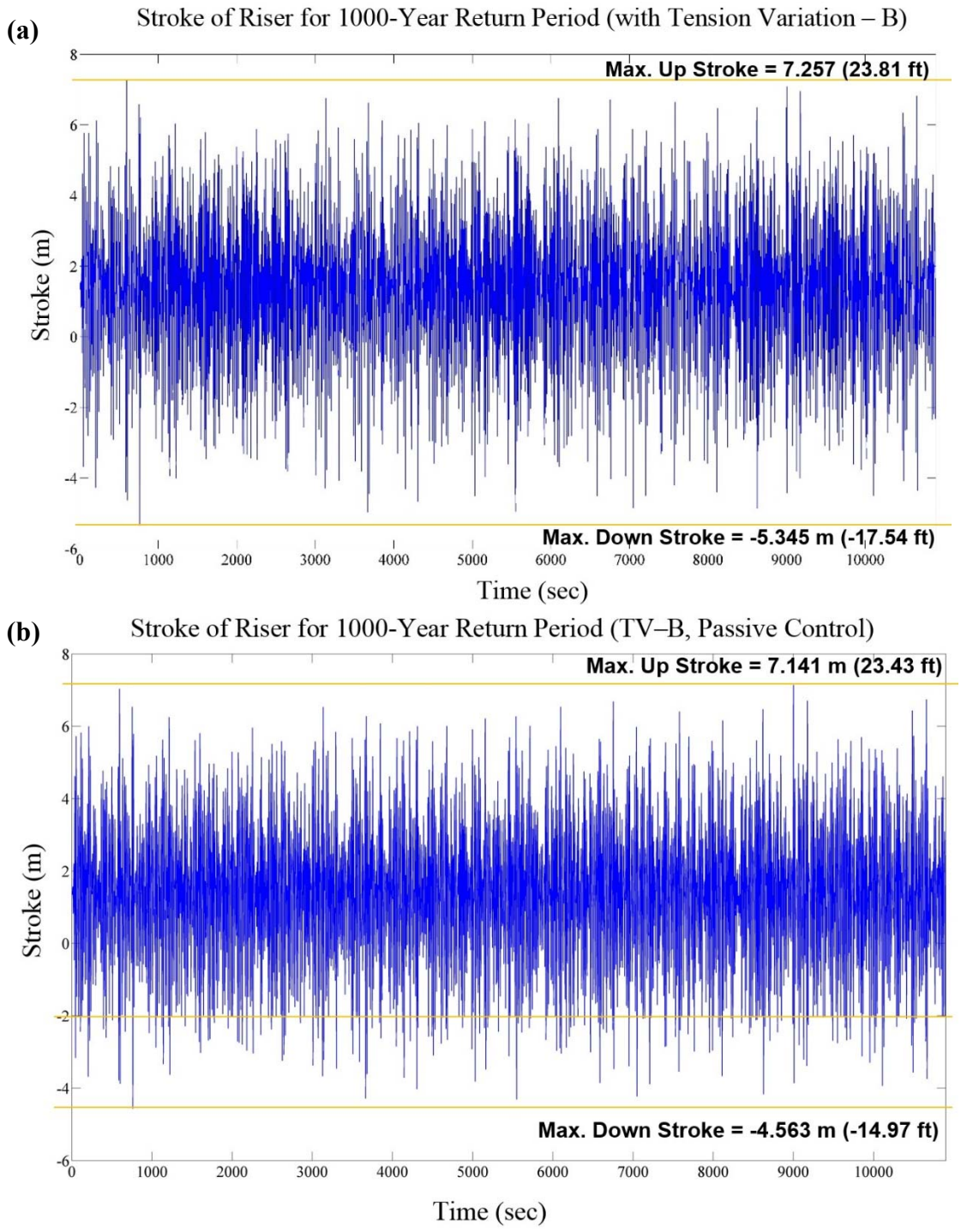

Figure 7.48 Stroke of TTR interface in DTS platform in time domain for (a) uncontrolled base-case, (b) passive control mode.

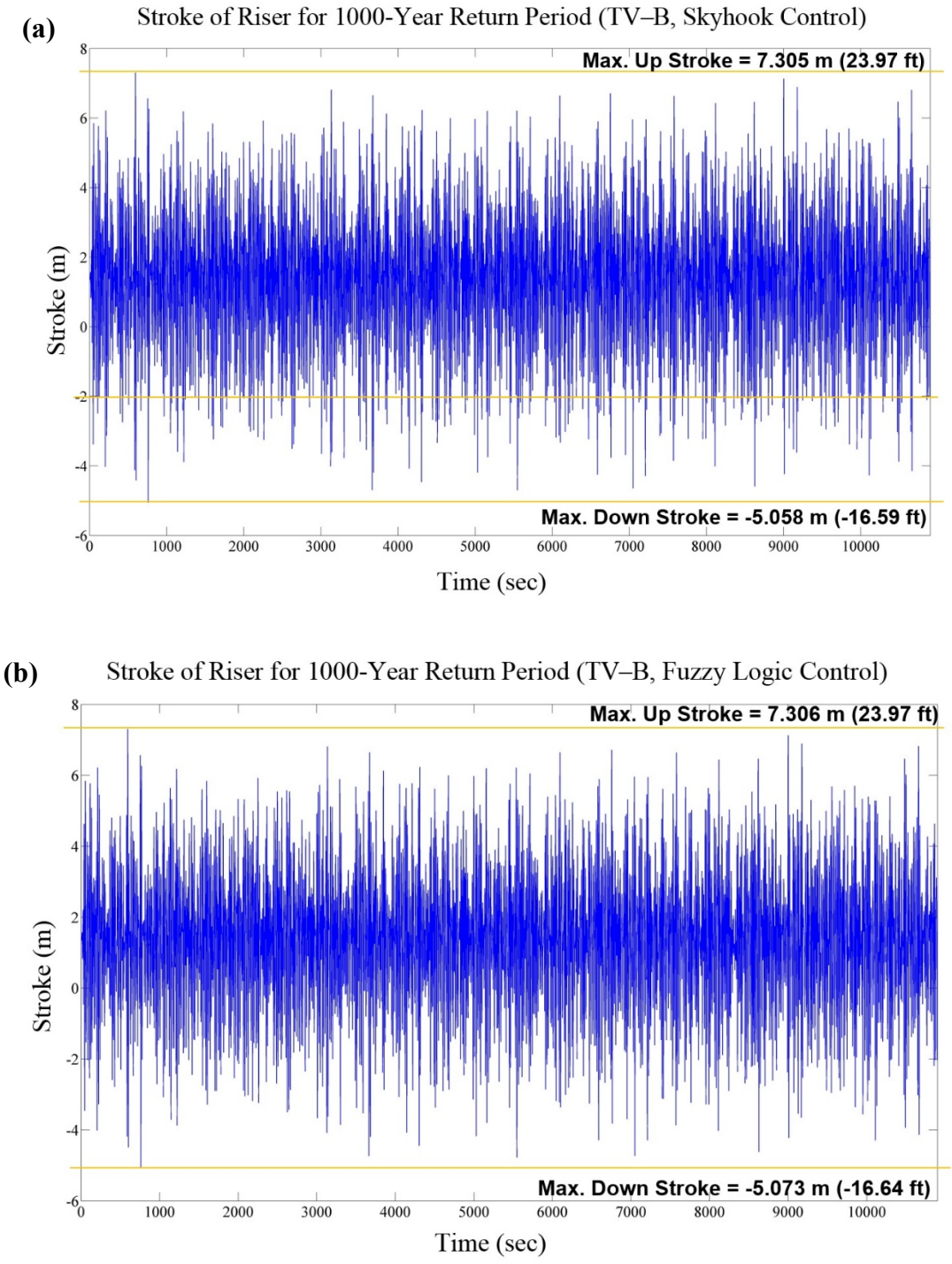

Figure 7.49 Stroke of TTR interface in DTS platform in time domain for (a) semi-active Skyhook control mode, (b) semi-active fuzzy logic control mode.

Table 7.9 Maximum up-stroke, maximum down-stroke, and required riser stroke length under different control schemes

	PT	**TV-A**	**TV-B**	**TV-B +Passive**	**TV-B +Skyhook**	**TV-B +FLC**
Maximum upstroke	7.667 m *(25.2 ft)*	6.413 m *(21.04 ft)*	7.257 m *(23.81 ft)*	7.141 m *(23.43 ft)*	7.305 m *(23.97 ft)*	7.306 m *(23.97 ft)*
Maximum down	-5.675 m *(-18.6 ft)*	-6.464 m *(-21.21 ft)*	-5.345 m *(-17.54 ft)*	-4.563 m *(-14.97 ft)*	-5.058 m *(-16.59 ft)*	-5.073 m *(-16.64 ft)*
Total required stroke length	13.342 m *(43.77 ft)*	12.877 m *(42.25 ft)*	12.602 m *(41.35 ft)*	11.704 m *(38.40 ft)*	12.363 m *(40.56 ft)*	12.379 m *(40.61 ft)*

The extreme dynamic profiles of TTR, and *envelopes* of axial tension, bending moments, and von-Mises stress for different control schemes are shown in Figs. 7.50 – 7.52. For the *passive* control scheme, the von-Mises stress is over the limit (~1.1 utilization) where the steel grade is Q125. There is noteworthy that the deviations in von-Mises stress is affected significantly by the bending moment in the passive control case (Poll et al., 2013). According to Poll et al., (2013), in the ram style tensioner, the top portion TTR does not rotate relative to the platform in roll and pitch angle because the volumetric envelope required to accommodate all possible combinations of stroke and angular motion would require too much clear area in the well bay and large spacing

between the risers. The only relative motion that must be accommodated by the jumper systems and vertical access structures is the vertical motion, hence, significant bending moment can be found in specific sections of the TTR that requires for structural reinforcement (typically by tapered stress joint forgings) (Poll et al., 2013).

The semi-active control schemes (Skyhook, and fuzzy logic) are better than the passive control in the structural integrity where the von-Mises stresses are within the limits (~0.9 utilization for both Skyhook and fuzzy logic schemes). Therefore, a suitable semi-active controller is important in the implementation of MR dampers in the LSRS tensioner system.

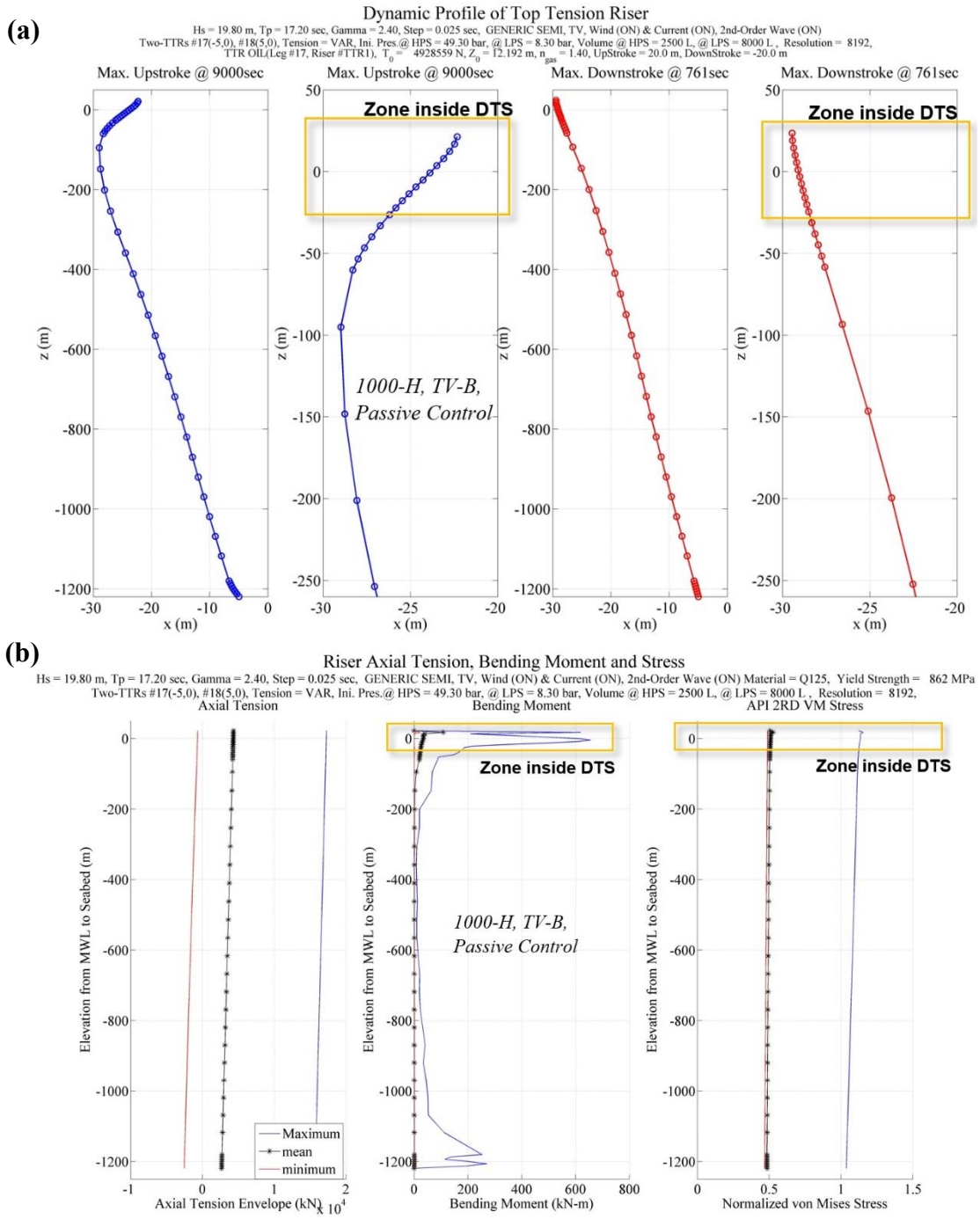

Figure 7.50 TTR (Leg #17) interfaced with DTS platform under passive control mode for (a) extreme dynamic profiles of TTR, and (b) axial tension, bending moment and von-Mises stress.

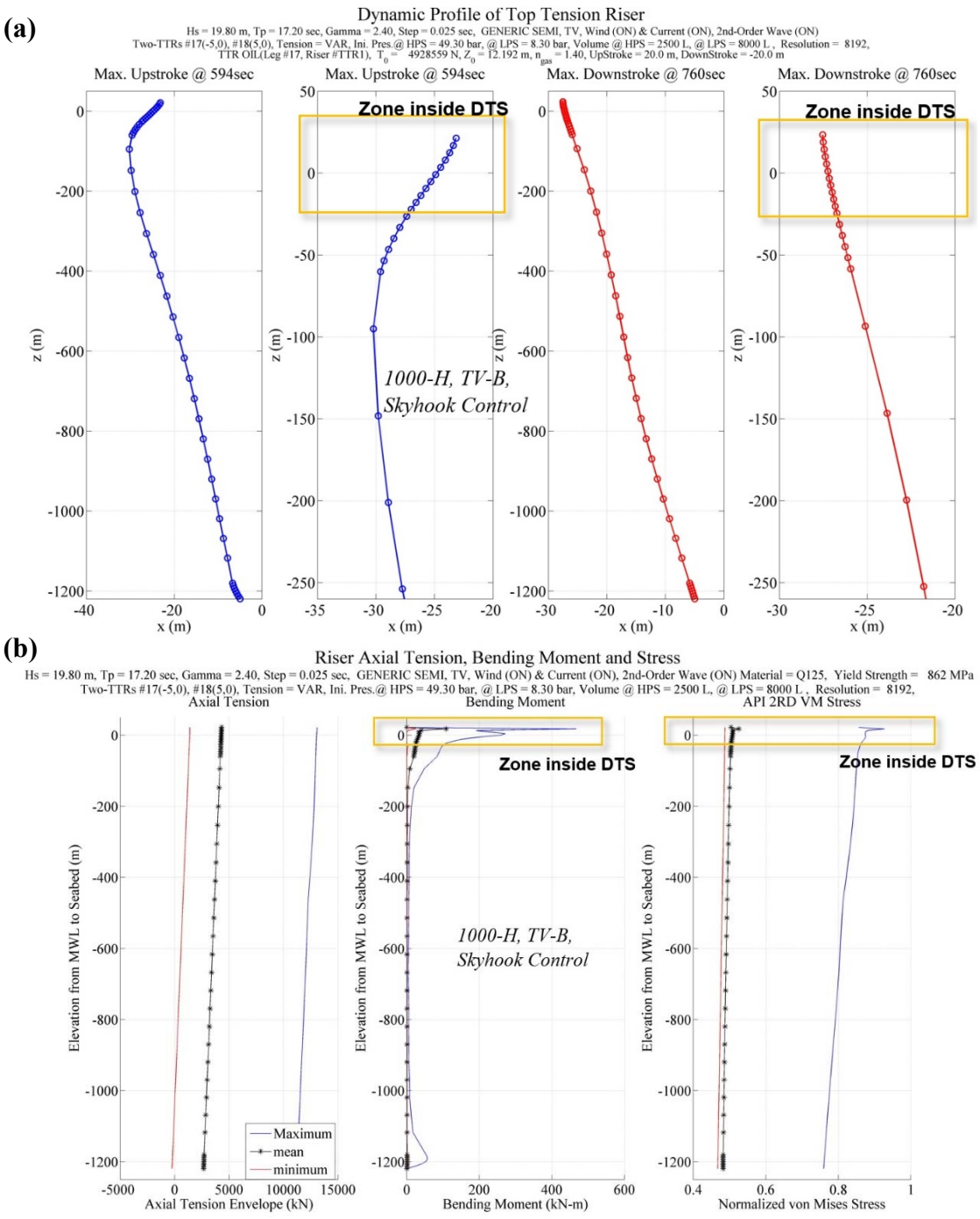

Figure 7.51 TTR (Leg #17) interfaced with DTS platform under semi-active Skyhook control mode for (a) extreme dynamic profiles of TTR, and (b) axial tension, bending moment and von-Mises stress.

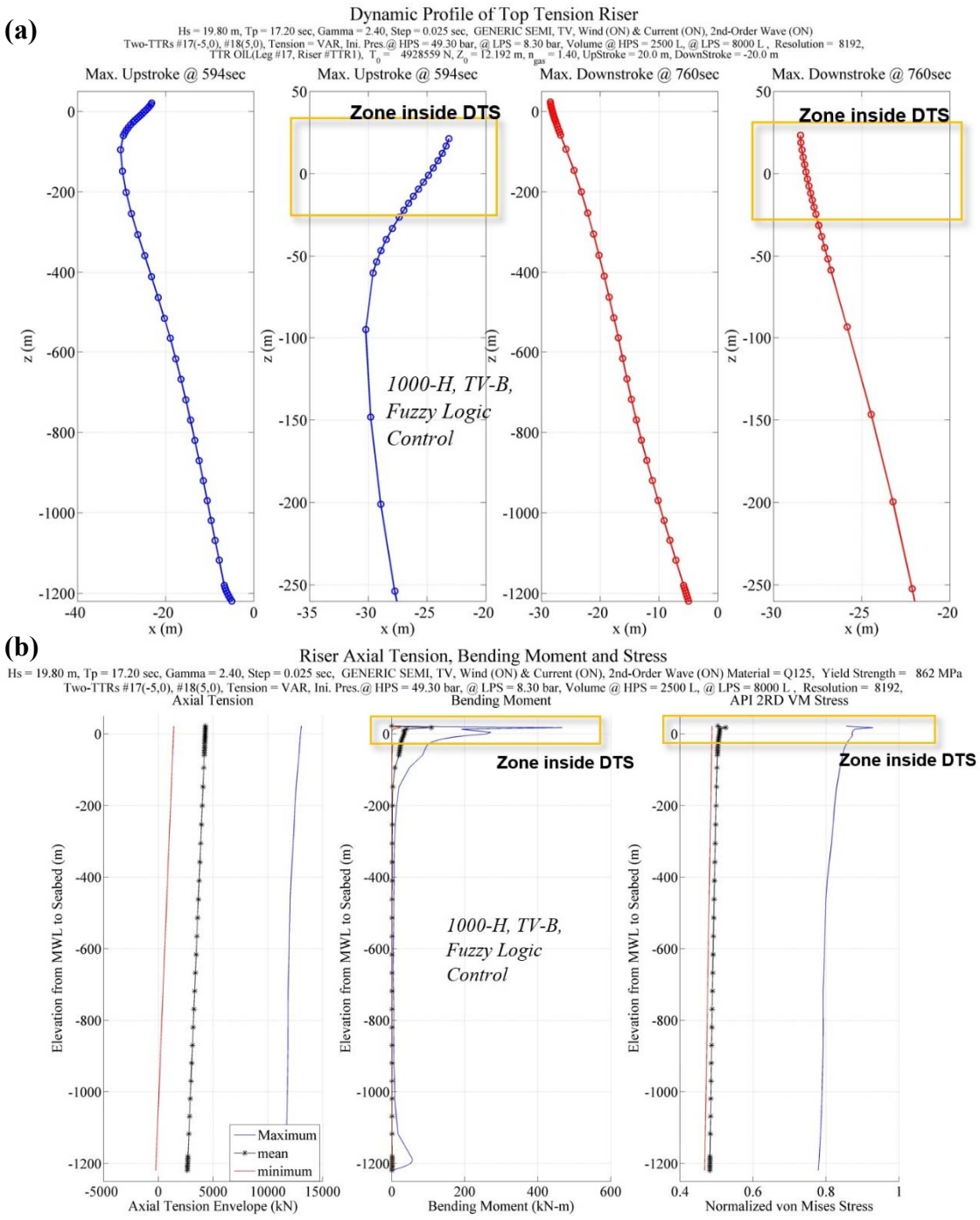

Figure 7.52 TTR (Leg #17) interfaced with DTS platform under semi-active fuzzy logic control mode for (a) extreme dynamic profiles of TTR, and (b) axial tension, bending moment and von-Mises stress.

The Mathieu stability diagram for the first two modes of the riser is shown in Fig. 7.53. The TTR first mode for all the tested control schemes are in the stable zone. Nevertheless, the second mode for the uncontrolled case is in the unstable zone if the damping ration is less than 0.25. There is noteworthy that the semi-active control schemes are able to significant stabilize the second mode by reducing the maximum tension variation.

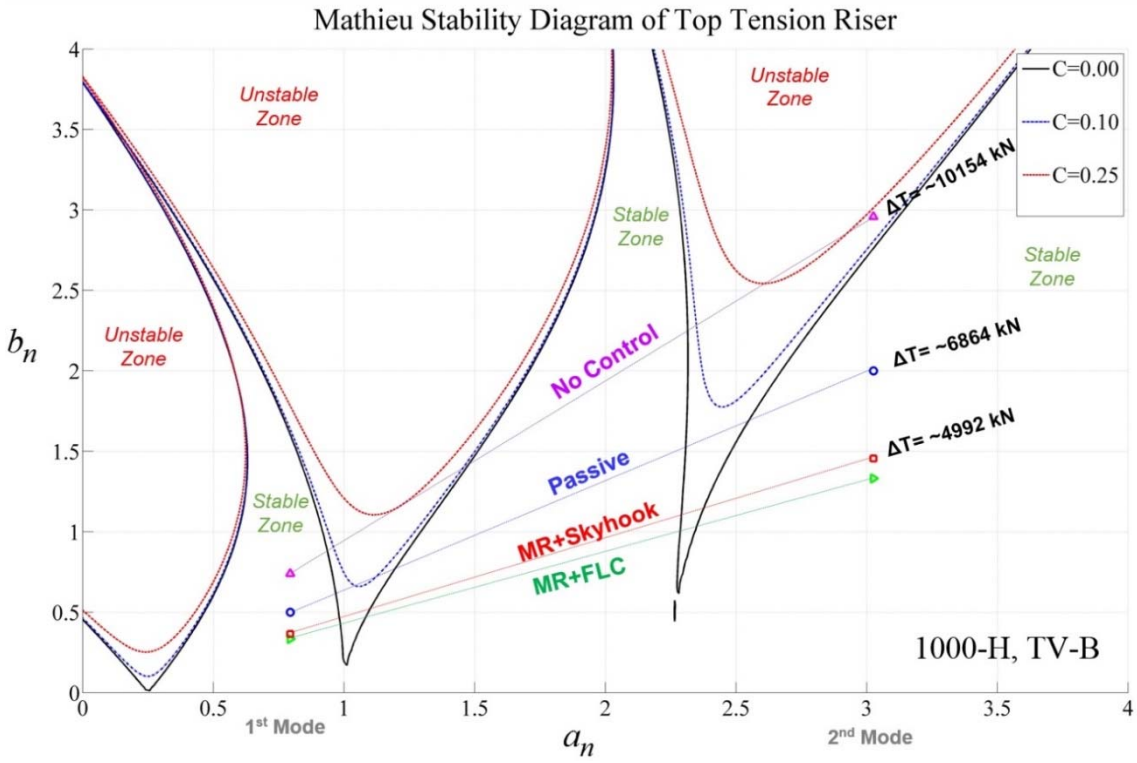

Figure 7.53 Mathieu stability analysis of TTR (Leg #17) interfaced with DTS platform under different control schemes.

The effects on platform global motion under different control schemes are studied in Figs. 7.54 – 7.55. The DTS motions in 1000-year return period condition after TTR incorporated with MRD protector are shown in frequency domain (Fig. 7.54). In this case study, the DTS motions in sway, roll, and yaw directions are very small, with at least two-order smaller than the platform motions in surge, heave, and pitch directions. It can be found that the motions of DTS are slightly affected by the controlled cases, where the amplitude of heave resonance peak is reduced. Besides, there are not apparent differences in the high-frequency (HF, low period) region.

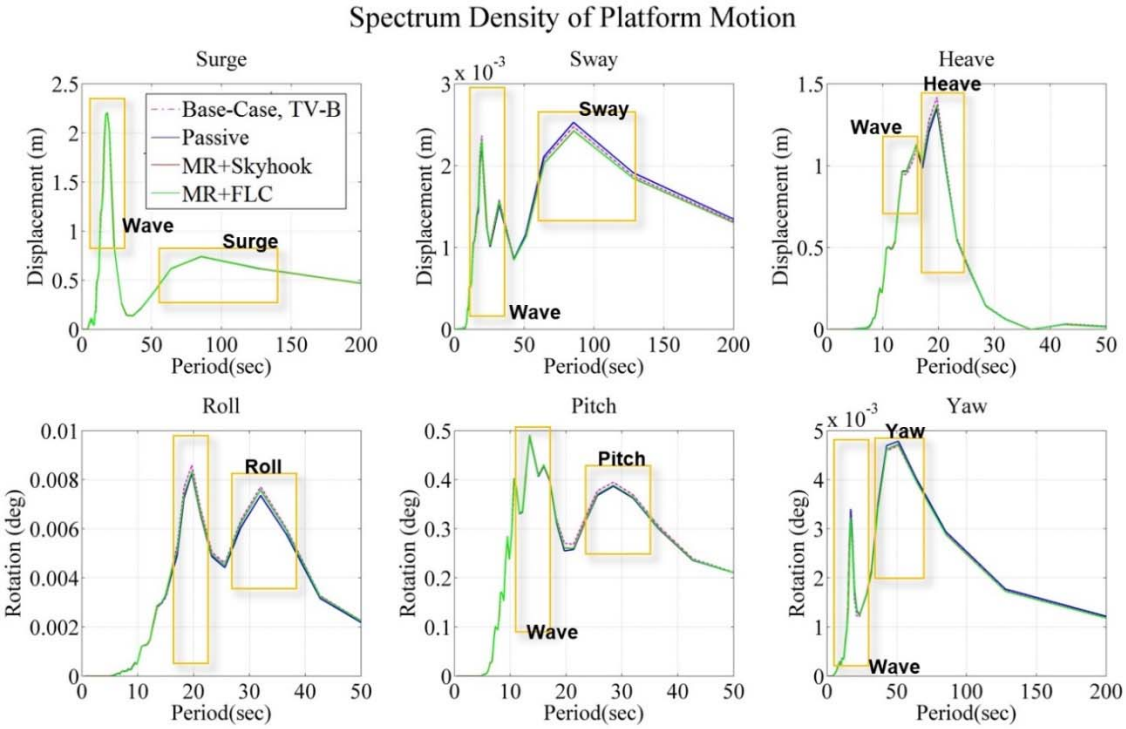

Figure 7.54 Platform motions in frequency domain under different control schemes.

The response amplitude operators (RAO) of DTS platform, under different control schemes, in this case study are shown in Fig. 7.55. In the RAO of heave motion, the cancellation period DTS is located at ~17.5 sec. The RAO in heave direction is very sensitive to the additional tensioner stiffness. The controlled cases slightly reduce the second peak of heave RAO.

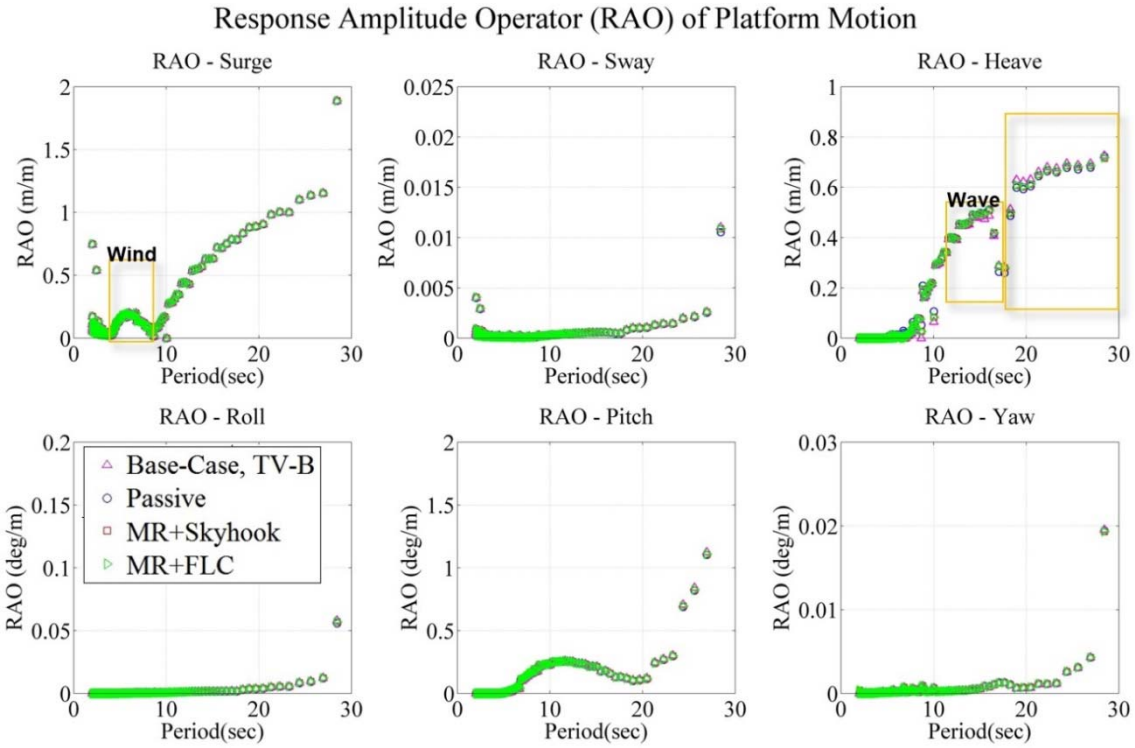

Figure 7.55 RAO of platform motions under different control schemes.

From the results of numerical analysis of LSRS-Tensioner with MRD as protector, there can be further concluded that:

(i) when the rigid hard stopper is replaced with a *Kelvin-Voigt* model, the tensioner ring is able to compress the MRD in more gradual form of energy dissipation cycles during the tensioner cylinder bottom-out motion. A suitable semi-active controller of MRD is crucial to obtain optimum stroke length, stress, tension, and stability as required;

(ii) the ability of MRD to redistribute the high tension in the tensioner cylinders during bottom-out can protect the cylinders from excessive cushioning and very sheer tension increment, as illustrated in Fig. 7.37, which is beneficial to the service life span of LSRS tensioner and the operational/maintenance expenditure (OPEX). In the worst-case scenario, the replacement of a MRD protector is more effective than replace/repair/realign the damaged LSRS tensioner cylinders, with the latter can cause significant operation down-time and technical difficulties;

(iii) a tunable MRD force can optimize and reduce the total stroke length needed for the development of DTS (stroke length is reduced 0.963 m *(3.16 ft)* in this case). However, there is noteworthy that this optimization is a *trade-off* in between the riser tension/stress and the piston/tensioner ring position and the stress and strength must be checked robustly to be within the allowable limits, the total stress is also dominant by the bending moment so that the coupled hull-mooring lines-risers analysis

must be conducted to comprehensively check the total stress (as in Figs. 7.51 – 7.52) and the dynamic response stability (as in Fig. 7.53). Any reduction of required tensioner length (or draft length) in DTS is able to enhance the *flexibility* of the platform designer in sizing and fabrication of the DTS and its LSRS tensioners. For instance, as highlighted by Koos (2013), tensioner rods and barrels for a 35 ft (*10.67 m*) stroke, 6 cylinder, and 1000 ton (*2204.62 kips*) ram tensioner would require ingots nearly 8 tons (*17.64 kips*), which put these components at the limit of what can be produced at pipe mills. Larger forged tubulars are available in very costly with long lead times and the manufacturer need to outsource the machining facilities between several shops due to the requirements of longer lathes and larger CNC mills, where the transporting is very costly (Koos, 2013).

8. CONCLUSION AND FUTURE WORK

8.1 Conclusion

A coupled dynamic analysis tool for magneto-rheological (MR) dampers, incorporated with TLP and DTS, was developed to expand the implementation of MR dampers in floating offshore platforms. This numerical tool combined with CHARM3D was able to analyze the specific characteristic of MR dampers in alternating the force exerted into the offshore structural dynamics and interactively changing the structural behaviors correspond to various external loadings. Since the implementation of MR dampers in offshore platform is currently very limited, and most of them concentrated on the fixed platforms, this numerical tool leads to advancement in developing a reliable and cost-effective way to protect the offshore floating hydrocarbon production modules in unfamiliar harsher environments by incorporating with the MR dampers technologies.

The differences of TTR behaviors into both TLP and DTS platforms have been identified in this research. In the TLP platform, since the heave motion is restrained by the high-stiffed tendons, the axial tension variations of TTR are mainly caused by the platform set-down motion. On the other hand, the DTS is vulnerable to larger heave motion; therefore deeper draft hull and long stroke tensioner are required. The heave motions of DTS can potentially amplify the dynamic tension variation in the dry-tree interface. Since the TTR is originally designed for the host platform of TLP, the developed analysis tools to calculate the TTR tension are available. However, most of these tools were primarily used *pneumatic*-based equation to approximate the tension

variations of a hydro-pneumatic (HP) tensioner system, where the viscous fluid frictional effects in the HP tensioner system is not considered in the calculation of tension variations. The traditional riser tension variations analysis by using *parametric* formulation is only conditionally valid under certain strict limits and potentially underestimate the total magnitudes of the tension variations. This phenomenon is especially important for the offshore operations where the dynamic axial tension of riser must be closely monitored, such as in the offshore drilling operation and excessive fatigue loads prevention on the connection points in between the riser and *dry-tree* production system. In this research, a more comprehensive formulation considering the hydraulic viscous fluid effects was developed to improve the reliability of TTR dynamic tension in the DTS. This new formulation was included into the coupled dynamic analysis tool.

The larger tension variation caused by larger velocity is reasonable for the cases of drillship and *dry-tree* Semi-submersible, where the platform's heave motion is no longer constrained by the high stiffed tendons, and for the cases of instantaneous velocity during anti-recoiling and TTR disconnection. The excessive tension variations in the TTR tensioner system leads to the necessity of reducing the tension variations by using MR damper. The specific characteristics of MR damper in alternating the damping forces have great potential to interactively suppress the tension variations corresponding to various sea conditions. The Equivalent Force Compensation Control (EFCC) is a conceptual scheme studied in TLP to compensate the tension variations in between the actual TTR tension and the desired tension by using a combination of MR dampers and

force actuators. System integration of MR dampers with the floating platforms is beneficial in the structural integrity management and to improve survivability in harsher environments. In the simulation case of TLP, the dynamic tension can be suppressed by as much as ~94%, where the tension variations reduced from ~18 kips (*~80 kN*) to less than 1 kips (*4.45 kN*)) by using the EFCC scheme. The reduction of dynamic tension variations of riser during offshore operation can be further implemented in the area such as to improve the short-term fatigue limits.

The Mathieu stability of TTR is very sensitive to the pretension of riser, length in deep water, and dynamic tension variations. The reduction of dynamic tension variation by using EFCC in TLP and semi-active fuzzy logic control scheme in DTS can further improve the stability of TTR. The first two vibration modes which have larger amplitudes were studied by using the Mathieu stability diagram, which predicts more conservative results in the lower modes than the Hill's equation. This is reasonable for the riser to be more stable when it is affected by the hydrodynamic damping in the water. However, the *first* unstable zone is less influenced by the damping coefficient, compared to the *second* unstable region, a very large damping coefficient is needed to change the unstable condition on the *first* unstable zone. Therefore, smaller pretension increases the tendency of instability for the TTR. For longer riser length in deep water, very small values of the parameters a_n and b_n are potential to trigger the lateral vibration of riser. As the riser's length increases, the operation point in the Mathieu stability diagram tends to the region near its origin (where the a_n and b_n are smaller). The dynamic behavior is very sensitive to small variations in the parameters a_n and b_n in this low mode region. If

the tension variation is larger, the operating point would shift towards the unstable zone. Most importantly, the reduction of dynamic tension variation ΔT on the top tension riser can move the operating point towards a stable zone. This finding provides an important control mechanism to maintain the stability of TTR, even if the lateral damping is low.

Since tensioner *bottom-out* is a very critical progress, especially to the structural health and integrity, and it has not been considered as one criterion in the experience of TLP-TTR applications, the safety prevention on the production modules during survival conditions is in critical concern. Interfacing with DTS and long stroke ram-style (LSRS) tensioner, the MR damper is able to perform as a *Kelvin-Voigt* model when the down-stroke position is lower than the threshold limit in order to provide a damped and deformed contact (instead of rigid and hard contact) in between the tensioner ring and MR dampers, and to dissipate energy caused by the tensioner cylinder bottom-out motion. The MR dampers can redistribute the high tension which originally to be withheld solely by the tensioner cylinders during bottom-out by adding the total MR dampers' stiffness and damping forces to the tensioner ring. Therefore, a major part of the required tension to be generated by tensioner cylinders can be transferred to the MR dampers. The tensioner cylinders can be protected from extreme cushioning and excessive tension increment. This is beneficial to the service life span of tensioner and the operational/maintenance expenditure (OPEX).

The total MR damper force output under different control schemes was studied. This is an important factor for identifying the capacity and size of MR damper that can support in the purposed system. The result implies that a relatively smaller scale MR

damper with fuzzy-logic controller is comparable, in performance, to a larger scale MR damper with the Skyhook controller. More importantly, MR damper incorporated with semi-active fuzzy logic controller can reduce the total required stroke length in DTS (stroke length is reduced 0.963 m *(3.16 ft)* in the study case) which enables the platform designer has more flexibility in the sizing of the DTS and LSRS tensioners. This optimization is a trade-off in between the riser tension/stress and the piston/tensioner ring position.

8.2 Future Work

One of the important limitations of this study is the consideration of interference effects between adjacent TTRs. For instance, the different phase motions of multiple TTRs system is worth to be studied in detailed in future and a more advanced central-type controller is required to monitor the response of each TTR at the same time to minimize the vibration caused by mutual-interference of MR dampers output force.

The development of optimization control and structural health monitoring of the MR damper in the DTS and TLP can be promoted using this currently developed tool, in this study, by incorporated with the advanced computations in vortex-induced vibration (VIV) effects in order to obtain a more accurate lateral parametric resonance scenario of the TTR. The accuracy of dynamic tension variations can also be improved by further considering the other factors, such as thermal effects of fluid properties in the HP tensioner and MR damper.

REFERENCES

API, 1998. API RP 2RD (R2006): Design of Risers for Floating Production Systems (FPSs) and Tension-Leg Platforms (TLPs). American Petroleum Institute (API), Washington DC.

Bae, Y.H., 2013. Coupled Dynamic Analysis of Multiple Unit Floating Offshore Wind Turbine. Doctoral dissertation, Texas A&M University, College Station, Texas, USA.

Bahar, A., Pozo, F., Acho, L., Rodellar, J., Barbat, A., 2010. Hierarchical semi-active control of base-isolated structures using a new inverse model of magnetorheological dampers. Computers & Structures 88 (7), 483-496.

Bian, S., Xiang, S., 2013. Manage tensioner stroke for dry tree semisubmersibles, In: Paper OMAE2013-10973 Proceedings, 32nd Int. Conf. on Ocean, Offshore and Arctic Engineering (OMAE2013), June 9-14, 2013, Nantes, France.

Bitaraf, M., Ozbulut, O.E., Hurlebaus, S., Barroso, L., 2010. Application of semi-active control strategies for seismic protection of buildings with MR dampers. Engineering Structures 32 (10), 3040-3047.

Brugmans, J., 2005. Parametric Instability of Deep-water Risers. Master thesis, Delft University of Technology, Delft, Netherlands.

Chandrasekaran, S., Chandak, N.R., Anupam, G., 2006. Stability analysis of TLP tethers. Ocean Engineering 33 (3), 471-482.

Chatjigeorgiou, I.K., Mavrakos, S.A., 2002. Bounded and unbounded coupled transverse response of parametrically excited vertical marine risers and tensioned cable legs for marine applications. Applied Ocean Research 24 (6), 341-354.

Colwell, S., Basu, B., 2009. Tuned liquid column dampers in offshore wind turbines for structural control. Engineering Structures 31 (2), 358-368.

Crotwell, G., Yu, A., 2011. Pull-style tensioner system for a top-tensioned riser, in: Patent, U.S. (Ed.), USA.

Dominguez, A., Sedaghati, R., Stiharu, I., 2008. Modeling and application of MR dampers in semi-adaptive structures. Computers & Structures 86 (3–5), 407-415.

Duan, Y.F., Ko, J.M., Ni, Y.Q., Chen, Z.Q., 2002. Field comparative tests of cable vibration control using magnetorheological (MR) dampers in single-and twin-damper setups, In: Proceedings, 3rd Int. Conf. on Advances in Steel Structures, December 9–11, 2002, Hong Kong, China.

Gallagher, C., Williams, D., Lang, D., 2012. Modelling of marine riser tensioner load variations and implications for minimum top tension settings in drilling risers, In: OMAE2012-83753 Proceedings, 31st Int. Conf. on Ocean, Offshore and Arctic Engineering (OMAE2012), July 1–6, 2012, Rio de Janeiro, Brazil, pp. 611-619.

Garrett, D.L., 1982. Dynamic analysis of slender rods. Energy Resources Technology 104 (4), 302-306.

Grønevik, A., 2013. Simulation Of Drilling Riser Disconnection - Recoil Analysis. Master thesis, Norwegian University of Science and Technology, Trondheim, Norway.

Haaland, S., 1983. Simple and explicit formulas for the friction factor in turbulent pipe flow. Fluids Engineering 105 (1), 89-90.

Hurlebaus, S., Gaul, L., 2006. Review: Smart structure dynamics. Mechanical Systems and Signal Processing 20 (2), 255-281.

Hurlebaus, S., Stocks, T., Ozbulut, O.E., 2011. Smart structures in engineering education. Professional Issues in Engineering Education & Practice 138 (1), 86-94.

Jansen, L.M., Dyke, S.J., 2000. Semiactive control strategies for MR dampers: comparative study. Engineering Mechanics 126 (8), 795-803.

Jiang, Z., Christenson, R., 2010. Experimental verification of an MR damper controlled highway bridge, In: Proceedings, 19th Analysis and Computation Specialty Conf., May 12-15, 2010, Orlando, Florida, United States.

Kanda, M., Miyajima, S., Nakagawa, H., Shimazaki, K., 1998. A non-linear coupled response of TLP hull and tendons in waves, In: OMAE-0472 Proceedings, 17th Int. Conf. on Offshore Mechanics and Arctic Engineering, July 5-6, 1998, Lisbon, Portugal.

Kang, H.S., Kim, M.H., Aramanadka, S.S.B., Kang, H.Y., 2014. Dynamic response control of top-tension risers by a variable damping and stiffness system with magneto-rheological damper, In: OMAE2014-23683 Proceedings, 33rd Int. Conf. on Ocean, Offshore and Arctic Engineering (OMAE2014), June 8–13, 2014, San Francisco, California, USA.

Kim, M.H., Tahar, A., Kim, Y.B., 2001. Variability of TLP motion analysis against various design methodologies/parameters, In: Proceedings, 11th Int. Offshore and Polar Engineering Conf., June 17-22, 2001, Stavanger, Norway.

Kim, Y., 2007. Nonlinear Identification and Control of Building Structures Equipped with Magnetorheological Dampers. Doctoral dissertation, Texas A&M University, College Station, Texas, USA.

Kim, Y.B., 2004. Dynamic Analysis of Multiple-Body Floating Platforms Coupled with Mooring Lines and Risers. Doctoral dissertation, Texas A&M University, College Station, Texas, USA.

Koo, B.J., Kim, M.H., Randall, R.E., 2004. Mathieu instability of a spar platform with mooring and risers. Ocean Engineering 31 (17), 2175-2208.

Koos, J., 2013. Long stroke ram-style tensioner technology, In: OTC23963-MS Proceedings, Offshore Technology Conf. (OTC2013), May 6-9, 2013, Houston, Texas, USA.

Kozik, T.J., 1975. An analysis of a riser joint tensioner system, In: OTC-2329-MS Proceedings, Offshore Technology Conf. (OTC1975), May 5-8, 1975, Houston, Texas, USA.

Kozik, T.J., Noerager, J., 1976. Riser tensioner force variations, In: OTC-2648-MS Proceedings, Offshore Technology Conf. (OTC1976), May 3-6, 1976, Houston, Texas, USA.

Kwok, N.M., Ha, Q.P., Nguyen, T.H., Li, J., Samali, B., 2006. A novel hysteretic model for magnetorheological fluid dampers and parameter identification using particle swarm optimization. Sensors and Actuators A: Physical 132 (2), 441-451.

Lee, C.H., Jang, M.G., 2011. Virtual surface characteristics of a tactile display using magneto-rheological fluids. Sensors 11 (3), 2845-2856.

Leverette, S., Bian, X., Rijken, O., 2013. Dry tree semisubmersibles for Gulf of Mexico, In: OTC-24148-MS Proceedings, Offshore Technology Conf. (OTC2013), May 6-9, 2013, Houston, Texas, USA.

Lewis, F.L., 2004. Lecture on Intelligent Control Systems: Fuzzy Logic, University of Texas, Arlington, Texas, USA.

Li, S., Campbell, M., Howells, H., Orsak, J., 2013. Tension loss of hydro-pneumatic riser tensioners, In: OMAE2013-10090 Proceedings, 32nd Int. Conf. on Ocean, Offshore and Arctic Engineering (OMAE2013), June 9–14, 2013, Nantes, France.

Manring, N., 2005. Hydraulic Control Systems. Wiley, Hoboken, New Jersey, USA, ISBN: 978-0-471-69311-6.

Mathworks, 2009. SimHydraulics Reference 1.5. Mathworks Inc., Natick, Massachusetts, USA.

Moideen, H., 2010. Prediction of Parametric Roll of Ships In Regular and Irregular Sea. Master Thesis, Texas A&M University, College Station, Texas, USA.

Morison, J., Johnson, J., Schaaf, S., 1950. The force exerted by surface waves on piles. Petroleum Technology 2 (05), 149-154.

Nayfeh, A.H., Balachandran, B., 2008. Applied Nonlinear Dynamics: Analytical, Computational and Experimental Methods. Wiley, Hoboken, New Jersey, USA, ISBN: 978-3-527-61755-5.

Nayfeh, A.H., Mook, D.T., 1977. Parametric excitations of linear systems having many degrees of freedom. Acoustical Society of America 62 (2), 375-381.

Ozbulut, O.E., Bitaraf, M., Hurlebaus, S., 2011. Adaptive control of base-isolated structures against near-field earthquakes using variable friction dampers. Engineering Structures 33 (12), 3143-3154.

Palazzoro, A., 2011. Lecture on Nonlinear Vibration, Texas A&M University, College Station, Texas, USA.

Patel, M.H., Park, H.I., 1991. Dynamics of tension leg platform tethers at low tension. Part I - Mathieu stability at large parameters. Marine Structures 4 (3), 257-273.

Patil, K.C., Jangid, R.S., 2005. Passive control of offshore jacket platforms. Ocean Engineering 32 (16), 1933-1949.

Poll, P., Kurup, N., Shi, S., Zou, J., 2013. An evaluation of strength, fatigue and operational performance of dry tree semisubmersible riser tensioning equipment, In: OTC-23926-MS Proceedings, Offshore Technology Conf. (OTC2013), May 6-9, 2013, Houston, Texas, USA.

Radhakrishnan, S., Datla, R., Hires, R.I., 2007. Theoretical and experimental analysis of tethered buoy instability in gravity waves. Ocean Engineering 34 (2), 261-274.

Ran, Z., 2000. Coupled Dynamic Analysis of Floating Structures in Waves and Currents. Doctoral dissertation, Texas A&M University, College Station, Texas, USA.

San Andrés, L., 2008. Lecture on Numerical Integration to Find Time Response of SDOF Mechanical System, MEEN 617, Lecture Notes 6, Texas A&M University, College Station, Texas, USA.

Sathishkumar, P., Jancirani, J., John, D., 2014. Reducing the seat vibration of vehicle by semi active force control technique. Mechanical Science and Technology 28 (2), 473-479.

Simos, A.N., Pesce, C.P., 1997. Mathieu stability in the dynamics of TLP's tethers considering variable tension along the length. Transactions on the Built Environment 29.

Sparks, C.P., 2007. Fundamentals of Marine Riser Mechanics: Basic Principles and Simplified Analyses. PennWell Books, Tulsa, Oklahoma, USA, ISBN: 978-1-593-70070-6.

Spencer Jr, B.F., Dyke, S.J., Sain, M.K., Carlson, J.D., 1997. Phenomenological model for magnetorheological dampers. Engineering Mechanics 123 (3), 230-238.

Sten, R., Hansen, M.R., Larsen, C.M., Sævik, S., 2010. Force variations on heave compensating system for ultra-deepwater drilling risers, In: OMAE2010-20011 Proceedings, 29th Int. Conf. on Ocean, Offshore and Arctic Engineering (OMAE2010), June 6–11, 2010, Shanghai, China.

Stoker, J.J., 1950. Nonlinear Vibrations in Mechanical And Electrical Systems. Interscience Publishers, New York, USA.

Symans, M.D., Constantinou, M.C., 1999. Semi-active control systems for seismic protection of structures: a state-of-the-art review. Engineering Structures 21 (6), 469-487.

Tahar, A., Kim, M., 2003. Hull/mooring/riser coupled dynamic analysis and sensitivity study of a tanker-based FPSO. Applied Ocean Research 25 (6), 367-382.

Trent, D., 2012. Tensioner system with recoil controls, in: Patent, U.S. (Ed.), USA.

Tse, T., Chang, C.C., 2002. Seismic protection of base-isolated structures using semi-active MR dampers. Advances in Building Technology 1, 529-536.

Tu, J., Liu, J., Qu, W., Zhou, Q., Cheng, H., Cheng, X., 2011. Design and fabrication of 500-kN large-scale MR damper. Intelligent Material Systems and Structures 22 (5), 475-487.

Van de Ven, J.D., Li, P.Y., 2009. Liquid piston gas compression. Applied Energy 86 (10), 2183-2191.

Wang, D.H., Liao, W.H., 2011. Magnetorheological fluid dampers: a review of parametric modelling. Smart Materials and Structures 20 (2).

Wang, J., Song, C., 2013. Computer simulation on fuzzy control of semi-active suspension system based on the whole vehicle. Multimedia and Ubiquitous Engineering 8 (6), 217-228.

Wang, T., Zou, J., 2006. Hydrodynamics in deepwater TLP tendon design. Hydrodynamics, Ser. B 18 (3), 386-393.

Watkins, C., 2003. Lecture on Adiabatic Bulk Moduli, Supplemental Notes, Massachusetts Institute of Technology, Cambridge, Massachusetts, USA.

Wilson, C.M.D., 2005. Fuzzy Control of Magnetorheological Dampers for Vibration Reduction of Seismically Excited Structures. Doctoral dissertation, Florida State University, Tallahassee, Florida, USA.

Xiang, S., Cao, P., Otten, J., Jiang, L., Bian, S., 2014. Top tensioned riser interface with dry-tree semisubmersible, In: OMAE2014-24624 Proceedings, 33rd Int. Conf. on Ocean, Offshore and Arctic Engineering (OMAE2014), June 8–13, 2014, San Francisco, California, USA.

Xiao, F., Yang, H.Z., 2014. Probabilistic assessment of parametric instability of a top tensioned riser in irregular waves. Marine Science and Technology 19 (3), 245-256.

Yang, C.K., 2009. Numerical Modeling of Nonlinear Coupling between Lines/Beams with Multiple Floating Bodies. Doctoral dissertation, Texas A&M University, College Station, Texas, USA.

Yang, C.K., Kim, M.H., 2010. Linear and nonlinear approach of hydropneumatic tensioner modeling for spar global performance. Offshore Mechanics and Arctic Engineering 132 (1).

Yang, G., Spencer Jr, B.F., Jung, H.-J., Carlson, J.D., 2004. Dynamic modeling of large-scale magnetorheological damper systems for civil engineering applications. Engineering Mechanics 130 (9), 1107-1114.

Yang, H., Xiao, F., Xu, P., 2013a. Parametric instability prediction in a top-tensioned riser in irregular waves. Ocean Engineering 70, 39-50.

Yang, M.G., Chen, Z.Q., Hua, X.G., 2011. An experimental study on using MR damper to mitigate longitudinal seismic response of a suspension bridge. Soil Dynamics and Earthquake Engineering 31 (8), 1171-1181.

Yang, M.G., Li, C.Y., Chen, Z.Q., 2013b. A new simple non-linear hysteretic model for MR damper and verification of seismic response reduction experiment. Engineering Structures 52, 434-445.

Yao, G., Yap, F., Chen, G., Li, W., Yeo, S., 2002. MR damper and its application for semi-active control of vehicle suspension system. Mechatronics 12 (7), 963-973.

Yu, A., Cheng, Y., Bhat, S., 2008. Evaluation of key hydraulic tensioner performance parameters for ultra deep water applications, In: OMAE2008-57465 Proceedings, 27th Int. Conf. on Offshore Mechanics and Arctic Engineering (OMAE2008), June 15–20, 2008, Estoril, Portugal, pp. 415-428.

Yu, X., Ma, T., Falzarano, J.M., 2010. Application of a new semi-active control strategy to dynamic response control of an offshore platform using MR dampers, In: OMAE2010-21070 Proceedings, 29th Int. Conf. on Ocean, Offshore and Arctic Engineering (OMAE2010), June 6–11, 2010, Shanghai, China, pp. 731-736.

Zeng, Y., Wanvik, L.G., Wang, T., Rasmussen, S., Lu, R., 2013. Dry-tree semi-submersible production and drilling unit, in: Patent, U.S. (Ed.), USA.

Zhang, L.B., Zou, J., Huang, E.W., 2002. Mathieu instability evaluation for DDCV/Spar and TLP tendon design, In: Proceedings, 11th Offshore Symposium, SNAME, Houston, Texas, USA.

Zou, J., 2008. Dynamic responses of a dry tree semi-submersible platform with ram style tensioners in the post-Katrina irregular seas, In: Proceedings, 18th Int. Offshore and Polar Engineering Conf., July 6–11, 2008, Vancouver, BC, Canada.

APPENDIX A

FINITE ELEMENT MODELING OF LINEAR DAMPER CONNECTION

In order develop the finite element modeling of a linear damper connection, the following relationship are initially defined as,

Change of displacement , $\Delta x_i^{(n)} = x_i^{(n+1)} - x_i^{(n)}$ (A.1)

Velocity or change of displacement within time interval, $\dot{x}_i^{(\mathrm{n})} = \dfrac{x_i^{(n+1)} - x_i^{(n)}}{\Delta t^{(\mathrm{n})}}$ (A.2)

Change of velocity , $\Delta \dot{x}_i^{(\mathrm{n})} = \dfrac{\Delta\left(x_i^{(n+1)} - x_i^{(n)}\right)}{\Delta t^{(\mathrm{n})}}$ (A.3)

Therefore,

$$\boxed{\Delta\left(x_i^{(n+1)} - x_i^{(n)}\right) = \Delta x_i^{(n+1)} - \Delta x_i^{(n)} = \Delta\left(\Delta x_i^{(\mathrm{n})}\right)} \quad \text{(A.4)}$$

Then, the damping force on the end node of the line is:

$$N_i^D = D\left(\dot{X}_i + C_{ij}\dot{\theta}_j - \dot{r}_i\right) \quad \text{(A.5)}$$

By using Newton's method, the damping force is expanded by using Taylor series expansion,

$$N_i^{D(n+1)} = N_i^{D(n)} + \frac{\partial N_i^{D(n)}}{\partial \dot{r}_j}\Delta \dot{r}_j + \frac{\partial N_i^{D(n)}}{\partial \dot{X}_j}\Delta \dot{X}_j + \frac{\partial N_i^{D(n)}}{\partial \dot{\theta}_j}\Delta \dot{\theta}_j + \ldots \quad \text{(A.6)}$$

By using Adams-Moulton implicit method, the integration of the connector force caused by linear damper yields:

$$\int_{t^{(n)}}^{t^{(n+1)}} N_i^D dt = \frac{\Delta t^{(\mathrm{n})}}{2}\left(N_i^{D(n+1)} + N_i^{D(n)}\right) \tag{A.7}$$

Since the damping force at time step $n+1$, $N_i^{D(n+1)}$ is function of the unknown velocity of the platform at time step $n+1$, thus, in order to solve this equation, Adams-Bashforth explicit method with Taylor series expansion as shown in Eqn. (A.6) is used to predict the value of $N_i^{D(n+1)}$.

$$\begin{aligned}\int_{t^{(n)}}^{t^{(n+1)}} N_i^D dt &= \frac{\Delta t}{2}\left(N_i^{D(n+1)} + N_i^{D(n)}\right) \\ &\approx \frac{\Delta t}{2}\left(\frac{\partial N_i^{D(n)}}{\partial \dot{r}_j}\Delta \dot{r}_j + \frac{\partial N_i^{D(n)}}{\partial \dot{X}_j}\Delta \dot{X}_j + \frac{\partial N_i^{D(n)}}{\partial \dot{\theta}_j}\Delta \dot{\theta}_j + 2N_i^{D(n)}\right)\end{aligned} \tag{A.8}$$

By substituting the definition in Eqn. (A.4), the terms in the right hand side of Eqn. (A.8) can be further written as:

$$\begin{aligned}\frac{\Delta t}{2}\left[\frac{\partial N_i^{D(n)}}{\partial \dot{r}_j}\Delta \dot{r}_j\right] &= \frac{1}{2}\left[\frac{\partial N_i^{D(n)}}{\partial \dot{r}_j}\Delta\left(\Delta r_j^{(\mathrm{n})}\right)\right] = \frac{\partial N_i^{D(n)}}{\partial \dot{r}_j}\left[\frac{1}{2}\left(\Delta r_j^{(n+1)} - \Delta r_j^{(n)}\right)\right] \\ &= -D\left[\frac{1}{2}\left(\Delta r_j^{(n+1)} - \Delta r_j^{(n)}\right)\right]\end{aligned} \tag{A.9}$$

$$\begin{aligned}\frac{\Delta t}{2}\left[\frac{\partial N_i^{D(n)}}{\partial \dot{X}_j}\Delta \dot{X}_j\right] &= \frac{1}{2}\left[\frac{\partial N_i^{D(n)}}{\partial \dot{X}_j}\Delta\left(\Delta X_j^{(\mathrm{n})}\right)\right] = \frac{\partial N_i^{D(n)}}{\partial \dot{X}_j}\left[\frac{1}{2}\left(\Delta X_j^{(n+1)} - \Delta X_j^{(n)}\right)\right] \\ &= D\left[\frac{1}{2}\left(\Delta X_j^{(n+1)} - \Delta X_j^{(n)}\right)\right]\end{aligned} \tag{A.10}$$

$$\begin{aligned}\frac{\Delta t}{2}\left[\frac{\partial N_i^{D(n)}}{\partial \dot{\theta}_j}\Delta \dot{\theta}_j\right] &= \frac{1}{2}\left[\frac{\partial N_i^{D(n)}}{\partial \dot{\theta}_j}\Delta\left(\Delta \theta_j^{(\mathrm{n})}\right)\right] = \frac{\partial N_i^{D(n)}}{\partial \dot{\theta}_j}\left[\frac{1}{2}\left(\Delta \theta_j^{(n+1)} - \Delta \theta_j^{(n)}\right)\right] \\ &= DC_{ij}\left[\frac{1}{2}\left(\Delta \theta_j^{(n+1)} - \Delta \theta_j^{(n)}\right)\right]\end{aligned} \tag{A.11}$$

$$\frac{\Delta t}{2}\left[2N_i^{D(n)}\right]=\Delta t\left[D\left(\dot{X}_i+C_{ij}\dot{\theta}_j-\dot{r}_i\right)\right]=\Delta t\cdot D\left(\frac{\Delta X_i}{\Delta t}+C_{ij}\frac{\Delta\theta_j}{\Delta t}-\frac{\Delta r_i}{\Delta t}\right)$$
$$=D\left(\Delta X_i^{(n)}+C_{ij}\Delta\theta_j^{(n)}-\Delta r_i^{(n)}\right)$$
$$=\frac{D}{2}\left(2\Delta X_i^{(n)}+2C_{ij}\Delta\theta_j^{(n)}-2\Delta r_i^{(n)}\right) \tag{A.12}$$

Therefore, rearranging the right hand side of Eqn. (A.8), the integration of the connector force that contributed by linear damper yields:

$$\int_{t^{(n)}}^{t^{(n+1)}}N_i^D dt=\frac{\Delta t}{2}\left(N_i^{D(n+1)}+N_i^{D(n)}\right)$$
$$\approx\frac{\Delta t}{2}\left[\frac{\partial N_i^{D(n)}}{\partial\dot{r}_j}\Delta\dot{r}_j+\frac{\partial N_i^{D(n)}}{\partial\dot{X}_j}\Delta\dot{X}_j+\frac{\partial N_i^{D(n)}}{\partial\dot{\theta}_j}\Delta\dot{\theta}_j+2N_i^{D(n)}\right]$$
$$=\frac{D}{2}\begin{bmatrix}-\left(\Delta r_j^{(n+1)}-\Delta r_j^{(n)}+2\Delta r_i^{(n)}\right)+\left(\Delta X_j^{(n+1)}-\Delta X_j^{(n)}+2\Delta X_i^{(n)}\right)\\+C_{ij}\left[\left(\Delta\theta_j^{(n+1)}-\Delta\theta_j^{(n)}+2\Delta\theta_j^{(n)}\right)\right]\end{bmatrix}$$
$$=D\left[-\frac{1}{2}\left(\Delta r_i^{(n+1)}+\Delta r_i^{(n)}\right)+\frac{1}{2}\left(\Delta X_i^{(n+1)}+\Delta X_i^{(n)}\right)+\frac{1}{2}C_{ij}\left(\Delta\theta_j^{(n+1)}+\Delta\theta_j^{(n)}\right)\right] \tag{A.13}$$

By approximating the time varying Δr_i, $\Delta\theta_j$ and ΔX_i in the time interval $t^{(n+1)}-t^{(n)}$ to be a constant $\Delta r_i^{\left(n+\frac{1}{2}\right)}, \Delta\theta_j^{\left(n+\frac{1}{2}\right)}, X_i^{\left(n+\frac{1}{2}\right)}$ which are the position at time $t^{(n)}+\frac{\Delta t}{2}$, for instance: $\Delta r_i^{\left(n+\frac{1}{2}\right)}=\frac{1}{2}\left(\Delta r_i^{(n+1)}+\Delta r_i^{(n)}\right)$, the Eqn. (A.13) can be simplified as:

$$\int_{t^{(n)}}^{t^{(n+1)}}N_i^D dt=D\left[-\frac{1}{2}\left(\Delta r_i^{(n+1)}+\Delta r_i^{(n)}\right)+\frac{1}{2}\left(\Delta X_i^{(n+1)}+\Delta X_i^{(n)}\right)+\frac{1}{2}C_{ij}\left(\Delta\theta_j^{(n+1)}+\Delta\theta_j^{(n)}\right)\right]$$
$$=D\left[-\Delta r_i^{\left(n+\frac{1}{2}\right)}+\Delta X_i^{\left(n+\frac{1}{2}\right)}+C_{ij}\Delta\theta_j^{\left(n+\frac{1}{2}\right)}\right] \tag{A.14}$$

Therefore, in the time domain simulation, the integration of the connector force yields:

For equation r_i:
$$\boxed{\int_{t^{(n)}}^{t^{(n+1)}} N_i^D dt = D\left[\Delta X_i^{\left(n+\frac{1}{2}\right)} + C_{ij}\Delta\theta_j^{\left(n+\frac{1}{2}\right)} - \Delta r_i^{\left(n+\frac{1}{2}\right)}\right]} \tag{A.15}$$

For equation X_i:
$$\boxed{\int_{t^{(n)}}^{t^{(n+1)}} F_i^D dt = -D\left[\Delta X_i^{\left(n+\frac{1}{2}\right)} + C_{ij}\Delta\theta_j^{\left(n+\frac{1}{2}\right)} - \Delta r_i^{\left(n+\frac{1}{2}\right)}\right]} \tag{A.16}$$

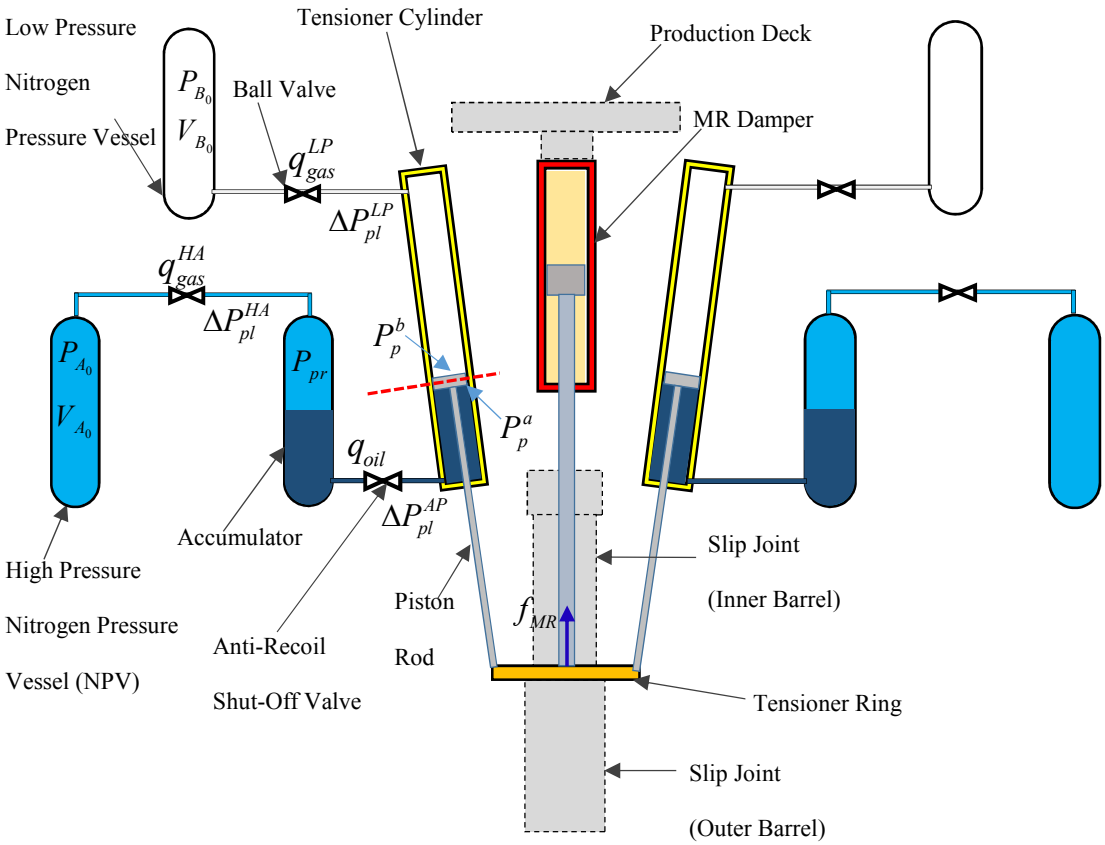

Figure A.1 The integration of MR damper in the direct-acting tensioner (DAT) system.

APPENDIX B

THE AVERAGE ACCELERATION METHOD (AAM)

The *average acceleration method* (AAM) (San Andrés, 2008) is an implicit method with numerically stable and consistent. For numerical integration of SDOF linear system:

$$M\ddot{X} + D\dot{X} + KX = F(t) \tag{B.1}$$

Let: $X_i = X(t_i)$, $X_{i+1} = X(t_{i+1})$, $F_i = F(t_i)$, $F_{i+1} = F(t_{i+1})$ (B.2)

Write Eqn. (B.1) at time step:

$$t = t_i: \quad M\ddot{X}_i + D\dot{X}_i + KX_i = F_i(t) \tag{B.3}$$

$$t = t_{i+1}: \quad M\ddot{X}_{i+1} + D\dot{X}_{i+1} + KX_{i+1} = F_{i+1}(t) \tag{B.4}$$

Subtract Eqn. (B.4) from Eqn. (B.3) to obtain:

$$M\Delta\ddot{X}_i + D\Delta\dot{X}_i + K\Delta X_i = \Delta F_i(t) \tag{B.5}$$

where,

$$\Delta X_i = X_{i+1} - X_i; \qquad \Delta\dot{X}_i = \dot{X}_{i+1} - \dot{X}_i;$$

$$\Delta\ddot{X}_i = \ddot{X}_{i+1} - \ddot{X}_i; \qquad \Delta F_i = F_{i+1} - F_i \tag{B.6}$$

Note that the known quantities at $t = t_i$ are $\{X_i, \dot{X}_i, \ddot{X}_i\}$. Assuming the acceleration is constant within the time interval $\Delta t_i = t_{i+1} - t_i$,

$$\ddot{X}(\tau) = a_i \qquad \text{for} \qquad 0 < \tau \le \Delta t_i \tag{B.7}$$

then, set an average value $a_i = \frac{1}{2}\left(\ddot{X}_{i+1} + \ddot{X}_i\right)$. Therefore, the velocity and displacement follow from integration within the time interval are shown as in Fig. B.1:

$$\dot{X}(\tau) = \dot{X}_i + a_i \tau \tag{B.8}$$

$$X(\tau) = X_i + \dot{X}_i \tau + \frac{1}{2} a_i \tau^2 \tag{B.9}$$

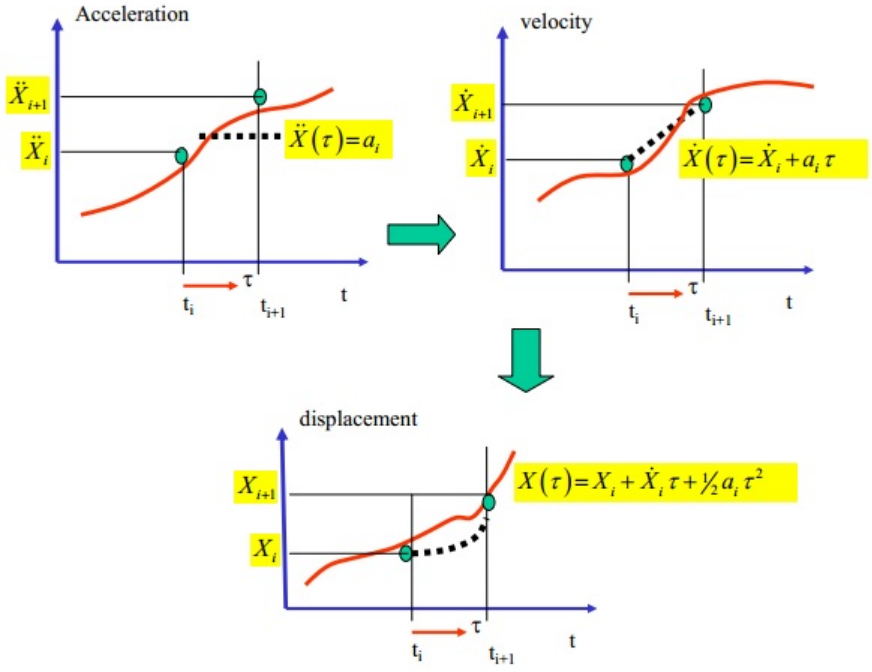

Figure B.1 Schematic representation of the average acceleration (AAM) method (San Andrés, 2008).

At the end of the time interval, the velocity and displacement are:

$$\dot{X}_{i+1} = \dot{X}\left(\Delta t_i\right) = \dot{X}_i + a_i \Delta t_i \tag{B.10}$$

$$X_{i+1} = X\left(\Delta t_i\right) = X_i + \dot{X}_i \Delta t_i + \frac{1}{2} a_i \left(\Delta t_i\right)^2 \tag{B.11}$$

and the differences in velocity and displacement are:

$$\begin{aligned} \Delta \dot{X}_i &= \left(\dot{X}_{i+1} - \dot{X}_i\right) = a_i \Delta t_i = \frac{1}{2}\left(\ddot{X}_{i+1} + \ddot{X}_i\right)\Delta t_i = \frac{1}{2}\left(\ddot{X}_{i+1} - \ddot{X}_i + 2\ddot{X}_i\right)\Delta t_i \\ &= \frac{1}{2}\left(2\ddot{X}_i + \Delta \ddot{X}_i\right)\Delta t_i \end{aligned} \tag{B.12}$$

$$\begin{aligned} \Delta X_i &= \left(X_{i+1} - X_i\right) = \dot{X}_i \Delta t_i + \frac{1}{2} a_i \left(\Delta t_i\right)^2 = \dot{X}_i \Delta t_i + \frac{1}{4}\left(\Delta t_i\right)^2 \left(\ddot{X}_{i+1} + \ddot{X}_i - \ddot{X}_i + \ddot{X}_i\right) \\ &= \dot{X}_i \Delta t_i + \frac{1}{4}\left(\Delta t_i\right)^2 \left(2\ddot{X}_i + \Delta \ddot{X}_i\right) \end{aligned} \tag{B.13}$$

From Eqn. (B.13), $\Delta \ddot{X}_i = -2\ddot{X}_i + \frac{4}{\Delta t_i^2}\left(\Delta X_i - \dot{X}_i \Delta t_i\right)$ (B.14)

and into Eqn. (B.12):

$$\begin{aligned} \Delta \dot{X}_i &= \frac{1}{2}\left(2\ddot{X}_i + \Delta \ddot{X}_i\right)\Delta t_i = \frac{1}{2}\left(2\ddot{X}_i - 2\ddot{X}_i + \frac{4}{\Delta t_i^2}\left(\Delta X_i - \dot{X}_i \Delta t_i\right)\right)\Delta t_i \\ &= \frac{2}{\Delta t_i}\Delta X_i - 2\dot{X}_i \end{aligned} \tag{B.15}$$

Note that in Eqns. (B.14) and (B.15), $\left\{\Delta \dot{X}_i, \Delta \ddot{X}_i\right\}$ depend on the known values obtained at the prior time step, i.e. $\left\{\dot{X}_i, \ddot{X}_i\right\}$ and the unknown ΔX_i. Thus, replace $\left\{\Delta \dot{X}_i, \Delta \ddot{X}_i\right\}$ into the Eqn. (B.5),

$$M\left\{-2\ddot{X}_i + \frac{4}{\Delta t_i^2}\left(\Delta X_i - \dot{X}_i \Delta t_i\right)\right\} + D\left\{\frac{2}{\Delta t_i}\Delta X_i - 2\dot{X}_i\right\} + K\Delta X_i = \Delta F_i \tag{B.16}$$

Rearrange terms leads to:

$$\hat{K}_i \Delta X_i = \Delta \hat{F}_i \tag{B.17}$$

$$\text{where, } \hat{K}_i = \left[K + \frac{2}{\Delta t_i} D + \frac{4}{\Delta t_i^2} M \right] \tag{B.18}$$

$$\Delta \hat{F}_i = \Delta F_i + 2M\ddot{X}_i + \left\{ 2D + \frac{4}{\Delta t_i} M \right\} \dot{X}_i \tag{B.19}$$

The $\hat{K}_i$ and $\Delta \hat{F}_i$ are known as **pseudo dynamic stiffness** and **dynamic force** respectively. The algorithm for the numerical integration to find the system time response is:

(i) At time t_i, known variables for current state are $\left\{ \dot{X}_i, X_i \right\}$, find from equation of motion: $\ddot{X}_i = M^{-1} \left(F_i - D\dot{X}_i - KX_i \right)$;

(ii) Form pseudo stiffness and forcing functions, $\left(\hat{K}_i, \Delta \hat{F}_i \right)$ from Eqns. (B.18) and (B.19);

(iii) Calculate $\Delta X_i = \left(\hat{K}_i \right)^{-1} \Delta \hat{F}_i$, and $\Delta \dot{X}_i = \frac{2}{\Delta t_i} \Delta X_i - 2\dot{X}_i$;

(iv) Substitute $X_{i+1} = X_i + \Delta X_i$ and $\dot{X}_{i+1} = \dot{X}_i + \Delta \dot{X}_i$ at t_{i+1}

(v) Increase time to t_{i+2} and return to step (i).

For numerical integration of SDOF nonlinear system, consider the system with equation of motion,

$$M\ddot{X} + g\left(\dot{X}, X \right) = F(t) \tag{B.20}$$

where $g\left(\dot{X}, X\right)$ is a nonlinear function, for example:

$$g\left(\dot{X}, X\right) = g_o + k_o X + k_3 X^3 + F_\mu \operatorname{sgn}\left(\dot{X}\right) \tag{B.21}$$

As with the linear system, evaluate Eqn. (B.20) at two times (closely spaced):

$$t = t_i: \quad M\ddot{X}_i + g\left(\dot{X}_i, X_i\right) = F_i \tag{B.22}$$

$$t = t_{i+1}: \qquad M\ddot{X}_{i+1} + g\left(\dot{X}_{i+1}, X_{i+1}\right) = F_{i+1} \tag{B.23}$$

Subtract Eqn. (B.23) from Eqn. (B.22) to obtain:

$$M\,\Delta\ddot{X}_i + g_{i+1} - g_i = \Delta F_i \tag{B.24}$$

where

$$\Delta\ddot{X}_i = \ddot{X}_{i+1} - \ddot{X}_i, \qquad \Delta F_i = F_{i+1} - F_i, \qquad g_i = g\left(\dot{X}_i, X_i\right),$$
$$g_{i+1} = g\left(\dot{X}_{i+1}, X_{i+1}\right) \tag{B.25}$$

A Taylor series expansion of the nonlinear function at $t = t_i$ gives

$$g_{i+1} = g_i + \left.\frac{\partial g}{\partial X}\right|_{X_i, \dot{X}=0} \Delta X_i + \left.\frac{\partial g}{\partial \dot{X}}\right|_{\dot{X}_i} \Delta\dot{X}_i + O\left(\Delta X_i^2, \Delta\dot{X}_i^2\right) \tag{B.26}$$

Define **local linearized stiffness** and **damping** coefficients as

$$K_i = \left.\frac{\partial g}{\partial X}\right|_{X_i, \dot{X}_i} \tag{B.27}$$

$$D_i = \left.\frac{\partial g}{\partial \dot{X}}\right|_{X_i, \dot{X}_i} \tag{B.28}$$

Hence, $g_{i+1} - g_i \approx K_i \Delta X_i + D_i \Delta\dot{X}_i$ (B.29)

and the difference Eqn. (B.24) becomes linearized;

$$M\Delta\ddot{X}_i + g_{i+1} - g_i = \Delta F_i$$
$$M\Delta\ddot{X}_i + D_i\Delta\dot{X}_i + K_i\Delta X_i = \Delta F_i \tag{B.30}$$

The Eqns. (B.27) and (B.28) are formally identical to the one devised for a linear system. Thus, the numerical treatment is similar, except that at each time step, linearized stiffness and damping coefficients need be calculated. The algorithm for the numerical integration to find the system time response is:

(i) At time t_i, known variables for current state are $\left\{\dot{X}_i, X_i\right\}$, find from equation of motion: $\ddot{X}_i = M^{-1}\left[F_i - g\left(\dot{X}_i, X_i\right)\right]$;

(ii) Find local (linearized) stiffness and damping coefficients, $K_i = \left.\frac{\partial g}{\partial X}\right|_{X_i, \dot{X}_i}$ and $D_i = \left.\frac{\partial g}{\partial \dot{X}}\right|_{X_i, \dot{X}_i}$;

(iii) Form pseudo stiffness and forcing functions, $\left(\hat{K}_i, \Delta\hat{F}_i\right)$ from Eqns. (B.18) and (B.19);

(iv) Calculate $\Delta X_i = \left(\hat{K}_i\right)^{-1}\Delta\hat{F}_i$, and $\Delta\dot{X}_i = \frac{2}{\Delta t_i}\Delta X_i - 2\dot{X}_i$;

(v) Substitute $X_{i+1} = X_i + \Delta X_i$ and $\dot{X}_{i+1} = \dot{X}_i + \Delta\dot{X}_i$ at t_{i+1}

(vi) Increase time to t_{i+2} and return to step (i).

On the other hand, for the equation of motion for a nonlinear multi-DOF system:

$$\mathbf{M}\ddot{\mathbf{U}} + \mathbf{F}_{NL_{(t)}} = \mathbf{F}_{(t)} \tag{B.31}$$

where $\mathbf{F}_{NL_{(t)}} = f_{NL}\left(\mathbf{U}, \dot{\mathbf{U}}, \ddot{\mathbf{U}}\right)$ is a nonlinear function of $\mathbf{U}, \dot{\mathbf{U}}, \ddot{\mathbf{U}}$ (the vectors of generalized displacement, velocity, and acceleration).

$$t = t_i: \quad \mathbf{M}\ddot{\mathbf{U}}_t + \mathbf{F}_{NL_{(t)}} = \mathbf{F}_{(t)} \tag{B.32}$$

$$t = t_{i+1} = t + \Delta t: \qquad \mathbf{M}\ddot{\mathbf{U}}_{t+\Delta t} + \mathbf{F}_{NL_{(t+\Delta t)}} = \mathbf{F}_{(t+\Delta t)} \tag{B.33}$$

Subtract Eqn. (B.33) from Eqn. (B.32) to obtain:

$$\mathbf{M}\Delta\ddot{\mathbf{U}}_t + \Delta\mathbf{F}_{NL_{(t)}} = \Delta\mathbf{F}_{(t)} \tag{B.34}$$

Let,

$$\begin{aligned}\Delta\mathbf{F}_{NL_{(t)}} &= \mathbf{F}_{NL_{(t+\Delta t)}} - \mathbf{F}_{NL_{(t)}} \\ &\approx \left(\frac{\partial\mathbf{F}_{NL}}{\partial\mathbf{U}}\right)_t \Delta\mathbf{U}_t + \left(\frac{\partial\mathbf{F}_{NL}}{\partial\dot{\mathbf{U}}}\right)_t \Delta\dot{\mathbf{U}}_t + \left(\frac{\partial\mathbf{F}_{NL}}{\partial\ddot{\mathbf{U}}}\right)_t \Delta\ddot{\mathbf{U}}_t\end{aligned} \tag{B.35}$$

where

$$\Delta\ddot{\mathbf{U}}_t = \left(\ddot{\mathbf{U}}_{t+\Delta t} - \ddot{\mathbf{U}}_t\right), \quad \Delta\dot{\mathbf{U}}_t = \left(\dot{\mathbf{U}}_{t+\Delta t} - \dot{\mathbf{U}}_t\right), \quad \Delta\mathbf{U}_t = \left(\mathbf{U}_{t+\Delta t} - \mathbf{U}_t\right) \tag{B.36}$$

and define the following matrices, evaluated at each time step,

$$\mathbf{K}_t = \left(\frac{\partial\mathbf{F}_{NL}}{\partial\mathbf{U}}\right)_t; \qquad \mathbf{D}_t = \left(\frac{\partial\mathbf{F}_{NL}}{\partial\dot{\mathbf{U}}}\right)_t; \qquad \mathbf{M}_t = \left(\frac{\partial\mathbf{F}_{NL}}{\partial\ddot{\mathbf{U}}}\right)_t \tag{B.37}$$

These matrices represent linearized stiffness, viscous damping, and inertia coefficients. The difference Eqn. (B.34) becomes,

$$\begin{aligned}\mathbf{M}\Delta\ddot{\mathbf{U}}_t + \Delta\mathbf{F}_{NL_{(t)}} &= \Delta\mathbf{F}_t \\ \left(\mathbf{M} + \mathbf{M}_t\right)\Delta\ddot{\mathbf{U}}_t + \mathbf{D}_t\Delta\dot{\mathbf{U}}_t + \mathbf{K}_t\Delta\mathbf{U}_t &= \Delta\mathbf{F}_t\end{aligned} \tag{B.38}$$

The solution of this algebraic equation proceeds in the same form as for the S-DOF system.

APPENDIX C

ADIABATIC PROCESS OF IDEAL GAS IN PRESSURE VESSEL / HYDRO-PNEUMATIC TENSIONER

From the *first law* of thermodynamics:

$$dU = dQ - dW \tag{C.1}$$

The pressure-volume work done dW by the system is defined as:

$$dW = P \cdot dV \tag{C.2}$$

The internal energy of a gas is a state variable, and hence is a function of temperature. This allows us to state that:

$$dU = nC_V dT \tag{C.3}$$

For an adiabatic process, no heat is added ($dQ = 0$). Note that this does not mean that $dT = 0$; in fact, for an adiabatic process, none of the intensive quantities ($P, T, V/n$) will be constant (Watkins, 2003). Therefore, substituting Eqns. (C.2) and (C.3) into the Eqn. (C.1):

$$nC_V dT = -PdV \tag{C.4}$$

From the *Ideal Gas Law*, $PV = nRT$, differentiating this equation and we can obtain:

$$VdP + PdV = nRdT \tag{C.5}$$

$$dT = \frac{1}{nR}\left(VdP + PdV\right) \tag{C.6}$$

Upon the substitution of Eqn. (C.6) into Eqn. (C.4),

$$C_V\left(VdP+PdV\right)=-RPdV \tag{C.7}$$

$$VdP+PdV=-\frac{R}{C_V}PdV \tag{C.8}$$

From ideal gas law for a constant pressure process, we obtain the relation of $C_P=C_V+R$, substituting it into Eqn. (C.8) and hence:

$$VdP+PdV=-\frac{C_P-C_V}{C_V}PdV \tag{C.9}$$

The Eqn. (C.9) is divided by PV;

$$\frac{dP}{P}+\frac{dV}{V}=-\frac{C_P-C_V}{C_V}\frac{dV}{V} \tag{C.10}$$

$$\left(1+\frac{C_P-C_V}{C_V}\right)\frac{dV}{V}+\frac{dP}{P}=0 \tag{C.11}$$

$$\left(\frac{C_P}{C_V}\right)\frac{dV}{V}+\frac{dP}{P}=0 \tag{C.12}$$

Let $\gamma=C_P/C_V$ is defined as the heat capacity ratio; the Eqn. (C.12) can be rearranged as:

$$\gamma\frac{dV}{V}+\frac{dP}{P}=0 \tag{C.13}$$

Integrating Eqn. (C.13) to obtain:

$$\gamma\ln\left(V\right)+\ln\left(P\right)=C \tag{C.14}$$

Hence, rearranging Eqn. (C.14) and the equation to relate the pressure and volume for an adiabatic process is:

$$PV^{\gamma} = C \tag{C.15}$$

For the variation of pressure and volume during the adiabatic process, the Eqn. (C.15) can be further written as:

$$P_0 \cdot V_0^{\gamma} = P_1 \cdot V_1^{\gamma} = C \tag{C.16}$$

Let $P_1 = P_0 + \Delta P$ and $V_1 = V_0 - \Delta V$ during the compression of gas volume which increase the system pressure;

$$\frac{P_1}{P_0} = \left(\frac{V_1}{V_0} \right)^{-\gamma} \tag{C.17}$$

$$\frac{P_0 + \Delta P}{P_0} = \left(\frac{V_0 - \Delta V}{V_0} \right)^{-\gamma} \tag{C.18}$$

$$1 + \frac{\Delta P}{P_0} = \left(1 - \frac{\Delta V}{V_0} \right)^{-\gamma} \tag{C.19}$$

$$\frac{\Delta P}{P_0} = \left(1 - \frac{\Delta V}{V_0} \right)^{-\gamma} - 1 \tag{C.20}$$

$$\Delta P = P_0 \left(\frac{1}{\left(1 - \Delta V / V_0 \right)^{\gamma}} - 1 \right) \tag{C.21}$$

Therefore, the pressure variation in the gas tank / pressure vessel can be expressed as:

$$\Delta P_A = P_{A_0} \left(\frac{1}{\left(1 - \Delta V_A / V_{A_0} \right)^{\gamma}} - 1 \right) \tag{C.22}$$

In the industrial practice, this adiabatic equation is further utilized in order to determine the tension exerted by the hydro-pneumatic tensioner, in which the pressure is expressed as $P = T/A$:

$$\frac{P_0 + \Delta P}{P_0} = \left(\frac{V_0 - \Delta V}{V_0} \right)^{-\gamma} \tag{C.23}$$

$$\frac{T_0/A + \Delta T/A}{T_0/A} = \left(\frac{V_0 - \Delta V}{V_0} \right)^{-\gamma} \tag{C.24}$$

Since the cross-sectional area in the tensioner cylinder is *constant*, therefore,

$$\frac{T_0 + \Delta T}{T_0} = \left(\frac{z_0 - \Delta z}{z_0} \right)^{-\gamma} \tag{C.25}$$

$$T_0 + \Delta T = T_0 \left(1 - \frac{\Delta z}{z_0} \right)^{-\gamma} \tag{C.26}$$

$$T = T_0 \left(1 - \frac{\Delta z}{z_0} \right)^{-\gamma} \tag{C.27}$$